1136

TRANSPORTATION RESEARCH RECORD

Pavement Design

TRANSPORTATION RESEARCH BOARD
NATIONAL RESEARCH COUNCIL
WASHINGTON, D.C. 1987

Transportation Research Record 1136
Price: $18.50
Editor: Elizabeth W. Kaplan

mode
1 highway transportation

subject area
24 pavement design and performance

Transportation Research Board publications are available by ordering directly from TRB. They may also be obtained on a regular basis through organizational or individual affiliation with TRB; affiliates or library subscribers are eligible for substantial discounts. For further information, write to the Transportation Research Board, National Research Council, 2101 Constitution Avenue, N.W., Washington, D.C. 20418.

Printed in the United States of America

Library of Congress Cataloging-in-Publication Data
National Research Council. Transportation Research Board.

Pavement design.

(Transportation research record, ISSN 0361-1981 ; 1136)
1. Pavements, Concrete—Design and construction. 2. Pavements, Concrete—Testing. I. National Research Council (U.S.) Transportation Research Board. II. Series.
TE7.H5 no. 1136 [TE278] 88-600116 625.8'4
ISBN 0-309-04516-9

Transportation Research Record 1136

The **Transportation Research Record** series consists of collections of papers on a given subject. Most of the papers in a Transportation Research Record were originally prepared for presentation at a TRB Annual Meeting. All papers (both Annual Meeting papers and those submitted solely for publication) have been reviewed and accepted for publication by TRB's peer review process according to procedures approved by a Report Review Committee consisting of members of the National Academy of Sciences, the National Academy of Engineering, and the Institute of Medicine.

The views expressed in these papers are those of the authors and do not necessarily reflect those of the sponsoring committee, the Transportation Research Board, the National Research Council, or the sponsors of TRB activities.

Transportation Research Records are issued irregularly; approximately 50 are released each year. Each is classified according to the modes and subject areas dealt with in the individual papers it contains. TRB publications are available on direct order from TRB, or they may be obtained on a regular basis through organizational or individual affiliation with TRB. Affiliates or library subscribers are eligible for substantial discounts. For further information, write to the Transportation Research Board, National Research Council, 2101 Constitution Avenue, N.W., Washington, D.C. 20418.

Contents

Foreword

This Record contains 12 papers on the design and performance of pavements. Subjects include prestressed concrete pavements, finite-element analysis of concrete pavements, roller-compacted concrete, rutting of asphalt concrete overlays, laboratory and field measurements of pavement materials, and axle load restrictions on pavements with limited structural capacity.

Powers and Zaniewski report on the performance of a prestressed pavement built in Arizona in 1977. The traffic on the pavement has greatly exceeded the design assumptions, yet the pavement has performed adequately. Experiments conducted at the time of construction provide valuable data. Annual measurements of roughness and friction number have been collected along with periodic condition surveys. Distress that has developed since the last survey in 1983 is related to the design and construction of the pavement.

A computer program named FEACONS III (Finite Element Analysis of Concrete Slabs) was developed in Florida by Tia et al. in response to a need for a suitable analytical model to analyze the behavior of concrete pavements efficiently and realistically. The program has been used extensively in the analysis of existing concrete pavement and on a test road in Florida. The analytical model and computational procedure used by FEACONS III are described in detail, and the analytical results from the program are compared with actual measured results for a few specific cases.

Tayabji and Halpenny report on an investigation to develop procedures for the thickness design of roller-compacted concrete (RCC) for use in truck-parking areas, log-sorting yards, and pavements. The proposed procedures require computation of the allowable pavement stress based on the number of total load applications and computation of the expected pavement stress due to the design wheel loading. A design thickness is selected such that the expected pavement stress is less than the allowable pavement stress.

Tayabji and Okamoto report on a study conducted to determine the engineering properties and mix proportioning procedures for RCC. Specimens for laboratory tests were obtained from a full-scale test section constructed using a 10-ton vibratory roller. SPecimens were tested for flexural, split-tensile, and compressive strength; modulus of elasticity; and fatigue properties. The engineering behavior of RCC was determined to be similar to that of conventional concrete. Specimens for mix proportioning were prepared using a vibrating table.

Thirty-two projects in which asphalt concrete was overlaid on portland cement concrete pavements were analyzed by Carpenter and Enockson to develop regression relations between rutting and mixture properties of asphalt concrete. The analysis shows the importance of material properties, particularly gradation parameters, to the development of rutting. Structural tests of cored specimens show that stiffness and indirect tensile strength have a strong relationship with rutting that can develop in the overlay during its life. Permanent deformation can be controlled if the variability of the mixture coming out of the plant can be decreased.

Sousa and Monismith describe a laboratory study of equipment development and tests to determine the dynamic properties of paving materials in axial and torsional loading. Dynamic properties of an asphalt concrete and a uniform sand were determined by the excitation of hollow cylindrical specimens using two independent sinusoidal loads with frequencies up to 30 Hz.

The Commonwealth of Pennsylvania has the authority to restrict axle loads on its roads when it is believed that those axle loads will result in excessive damage to the pavement structure. Fernando et al. evaluated the sensitivity of pavement response and predicted performance to variations in load, layer moduli, and layer thicknesses. A theoretical elastic

layer analysis was conducted that considered various load magnitudes and configurations for different pavement thickness and material properties. Equivalence factors calculated for a broad range of pavement structures suggest that the use of AASHTO equivalence factors for evaluating the effects of alternative load limit policies is not advisable. A Pennsylvania load limit procedure produced results in closer agreement with the AASHO Road Test data than the AASHTO equivalence factors.

Potter shows by statistical analysis of flexible pavements designed by the California bearing ratio method that about one-half of the pavements will survive longer than their design life and one-half will fail before they reach their design service life.

Sanchez-Salinero et al. show that the Spectral-Analysis-of-Surface-Waves (SASW) method is a promising nondestructive technique for evaluating the mechanical properties of pavement systems and soil deposits. In this paper, the dispersion curves (frequency or wavelength versus phase velocity) obtained by assuming generation of only Rayleigh waves are compared with dispersion curves obtained when all types of waves are considered. Several cases with different types of layering are studied, and emphasis is placed on typical pavement systems.

Nazarian et al. show that the SASW method is quite sensitive to the modulus of the upper layers in secondary roads. Two sites on a secondary road were tested to determine the possible reasons for one section rutting while the other one did not. It was found that the SASW method is well suited for delineating layers that have low moduli or in which moduli appear to be decreasing and hence causing deterioration of the pavement.

Faraggi et al. present both theoretical and practical aspects of combining fluctuating thermal-warping stresses with repeated-loading stresses for predicting the behavior of concrete pavements. A new structural design method for Spain is also included.

Van Dam et al. look at bonding techniques, bond loss detection, and the effect of bond loss on the response and performance of bonded concrete overlays. Practices important to bond retention and relative performance of bonded verus disbonded concrete overlays are described.

Nine-Year Performance Evaluation of Arizona's Prestressed Concrete Pavement

RICHARD L. POWERS AND JOHN P. ZANIEWSKI

The Arizona Department of Transportation constructed an experimental prestressed pavement in 1977 and has monitored its condition for the past 9 years. The traffic volume on the pavement has greatly exceeded the design assumptions. Experiments conducted at the time of construction provide valuable data on curling and warping, shrinkage, elastic shortening, and so forth. Annual measurements of roughness and friction number have been collected, and periodic condition surveys have been made. The condition survey conducted in 1986 found that distress had developed in the pavement since the last survey in 1983.

Prestressed concrete pavements are an alternative to conventional concrete pavements. Prestressing the pavement provides two primary advantages, conservation of materials and greatly expanded joint spacing. Between 1971 and 1979, four full-scale experimental prestressed concrete pavements were constructed across the United States (*1*). One section constructed in Arizona in 1977 has been carrying high traffic volumes for the past 9 years. The performance of this pavement has been monitored periodically by the Arizona Department of Transportation (ADOT). The most recent distress evaluation was performed in the summer of 1986. Significant new distress had developed since the last condition survey 3 years before.

DESIGN AND CONSTRUCTION FEATURES

The experimental section of prestressed pavement is located on the Superstition Freeway (State Route 360) in Tempe, Arizona, beginning at Price Road and extending easterly to Dobson Road for a distance of approximately 1.2 mi. The main-line pavement consists of 30 prestressed slabs, 31.5 ft wide, 6 in. thick, and nominally 400 ft long (two slabs are 500 ft long). Each slab contains 16 strands 1/2 in. in diameter with 7 wires per strand. The strands were placed 1/2 in. below the slab center and were 24 in. on center. The slabs were stressed by the posttensioning method. The prestressed pavement cross section is composed of two 12-ft driving lanes and a 7.5-ft shoulder. A cross-sectional view of the prestressed pavement is shown in Figure 1 (*1*). Conventionally reinforced concrete slabs 8 ft long and 10 in. thick were placed between prestressed slabs to facilitate tensioning.

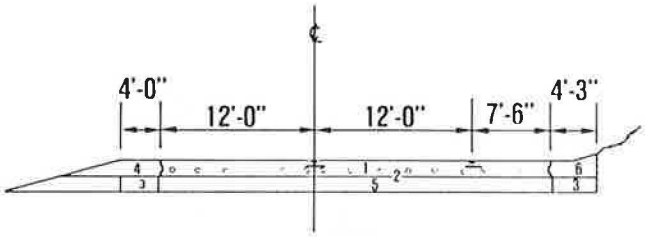

1. 6" P.C.C.P. W/16-1/2" Ø 270 ksi STRANDS
2. SAND LEVELING COURSE + DOUBLE LAYER H.S. 6 MILL POLYETHYLENE
3. 4" CEMENTED TREATED BASE COURSE
4. 6" ASPHALTIC CONCRETE
5. 4" LEAN CONCRETE BASE
6. SPECIAL CURB AND GUTTER

FIGURE 1 Cross section of prestressed pavement (*1*).

The joint design of prestressed concrete pavements is extremely important because the slabs are nominally 400 ft long. Thus extensive movement may be anticipated at the joints. On the basis of an assumed annual temperature variation of 100°F and a thermal coefficient of 6×10^{-6} in./in./°F, the calculated maximum differential movement at the slab ends was 1 1/2 in. An additional 1/2-in. gap was added to the design to ensure adequate joint width regardless of the time of year of construction. The details of the joint design are shown in Figures 2 and 3. A steel extrusion across the width of the pavement was selected to hold a neoprene seal. Stainless steel dowel bars 1 1/4 in. in diameter were used for load transfer. The dowel bars were spaced 12 in. on center.

Construction was conducted with a slip form paver modified to place the prestressing strands at the desired depth as it advanced down the roadway. The construction sequence was as follows (*2, 3*):

1. A sand leveling course and double-layer polyethylene sheet were placed on top of the lean concrete base (LCB) to reduce frictional resistance.
2. Steel prestressing cables were positioned on top of the polyethylene sheets.
3. A slip form paver was used to position the prestressing cables at a depth of 3.5 in. and to place the concrete on the roadway. A nylon bristle broom was dragged longitudinally along the pavement to provide surface texture.

R. L. Powers, Arizona Department of Transportation, 2104 South 22nd Avenue, Phoenix, Ariz. 85009. J. P. Zaniewski, Department of Civil Engineering, Arizona State University, Tempe, Ariz. 85287.

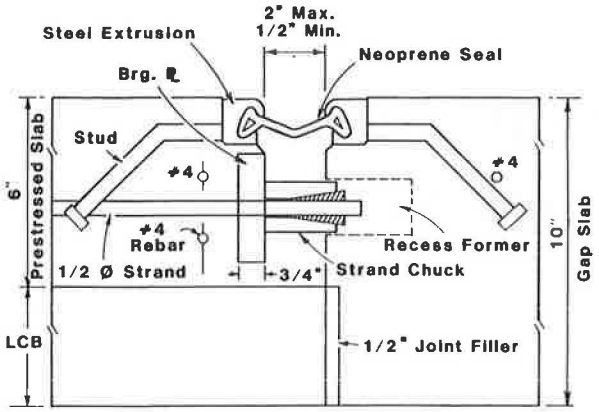

FIGURE 2 Joint detail: strand location.

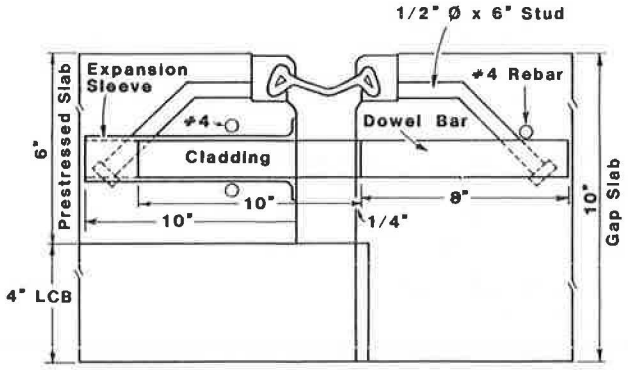

FIGURE 3 Joint detail: dowel bar location.

4. The following joint hardware was installed: dowel assembly, steel extrusion, bearing plates, reinforcing steel for bearing stress, and bulkhead.

5. Prestressing hardware was installed and the slabs were stressed in stages. The first stage of stressing was performed the day after concrete placement when the concrete had attained an average compressive strength of 1,300 psi. Second-stage stressing was performed 1 day after the initial stressing operation when average compressive strengths were approximately 2,400 psi. The final stage of prestressing was performed an average of 3 1/2 days after concrete placement when concrete cylinder strengths exceeded 3,000 psi. The actual amount of stressing depended on the concrete cylinder strength for each particular slab at the time the slabs were stressed. Table 1 gives the relationship between prestressed jacking force and concrete compressive strength used during construction of the slabs (*3*).

6. Gap slabs were constructed between consecutive prestressed pavement sections to facilitate prestress jacking operations. These slabs were conventionally reinforced concrete 31.5 ft wide, 8 ft long, and 10 in. thick. (These slabs are called gap slabs because they are used to fill the gap between adjacent prestressed slabs.)

7. The final items installed were the neoprene joint seals, used to prevent the intrusion of foreign objects into the joints.

The 30 prestressed slabs were placed between March 31, 1977, and April 13, 1977; installation took a total of 9 working days. Thirty-four gap slabs were placed from May 12, 1977, to May 17, 1977; this required a total of 4 working days. The installation of the neoprene joint seals took an additional 4 working days to complete (*3*).

TABLE 1 CONCRETE CYLINDER STRENGTH VERSUS JACKING FORCE

Cylinder Strength (psi)	Jacking Force (kips)
3,000	31
2,900	30
2,800	29
2,700	28
2,600	27
2,500	26
2,400	24
2,300	23
2,200	22
2,100	21
2,000	19
1,900	18
1,800	17
1,700	16
1,600	15
1,500	13
1,400	12
1,300	11
1,200	10
1,100	9

The major difficulty during construction was that the top sheet of the polyethylene film would slide over the bottom layer as the paver moved forward. The problem was at least partly resolved by nailing the sheet to the base layer.

Problems were encountered with the paving train as well. The paver broke down on several occasions causing undulations of the pavement profile. The nylon bristle broom was left stationary and induced transverse depressions across the entire width of the pavement at several locations.

Poor consolidation of the concrete material around the joint hardware was noted in most of the eastbound slabs. Apparently there was an unnoted change in the construction process for the subsequent construction of the westbound lanes; the consolidation problem is not as apparent in these slabs.

Approximate quantities and costs for the experimental section of prestressed pavement are given in Table 2 (*3*).

TRAFFIC VOLUMES

The Superstition Freeway primarily serves commuter traffic of three cities east of Phoenix. Design traffic was estimated to be 26,000 average daily traffic (ADT) with 1 percent trucks, with a 20-year total of 191 million vehicles (*3, 4*). The facility was constructed in the spring of 1977. In the fall of that year traffic was measured at 62,000 ADT with 2 percent trucks (*3, 4*). In 1984 the traffic count was 80,000 ADT with 3 to 4 percent trucks, and it increased to 98,000 ADT by 1986. Additional lanes were added to the facility to handle the

TABLE 2 APPROXIMATE PRESTRESSED PAVEMENT COST

Item	Unit	Quantity	Bid Price ($)	Total ($)
Prestressed concrete pavement (6 in.)	yd^2	40,700	9.00	366,300
Gap slab concrete pavement (10 in.)	yd^2	1,060	17.00	18,020
Prestressing concrete pavement	Lump sum	1	50,000.00	50,000
Polyethylene membrane	yd^2	40,700	0.75	30,525
Load transfer dowel assembly	Each	1,920	6.00	11,520
Expansion joint sealing	Linear ft	1,900	42.00	79,800
Total				556,165

Note: Total pavement area = 41,760 yd^2.

increased traffic volumes, but the majority of the truck traffic is on the prestressed concrete pavement. Thus the volume of truck traffic on this pavement was underestimated by an order of magnitude. The pavement has already carried more truck traffic than estimated for its entire design life.

EVALUATION OF PAVEMENT PERFORMANCE

The research plan for the experimental section called for two phases of pavement evaluation, a short-term study during and after construction and a long-term pavement performance evaluation. The short-term study consisted of measurement of temperature of the slab, slab movements due to stressing operations, joint width variations, and slab curling and cracking (*5, 6*). Long-term pavement performance evaluation consists of monitoring roughness, skid or frictional resistance, joint performance, and surface condition.

Short-Term Evaluation

Temperature

Concrete temperature measurements were made using thermistors embedded in the slab. Three locations were chosen to monitor variations in slab temperature. Two slabs were instrumented 4 ft from the shoulder and 4 ft from the expansion joint. The third location was midlength and 4 ft from the shoulder. The concrete temperature at each site was measured by six thermistors, two each at depths of 0.5, 3.5, and 5.5 in. An example of the temperature reading for one slab is given in Table 3 (*3*). The temperatures in the pavement were independent of pavement depth during the morning hours. As expected, the surface of the pavement was hotter than the bottom of the pavement during the afternoons. The maximum observed difference was 12° F.

TABLE 3 CONCRETE TEMPERATURE IN SLAB 15 *(3)*

		Temperature (°F)		
Date	Time	Top	Middle	Bottom
06/08/77	7:00 a.m.	97	101	99
	3:00 p.m.	130	123	122
06/23/77	7:00 a.m.	106	105	106
	3:00 p.m.	143	133	131
07/07/77	7:00 a.m.	105	104	105
	3:00 p.m.	146	144	144
07/21/77	7:00 a.m.	98	101	101
	3:00 p.m.	137	131	127
08/04/77	7:00 a.m.	100	100	104
	3:00 p.m.	134	130	126
08/18/77	7:00 a.m.	99	99	100
	3:00 p.m.	131	127	123
09/01/77	7:00 a.m.	93	87	87
	3:00 p.m.	110	104	104
09/15/77	7:00 a.m.	85	81	80
	3:00 p.m.	104	98	97
09/28/77	7:00 a.m.	80	78	78
	3:00 p.m.	102	95	90
10/13/77	7:00 a.m.	69	70	71
	3:00 p.m.	100	93	90

TABLE 4 LENGTH MEASUREMENTS OF SLAB 27 (3)

Date	Time	Air Temperature (°F)	Slab Length Between Pins (ft)
4/13/77	11:00 a.m.	79	396.364
4/14/77	9:30 a.m.	79	396.340
4/15/77	8:30 a.m.	68	396.305
4/18/77	9:00 a.m.	75	396.301
4/19/77	8:20 a.m.	70	396.285
6/08/77	8:45 a.m.	87	396.270
9/28/77	1:15 p.m.	95	396.286

Note: Concrete placed 4/12/77. The first reading was taken before any slab prestressing. The reading on 4/18/77 was taken after final prestressing had been applied to the slab.

Slab Movement

Changes in slab length were measured before application of the prestress jacking force, after each stage of prestressing, after 28 days, and intermittently thereafter. The results of these measurements for one slab are given in Table 4 (*3*). As the data in the table indicate, the slab shortened 0.024 ft on initial prestressing, 0.063 ft after final prestressing, and 0.078 ft 5 months after construction. The initial shortening was caused by the application of the prestressing force to the slab (i.e., elastic shortening); the final 0.015 ft of shortening is due to the effects of long-term shrinkage and creep of the concrete section. The average change in slab length was 0.0575 ft with a low of 0.024 ft and a high of 0.10 ft.

The change in slab length is also a function of the frictional resistance between the LCB and the prestressed slab. When the prestressing force was high enough to overcome the friction, slab movement began; this explains the time lag between prestress application and recorded slab movement.

Joint Widths

Joint widths were monitored in conjunction with the slab length measurements. Joint movement data are provided for Slab 2 in Table 5 (*3*). The original design called for a 2-in. maximum joint opening and a 1/2-in. minimum joint opening. The data indicate a consistent joint width with time; however, temperatures are missing for cooler periods.

TABLE 5 JOINT MOVEMENTS FOR SLAB 2 *(3)*

Date	Concrete Temperature(°F)	Joint Opening (in.)	
		West	East
06/08/77	113	1.726	1.771
06/23/77	124	1.781	1.828
09/28/77	84	2.047	1.109
10/13/77	94	1.813	1.859
10/31/77		1.969	2.000
11/21/77		1.859	1.906

Note: Pavement placed 4/4/77; joint placed 5/12/77.

Slab Curling

Slab curling was also monitored after construction of the pavement. Two slabs were instrumented with elevation plates mounted at approximately 4-ft intervals on the pavement surface. The vertical movement due to warping was measured with a level and precise leveling rod. The results of these measurements for the corner of the slab are given in Tables 6 and 7 (*3*). Positive numbers indicate an upward curl and negative numbers indicate a downward curl. Air temperature and concrete temperature were recorded. The data were recorded for approximately 32 hr. As expected, the corner of the slab moved downward as the temperature increased.

Initial Cracking

Crack surveys were conducted after completion of concrete placement and periodically after the stressing operation. An

TABLE 6 SLAB CURL DATA: BEGIN SLAB 19 *(3)*

Time	Reading (in.)	Change (in.)	Air Temperature (°F)	Concrete Temperature (°F)
7:15 a.m.	0.700			
8:45 a.m.	0.740	-0.040		
9:30 a.m.	0.755	-0.015	76	80
10:30 a.m.	0.774	-0.019	76	
11:30 a.m.	0.788	-0.014	80	
12:30 p.m.	0.799	-0.011	82	
1:30 p.m.	0.804	-0.005	84	
2:30 p.m.	0.808	-0.004	86	
3:30 p.m.	0.810	-0.002	88	112
4:30 p.m.	0.805	+0.005	83	108
5:30 p.m.	0.798	+0.007	83	103
6:30 p.m.	0.780	+0.018	82	88
7:30 p.m.	0.752	+0.028	78	82
8:30 p.m.	0.736	+0.016	76	78
9:30 p.m.	0.721	+0.015	74	78
10:30 p.m.	0.713	+0.008	72	72
11:30 p.m.	0.709	+0.004	70	72
12:30 a.m.	0.705	+0.004	64	66
1:30 a.m.	0.700	+0.005	62	64
2:30 a.m.	0.695	+0.005	60	60
3:30 a.m.	0.690	+0.005	58	60
4:30 a.m.	0.686	+0.004	58	56
5:30 a.m.	0.685	+0.001	60	58
6:30 a.m.	0.688	-0.003	58	58
7:30 a.m.	0.711	-0.023	68	74
8:30 a.m.	0.741	-0.030	74	88
9:30 a.m.	0.769	-0.028	80	94
10:00 a.m.	0.777	-0.008	80	100
10:30 a.m.	0.783	-0.006	80	100
11:30 a.m.	0.799	-0.016	90	104
12:30 p.m.	0.805	-0.006	86	102
1:30 p.m.	0.806	-0.001	88	110
2:30 p.m.	0.803	+0.003	86	98
3:30 p.m.	0.805	-0.002	88	91

Note: Readings taken on 5/11/77. + = slab curling upward and - = slab curling downward.

TABLE 7 SLAB CURL DATA: END SLAB 20 *(3)*

Time	Reading (in.)	Change (in.)	Air Temperature (°F)	Concrete Temperature (°F)
7:30 a.m.	0.500			
8:45 a.m.	0.467	-0.033		
9:30 a.m.	0.452	-0.015	76	80
10:30 a.m.	0.435	-0.017	76	
11:30 a.m.	0.421	-0.014	80	
12:30 p.m.	0.418	-0.003	82	
1:30 p.m.	0.418	0.000	84	
2:30 p.m.	0.418	0.000	86	
3:30 p.m.	0.418	0.000	88	115
4:30 p.m.	0.424	+0.006	83	111
5:30 p.m.	0.431	+0.007	83	105
6:30 p.m.	0.444	+0.013	82	89
7:30 p.m.	0.459	+0.015	78	80
8:30 p.m.	0.467	+0.008	76	76
9:30 p.m.	0.479	+0.012	74	72
10:30 p.m.	0.484	+0.005	72	70
11:30 p.m.	0.490	+0.006	64	64
12:30 p.m.	0.496	+0.006	64	64
1:30 a.m.	0.500	+0.004	62	66
2:30 a.m.	0.506	+0.006	60	60
3:30 a.m.	0.513	+0.007	58	58
4:30 a.m.	0.515	+0.002	58	58
5:30 a.m.	0.516	+0.001	60	58
6:30 a.m.	0.515	-0.001	58	58
7:30 a.m.	0.509	-0.006	68	68
8:30 a.m.	0.468	-0.041	74	82
9:30 a.m.	0.455	-0.013	74	94
10:00 a.m.	0.439	-0.016	80	100
10:30 a.m.	0.431	-0.008	80	102
11:30 a.m.	0.419	-0.012	80	102
12:30 p.m.	0.417	-0.002	86	102
1:30 p.m.	0.416	-0.001	88	108
2:30 p.m.	0.420	+0.004	88	98
3:30 p.m.	0.426	+0.006	88	94

Note: Readings taken on 5/11/77. + = slab curling upward and - = slab curling downward.

example of the crack survey information for one slab is shown in Figure 4. As shown in the figure, the cracks were measured and recorded twice daily after placement of the concrete and periodically after final prestressing. This example shows two longitudinal joints and several transverse cracks. The longitudinal joints were formed between lanes and between the driving lane and shoulder by placing plastic strips in the pavement at the time of construction. The transverse crack widths are small, on the order of 1/64 to 1/4 in. The final prestressing force closed several of the transverse cracks as indicated in Figure 4.

Long-Term Pavement Evaluation

The long-term performance of prestressed pavements is an important factor in the consideration of this method as a cost competitive alternative to conventional paving techniques. The life-cycle costs must be determined in order to evaluate the overall effectiveness of the prestressed pavement alternative. Four measures of long-term performance are monitored: (*a*) longitudinal profile characteristics or roughness, (*b*) surface skid or frictional resistance, (*c*) joint performance, and (*d*) surface distress.

Roughness

The ride quality of the experimental section of prestressed pavement was found to be considerably poorer than that of conventional concrete pavement sections immediately after construction. The initial roughness as measured by the Mays ride meter ranged from 180 to 270 in./mi whereas that of conventional concrete pavements generally ranges from 100 to 150 in./mi (*4*). This initial roughness is attributable to the type of surface texture used on the prestressed pavement section and problems encountered during construction.

The variation of surface roughness with time for the prestressed section based on Mays meter results is shown in Figure 5. For 3 years after construction, the roughness apparently increased significantly. In 1981 the roughness measurements dropped significantly and then were stable but highly variable from year to year. Much of the variability in the roughness measurements may be attributed to variations

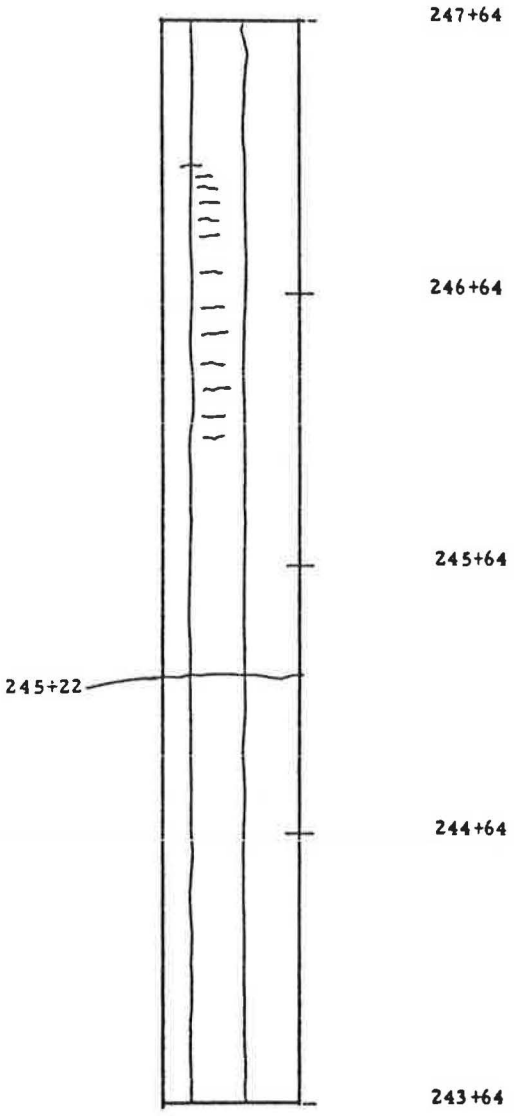

04-12-77	9:15 A.M. - No apparent cracks.
	3:15 P.M. - No apparent cracks.
04-13-77	7:45 A.M. - STA 245 + 22 ± full transverse 3/32" to 1/4" ±.
	4:00 P.M. - STA 245 + 22 ± full transverse 1/64" to 1/32" ±.
04-14-77	8:00 A.M. - STA 245 + 22 ± full transverse barely visible.
	31k
04-15-77	7:30 A.M. - STA 245 + 22 ± full transverse hairline.
04-18-77	10:30 A.M. - STA 245 + 22 ±.
04-26-77	9:30 A.M. - STA 245 + 22 ± full transverse closed.
	STA 246 + 95 ± 28' from median 3' long 3/16 - 1/16.
06-28-77	245 + 22 crack closed.
	246 + 93 to 246 + 97 three transverse.
	Cracks 10' in from shoulder.
	Two 12" and one 3' long, width between 1/32" and 3/32".
	245 + 77 to 245 + 83 seven cracks both longitudinal and transverse 10' in from shoulder. Widths from hairline to 1/16".
09-21-77	Same as 06-28-77.
03-06-78	Same as 06-28-77.
	246 + 50 4 transverse cracks in travel lane only.
	246 + 25 transverse crack in distress lane.
	243 + 85 2' long crack in right W.P in travel lane.
05-31-79	245 + 80 6 small 1 1/2' cracks in D.L. otherwise same as last survey.
02-18-81	Many small cracks at about 8' from edge of prestress pavement.
04-12-83	Many small transverse cracks in drive lane. Transverse crack at STA 245 + 60 across drive lane.

FIGURE 4 Example of crack survey data (westbound Slab 23).

in the Mays meter. ADOT has an active program for maintaining the calibration of their Mays meter, so the measurements shown in Figure 5 are on a common scale.

Friction

Measurements of frictional (skid) resistance were conducted after completion of construction and annually thereafter with the use of a Mu-Meter. The results of friction measurements of the pavement are given in Table 8 (*3*). The initial friction number is high because traffic has not worn down the rough surface texture. The friction number appears to have reached a consistent value of approximately 45 for both the westbound and the eastbound roadway sections. This value is within the safe range of frictional resistance, and the pavement surface appears to be withstanding the heavy traffic volumes.

Joint Performance

The performance of joints has been a major problem for the prestressed pavement section. Maintenance forces have repaired these joints several times during the life of the pavement. The poor joint performance also partly explains why the roughness values are so high. Spalling of the joints has been the biggest problem to date. Poor consolidation of the concrete material around the joint hardware is probably the main cause of spalling at the joints. High stresses induced by truck loading also could have caused spalling at the joints. Most spalled areas have been repaired with epoxy. The steel extrusions were welded and the neoprene joint material was replaced by maintenance forces on several joints. Before repair, however, foreign material entered some of the joints and may pose a problem in the future. During the condition survey in 1986, it was noted that joint condition had again deteriorated. The neoprene seal is missing from practically all of the joints. The joints are filled with sand, gravel, and other

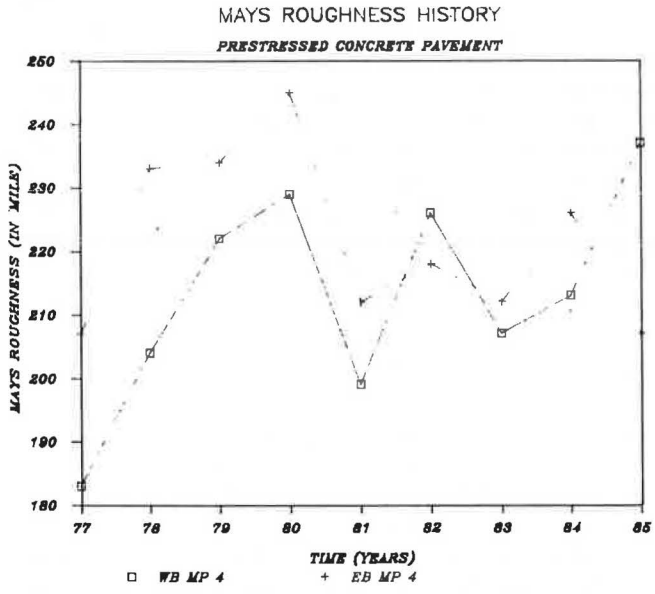

FIGURE 5 Roughness versus time for the prestressed pavement.

TABLE 8 MU-METER VALUES FOR PRESTRESSED PAVEMENT *(3)*

	1977	1978	1979	1980	1981	1982	1983	1984
Eastbound								
MP 4	89		54	38	50	43	43	58
MP 5			52	41	52	41	49	46
Westbound								
MP 4	82		46	38	45	32	39	40
MP 5			53	42	47	41	41	50

Note: Average values for both lanes. MP = milepost.

debris. The steel extrusion is broken at one joint. Many of the joints have spalling and corner breaks. Maintenance crews have placed asphalt patches in several locations.

Surface Condition Surveys

Condition surveys have been performed several times to monitor the performance of each slab with time. The location and severity of all cracks in the prestressed concrete slabs were recorded as shown in Figure 4. After completion of construction in 1977, subsequent crack surveys were conducted in 1978, 1979, 1981, 1983, and 1986. Figure 4 shows the history of each slab with time and the progression of cracks in the pavement section.

The prestressed pavement section was evaluated by the authors during July 1986. The surveys were conducted early in the morning when traffic volumes were relatively low and temperatures ranged between 90° F and 100° F. Even though the surveys were performed early in the morning, the traffic volumes forced the observation of distress from the shoulder.

Eastbound Roadway Section The most notable problem with the eastbound section was the number of joints patched the entire width with epoxy. This condition was probably caused by impact loading at the joints and underconsolidation of the concrete around the joint hardware, which resulted in premature cracking and spalling along the joint. Several of the welded steel extrusions have been broken and repaired by ADOT maintenance crews. Figure 6 shows the epoxy patches and the transverse cracks near the joint indicating impending joint failure. Figure 7 shows spalling typical of several of the slabs near the joints. This figure shows the effect of underconsolidation of the concrete; the steel extrusions have caused the spalling to accelerate. The condition survey indicated that 90 percent of the joints in the eastbound direction have been repaired with epoxy patches.

During the summer of 1985 one prestressing strand anchor failed on the east end of Slab 1. The bearing plate was removed, the strand cut, and an asphalt patch installed. This repair is shown in Figure 8. Figure 9 shows a close-up of the longitudinal crack located near the broken strand. The longitudinal crack between the shoulder and the driving lane is continuous along the section but has significantly widened near the broken strand. Heavy truck loading is applied in close proximity to the strand. It is assumed that the prestressing force has been entirely dissipated and is not contributing to the structural capacity of the pavement section. A detailed investigation of the effects of this failure will be undertaken.

A section of prestressed concrete pavement was removed and replaced in Slab 4 as shown in Figure 10. The repair appears to be performing well although new longitudinal cracks have appeared in the original pavement on either side of the repair. The continuity of the prestressing steel was maintained for this repair.

Several slabs and gap slabs have experienced corner breaks due to warping stress, restraint provided by the load transfer devices, and incompressible materials in the joints. In many cases the patches are also failing as shown in Figure 11.

Several surface defects were noted in the prestressed pavement slabs of the eastbound lanes including pop-outs, spalling of the cracks, poor concrete consolidation, depressions caused by the paving and texturing operations, map cracking, transverse cracking, and longitudinal cracking. The longitudinal cracks have appeared since the last condition survey in 1983. Several of the transverse cracks have opened and spalled since the previous survey.

Westbound Roadway Section The condition of the westbound section was much better than that of the eastbound section. Only a few of the joints had been repaired with epoxy patches across the entire roadway. The westbound section was constructed after the eastbound and special care was taken to provide adequate consolidation of the concrete near the joint hardware. Several of the joints are, however, beginning to show some cracking. Some of the joints were filled with debris. Longitudinal cracks are much less frequent than on the eastbound lanes.

One joint had experienced a corner break and was patched with asphalt. The patching material is damaged as shown in Figures 12 and 13. Note the size of the studs and their close spacing. The studs are 1/2 in. in diameter, 6 in. long, and spaced 6 in. apart. It is hypothesized that this design has resulted in stress concentrations in a plane 6 in. from the joint. Failure of both the concrete and the steel studs indicates that this is an inadequate design for the joints.

Several surface defects were noted in the westbound section including depressions caused by paving operations (Figure 14), poor concrete consolidation, polishing, transverse cracks with spalling (Figure 15), pop-outs, transverse cracks, crescent cracks in the wheel path, and longitudinal cracks.

FIGURE 6 Epoxy patch and transverse crack at a joint.

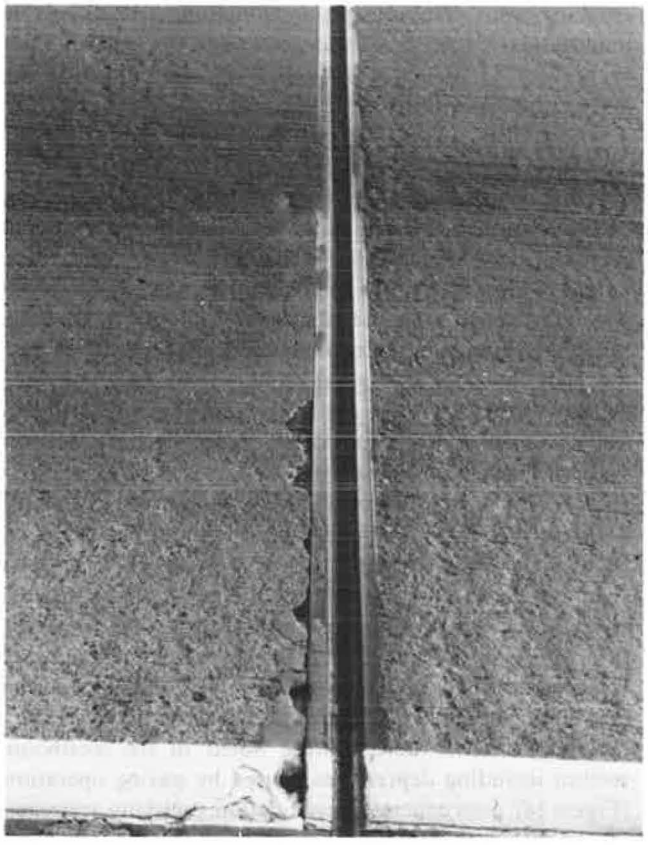

FIGURE 7 Spalling at a joint.

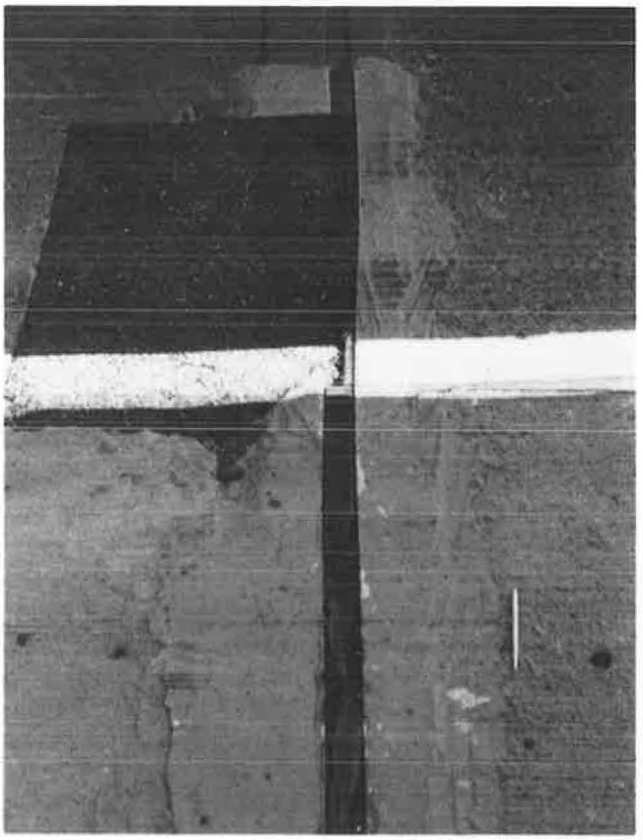

FIGURE 8 Repair patch at location of broken strand.

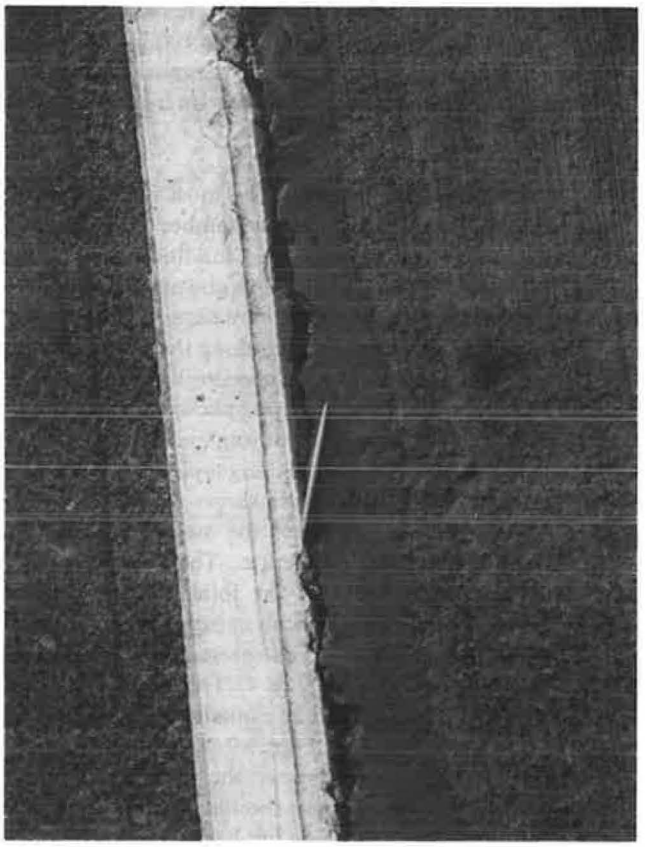

FIGURE 9 Close-up of longitudinal crack where the tendon is broken.

FIGURE 10 Repair of concrete.

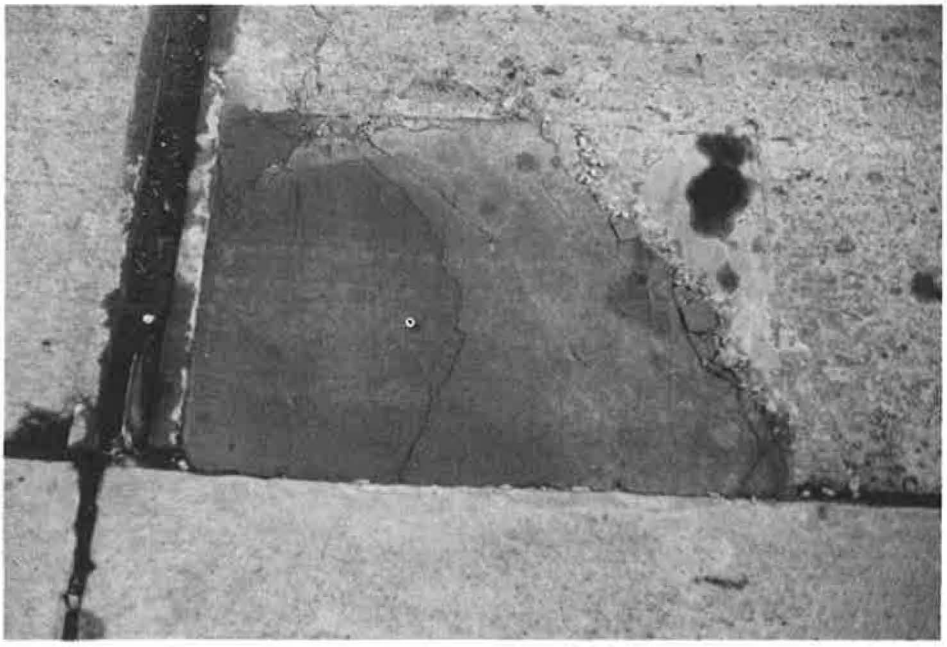

FIGURE 11 Example of failed patch at corner break.

CONCLUSIONS

Prestressed pavement in Arizona has performed well for the past 9 years but is now showing distress. Truck traffic volume on the facility has exceeded design assumptions. The pavement has carried more trucks than the volumes estimated during design.

The predominant maintenance problem is correction of spalling at the joints. This is particularly bad on the eastbound lanes, which were the first constructed. The distress at the joints may be attributed primarily to poor consolidation of the concrete. The joint design may further aggravate the failure problem at the joints.

The excessive roughness of the pavement may be attributed to construction problems. The problems with construction may be largely charged to the experimental nature of the project. There was a significant reduction in problems during construction of the second part of the project.

Although the levels of distress are relatively minor, there has been a significant increase in the amount of distress during the past 3 years. The most notable types of new distress are spalling of the midslab transverse cracks and

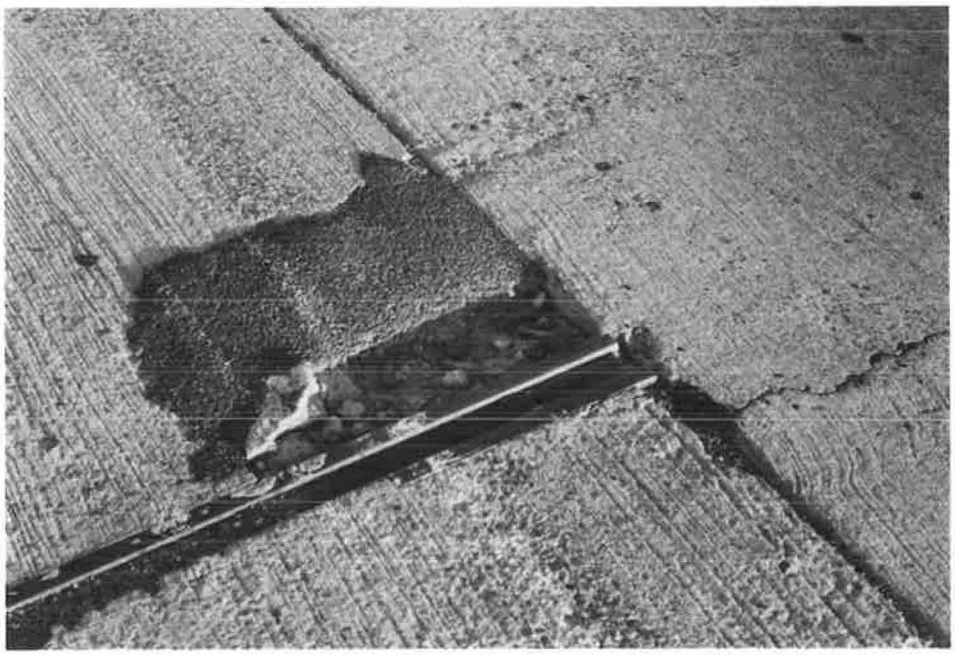

FIGURE 12 Failed asphalt patch at corner break.

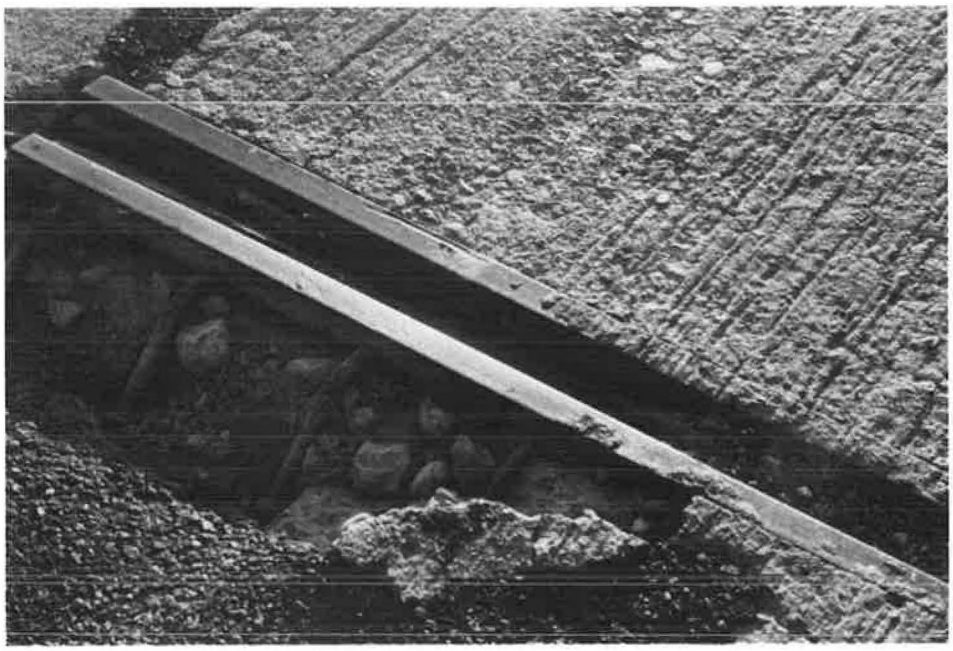

FIGURE 13 Exposed extruded steel at joint.

development of longitudinal cracks. These types of distress are of greater concern in a prestressed pavement than in a conventional pavement because of the thickness of the slab. For the pavement to continue to perform, aggregate interlock must provide load transfer across the longitudinal crack. The prestress design will not assist in maintaining the aggregate interlock of the longitudinal cracks.

The performance of the prestressed pavement could have been significantly improved through better design and construction. The paver train was stopped several times during construction; this contributed to the excessive initial roughness of the pavement. The gap slabs should be eliminated, thereby removing one-half of the joints. Actual joint design could be improved to facilitate construction. Slab length could be increased to further reduce the number of joints. The neoprene joint sealer was inadequate and a new method is required for sealing joints. The 500-ft-long slabs are performing as well as the other slabs.

These conclusions were derived with the benefits of hindsight. The performance of the prestressed pavement has been adequate, and the lessons learned from the pavement have made the experiment a success. Prestressed pavements

FIGURE 14 Depression caused when paving train stopped.

FIGURE 15 Spalling of transverse crack.

appear to be a viable alternative to conventional concrete pavements at least for the initial design period. Maintenance and rehabilitation of the structure are now primary concerns.

ACKNOWLEDGMENTS

The work of Gene R. Morris and Hal C. Emery was instrumental in developing and constructing Arizona's prestressed section. Appreciation is also expressed to ADOT's Materials Section and Transportation Planning Section for the information they provided.

REFERENCES

1. W. L. Gramling, T. P. Teng, and G. R. Morris. *Prestressed Pavement Performance in Four States, A Panel Report.* FHWA Report FHWA/RD-82/169. FHWA, U.S. Department of Transportation, Sept. 1983.
2. H. C. Emery. *Prestressed Concrete Pavement Construction.* Internal Report. Arizona Department of Transportation, Phoenix, 1977.
3. G. R. Morris and H. C. Emery. *FHWA Demonstration Project 17: Prestressed Concrete Pavement Construction, Arizona's Prestressed Concrete Pavement.* Research Section, Arizona Department of Transportation, Phoenix, Oct. 1977.
4. G. R. Morris, F. R. McCullagh, and E. B. Smithson. Prestressed Concrete Pavement: Six Year Performance of the Arizona Project. Presented at the 21st Paving and Transportation Conference, The University of New Mexico, Albuquerque, Jan. 9-11, 1984.
5. G. R. Morris, R. J. Peters, and P. E. Mueller. Arizona's Superstition Freeway: A Continuing Test Road for Concrete Pavement Design. Presented at the American Concrete Institute Annual Convention, San Diego, Calif., March 1977.
6. G. R. Morris, R. J. Peters, and P. E. Mueller. *Concrete Pavement Test Sections in Arizona's Superstition Freeway.* Internal Report. Arizona Department of Transportation, Phoenix, 1977.

Publication of this paper sponsored by Committees on Rigid Pavement Design, on Rigid Pavement Construction and Rehabilitation, and on Pavement Rehabilitation.

FEACONS III Computer Program for Analysis of Jointed Concrete Pavements

MANG TIA, JAMSHID M. ARMAGHANI, CHUNG-LUNG WU, SHAU LEI, AND KEVIN L. TOYE

A computer program named FEACONS III (Finite Element Analysis of CONcrete Slabs) was developed in response to a need for a suitable analytical model to analyze the behavior of concrete pavements effectively and realistically. The program has been used extensively in the analysis of existing concrete pavements and a test road in Florida. The analytical model and computational procedure used by FEACONS III are described in detail, and the analytical results from the program are compared with actual measured results for a few specific cases. The FEACONS III program was shown to be both versatile and effective in the analysis of concrete pavement response. The modeling of the edge by means of edge stiffness and the joint by means of linear joint stiffness and torsional joint stiffness produced fairly realistic analytical results. It is hoped that this paper can enhance understanding and proper usage of the program and increase the awareness of highway engineers of the importance of the effects of temperature, joint, edge, and subgrade conditions to concrete pavement response.

During the past few years the University of Florida has been working with the Florida Department of Transportation in the testing and evaluation of concrete pavements in Florida. Some of the objectives of this ongoing research work include (*a*) better understanding of the effects of temperature, moisture, joint, edge, and subgrade conditions on pavement behavior and performance; (*b*) determination of causes of failure in existing pavements; and (*c*) development of an effective and convenient procedure for the use of the falling-weight deflectometer in the evaluation of pavement conditions. In the course of this work, a need arose for a suitable analytical model that could be used to analyze the behavior of concrete pavements effectively and realistically. Subsequently, a computer program named FEACONS (Finite Element Analysis of CONcrete Slabs) was developed. FEACONS was written in a structured fashion such that it could be easily modified and enhanced. The present or third version of the program, named FEACONS III, can analyze the response of a concrete pavement system subjected to combinations of concentrated and uniform vertical loads. It can consider the following factors in the analysis:

1. Weight of concrete slabs,
2. Subgrade voids beneath concrete slabs,
3. Effects of joints,
4. Looseness of dowel bars,
5. Effects of edges,
6. Effects of temperature differentials between the top and the bottom of slabs, and
7. Nonlinear subgrade response characteristics.

The output of the program may include the following:

1. Deflections of concrete slabs due to their own weight and temperature effects;
2. Deflections of concrete slabs due to applied loads;
3. Moments, stresses, and principal stresses in concrete slabs; and
4. Maximum deflection, moments, stresses, and principal stresses in concrete slabs.

FEACONS III has been used extensively in the analysis of existing concrete pavements on a test road in Florida, and some of the results were presented at the Annual Meeting of the Transportation Research Board in 1986 (*1*). The purpose of this paper is to describe in full detail the analytical model and the computational procedure used by FEACONS III and to compare the analytical results from the program with actual measured results for a few specific cases. It is hoped that this paper can enhance the understanding and proper usage of the program and increase awareness of highway engineers of the importance of the effects of temperature, joint, edge, and subgrade conditions to concrete pavement performance.

MODELING OF CONCRETE PAVEMENT

A jointed concrete pavement is modeled by a three-slab system as shown in Figure 1. Each concrete slab is modeled as an assemblage of rectangular plate bending elements with three degrees of freedom at each node, namely,

1. Translation in the vertical (z) direction,
2. Rotation about the x-axis, and
3. Rotation about the y-axis.

The finite-element formulation of the rectangular plate bending element, known as the MZC rectangle, was developed

Department of Civil Engineering, University of Florida, Gainesville, Fla. 32611.

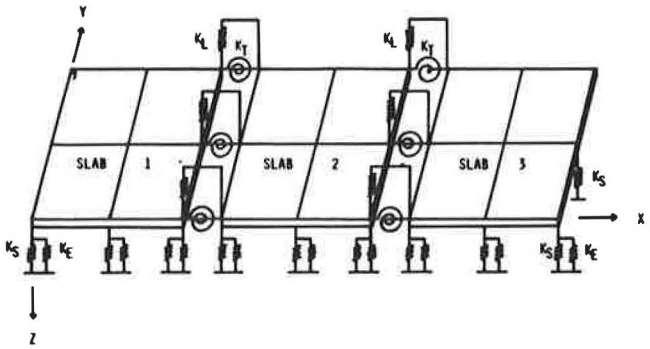

FIGURE 1 Finite-element modeling of a three-slab pavement system.

by Melosh (*2*) and Zienkiewicz and Cheung (*3*). The MZC rectangle has been used widely to model concrete pavement slab behavior in finite-element computer programs such as WESLIQUID and WESLAYER developed by the U.S. Army Corps of Engineers Waterway Experiment Station (*4*), ILLISLAB developed by the University of Illinois (*5*), and the finite-element programs developed by Purdue University (*6*) and the University of Kentucky (*7*). The formulation and characteristics of the MZC rectangular element are presented in the Appendix.

Load transfers across the joints between two adjoining slabs are modeled by shear (or linear) and torsional springs connecting the slabs at the nodes of the elements along the joint. The linear and torsional spring elements and the corresponding stiffness matrix are shown in Figure 2. Looseness of the dowel bars is modeled by a specified slip distance, such that shear and moment stiffnesses become fully effective only when the slip distance is overcome. The effective dowel stiffnesses are modeled as varying linearly with the difference in deflection at the joint, when the difference in deflection is less than the slip distance. The relationship of effective joint stiffnesses and difference in deflection at the joint is shown in Figure 3. Frictional effects at the edges are modeled by shear springs at the nodes along the edges. The subgrade is modeled as a liquid or Winkler foundation by a series of vertical springs at the nodes. Subgrade voids are modeled as initial gaps between the slab and the springs at the specified nodes. A spring stiffness of zero is used when a gap exists. Either a linear or a nonlinear load-deformation relationship for the springs can be specified. For the linear case, the subgrade stiffness remains constant as long as the slab and the subgrade are in contact with one another. For the nonlinear case, a load-deformation relationship of the following form is used:

$$F = Ad + Bd^2 \tag{1}$$

where

F = force/area,
d = deflection, and
A and B = coefficents to be specified in the input.

The subgrade stiffness is thus equal to $A + 2Bd$, which varies with the deflection.

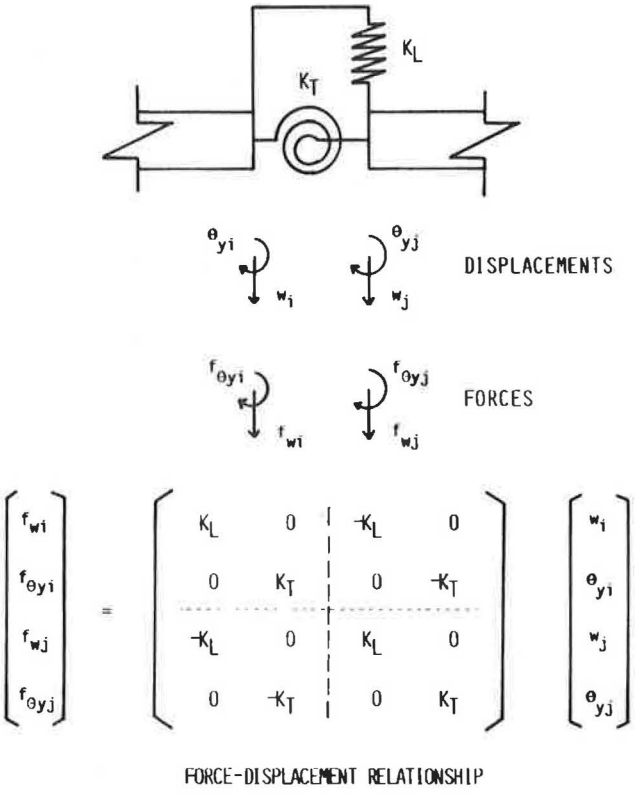

FIGURE 2 Linear and torsional spring elements modeling joint behavior.

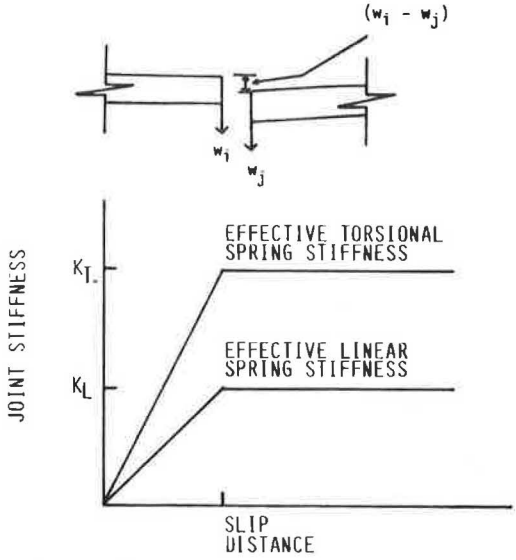

FIGURE 3 Effective joint stiffnesses as functions of the difference in deflection at the joint.

SCHEME OF THE COMPUTER PROGRAM

Figure 4 is a flowchart showing the major computational steps in the FEACONS III program. The program computes the total induced slab deflections in three major steps: First,

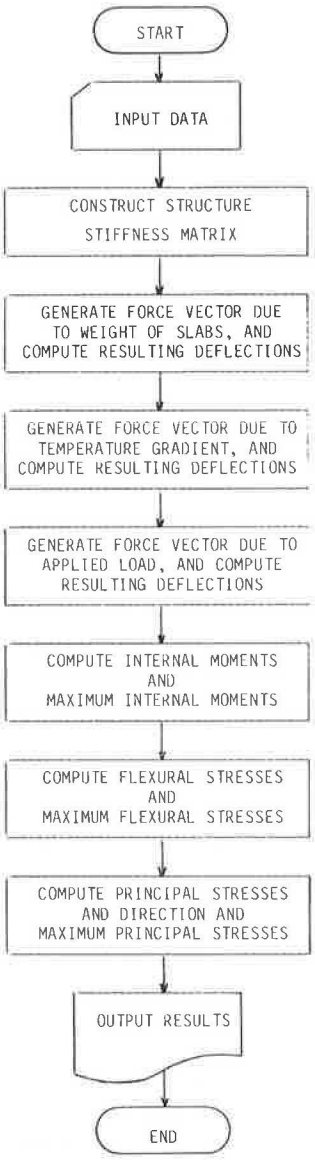

FIGURE 4 Simplified flow chart showing the major steps of FEACONS III.

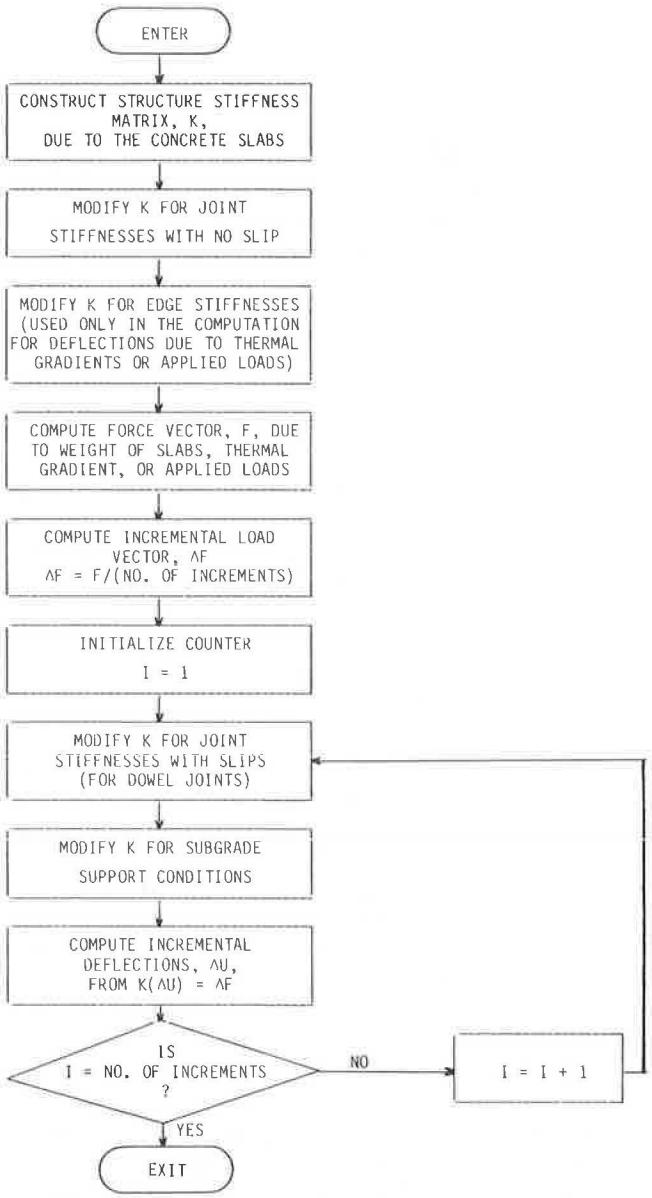

FIGURE 5 Flow chart of scheme for computing slab deflections.

the deflections caused by the weight of the slab are computed. Second, the additional deflections caused by thermal curling are computed. Third, the additional deflections caused by applied loads are computed. The program then computes the internal moment intensities, flexural stresses, and principal stresses in the slab from the final total slab deflections. Computational schemes used in these major steps are described in the following subsections.

Computation of Slab Deflections

Figure 5 is a flowchart that shows the scheme for computing the deflections due to the weight of the slabs, thermal gradients, or applied loads. An incremental computational procedure is used. The force vector (F) due to the weight of the slab, thermal gradients, or applied loads is first computed. The force vector is then divided by the number of increments specified to obtain the incremental load vector (ΔF). The deflections (ΔU) caused by the incremental force vector are computed from the stiffness equation

$$K(\Delta U) = \Delta F \tag{2}$$

where

K = structure stiffness matrix,
ΔU = vector of incremental nodal deflections, and
ΔF = vector of incremental nodal forces.

The structure stiffness matrix (K) is constructed from the stiffness matrices of the plate elements (see Appendix), the stiffness matrices of the joint spring elements, the stiffnesses of the edge springs, and the stiffnesses of the subgrade

springs, according to the finite-element mesh selected and the deflections of the slab at that point. Edge springs are used to model the frictional effects at the edges and thus are used only in the computation for the deflections due to thermal curling and applied loads. After each computation of incremental deflections, K is modified according to the newly deflected positions of the slab. The new K is then used to compute the next set of incremental deflections.

Three numbers, indicating the numbers of increments to be used in the three major computational steps, have to be specified in the program input. In general, the higher the number of increments, the better the accuracy of the results of analysis will be. However, if K does not change throughout a computational step, only an increment of 1 needs to be specified for that computational step. This applies to the case in which the subgrade contact conditions do not change throughout a computational step and no slips are specified at the joints.

The weight of the slabs is modeled as a uniform distributed load. The structure force vector due to the weight of the slabs is constructed from the force vectors of the plate elements due to a uniform distributed load. The explicit expression for the element force vector due to a uniform distributed load is given in Equation A-25 in the Appendix.

The expression for the equivalent nodal forces on a plate element due to a uniform thermal gradient is given in Equation A-27 in the Appendix. These element force vectors are used to generate the structure force vector for the thermal effects.

The structure force vector due to applied loads is constructed from the concentrated nodal forces and the element force vector due to uniform distributed loads.

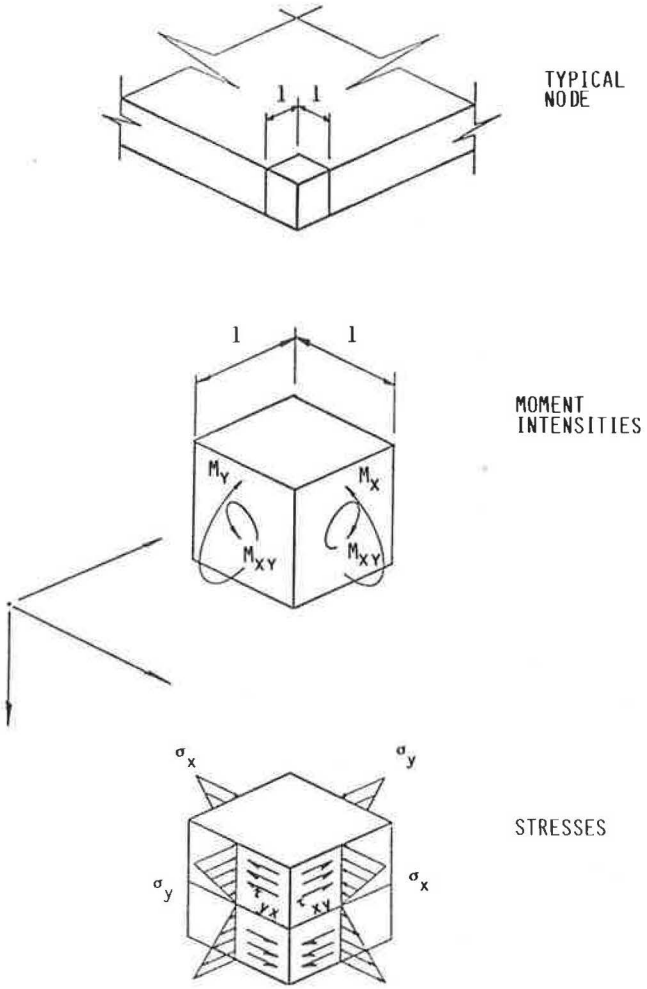

FIGURE 6 Moment intensities and stresses at a node.

Computation of Internal Moment Intensities

The internal moments per unit length at the nodes are calculated from the final nodal deflections. The nodal deflections for each element are first extracted from the final structure deflection vector and then used to compute the internal moment intensities of the element at the nodes. The expression for computing the internal moment intensities is given in Equation A-29 in the Appendix. The moment intensities at each node are the two bending moment intensities (M_x and M_y) and the twisting moment intensity (M_{xy}). M_x is the bending moment intensity due to σ_x, flexural stress in the x-direction. M_y is due to σ_y, flexural stress in the y-direction. M_{xy} is due to τ_{xy}, shearing stress in the xy-direction. The directions of these moment intensities and the corresponding stresses are shown in Figure 6.

Two elements that are incident at the same node may have different moment intensities for that node. This is because only continuity of nodal displacements is required and the moment intensities are dependent on the individual geometry of an element and thus are unique for an individual element. To obtain more representative values of moment intensities for a node, the program calculates the average values of the moment intensities as computed from the adjoining elements and uses them for the computation of stresses.

Computation of Stresses

Flexural and shearing stresses are calculated from the moment intensities using the following equations from classical thin plate theory:

$$\sigma^x = \frac{12z}{t^3} = M_x \tag{3}$$

$$\sigma_y = \frac{12z}{t^3} M_y \tag{4}$$

$$\tau_{xy} = \frac{-12z}{t^3} M_{xy} \tag{5}$$

where t is thickness of the slab and z is distance from the centroid of the slab. The program computes the stresses at the bottom of the slab by setting $z = t/2$ in the equations.

COMPARISON OF FWD MEASUREMENTS WITH ANALYTICAL RESULTS

The FEACONS III program has been used to analyze falling-weight deflectometer (FWD) data obtained from existing concrete pavements. A few examples are presented here to illustrate how the FWD data can be analyzed and how well the analytical results obtained from the FEACONS III program match actual FWD measurements.

Modeling of an FWD Load

The FWD applies an impulse load to the pavement by means of a weight dropped from a specified height onto a circular loading plate, which is usually 30.5 cm (12 in.) in diameter. The FWD load was modeled in the analysis as a static load uniformly distributed over a square area 30.5 × 30.5 cm (12 × 12 in.).

FWD Load at the Center of a Slab

The deflection basin caused by an FWD load applied at the center of a slab can be used to evaluate the subgrade modulus and the concrete modulus of a pavement. A deflection basin is defined here as a profile of maximum induced deflections, which are measured by geophones placed at appropriate positions on the slab. Several prediction equations have been developed by the authors to relate FWD deflections to subgrade modulus. These prediction equations can be used to estimate the subgrade modulus from the FWD deflection data. The FEACONS program can then use these values as the material parameters and compute the expected deflection basin. The computed deflection basin can then be compared with the measured one to determine if the estimated parameter values are reasonable and to adjust these parameter values, if necessary. The details of the interpretation of FWD data will be presented in a follow-up paper. Here, the main purpose is to show how well deflections computed by the FEACONS model match measured deflections.

Example 1 is a 9-kip (40-kN) FWD load at the center of a slab from a test section of I-10 in Jefferson County, Florida. The concrete slab is 12 ft wide, 20 ft long, and 9 in. thick and has doweled joints. The test was run at midnight when the recorded temperature differential between the top and the bottom of the slab is negative. With the temperature lower at the top of the slab, the slab should be curled slightly downward at the center and thus should have full contact with the subgrade at the center. The full contact condition was verified by a plot of FWD load versus deflection at the center of the load that indicated a linear load-deflection relationship. The elastic modulus of the concrete was determined to be 4,076 ksi (28.08 GPa) from core samples taken from the test slab and tested in the laboratory. The subgrade modulus was determined to be 221 pci (60.01 MN/m^3) by the following regression equation:

$$\log_{10}K_s = 3.2507 - 1.8966 \log_{10}D_o \quad (6)$$

where K_s is subgrade modulus (in kci) and D_o is deflection (in μm) at the center of a 9-kip FWD load applied at the center of the slab.

This regression equation is applicable for a concrete slab with a thickness of 9 in. (23 cm) and an elastic modulus of 4,000 ksi (28 GPa) and is an example of the regression equations developed in this study.

The determined values of concrete modulus and subgrade modulus were used as input parameters in the FEACONS III program, and the deflection basin caused by a 9-kip (40-kN) FWD load at the center of the slab was computed. Figure 7 shows the comparison of the measured deflection basin along the longitudinal centerline with the deflection basin computed by the FEACONS III program. It can be noted that the computed deflection basin matches the measured one fairly well.

For this loading condition, results of analysis indicated that edge stiffness (K_E) and joint stiffness (K_L and K_T) had negligible effects because the edges and joints were far from the FWD load.

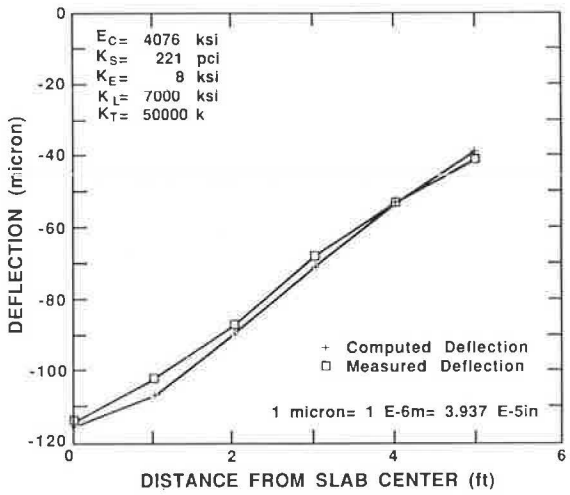

FIGURE 7 Deflection basin along longitudinal centerline due to a 9-kip FWD load at the center of the slab.

FWD Load at the Edge of a Slab

Example 2 is a 9-kip (40-kN) FWD load at the center of the edge of a slab. The test slab is the same one used in Example 1, and thus the material parameters are the same. Tests were conducted at midday when the recorded temperature differential is positive. With the temperature higher at the top of the slab, the slab was curled downward at the edges and had full contact with the subgrade at the edges. This full contact condition was verified by the linear load-deflection relationship observed from the FWD data.

Using the same concrete modulus and subgrade modulus used in Example 1, various deflection basins were calculated by varying K_E and compared with the measured one. By this trial-and-error procedure, K_E was determined to be 8 ksi (55 MPa). Figure 8 shows the comparison of the measured deflection basin along the edge with the computed one from

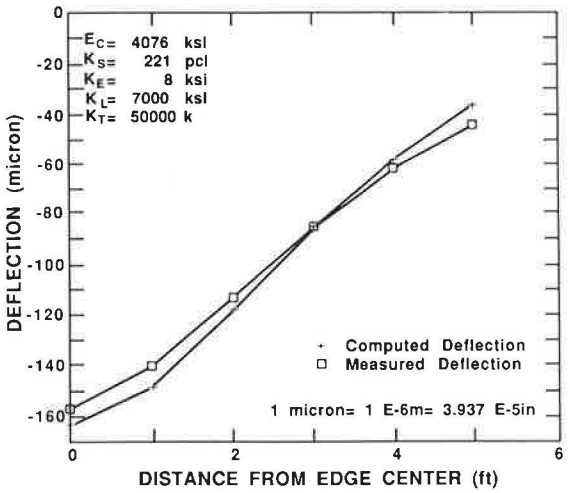

FIGURE 8 Deflection basin along the edge due to a 9-kip FWD load at the edge center.

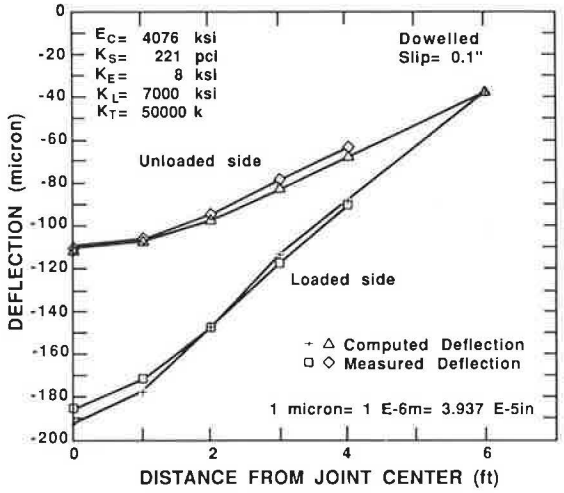

FIGURE 9 Deflection basins along a doweled joint due to a 9-kip FWD load at the center of the joint.

the FEACONS III program. The computed deflection basin matches the measured one fairly well. For this loading condition, analysis results indicated that joint stiffnesses had negligible effects. This was because the joint was far away from the load.

FWD Load at a Doweled Joint

Example 3 is a 9-kip (40-kN) FWD load at the center of a doweled joint. The test slab is the same one used in Examples 1 and 2. Tests were conducted at midday when the slab was curled downward at the edges and joints. It was found that, when the looseness in the dowel bars was modeled with a slip of 0.1 in. (2.54 mm), the computed deflection basin matched the measured one fairly well. Figure 9 shows the comparison of the computed deflection basins and the measured ones along the loaded and the unloaded sides of the doweled joint.

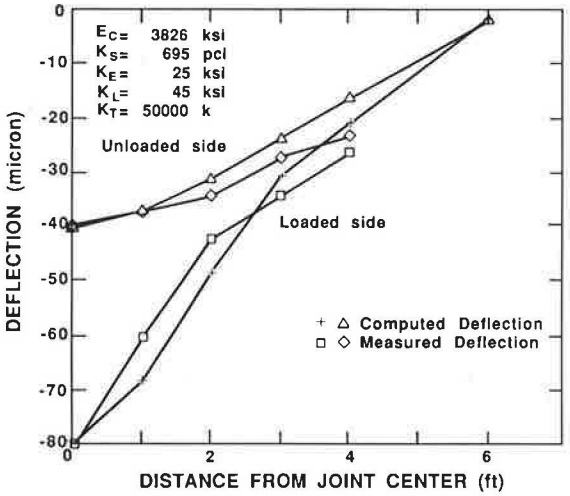

FIGURE 10 Deflection basins along an undoweled joint due to a 9-kip FWD load at the center of the joint.

FWD Load at an Undoweled Joint

Example 4 is a 9-kip (40-kN) FWD load at the center of an undoweled joint. The test was run on a pavement slab on I-10 in Jefferson County, Florida, at midday when the slab was curled downward at the joints and edges. It was found that, by using a linear stiffness of 45 ksi (310 MPa) and a torsional stiffness of 50,000 kips (222.5 MN), a good match between the computed deflection basin and the measured one was achieved. Figure 10 shows the comparison of the computed and measured deflections along the loaded and the unloaded sides of the undoweled joint. Comparison of the performance of the doweled joint and the undoweled joint (Figures 9 and 10) indicates that a doweled joint may not provide a better load transfer mechanism than an undoweled joint, especially when there is excessive looseness in the dowel bars. For this comparison, the deflections at the doweled joint were actually much higher than those at the undoweled joint. This was partly because the subgrade stiffness of the doweled slab was much lower than that of the undoweled slab and partly because there was excessive slip in the doweled joint.

FWD Load at a Doweled Joint with Voids

Example 5 is a 9-kip (40-kN) FWD load at the center of a doweled joint with appreciable voids under the joint. The test was run on a pavement slab on I-10 in Walton County, Florida, at midday when the recorded temperature plots showed that the temperature was higher at the top of the slab. In this case, it was found that a good match between the computed deflections and the measured deflections was achieved by modeling the joint as having a strip of subgrade voids, 12 in. (30 cm) wide and 0.01 in. (0.254 mm) deep, along the entire joint. Figure 11 shows these computed and measured deflection basins along the loaded and the unloaded sides of the joint. In this case, the induced deflections on both sides of the joint were high.

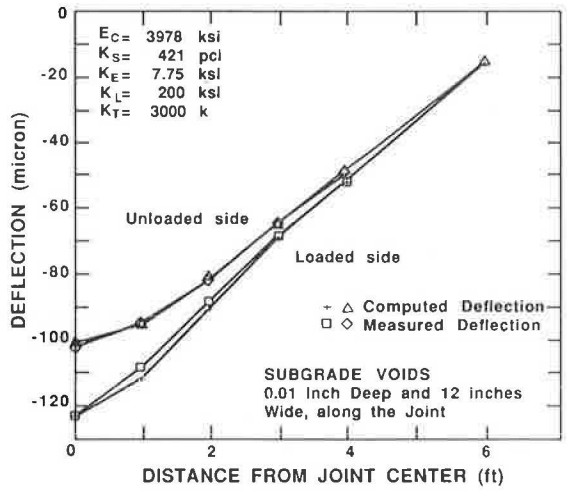

FIGURE 11 Deflection basins along a doweled joint with voids underneath due to a 9-kip FWD load at the center of the joint.

CONCLUSIONS

The analytical model and the computational scheme used by the FEACONS III program for analysis of concrete pavements have been presented in this paper. The computer model used by the FEACONS III program has been shown to be both versatile and effective in the analysis of concrete pavement response.

It has been demonstrated that the edge, joint, and subgrade conditions need to be properly modeled in the analysis. Modeling edge and joint behavior by means of edge stiffness (K_E), linear joint stiffness (K_L), and torsional joint stiffness (K_T) and modeling the subgrade as a Winkler foundation, as used by the FEACONS III program, produced fairly realistic analytical results. The program can be used to estimate pavement parameters (such as subgrade modulus, elastic modulus of concrete, and joint and edge stiffnesses) and to compute the critical induced deflections and stresses caused by a combination of traffic loads and thermal conditions.

ACKNOWLEDGMENTS

The first and second versions of the FEACONS program were developed by K. L. Toye and S. Lei, the fifth and fourth authors of this paper, as their master's theses. The examples presented in the paper were obtained from the results of the project Field Evaluation of Rigid Pavements for the Development of a Rigid Pavement Design System, sponsored by the Florida Department of Transportation. The technical advice and suggestions of B. E. Ruth, L. L. Smith, and T. J. Larsen about the development of the program are gratefully acknowledged. The invaluable technical support and cooperation of C. R. Davis, G. M. Padgett, and J. A. Hughes are greatly appreciated.

APPENDIX: FINITE-ELEMENT FORMULATION OF THE MZC RECTANGLE

Assumptions

The finite-element formulation of the MZC rectangular plate bending element as developed by Melosh (*2*) and Zienkiewicz and Cheung (*3*) is presented in this section. The formulation is based on classical thin plate theory that assumes that (*a*) the thickness of the plate is small compared with its length and width, (*b*) the lateral bending displacements are small compared with the thickness of the plate, and (*c*) normals to the neutral surface remain straight and normal during deformation.

Normal Displacements and Forces

A rectangular plate element is shown in Figure A-1. The three independent displacements at each node are (*a*) lateral deflection (w), (*b*) rotation about the x-axis (Θ_x), and (*c*) rotation about the y-axis (Θ_y). The two rotations (Θ_x and Θ_y) are related to w by the following equations:

$$\Theta_x = -\frac{\partial w}{\partial y} \tag{A-1}$$

$$\Theta_y = \frac{\partial w}{\partial x} \tag{A-2}$$

The three displacements at node i can be denoted as

$$u_i = \begin{bmatrix} w_i \\ \Theta_{xi} \\ \Theta_{yi} \end{bmatrix} \tag{A-3}$$

The 12 nodal displacements of the element can be denoted as

$$u^e = \begin{bmatrix} u_i \\ u_j \\ u_k \\ u_l \end{bmatrix} \tag{A-4}$$

The corresponding forces at each node are (*a*) the downward force (f_w), (*b*) the moment in the x-direction ($f_{\Theta x}$), and (*c*) the moment in the y-direction ($f_{\Theta y}$). The forces at node i are denoted as

$$f_i = \begin{bmatrix} f_w \\ f_{\Theta x} \\ f_{\Theta y} \end{bmatrix} \tag{A-5}$$

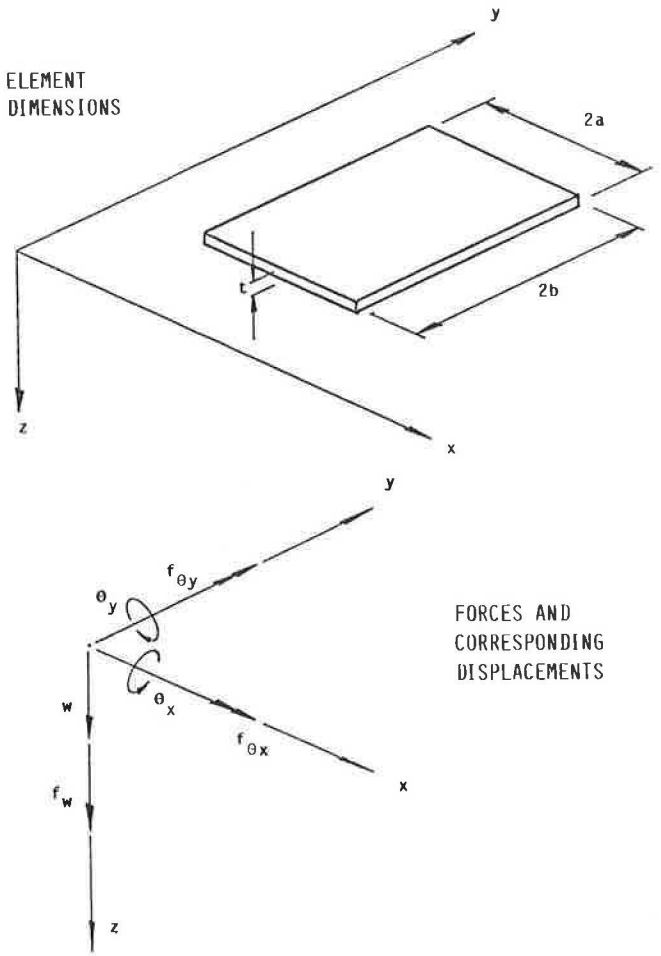

FIGURE A-1 Rectangular plate element.

The 12 nodal forces of the element are denoted as

$$f^e = \begin{bmatrix} f_i \\ f_j \\ f_k \\ f_l \end{bmatrix} \tag{A-6}$$

The displacement function (w) is represented by a polynomial in terms of x and y as

$$\begin{aligned} w = {} & A_1 + A_2x + A_3y + A_4x^2 + A_5xy + A_6y^2 \\ & + A_7x^3 + A_8x^2y + A_9xy^2 + A_{10}y^3 + A_{11}x^3y \\ & + A_{12}xy^3 \end{aligned} \tag{A-7}$$

By investigating this polynomial, it can be seen that along any boundary line, where either x or y is constant, w will vary as a cubic function. Because a cubic function is uniquely defined by four constants, the two end values of slopes and displacements at the two ends will define the displacement along this boundary line uniquely. Because such end values are common to adjacent elements, continuity of w will be imposed all along any interface.

The displacements at node i can now be expressed in terms of x and y coordinates as

$$u_i = \begin{bmatrix} w_i \\ \Theta_{xi} \\ \Theta_{yi} \end{bmatrix} = \begin{bmatrix} w_i \\ \left(-\dfrac{\partial w}{\partial y}\right)_i \\ \left(\dfrac{\partial w}{\partial x}\right)_i \end{bmatrix} = \begin{bmatrix} A_1 + A_2x_i + A_3y_i + A_4x_i^2 + \cdots \\ -A_3 + A_5x_i + 2A_6y_i + A_8x_i^2 + \cdots \\ A_2 + 2A_4x_i + A_5y_i + 3A_7x_i^2 + \cdots \end{bmatrix} \tag{A-8}$$

The 12 nodal displacements of each element can be expressed as

$$u^e = CA \tag{A-9}$$

where C is a 12×12 matrix in terms of the coordinates of the nodes and A is a column matrix of the constants.

Thus the constants A can be expressed as

$$A = C^{-1}u^e \tag{A-10}$$

Curvatures and Internal Moments

The curvatures and twists at any point of the plate can be expressed as

$$\chi = \begin{bmatrix} -\dfrac{\partial^2 w}{\partial x^2} \\ -\dfrac{\partial^2 w}{\partial y^2} \\ 2\dfrac{\partial^2 w}{\partial x \partial y} \end{bmatrix} = \begin{bmatrix} -2A_4 - 6A_7x - 2A_8y - 6A_{11}xy \\ -2A_6 - 2A_9x - 6A_{10}y - 6A_{12}xy \\ 2A_5 + 4A_8x + 4A_9y + 6A_{11}x^2 + 6A_{12}y^2 \end{bmatrix} \tag{A-11}$$

or

$$\chi = BA = BC^{-1}u^e \tag{A-12}$$

where B is a 3×12 matrix in terms of the x- and y-coordinates.

The internal moment intensities (moments per unit length) are related to the curvatures by

$$M = \begin{bmatrix} M_x \\ M_y \\ M_{xy} \end{bmatrix} = D(\chi - \chi_T) \tag{A-13}$$

where

$D = \dfrac{Et^3}{12(1-\nu^2)} \begin{bmatrix} 1 & \nu & 0 \\ \nu & 1 & 0 \\ 0 & 0 & 12(1-\nu) \end{bmatrix}$ for an isotropic material,

E = elastic modulus,

ν = Poisson's ratio,

t = thickness of plate, and

χ_T = curvature changes occurring in an unrestrained element due to temperature alone.

Internal and External Virtual Works

By the principle of virtual work,

$$\delta U_e = \delta W_e \tag{A-14}$$

where δU_e is the virtual internal work (strain energy) and δW_e is the virtual external work on the element caused by a set of virtual nodal displacements (δu^e).

The virtual external work due to the concentrated nodal loads f_c is

$$\delta W_{ec} = (\delta u^e)^T f_c \tag{A-15}$$

The virtual external work due to the distributed load q is

$$\delta W_{eD} = \iint (\delta w)^T q \, dx \, dy \tag{A-16}$$

Equation A-7 can be rewritten as

$$\begin{aligned} w &= \{1,x,y,x^2,xy,y^2,x^3,x^2y,xy^2,y^3,x^3y,xy^3\}A \\ &= PA \end{aligned} \tag{A-17}$$

From Equations A-10 and A-17,

$$\begin{aligned} \delta w &= \delta(LC^{-1} u^e) \\ &= PC^{-1} \delta u^e \end{aligned} \tag{A-18}$$

Substituting Equation A-18 into A-16 gives

$$\begin{aligned} \delta W_{eD} &= \iint (PC^{-1}\delta u^e)^T q \, dx \, dy \\ &= (\delta u^e)^T (C^{-1})^T \iint P^T q \, dx \, dy \end{aligned} \tag{A-19}$$

The total virtual internal work can be expressed as

$$\delta U_e = \iint (\delta \chi)^T M \, dx \, dy \tag{A-20}$$

By using Equation A-12,

$$\delta \chi = BC^{-1}\delta u^e \tag{A-21}$$

Substituting Equations A-13 and A-21 into A-20 gives

$$\begin{aligned} \delta U_e &= \iint (BC^{-1}\delta u^e)^T D(\chi - \chi_T) \, dx \, dy \\ &= \iint (BC^{-1}\delta u^e)^T D(BC^{-1}u^e - \chi_T) \, dx \, dy \\ & (\delta u^e)^T [(C^{-1})^T \{\iint B^T DB \, dx \, dy\} C^{-1} u^e \\ & - (C^{-1})^T \iint BD\chi_T \, dx \, dy] \end{aligned} \tag{A-22}$$

Force-Displacement Relationship

Substituting the expressions for virtual external work and virtual internal work into the virtual work Equation A-14,

$$\begin{aligned} & \delta U_e = \delta W_{ec} + \delta W_{eD} \\ & \rightarrow (\delta u^e)^T [(C^{-1}) \{ \iint B^T DB \, dx \, dy \} C^{-1} u^e - (C^{-1})^T \iint BD\chi_T dx \, dy] \\ & \quad = (\delta u^e)^T f^c + (\delta u^e)^T (C^{-1})^T \iint P^T q \, dx \, dy \\ & \rightarrow (C^{-1})^T \{\iint B^T DB \, dx \, dy\} C^{-1} u^e - (C^{-1})^T \iint BD\chi_T dx \, dy \\ & \quad = f_c + (C^{-1})^T \iint P^T q \, dx \, dy \\ & \rightarrow ku^e - f_T = f_C + f_D \\ & \rightarrow ku^e = f_C + f_D + f_T \end{aligned} \tag{A-23}$$

where

k = $(C^{-1})^T (\iint B^T DB \, dx \, dy) C^{-1}$, element stiffness matrix;
f_D = $(C^{-1})^T \iint P^T q \, dx \, dy$, equivalent nodal loads due to distributed loads; and
f_T = $(C^{-1})^T \iint BD\chi_T \, dx \, dy$, equivalent nodal loads due to temperature changes.

Element Stiffness Matrix

The explicit expression for the element stiffness matrix has been evaluated by Zienkiewicz (*8*). For an isotropic material, it can be expressed as

$$\begin{aligned} k = \frac{Et^3}{720\,ab(1-\nu^2)} [L] \Big(& [SK]_1 + [SK]_2 + \nu[SK]_3 \\ & + \frac{(1-\nu)}{2} [SK]_4 \Big) [L] \end{aligned} \tag{A-24}$$

where

$2a$ = length of the element,
$2b$ = width of the element,
$[L]$ = $\begin{bmatrix} J & & & \\ & J & & \\ & & J & \\ & & & J \end{bmatrix}$ and $J = \begin{bmatrix} 1 & 0 & 0 \\ 0 & 2b & 0 \\ 0 & 0 & 2a \end{bmatrix}$,
E = elastic modulus,
ν = Poisson's ratio,
t = thickness of plate, and
$[SK]_1$, $[SK]_2$, $[SK]_3$, and $[SK]_4$ are as given in Table A-1.

Equivalent Nodal Loads Due to Uniform Distributed Loads

When a uniform distributed load of q acts over an element, the equivalent nodal loads can be calculated to be

$$fD = (C^{-1})^T \iint P^T q \, dx \, dy = 4\,abq \begin{bmatrix} 1/4 \\ -b/12 \\ a/12 \\ 1/4 \\ b/12 \\ a/12 \\ 1/4 \\ -b/12 \\ -a/12 \\ 1/4 \\ b/12 \\ -a/12 \end{bmatrix} \tag{A-25}$$

TABLE A-1 COMPONENT MATRICES OF ELEMENT STIFFNESS MATRIX

$[SK]_1 = p^{-2}$

$p^{-2} = \frac{b^2}{a^2}$

60											
0	0										
30	0	20									
30	0	15	60								
0	0	0	0	0							
15	0	10	30	0	20						
-60	0	-30	-30	0	-15	60					
0	0	0	0	0	0	0	0				
30	0	10	15	0	5	-30	0	20			
-30	0	-15	-60	0	-30	30	0	-15	60		
0	0	0	0	0	0	0	0	0	0	0	
15	0	5	30	0	10	-15	0	10	-30	0	20

Symmetrical

$[SK]_3 =$

30											
-15	0										
15	-15	0									
-30	0	-15	30								
0	0	0	15	0							
-15	0	0	15	15	0						
-30	15	0	30	0	0	30					
15	0	0	0	0	0	-15	0				
0	0	0	0	0	0	-15	15	0			
30	0	0	-30	-15	0	-30	0	15	30		
0	0	0	-15	0	0	0	0	0	15	0	
0	0	0	0	0	0	15	0	0	-15	-15	0

Symmetrical

$[SK]_2 = p^2$

$p^2 = \frac{a^2}{b^2}$

60											
-30	20										
0	0	0									
-60	30	0	60								
-30	10	0	30	20							
0	0	0	0	0	0						
30	-15	0	-30	-15	0	60					
-15	10	0	15	5	0	-30	20				
0	0	0	0	0	0	0	0	0			
-30	15	0	30	15	0	-60	30	0	60		
-15	5	0	15	10	0	-30	10	0	30	20	
0	0	0	0	0	0	0	0	0	0	0	0

Symmetrical

$[SK]_4 =$

84											
-6	8										
6	0	8									
-84	6	-6	84								
-6	-2	0	6	8							
-6	0	-8	6	0	8						
-84	6	-6	84	6	6	84					
6	-8	0	-6	2	0	-6	8				
6	0	-2	-6	0	2	-6	0	8			
84	-6	6	-84	-6	-6	-84	6	6	84		
6	2	0	-6	-8	0	-6	-2	0	6	8	
-6	0	2	6	0	-2	6	0	-8	-6	0	8

Symmetrical

Equivalent Nodal Loads Due to Uniform Temperature Gradients

When the temperature varies linearly from the top to the bottom of the plate with a temperature differential of ΔT, the curvatures of the unrestrained plate element will be

$$\chi_T = \begin{bmatrix} -\dfrac{\partial^2 w}{\partial x^2} \\ -\dfrac{\partial^2 w}{\partial y^2} \\ 2\dfrac{\partial^2 w}{\partial x \partial y} \end{bmatrix}_T = \begin{bmatrix} -\dfrac{\alpha \Delta T}{t} \\ -\dfrac{\alpha \Delta T}{t} \\ 0 \end{bmatrix} \quad \text{(A-26)}$$

where

α = coefficient of thermal expansion,
ΔT = (temperature at top) - (temperature at bottom), and
t = thickness of plate element.

The equivalent nodal loads due to this uniform temperature gradient can be evaluated explicitly to be

$$f_T = (C^{-1})^T \iint B D \chi_T \, dx \, dy = \frac{Et^2 \, \alpha \Delta T}{12(1 - \nu)} \begin{bmatrix} 0 \\ a \\ -b \\ 0 \\ -a \\ -b \\ 0 \\ a \\ b \\ 0 \\ -a \\ b \end{bmatrix} \quad \text{(A-27)}$$

Computation of Internal Moments

After the nodal displacements of an element (u^e) have been determined, the internal moments can be calculated by using Equations A-12 and A-13 as

$$M = \begin{bmatrix} M_x \\ M_y \\ M_{xy} \end{bmatrix} = D(\chi - \chi_T)$$

$$= DBC^{-1} u^e - D\chi_T$$
$$= Su^e - D\chi_T \quad \text{(A-28)}$$

TABLE A-2 STRESS MATRIX

$$S = \frac{1}{4ab}$$

$6p^{-1}D_x + 6pD_1$	$-8aD_1$	$8bD_x$	$-6pD_1$	$-4aD_1$	0	$-6p^{-1}D_x$	0	$4bD_x$	0	0	0
$6pD_y + 6p^{-1}D_1$	$-8aD_y$	$8bD_1$	$-6pD_y$	$-4aD_y$	0	$-6p^{-1}D_1$	0	$4bD_1$	0	0	0
$-2D_{xy}$	$4bD_{xy}$	$-4aD_{xy}$	$2D_{xy}$	0	$4aD_{xy}$	$2D_{xy}$	$-4bD_{xy}$	0	$-2D_{xy}$	0	0
$-6pD_1$	$4aD_1$	0	$6p^{-1}D_x + 6pD_1$	$8aD_1$	$8bD_x$	0	0	0	$-6p^{-1}D_x$	0	$4bD_x$
$-6pD_y$	$4aD_y$	0	$6pD_y + 6p^{-1}D_1$	$8aD_y$	$8bD_1$	0	0	0	$-6p^{-1}D_1$	0	$4bD_1$
$-2D_{xy}$	0	$-4aD_{xy}$	$2D_{xy}$	$4bD_{xy}$	$4aD_{xy}$	$2D_{xy}$	0	0	$-2D_{xy}$	$-4bD_{xy}$	0
$-6p^{-1}D_x$	0	$-4bD_x$	0	0	0	$6p^{-1}D_x + 6pD_1$	$-8aD_1$	$-8bD_x$	$-6pD_1$	$-4aD_1$	0
$-6p^{-1}D_1$	0	$-4bD_1$	0	0	0	$6pD_y + 6p^{-1}D_1$	$-8aD_y$	$-8bD_1$	$-6pD_y$	$-4aD_y$	0
$-2D_{xy}$	$4bD_{xy}$	0	$2D_{xy}$	0	0	$2D_{xy}$	$-4bD_{xy}$	$-4aD_{xy}$	$-2D_{xy}$	0	$4aD_{xy}$
0	0	0	$-6p^{-1}D_x$	0	$-4bD_x$	$-6pD_1$	$4aD_1$	0	$6p^{-1}D_x + 6pD_1$	$8aD_1$	$-8bD_x$
0	0	0	$-6p^{-1}D_1$	0	$-4bD_1$	$-6pD_y$	$4aD_y$	0	$6pD_y + 6p^{-1}D_1$	$8aD_y$	$-8bD_1$
$-2D_{xy}$	0	0	$2D_{xy}$	$4bD_{xy}$	0	$2D_{xy}$	0	$-4aD_{xy}$	$-2D_{xy}$	$-4bD_{xy}$	$4aD_{xy}$

$p = a/b$ FOR ISOTROPIC MATERIALS:

$D = D_x = D_y = Et^3/12(1 - \nu^2)$ $\quad D_1 = \nu D$ $\quad D_{xy} = (1 - \nu)D/2$

where S is DBC^{-1}, stress matrix.

The explicit expressions for the stress matrix (S) are given in Table A-2. For uniform temperature gradients, the internal moments can be evaluated to be

$$M = Su^e + \frac{Et^2\alpha\Delta T}{12(1 - \nu)}\begin{bmatrix}1\\1\\0\end{bmatrix} \qquad \text{(A-29)}$$

where ΔT is (top temperature) - (bottom temperature).

REFERENCES

1. J. M. Armaghani, J. M. Lybas, M. Tia, and B. E. Ruth. Concrete Pavement Joint Stiffness Evaluation. In *Transportation Research Record 1099,* TRB, National Research Council, Washington, D.C., 1986, pp. 22-37.
2. R. J. Melosh. Basis of Derivation of Matrices for the Direct Stiffness Method. *AIAA Journal,* Vol. 1, No. 7, July 1963, pp. 1631-1637.
3. O. C. Zienkiewicz and Y. K. Cheung. The Finite Element Method for Analysis of Elastic Isotropic and Orthotropic Slabs. *Proc., Institute of Civil Engineers,* Vol. 28, 1964, pp. 471-488.
4. Y. T. Chou. *Structural Analysis Computer Programs for Rigid Multicomponent Structures with Discontinuities—WESLIQUID and WESLAYER.* Technical Report GL-80. U.S. Army Waterways Experiment Station, Vicksburg, Miss., Sept. 1980.
5. A. Tabatabaie and E. J. Barenberg. Finite Element Analysis of Jointed or Cracked Concrete Pavements. In *Transportation Research Record 671,* TRB, National Research Council, Washington, D.C., 1978, pp. 11-20.
6. J. Larralde and W. F. Chen. Computer Model for Analysis of Rigid Pavements with Fatigue. *Proc., Third International Conference on Concrete Pavement Design and Rehabilitation,* Purdue University, West Lafayette, Ind., April 1985, pp. 537-547.
7. Y. H. Huang. Finite Element Analysis of Concrete Slab and Its Implications for Rigid Pavement Design. In *Highway Research Record 466,* HRB, National Research Council, Washington, D.C., 1973, pp. 55-99.
8. O. C. Zienkiewicz. *The Finite Element Method,* 3d ed. McGraw-Hill Book Company, London, England, 1977.

Publication of this paper sponsored by Committees on Rigid Pavement Design, on Rigid Pavement Construction and Rehabilitation, and on Pavement Rehabilitation.

Thickness Design of Roller-Compacted Concrete Pavements

SHIRAZ D. TAYABJI AND DAVID J. HALPENNY

Roller-compacted concrete (RCC) is a relatively stiff or zero-slump concrete mixture that is compacted by vibratory roller. RCC is capable of providing concrete with relatively high in-place strength, and its engineering behavior is similar to that of conventional concrete. RCC is being used as a paving material at off-highway facilities such as container ports, intermodal yards, log-sorting yards, truck parking areas, and tank aprons (hardstands). An investigation was recently conducted to develop engineering data and procedures for design of RCC pavements. A procedure for thickness design of RCC pavements is presented in this paper. The design approach used for RCC pavements is similar to the procedure used by the Portland Cement Association for design of concrete airfield and heavy industrial pavements. The proposed procedure requires computation of allowable pavement stress based on the number of total load applications and computation of expected pavement stress due to the design wheel loading. A design thickness is selected such that the expected pavement stress is less than the allowable pavement stress. The proposed procedure is also applicable to mixed traffic loading.

Roller-compacted concrete (RCC) is a relatively stiff or zero-slump concrete mixture that is compacted by vibratory rollers. Although the term roller-compacted concrete is of recent origin (early 1970s), similar materials—mixtures of cement, aggregate, and water—have been used for a much longer time. These mixtures have been called cement-treated base (CTB), cement aggregate mixture (CAM), or granular soil cement (SC). However, CTB, CAM, and granular SC usually are lower-strength materials with 28-day compressive strengths of less than about 1,000 psi. RCC as used for paving can be designed to achieve 28-day compressive strengths similar to those of conventional concrete.

Since the first use of RCC in dam construction in the United States during the 1970s, its use has been increasing for other applications such as paving. Early use of RCC for paving was made in western Canada where pavements were constructed in remote areas. Because of its low cost, ease of placement, and good performance record in western Canada, RCC use is increasing the United States for off-highway facilities subjected to heavy vehicle loading. RCC has been used principally for off-highway facilities such as

1. Container ports,
2. Intermodal yards,
3. Log-haul roads,
4. Log-sorting yards,
5. Truck-parking areas,
6. Airfield apron areas, and
7. Tank aprons (hardstands).

S. D. Tayabji, Construction Technology Laboratories, Inc., 5420 Old Orchard Road, Skokie, Ill. 60077. D. J. Halpenny, Portland Cement Association, 5420 Old Orchard Road, Skokie, Ill. 60077.

BACKGROUND

The first large-scale use of RCC as paving was made in British Columbia in 1976. Since then several large paving projects using RCC have been constructed in British Columbia and elsewhere in Canada. Since 1984 RCC has also been used in the United States for paving. During 1985 a total of 81,000 yd^2 of 12- and 17-in.-thick RCC pavement was constructed at an intermodal yard in Tacoma. On this project, crushed aggregate with 5/8-in. maximum size aggregate was used. Cement content specified was 450 lb/yd^3, and fly ash specified was 100 lb/yd^3. Average flexural strength at 28 days measured from sawed beams was about 750 psi.

During 1985 a 40,000-yd^2 aircraft parking apron was also constructed using RCC at the Portland International Airport. On this project pavement thickness was 14 in. Cement content of 488 lb/yd^3 and fly ash content of 119 lb/yd^3 were used for the RCC. During 1986 several large RCC paving projects were constructed in the United States.

During October 1986, RCC was used for pavement construction at Berths 11 and 12 of the Conley Terminal in Boston. The RCC mix used contained 600 lb/yd^3 of cement and 100 lb/yd^3 of fly ash. The aggregate was well graded with a maximum aggregate size of 3/4 in. Pavement thickness was 18 in. Lanes were constructed in two or three lifts. Lanes were 450 ft long and about 15 ft wide. Figure 1 (top) shows a view of the pugmill, aggregate stockpile, and a test section that was constructed about 1 month before actual construction. Figure 1 (bottom) shows the placement of RCC using two pavers placing adjacent lanes.

To summarize the experience with RCC pavements, the following items are noted:

1. RCC is generally mixed in a twin-shaft pugmill.
2. Cement content used has ranged from about 300 to 600 lb/yd^3. At some projects, fly ash was used in the range of 15 to 20 percent by weight of cementitious materials.
3. RCC is usually placed using an asphalt paver. Maximum compacted lift thickness that can be placed using currently available pavers is about 9 to 10 in. However,

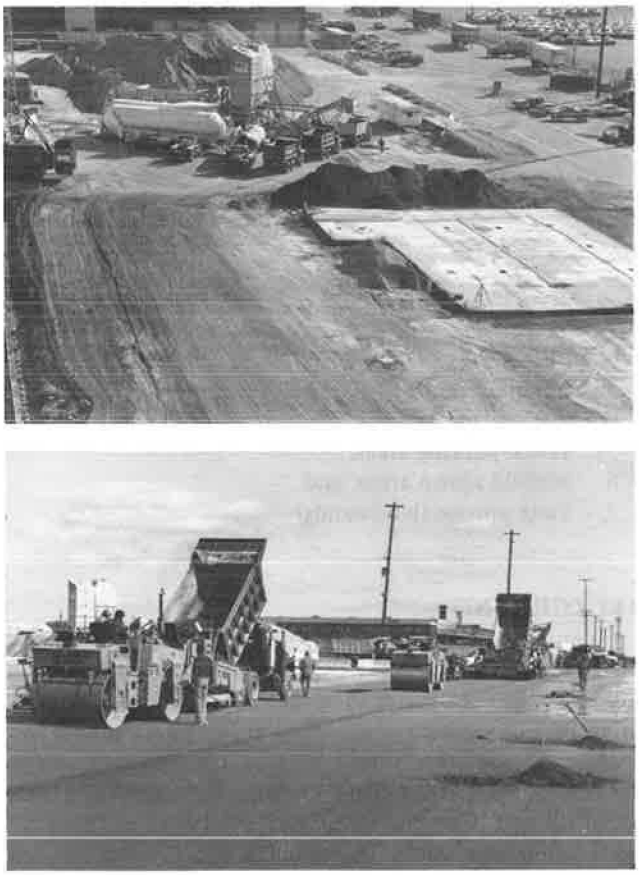

FIGURE 1 RCC pavement construction: (*top*) pugmill and (*bottom*) two-lane placement of RCC.

pavers can be modified to provide a compacted lift of about 12 in.

4. RCC is compacted using 10- to 12-ton vibratory rollers to achieve specified density.

5. Contraction joints are not provided in RCC pavements. Instead, shrinkage cracking is allowed to occur naturally. Spacing of shrinkage cracks is about 50 to 60 ft.

6. Pavements constructed with RCC have excellent performance records under very heavy vehicle loadings.

PROJECT OBJECTIVES

Although RCC has been in use for paving for many years, no detailed study has been carried out to investigate its engineering properties and to establish a thickness design procedure for RCC pavements. A study was recently sponsored by the Portland Cement Association (PCA) to develop engineering data and procedures for design of RCC pavements. The scope of work of the PCA study included the following items:

1. Evaluation of engineering properties of RCC,
2. Evaluation of mix proportioning procedures,
3. Evaluation of RCC durability, and
4. Establishment of a thickness design procedure for RCC pavements.

Results of the first two work items are presented in a companion paper by Tayabji and Okamoto in this Record. A procedure for thickness design of RCC pavements is presented here. Investigation of RCC durability is still in progress.

ENGINEERING PROPERTIES OF RCC

The PCA's evaluation of the engineering properties of RCC indicates that the behavior of RCC is similar to that of conventional concrete. This evaluation was based on testing of specimens obtained from a full-scale test section and review of test data from several RCC paving projects. RCC can be made with 3 to 6 bags of cement per cubic yard of RCC. Depending on the cement content, the 28-day compressive strength of RCC can range from about 3,500 to more than 5,000 psi, and the 28-day flexural strength can range from about 500 to more than 700 psi. Data on strength characteristics of RCC are given in the paper by Tayabji and Okamoto in this Record.

FATIGUE BEHAVIOR OF RCC

As part of the PCA's investigation, tests were conducted to determine flexural fatigue characteristics of RCC. Flexural fatigue testing was performed on beam specimens obtained from a full-scale section. Fatigue test results are shown in Figure 2. Linear regression was used to develop a fatigue curve for the test data for the four different RCC mixes used.

Fatigue test results of the RCC mixes are compared in Figure 2 with results from fatigue tests on conventional concrete conducted by Murdoch and Kesler (*1*) and Ballinger (*2*). In addition, the PCA fatigue curve used for design of concrete pavement (*3*) is shown in Figure 3. The Murdoch-Kesler curve for conventional concrete shown in Figure 3 was drawn so that 95 percent of the test results would fall above the line. The PCA curve for conventional concrete pavement design is conservatively set below the 95 percent Murdoch-Kesler curve.

A design fatigue curve for RCC was developed using a degree of conservatism similar to that used to develop the design fatigue curve for conventional concrete. The design fatigue curve for RCC, shown in Figure 4, is set about 15 percent below the 95 percent curve for RCC. Information for the design fatigue curve is given in Table 1.

THICKNESS DESIGN OF RCC PAVEMENTS

Although RCC pavements have primarily been used for off-highway facilities, RCC pavements can also be used for industrial driveways and truck-parking areas. As discussed earlier, the engineering behavior of RCC can be considered similar to that of conventional paving concrete at equal strength levels. Properly designed and constructed RCC can provide compressive and flexural strengths comparable to those generally specified for conventional paving concrete.

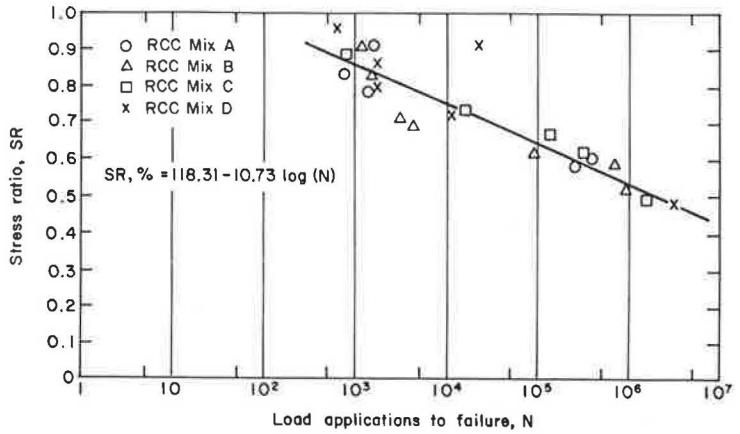

FIGURE 2 Fatigue relationship for RCC.

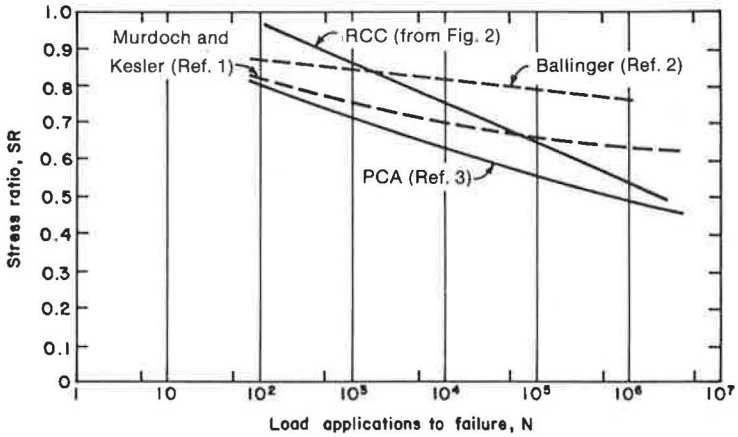

FIGURE 3 Comparison of fatigue relationship.

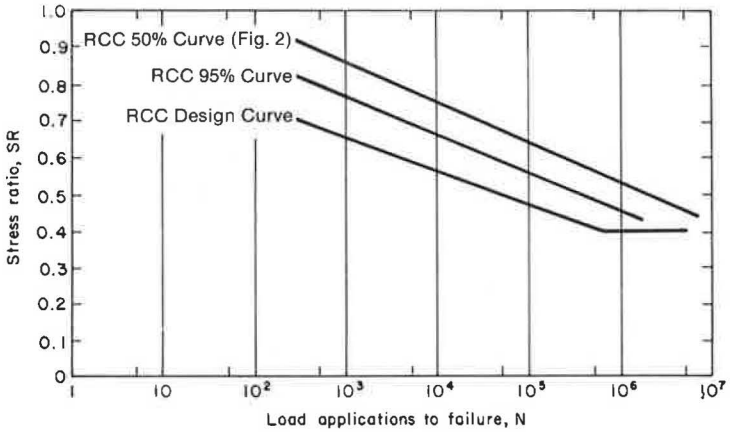

FIGURE 4 Design fatigue curve for RCC.

Design Procedure

Because the engineering properties of RCC are similar to those of conventional paving concrete, the thickness design procedures used for concrete pavements can be directly applied to design of RCC pavements. The primary parameters affecting thickness design of concrete pavements are concrete flexural strength and concrete fatigue behavior. The design fatigue relationship for RCC presented earlier is considered applicable to thickness design of RCC pavements.

For facilities using RCC pavements, the critical load placement is considered to be at the interior of the pavement. Use of the interior load placement is based on the following reasoning:

1. Transverse shrinkage crack spacing for RCC pavements is generally about 50 to 60 ft with little intermediate cracking.
2. Traffic at off-highway facilities and industrial driveways and yards is at relatively low speeds and is generally two

TABLE 1 STRESS RATIO AND ALLOWABLE LOAD REPETITIONS FOR DESIGN OF RCC PAVEMENTS

Stress Ratio	Allowable Repetitions	Stress Ratio	Allowable Repetitions
0.40	600,000	0.56	9,700
0.41	465,000	0.57	7,500
0.42	360,000	0.58	5,800
0.43	280,000	0.59	4,500
0.44	210,000	0.60	3,500
0.45	165,000	0.61	2,700
0.46	130,000	0.62	2,100
0.47	100,000	0.63	1,600
0.48	76,000	0.64	1,200
0.49	59,000	0.65	950
0.50	46,000	0.66	740
0.51	35,000	0.67	570
0.52	27,000	0.68	440
0.53	21,000	0.69	340
0.54	16,000	0.70	260
0.55	12,000		

NOTE: Stress ratio is pavement stress due to wheel load divided by RCC flexural strength. Design fatigue for RCC.

$\text{Log}(N) = 10.258 - 11.198(SR)$ where N is allowable load repetitions and SR is stress ratio.

directional. Thus problems of faulting and pumping at joints are minimized or nonexisient.

3. Field surveys of facilities using RCC pavements show no consequential problems at shrinkage cracks (*4, 5*).

The design procedure proposed for RCC pavements is similar to the procedure used by PCA for concrete airfield and heavy industrial pavements.

Design Requirements

A variety of vehicles may be used at facilities with RCC pavements. These vehicles include large-capacity forklift trucks, straddle carriers, log stackers, and logging or heavy freight trucks. Wheel loads on these vehicles may range up to 100,000 lb, greatly exceeding those of highway trucks. Total loads on these vehicles are equal to and sometimes greater than those of the heaviest commercial aircraft.

For design of RCC pavements, charts have been prepared to enable computation of the required pavement thickness. These charts were prepared using Pickett's extension (*6*) of Westergaard's analysis for loads at the interior of a slab supported by a dense liquid subgrade (*7*). Pickett's extension of Westergaard's analysis has been programmed for solution using IBM-compatible personal computers (*8*). The design charts presented for single wheel loading and for dual wheel loading require the following information:

1. Supporting strength of the subgrade;
2. Vehicle characteristics
   - Wheel loads,
   - Wheel configuration, and
   - Tire characteristics;
3. Flexural strength of RCC; and
4. Modulus of elasticity of RCC.

Subgrade Support

The support given to the RCC pavement by the subgrade, and by the subbase where one is used, is a major element in thickness design. Subgrade and subbase support is expressed in terms of the Westergaard modulus of subgrade reaction (k). The k-value is determined by a nonrepetitive plate load test (ASTM D 1196) and is equal to the load in pounds per square inch on a 30-in.-diameter plate divided by the deflection in inches for that load, or the total load in pounds divided by the total volume displaced in cubic inches. The k-value is expressed in units of pounds per square inch per inch (psi/in.) or pounds per cubic inch (pci).

When time and equipment are not available to determine k-values, the relationships shown in Figure 5 are satisfactory for estimating the k-value. These k-values are based on correlation with soil strength tests and general soil types. Where a subbase is used there will be an increase in k that should be used in the thickness design. The approximate increase in k may be taken from Table 2.

Vehicle Loads

Estimating the expected traffic is an important factor in pavement design. Required traffic information includes the wheel load magnitudes, wheel configurations, and frequency of operations of the heaviest vehicles that will use the pavement. As complete data as possible should be gathered from planning and operations departments and manufacturers of the lift trucks, straddle carriers, and other heavy vehicles that will use the pavement.

Usually the vehicle with the heaviest wheel load will control the design, but the design should also be checked for adequacy if other vehicle wheel loads are almost as heavy and travel the pavement frequently.

The maximum wheel load is one-half of the heaviest axle load for the vehicle at its rated maximum capacity. This information is usually available from the vehicle manufacturer.

The load contact area used in the charts is the area of slab contact of each tire carrying the maximum wheel load. It may be estimated by dividing the wheel load by the tire inflation pressure. The contact area to be used is sometimes referred to as the gross contact area—the total area encompassed by the contact envelope regardless of the tire tread design.

The distance between wheels of the vehicle can be an important design factor. If this spacing is close (closer than three times the radius of relative stiffness) it is necessary to consider the effect of more than one wheel load in the computation of pavement stress. In this regard, the wheel configurations of almost all heavy vehicles at terminals and industrial storage areas are classified as either single wheel load (e.g., a single wheel on each side of an axle) or dual wheel load (e.g., dual wheels on each side of an axle; in this case two

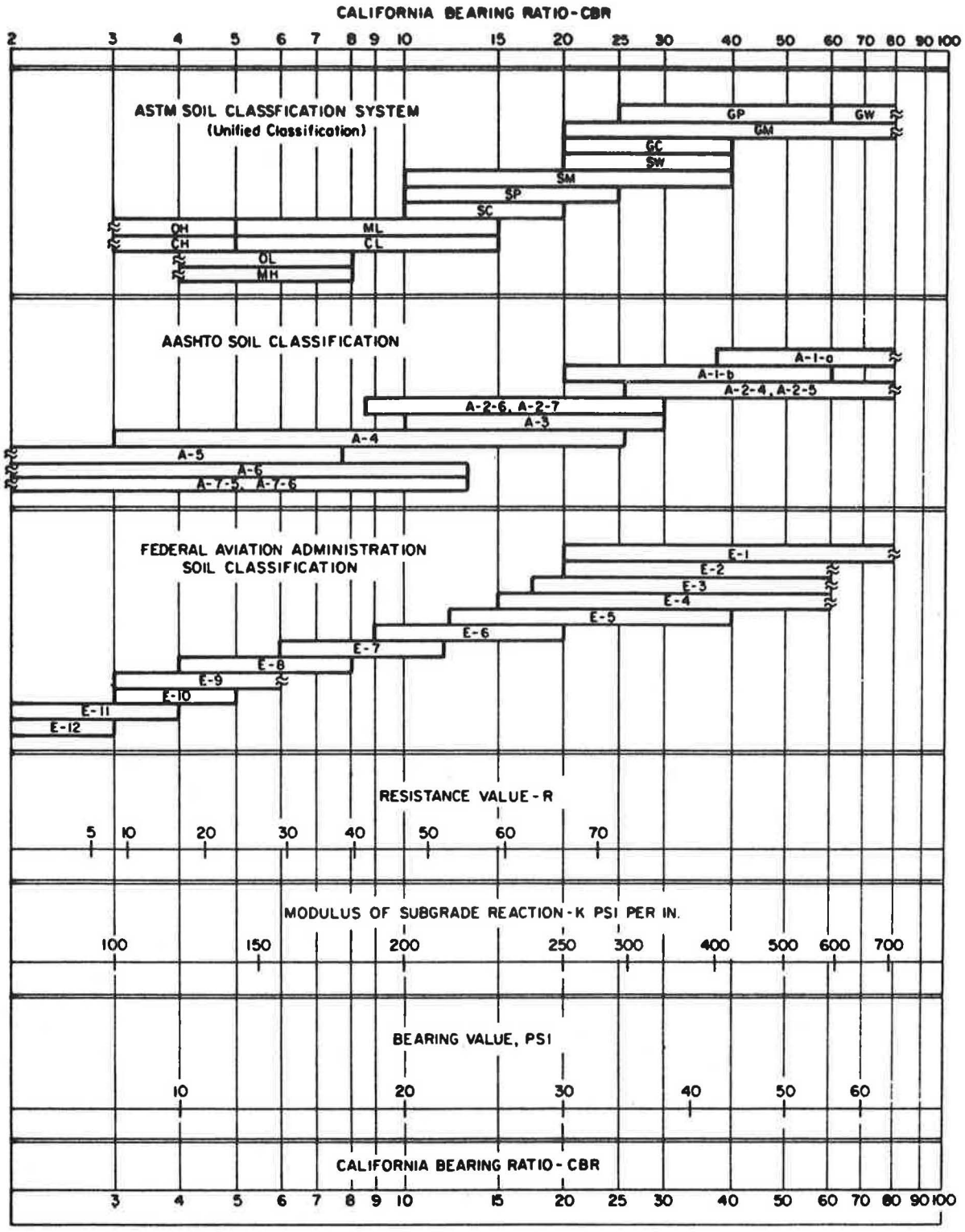

FIGURE 5 Estimation of modulus of subgrade reaction.

wheels are spaced closely enough that their combined effect on pavement stress must be considered). A load on dual wheels creates less pavement stress than the same load on a single wheel. For this reason, separate design charts are shown for single and dual wheel loads.

Allowable Pavement Stress

The RCC pavement design procedure requires determination of the allowable pavement stress and the expected pavement stress due to wheel loads. A design thickness is selected such

TABLE 2 EFFECT OF SUBBASE THICKNESS ON k-VALUES

Subgrade k-Value (pci)	Subbase k-Value (pci) at				
	4 in.	6 in.	8 in.	9 in.	12 in.
Granular subbase					
50	65	75		85	110
100	130	140		160	190
200	220	230		270	320
300	320	330		370	430
Stabilized subbase					
50	170	230	310		
100	280	400	520		
200	470	640	830		

that the expected pavement stress is less than the allowable pavement stress.

The allowable pavement stress is dependent on the number of load repetitions of the design wheel loads anticipated during the design period. When the number of load repetitions during the design period is known, the allowable stress ratio (SR) can be obtained from Table 1. Then the allowable pavement stress is computed as follows:

Allowable stress = Stress ratio × RCC flexural strength

Determination of the design pavement thickness on the basis of single and dual wheel loads is discussed next.

Charts for Determining Pavement Thickness

The chart shown in Figure 6 is for computing stress due to single wheel loading and the chart shown in Figure 7 is for computing stress due to dual wheel loading. For a more complex wheel configuration, the computer program available for IBM-compatible personal computers may be used (*8*).

Examples

Examples are presented to illustrate the use of the design charts. The design chart for dual wheel loading requires a value for radius of relative stiffness (l). The l-value is given as follows:

$$l = \left[\frac{Eh^3}{12(1-\mu^2)k}\right]^{0.25}$$

where

E = RCC modulus of elasticity (psi);
h = RCC pavement thickness (in.);
μ = RCC Poisson's ratio, usually assumed to be 0.15; and
k = modulus of subgrade reaction (pci).

Values of l are given in Table 3.

Design Example 1 (single wheel) The vehicle is a straddle carrier. The following parameters are taken into consideration:

- Number of wheels = 4;
- Maximum single wheel load = 26,000 lb;
- Tire inflation pressure = 100 psi;
- Tire contact area = 260 in.^{2};
- RCC flexural strength = f_r = 700 psi;
- Subgrade strength, k = 100 pci;
- Daily number of channelized wheel load applications (design) = 20;
- Number of wheel load applications over 20-year design period = 146,000;
- Design stress ratio (Table 1), SR = 0.45;
- Allowable stress, $\sigma = f_s \times SR = 700 \times 0.045$ = 315 psi; and
- Allowable stress per 1,000-lb load

$$= \frac{\sigma}{P/1{,}000} = \frac{315}{26} = 12.1 \text{ psi/kip.}$$

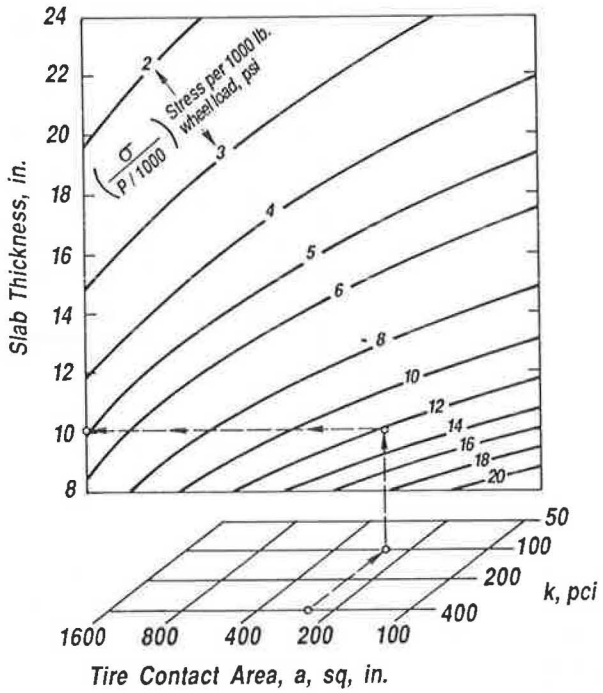

FIGURE 6 Design chart for single wheel load.

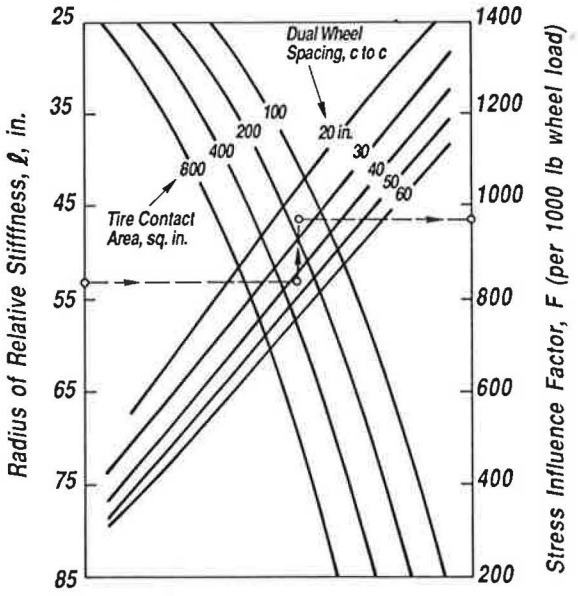

FIGURE 7 Design chart for dual wheels (sequence: *l* to area to spacing to *f*).

Enter the design chart for single wheels (Figure 6) at the bottom with a tire contact area of 260 in.^{2} and a k-value of 100 pci. For an allowable stress of 12.1 psi/kip, a slab thickness of 10.1 in. is required (use 10 in.). Use of the chart is shown by the dashed-arrow line.

Design Example 2 (dual wheels) The vehicle is a mobile gantry crane (lift capacity 40 tons). The following parameters are taken into consideration:

- Number of wheels = 8 (4 duals);
- Maximum dual wheel load = 90,000 lb;
- Dual wheel spacing = 26 in. center to center;
- Tire inflation pressure = 160 psi;
- Tire contact area (each tire) = 90,000/2/160 = 281 in.^{2};
- RCC flexural strength, f_r = 700 psi;
- Subgrade-subbase strength, k = 200 pci;
- Daily number of channelized dual wheel load applications = 40;
- Number of wheel load applications over 20-year design period = 292,000;
- Design stress ratio (Table 1), SR = 0.43; and
- Allowable stress, $\sigma = f_s \times SR = 700 \times 0.043 = 301$ psi.

TABLE 3 VALUES OF *l*, RADIUS OF RELATIVE THICKNESS

h in in.	k = 50	k = 100	k = 150	k = 200	k = 250	k = 300	k = 350	k = 400	k = 500
6	34.84	29.30	26.47	24.63	23.30	22.26	21.42	20.72	19.59
6.5	36.99	31.11	28.11	26.16	24.74	23.64	22.74	22.00	20.80
7	39.11	32.89	29.72	27.65	26.15	24.99	24.04	23.25	21.99
7.5	41.19	34.63	31.29	29.12	27.54	26.32	25.32	24.49	23.16
8	43.23	36.35	32.85	30.57	28.91	27.62	26.58	25.70	24.31
8.5	45.24	38.04	34.37	31.99	30.25	28.91	27.81	26.90	25.44
9	47.22	39.71	35.88	33.39	31.58	30.17	29.03	28.08	26.55
9.5	49.17	41.35	37.36	34.77	32.89	31.42	30.23	29.24	27.65
10	51.10	42.97	38.83	36.14	34.17	32.65	31.42	30.39	28.74
10.5	53.10	44.57	40.28	37.48	35.45	33.87	32.59	31.52	29.81
11	54.89	46.16	41.71	38.81	36.71	35.07	33.75	32.64	30.87
11.5	56.75	47.72	43.12	40.13	37.95	36.26	34.89	33.74	31.91
12	58.59	49.27	44.52	41.43	39.18	37.44	36.02	34.84	32.95
12.5	60.41	50.80	45.90	42.72	40.40	38.60	37.14	35.92	33.97
13	62.22	52.32	47.27	43.99	41.61	39.75	38.25	36.99	34.99
13.5	64.00	53.82	48.63	45.26	42.80	40.89	39.35	38.06	35.99
14	65.77	55.31	49.98	46.51	43.98	42.02	40.44	39.11	36.99
14.5	67.53	56.78	51.31	47.75	45.16	43.15	41.51	40.15	37.97
15	69.27	58.25	52.63	48.98	46.32	44.26	42.58	41.19	38.95
15.5	70.99	59.70	53.94	50.20	47.47	45.36	43.64	42.21	39.92
16	72.70	61.13	55.24	51.41	48.62	46.45	44.70	43.23	40.88
16.5	74.40	62.56	56.53	52.61	49.75	47.54	45.74	44.24	41.84
17	76.08	63.98	57.81	53.80	50.88	48.61	46.77	45.24	42.78
17.5	77.75	65.38	59.48	54.98	52.00	49.68	47.80	46.23	43.72
18	79.41	66.78	60.35	56.16	53.11	50.74	48.82	47.22	44.66
19	82.70	69.54	62.84	58.48	55.31	52.84	50.84	49.17	46.51
20	85.95	72.27	65.30	60.77	57.47	54.92	52.84	51.10	48.33
21	89.15	74.97	67.74	63.04	59.62	56.96	54.81	53.01	50.13
22	92.31	77.63	70.14	65.28	61.73	58.98	56.75	54.89	51.91
23	95.44	80.26	72.52	67.49	63.83	60.98	58.68	56.75	53.67
24	98.54	82.86	74.87	69.68	65.90	62.96	60.58	58.59	55.41

NOTE: In inches E = 4,000,000 psi and μ = 0.15

$$l = 4\left(\frac{Eh^3}{12(1-\mu^2)k}\right)^{1/4}$$

The first step in the use of the design chart for dual wheels is to arbitrarily select a trial slab thickness, say 15 in.

Corresponding to this thickness and a k-value of 200 pci, an l-value of 49.0 is determined from Table 3.

From the determined l-value on the design chart (Figure 7) proceed to the right to intersect with the tire contact area, then move vertically to intersect with the dual wheel spacing. From this point move to the right to read an F-value (stress influence factor per 1,000-lb dual wheel load) of 930.

Compute stress due to load as

$$\text{Stress} = \frac{\text{Dual wheel load}}{1{,}000} \times \frac{1}{(\text{Slab thickness})^2} \times \overline{F}$$

$$= \frac{90{,}000}{1{,}000} \times \frac{1}{15^2} \times 930 = 372 \text{ psi.}$$

The process is repeated to determine stresses for other trial slab thicknesses and data are tabulated as follows:

Trial Slab Thickness (in.)	*l-Value (in.) from Table*	*F (from design chart)*	*Stress Due to Load (psi)*
15	49.0	930	372
16	51.4	955	336
17	53.3	970	302

Select a design slab thickness for which the stress due to load is equal to or less than the allowable stress. In this example for an allowable stress of 301 psi, the design thickness is 17 in.

Design Procedure for Mixed Traffic

The design procedure presented is applicable when a single type of wheel loading can be identified as the design wheel loading. When mixed traffic exists, the cumulative fatigue damage due to the mixed traffic needs to be calculated. This approach requires the following steps:

1. Select pavement thickness.
2. Compute pavement stress (σ) using Figure 6 or 7 for each type of wheel loading.
3. Compute stress ratio (SR) for each type of wheel loading.
4. Determine the allowable number of load repetitions (N_a) for each type of wheel loading using Table 1.
5. Determine the fatigue consumption by each type of wheel loading as follows:

$$F_n = \frac{N_{e,n}}{N_{a,n}}$$

where

F_n = fatigue consumption for wheel load n,
$N_{e,n}$ = expected number of load repetitions of wheel load n during the design period, and
$N_{a,n}$ = allowable number of load repetitions of wheel load n (see Step 4).

6. Add the fatigue consumption for all wheel loadings.
7. If fatigue consumption is more than 100 percent or less than 100 percent, repeat Steps 2-6 with a larger or smaller pavement thickness as the case may be. The design thickness is the one that results in total fatigue consumption of 100 percent or less.

ADDITIONAL NOTES

RCC is placed in a single lift when pavement thickness is about 10 in. or less. When pavement thickness is more than 10 in., RCC may be placed in two or three lifts. Minimum lift thickness is about 5 in. When a multiple-lift placement procedure is used, sufficient consideration must be given to the time interval between placement of successive lifts. In warm weather, the time interval between placement of successive lifts should not be greater than 1 hr. In cooler weather and if wind conditions permit, a time interval of 2 to 3 hr may be permissible. The time interval is critical to ensure adequate bonding at the interface of successively placed lifts. Adequately bonded interfaces should develop shear strength of at least 200 psi at 90 days. If adequate shear strength is not developed at the interface, each lift may behave independently of the other lifts. This behavior would reduce the load-carrying capability of the pavement. The thickness design procedure presented in this paper assumes that the RCC pavement behaves monolithically when a multiple-lift construction procedure is used.

RCC is a dense material that is mixed, placed, and compacted in a relatively dry state. Because of the nature of the material, it has not been practical to entrain air in RCC mixtures on field projects. Many of the projects constructed in the past were located in coastal areas where numerous freeze-thaw cycles occur but where winter temperatures are not necessarily severe. During 1986 RCC pavements were constructed in the Denver and Boston areas. During 1985 the Corps of Engineers reported the results of an investigation conducted to evaluate frost resistance of RCC samples taken from nine field projects (*9*). Samples of RCC were tested for air content, parameters of air void system, resistance to rapid freezing and thawing, critical dilation, and compressive and flexural strengths. The Corps of Engineers' investigation indicated that the air void systems observed in many of the RCC samples should be sufficient to protect the pavement against frost damage in all but the most severe environments.

RCC samples obtained from field projects have not shown good durability when tested in the laboratory according to the procedures of ASTM C 666. However, this does not necessarily mean that RCC may not be durable in the field. Although ASTM C 666 is a useful test for evaluating durability of conventional concrete, its direct applicability to RCC is not clear. The best indicator of RCC durability is its performance in the field. The recently constructed RCC

pavements in the Denver and Boston areas will help to resolve the concern about RCC durability.

SUMMARY

In this paper are presented results of an investigation conducted to develop data and procedures for design of RCC pavements. Results of the investigation show that RCC is a viable paving alternative capable of providing satisfactory long-term performance.

The procedure for thickness design of RCC pavements is based on flexural fatigue considerations. This approach is similar to the PCA procedure for design of concrete pavements for off-highway facilities and industrial driveways and parking areas. However, the procedure for RCC pavements uses a newly established design fatigue relationship for RCC.

ACKNOWLEDGMENTS

Work was conducted by the Construction Technology Laboratories, Inc., under the direction of W. G. Corley, vice-president, and B. E. Colley, director, Transportation Development Department.

REFERENCES

1. J. W. Murdoch and C. E. Kesler. Effect of Range of Stress on Fatigue Strength of Plain Concrete Beams. *Journal of the American Concrete Institute,* Vol. 30, No. 2, Aug. 1958.
2. C. A. Ballinger. Cumulative Fatigue Damage Characteristics of Plain Concrete. In *Highway Research Record 370,* HRB, National Research Council, Washington, D.C., 1971, pp. 48-60.
3. R. G. Packard. *Thickness Design of Concrete Highway and Street Pavements.* Publication EB109. Portland Cement Association, Skokie, Ill., 1984.
4. S. D. Tayabji et al. Evaluation of Heavily Loaded Cement-Stabilized Bases. In *Transportation Research Record 839,* TRB, National Research Council, Washington, D.C., 1982, pp. 6-11.
5. R. W. Piggot. Roller-Compacted Concrete for Heavy-Duty Pavements: Past Performance, Recent Projects, and Recommended Construction Methods. In *Transportation Research Record 1062,* TRB, National Research Council, Washington D.C., 1986, pp. 7-13.
6. G. Pickett and G. K. Ray. Influence Charts for Concrete Pavements. Paper 2425. American Society of Civil Engineers, *Transactions,* Vol. 116, 1951.
7. H. M. Westergaard. Theory of Concrete Pavement Design *HRB Proc.,* Vol. 7, Part 1, 1927, pp 175-181.
8. R. G. Packard. *AIRPORT—Concrete Thickness Design for Airport and Industrial Pavements.* Concrete Design Software Library Program MC006X. Portland Cement Association, Skokie, Ill., 1986.
9. S. Ragan. Evaluation of the Frost Resistance of Roller-Compacted Concrete Pavements. In *Transportation Research Record 1062,* TRB, National Research Council, Washington, D.C., 1986, pp. 25-32.

DISCUSSION

ABASTASUIS M. IOANNIDES
Civil Engineering Department, University of Illinois, Urbana, Ill. 61801.

The design charts presented by the authors suffer from a number of limitations. The most important of these is that the charts are not plotted in terms of the variable that really controls the behavior of the system analyzed, namely the ratio (a/l) of the radius of the applied load to the radius of relative stiffness (l). In addition, Figure 7 assumes the use of the English unit system, while Figure 6 is even more restrictive in the sense that it only applies exactly for the E- and μ-values assumed in its derivation. These values are not explicitly given in the paper. There is no reason why two charts should be necessary because the single wheel load (SWL) case is simply the special dual wheel load (DWL) case in which spacing equals zero. Furthermore, ideally the SWL chart should give the same results as the Westergaard equation for the maximum stress under interior loading (*2*). Checking this, however, would be a tedious task in view of the way the chart is presented.

The purpose of graphic solutions is to present a concise picture of the phenomenon observed and to provide a fast but accurate way of determining the desired result. For these reasons, Figure 8 is submitted as an improvement of Figures 6 and 7. In this figure, the authors' charts are replotted in terms of a/l. The new graph was derived from and includes all of the SWL and DWL data presented in the paper (the dotted portions are extrapolations). The zero-spacing curve can easily be checked now and it is found to be in nearly perfect agreement with Westergaard's predictions for the SWL case. The effect of spacing is clearly shown in Figure 8. It would be a simple exercise in curve fitting to quantify the spacing effect as a function of the nondimensional ratio of the spacing to the load radius (S/a) and for a correction term to be added to the Westergaard equation. Similar correction terms for the finite size of the slab can also be obtained from nondimensional plots presented elsewhere (*3*).

Note that the abscissa in Figure 8 is the nondimensional stress $(\sigma h^2/P)$. Because three dimensionless ratios are used,

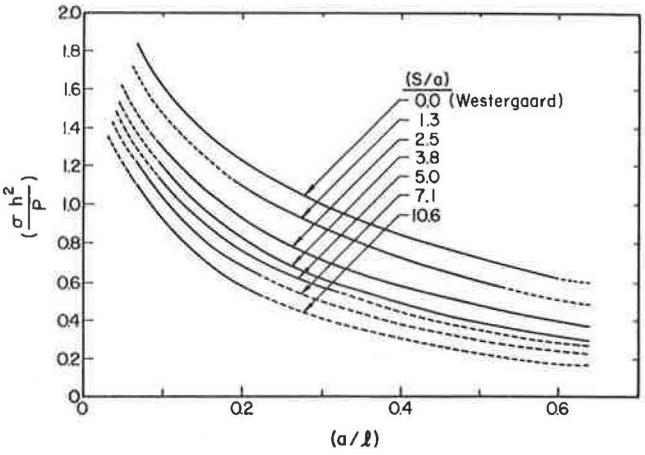

FIGURE 8 Nondimensional plot of effect of spacing.

Figure 8 can accommodate any system of units. It is noted that the authors' f-factor in Figure 7 is simply 1,000 times the nondimensional stress in the new graph. In obtaining Figure 8, E and μ for the slab were assumed to be 4 million psi and 0.15, respectively, but because of its nondimensional nature this plot applies to any selected parameters. The loaded areas were assumed to be circular, but this is of little consequence. Using Figure 8 is much simpler and involves one step only, compared with the iterative process required by the authors' charts. The ratio (S/l) could have been used instead of (S/a) in presenting the spacing effect in Figure 8 [as is done, for example, by the FAA according to Yoder and Witczak (*4*)] without any loss of generality. This is because (S/a) may be converted to (S/l) through multiplication by the governing ratio (a/l). Because it is admitted that "the behavior of RCC is similar to that of conventional concrete," the charts in Figures 6, 7, and 8 can be applied to the latter as well.

REFERENCES

1. A. M. Ioannides. Discussion of Response and Performance of Alternate Launch and Recovery Surfaces That Contain Layers of Stabilized Material by R. R. Costigan and M. R. Thompson. In *Transportation Research Record 1095,* TRB, National Research Council, Washington, D.C., 1986, pp. 70-71.
2. H. M. Westergaard. Stresses in Concrete Runways of Airports. *HRB Proc.*, Vol. 19, 1939, pp. 197-202. Also in *Stresses in Concrete Runways of Airports.* Portland Cement Association, Skokie, Ill., Dec. 1941.
3. A. M. Ioannides, M. R. Thompson, and E. J. Barenberg. Westergaard Solutions Reconsidered. In *Transportation Research Record 1043,* TRB, National Research Council, Washington, D.C., 1985, pp. 13-23.
4. E. J. Yoder and M. W. Witczak. *Principles of Pavement Design,* 2nd ed., John Wiley and Sons, Inc., New York, 1975.

AUTHORS' CLOSURE

The authors appreciate Ioannides' effort in trying to simplify Figures 6 and 7. The authors deliberately developed Figures 6 and 7 as separate figures to make them easy for practicing engineers to use. Figure 8, though correct and concise, may be more useful as a teaching aid.

Publication of this paper sponsored by Committees on Rigid Pavement Design, on Rigid Pavement Construction and Rehabilitation, and on Pavement Rehabilitation.

Engineering Properties of Roller-Compacted Concrete

SHIRAZ D. TAYABJI AND PAUL A. OKAMOTO

An investigation was conducted to develop a procedure for the design of roller-compacted concrete (RCC) pavements. This paper is a report on the laboratory portion of the investigation that was conducted to determine the engineering properties of RCC. Specimens for the laboratory tests were obtained from a full-scale test section constructed using a 10-ton vibratory roller. Specimens were tested for flexural, split-tensile, and compressive strength; modulus of elasticity; and fatigue properties. The engineering behavior of RCC was determined to be similar to that of conventional concrete. Test results for RCC made using 243 to 285 lb/yd^3 of cement show that RCC is capable of providing relatively high in-place strength. As with conventional concrete, RCC strengths produced are even higher when higher cement contents are used. In another phase of the investigation, mix proportioning procedures for RCC were investigated. Specimens were prepared using a vibrating table with a surcharge and the modified Proctor procedure. RCC mixes studied contained 3.5 and 6 bags/yd^3 of cement. Specimens prepared by using the vibrating table produced significantly lower densities and strengths because the moisture content was lowered.

Roller-compacted concrete (RCC) is a relatively stiff or zero-slump concrete mixture that is compacted by vibratory rollers. Although the term roller-compacted concrete is of recent origin (early 1970s), similar materials—mixtures of cement, aggregate, and water—have been used for a much longer time. These mixtures have been called cement-treated base (CTB), cement aggregate mixture (CAM), or granular soil cement (SC). However, CTB, CAM, and granular SC usually are relatively low-strength materials with 28-day compressive strengths of less than about 1,000 psi. RCC used for paving can be designed to achieve 28-day compressive strengths similar to or greater than those of conventional concrete.

Since the application of roller-compacted concrete for dam construction in the United States during the 1970s, its use has been increasing for other applications such as paving. Early use was made of RCC for paving in western Canada to provide durable pavements in remote areas. Because of its low cost, ease of placement, and good performance record in western Canada, RCC use is becoming widespread in the United States for off-highway facilities subjected to heavy vehicle loading. RCC has been used principally for off-highway facilities such as

1. Container ports,
2. Intermodal yards,
3. Log-haul loads,
4. Log-sorting yards,
5. Truck-parking areas,
6. Airfield apron areas, and
7. Tank apron (hardstands).

Construction Technology Laboratories, Inc., 5420 Old Orchard Road, Skokie, Ill. 60077.

BACKGROUND

The first large-scale use of RCC as paving was in British Columbia in 1976. This installation was a 4-acre log-sorting yard on Vancouver Island. The RCC pavement was 14 in. thick and was placed in two lifts. The first lift, with a compacted thickness of 8 in., contained 8 percent cement by weight. The second lift had 13 percent cement by weight. Since 1976 several large paving projects have been constructed using RCC in British Columbia. Most of these RCC projects used aggregate graded from 100 percent passing the 3/4-in. sieve to a maximum of about 14 percent passing the No. 200 sieve. Cement contents used have been about 13 percent by weight. Fly ash, in the range of from 15 to 20 percent by weight of total cementitious materials, was used on some projects. Typical RCC core strengths from some British Columbia projects are given in Table 1. A field evaluation of several RCC projects in British Columbia during 1980 indicated that the RCC pavements subjected to heavy loads were performing well (*1*).

The first significant use of RCC for paving in the United States was at Fort Hood in Texas. An 18,000-yd^2 area of 10-in.-thick RCC pavement was constructed for use as a parking apron for tanks and other tracked vehicles. The RCC mix at Fort Hood contained 300 lb/yd^3 of cement and 160 lb/yd^3 of fly ash. Most of the RCC used 1 1/2-in. maximum size aggregate. Beams obtained from the RCC pavement produced flexural strengths at 28 days of between 800 and 900 psi.

Another major use was made of RCC at the Port of Tacoma, Washington. The South Intermodal Yard constructed during early 1985 consisted of 52,000 yd^2 of 12- and 17-in.-thick RCC pavement. Crushed aggregate with 5/8-in. maximum size was used. Cement content specified was 450 lb/yd^3 and fly ash specified was 100 lb/yd^3. The pavement was constructed using a conventional asphalt paver equipped with a vibrating screed. Average flexural strength at 28 days measured from sawed beams averaged about 750 psi. The

TABLE 1 TYPICAL RCC CORE STRENGTHS FOR SOME BRITISH COLUMBIA PROJECTS

Project	Year Built	Date of Sample	Compressive Strength (psi)
Caycuse log-sorting yard	1976	1980	4,210[a]
		1984	5,880[a]
Lynterm container port	1977	1980	4,690[a]
Fraser Mills log-sorting yard	1982	1983	4,700[b]
Bullmoose coal mine	1983	1983	2,200[b]
Fraser Surrey dock	1984	1984	4,570[b]

[a]From Tayabji et al. (*1*).
[b]From Piggott (*2*).

North Intermodal Yard, constructed during the summer of 1985, consisted of 29,000 yd^2 of 12- and 17-in.-thick RCC. Aggregate type and cementitious content were similar to those for the South Intermodal Yard. Part of the paved area was constructed using a Barber Green asphalt paver equipped with a vibrating screed and part was paved using a German-made ABG paver, which is equipped with two tamping bars that consolidate the RCC to near specified density before rolling. Preconsolidation by the ABG paver helps to produce a nearly level surface.

A 40,000-yd^2 aircraft-parking apron was constructed during the summer of 1985 at the Portland International Airport. The aggregate consisted of a modification to the Oregon Department of Transportation specification for 3/4-in. maximum sized aggregate for asphalt pavements. The gradation was modified to include a higher percentage of fines, between 5 and 10 percent passing the No. 200 sieve. Specified cement content was 488 lb/yd^3 and specified fly ash content was 119 lb/yd^3. On this project, the 14-in.-thick pavement was constructed in two equal lifts using the German ABG paver equipped with two tamping bars. An 8-ton combination vibratory steel-wheeled and multitired roller was used to provide final compaction. Surface finish met requirements of a maximum of 1/4-in. roughness in 10 ft established by the Federal Aviation Administration for aircraft-parking aprons.

During October 1986 RCC was used for pavement construction of Berths 11 and 12 of the Conley Terminal in Boston. The RCC mix used contained 600 lb/yd^3 of cement and 100 lb/yd^3 of fly ash. The aggregate was well graded with a maximum size of 3/4 in. Pavement thickness was 18 in. Lanes were constructed in two or three lifts. Lanes were 450 ft long and about 15 ft wide.

To summarize the experience with RCC pavements, the following items are noted:

1. RCC is generally mixed in a twin-shaft pugmill.
2. Cement content used has ranged from about 300 to 600 lb/yd^3. On some projects, fly ash, in the range of 15 to 20 percent by weight of cementitious materials, was used.
3. RCC is usually placed using an asphalt paver. The maximum compacted lift thickness that can be placed using currently available pavers is about 9.0 to 10.0 in. However, pavers can be modified to provide a compacted lift of about 12 in.
4. RCC is compacted using 10- to 12-ton vibratory rollers to achieve specified density.
5. Contraction joints are not provided in RCC pavements. Instead, shrinkage cracking is allowed to occur naturally. Spacing of shrinkage cracks is about 50 to 60 ft.
6. Pavements constructed with RCC have excellent performance records under very heavy vehicle loadings.

OBJECTIVE OF THE PROJECT

The objective of the project was to develop data and procedures for the design of RCC pavements. The scope of work included the following items:

1. Evaluation of engineering properties of RCC,
2. Evaluation of mix proportioning procedures,
3. Evaluation of RCC durability, and
4. Establishment of a thickness design procedure for RCC pavements.

The results of the first two work items are presented in this paper. The thickness design procedure for RCC pavements is presented in a companion paper by Tayabji and Halpenny in this Record. Investigation of RCC durability is still in progress.

ENGINEERING PROPERTIES OF RCC

Although RCC has been in use for paving for many years, no detailed study has been carried out to investigate its engineering properties. In general, available information on RCC for paving involves only compressive strength. The reported 28-day compressive strengths for RCC range from about 3,000 psi to more than 5,000 psi.

The objectives of the PCA study were to investigate the different strength characteristics of RCC and to compare its engineering behavior with that of conventional concrete. The following strength-related information was considered necessary:

1. Compressive strength,
2. Flexural strength,
3. Split-tensile strength,

4. Modulus of elasticity, and
5. Fatigue behavior.

A laboratory test program was designed to provide preliminary data on proportioning and compaction of RCC mixes. The laboratory test program was used to identify four mixes for construction of full-scale test slabs. Specimens were obtained from the full-scale test slabs and tested for strength, modulus of elasticity, and fatigue properties.

Laboratory Test Program

RCC mixes were prepared in the laboratory to investigate the influence of coarse aggregate volume, paste-to-mortar volume, and water-to-cementitious material ratio on consistency, compactibility, and compressive strength of RCC. The laboratory mixes were designed using procedures discussed in the American Concrete Institute's Committee 207 report on Roller Compacted Concrete (*3*). Although this report, published in 1980, was limited in its applicability, at the time it was the only available reference containing a detailed discussion on different aspects of RCC.

Material Characteristics

The following materials were used:

- Cement: Type I,
- Fly ash: Class F, and
- Aggregate: locally available gravel and sand.

Coarse aggregate was a bank-run gravel from Elgin, Illinois. The coarse aggregate had a maximum aggregate size of 1 1/2 in. and was blended to meet the gradation requirements of Size 467 of ASTM C 33. The fine aggregate was Elgin sand. The gradations of the coarse and fine aggregate are given in Table 2.

TABLE 2 AGGREGATE GRADATIONS FOR LABORATORY MIXES

	Percentage Passing	
Sieve Size	Actual	ASTM C 33[a]
Coarse Aggregate		
1 1/2 in.	100.0	95-100
3/4 in.	61.3	35-70
3/8 in.	10.9	10-30
No. 4	2.2	0-5
Fine Aggregate		
No. 4	100.0	95-100
No. 8	100.0	80-100
No. 16	61.8	50-85
No. 30	39.2	25-60
No. 50	16.8	10-30
No. 100	3.1	2-10

[a]Coarse aggregate gradation is for Size 467.

Laboratory Mixes

The mixes prepared in the laboratory incorporated the following parameters:

- Cement content: 282 lb/yd^3,
- Coarse aggregate volume: 52 to 59 percent,
- Fine aggregate volume: 23 to 28 percent,
- Fly ash/cement (by weight): 0 to 20 percent,
- Water/(cement + fly ash) (by weight): 0.55 to 0.60,
- Fine aggregate/mortar (by volume): 60 percent,
- Paste/mortar (by volume): 38 to 42 percent, and
- Theoretical unit weight: 156 to 158 pcf (air free).

Consistency of the mix was measured using Vebe equipment. Details of the test procedure using Vebe equipment are given elsewhere (*3*). The consistency value is the number of seconds required to consolidate the volume of concrete into a 9.5-in.-diameter bucket mounted on a vibrating table assembly. For testing RCC mixes, a 27.5-lb surcharge was used instead of the standard 7.5-lb surcharge.

Cylinders for measuring compressive strength were prepared on a vibrating table. A surcharge of 27.5 lb was used for the 6- by 12-in. cylinders. The cylinders were compacted in a single lift. The cylinders were also used to obtain densities. The effect of vibration time on density and on compressive and flexural strengths was also evaluated. Beams for flexural strength were compacted in one lift using a surcharge of 50 lb for 6- by 6- by 30-in. beams.

Test Results

The following test results were obtained:

1. Vibration time in excess of 1 min did not have a significant effect on either compacted density or compressive and flexural strengths.
2. There exists an optimum coarse aggregate volume for obtaining maximum compressive strength. For the mixes tested, the optimum coarse aggregate volume was determined to be 55 percent.
3. There did not appear to be an optimum paste-to-mortar ratio for the mixes.
4. Although the mixes were designed to provide a 28-day compressive strength of about 3,000 psi, measured compressive strengths were generally between 4,000 and 5,000 psi.
5. Use of up to 20 percent Class F fly ash by weight of cement did not have a noticeable effect on 28-day compressive strengths.

As stated, the preliminary laboratory test program was undertaken to provide an understanding of the effects of different mixes and specimen preparation methods on the compacted properties of RCC. On the basis of results from the laboratory program, the following parameters were selected for construction of a full-scale test slab.

1. Use vibrating time of 1 min and surcharge of 27.5 lb for compacting 6- by 12-in. compressive strength cylinders in one lift,
2. Use vibrating time of 1 min and surcharge of 50 lb for compacting beams for flexural strength in one lift,
3. Use coarse aggregate volume of about 60 percent of the total volume, and
4. Use a paste-to-mortar ratio of about 0.40.

Full-Scale Test Panels

Four full-scale test panels were constructed in an outdoor location at the facilities of the Portland Cement Association in Skokie, Illinois, during September 1984. Each panel was constructed using a different mix, designated Mixes A, B, C, and D. Panels constructed with Mixes A, B, C, and D were designated Panels A, B, C, and D, respectively.

Details of Test Section

Test panels were 13.5 ft wide and about 12 ft long. Panels were designed to have a compacted thickness of 8 in.

Mix Designs

Details of the mixes used are given in Table 3. The mixes were designed to obtain the following information:

1. Effect of fly ash: Mix A versus Mix B for same mortar and paste content,
2. Effect of mortar content: Mix B versus Mix C for same fly ash-to-cement ratio, and
3. Effect of fly ash-to-cement ratio: Mix B versus Mix D for same mortar volume.

The test program was also designed to allow a comparison to be made between molded test specimens and specimens obtained from the full-scale test panels.

Construction of Test Panels

The RCC for each test panel was batched at a local ready-mix concrete plant. The RCC material was then transported to the site in a transit mixer and deposited on a prepared 4-in.-thick granular subbase. The RCC material was spread manually between wood forms that were staked into the ground to provide restraint during compaction. The uncompacted thickness was maintained at about 10 in.

After the RCC material had been uniformly spread, a tandem vibratory roller was used to obtain the desired compaction. Details of the vibratory roller are as follows:

- Model: Case 752;
- Drum width: 63 in.;
- Drum diameter: 47 in.;
- Total applied force: 445 lb/in. width of drum, 28,000 lb/drum;
- Frequency: 2,000 vpm; and
- Amplitude: 0.08 in. (peak to peak).

For each area undergoing compaction, one pass was made in the static mode followed by four passes in the vibratory mode. Density was measured after each pass by means of a nuclear gauge operated in the back-scatter mode. Measured density data are given in Table 4. Final measured compacted wet densities ranged from 152.2 to 154.2 pcf.

TABLE 3 MIXES USED FOR FULL-SCALE TEST PANELS

	Mix			
	A	B	C	D
CA (lb/yd^3)	2,734	2,749	2,556	2,707
FA (lb/yd^3)	1,044	1,049	1,156	1,069
C (lb/yd^3)	285	243	266	263
F (lb/yd^3)	0	48	54	45
W (lb/yd^3)	151	139	161	142
F/C (weight)	0	0.20	0.20	0.17
W/C+F (weight)	0.53	0.48	0.50	0.46
W/C+F (volume)	1.67	1.46	1.54	1.41
CA volume (%)	60	61	57	60
FA volume (%)	23	23	26	24
Mortar volume (%)	37	37	41	38
Paste volume (%)	14	14	16	14
CA specific gravity	2.68	2.68	2.68	2.68
FA specific gravity	2.68	2.68	2.68	2.68
C specific gravity	3.15	3.15	3.15	3.15
F specific gravity	—	2.66	2.66	2.66
Theoretical unit weight (pcf, air free)	159.2	159.8	158.5	159.7

NOTE: Mortar and paste volumes are air free. Air content of 2 percent by volume is assumed. CA = coarse aggregate, FA = fine aggregate, C = cement, F = fly ash, and W = water.

TABLE 4 MEASURED WET DENSITY DATA

Roller Pass	Slab A	Slab B	Slab C	Slab D
As spread	127.8	128.7		129.7
Static	149.7	147.6		146.2
First vibratory	150.9			
Second vibratory	152.9	152.1		151.2
Fourth vibratory	152.9	154.2	152.2	153.4

NOTE: Densities (pcf) were measured using a nuclear gauge operated in the back-scatter mode.

The as-placed RCC material appeared to be slightly drier than optimum moisture. However, under vibratory rolling, mortar appeared to be migrating upward toward the surface, and the surface appeared to be rebounding under the vibratory loading. The four panels were constructed over a period of 2 days. Daytime temperature during construction was about 85°F. Compaction of each panel was generally completed within 30 min after placement of the RCC material.

The as-constructed surfaces of the test panels had localized areas where the coarser aggregate was exposed without adequate mortar.

Each test panel was covered with a layer of polyethylene on completion of compaction. For the next 7 days, the test panel surfaces were wet-cured by regularly spraying with water and then recovering them with polyethylene sheets. After 7 days of wet-cure, a clear curing compound was applied.

Preparation of Beams and Cylinders

Beam and cylindrical specimens were prepared during construction of the test panels. These specimens were prepared to make possible comparison with cores and beams obtained from the test panels. During construction of each test panel, samples of RCC material were obtained for preparing the molded specimens. All beams and cylinders were moist-cured until testing.

Cylindrical Specimens Cylinders were prepared using conventional steel molds 6 in. in diameter by 12 in. deep. Cylinders were compacted full depth (in a single layer) on a vibrating table using a surcharge weight of 27.5 lb and vibrating time of 1 min. A total of 22 cylinders were prepared for each RCC mix.

Beam Specimens Beams were prepared using conventional steel molds for making 6- by 6- by 30-in. beams. Beams were compacted full depth (in a single layer) on a vibrating table using a surcharge weight of 50 lb and vibration time of 1 min. A total of eight beams were prepared for each RCC mix.

Obtaining Cores and Sawed Beams from Test Panels

Initially, three cores were obtained from each test panel 7 days after construction of the panels. Cores were nominally 4 in. in diameter. Subsequently, twelve 4-in. nominal diameter cores and 12 beams were obtained from each test panel 28 days after construction of the test panels. Beams were cut to provide a nominal width of 6 in. and a length of 30 in. All beams and cores were moist-cured until they were tested.

Testing Program

The testing program was developed to determine the following strength-related characteristics of the RCC mixes:

1. Compressive strength,
2. Flexural strength,
3. Split-tensile strength,
4. Modulus of elasticity, and
5. Fatigue behavior.

Details of the planned testing program are given in Table 5.

Test Results

Test results obtained for compressive, flexural, and split-tensile strength and modulus of elasticity are summarized in Table 6 for the four RCC mixes.

Compressive Strength Compressive strength of cores was generally lower than that of molded cylinders. Core compressive strength at 7 days ranged from 1,800 psi for Mix D to 3,610 psi for Mix C. Core compressive strength at 28 days ranged from 2,480 psi for Mix D to 4,390 psi for Mix C. Core and cylinder strengths are compared in Figure 1. Compressive strength development with time is shown in Figure 2 for cores.

TABLE 5 PLANNED TEST PROGRAM

Test	No. of Specimens tested at[a] 7 days	28 days	90 days
Compressive strength			
6-in. cylinders	3	3	3
4-in. cores	3	3	3
Flexural strength			
Molded beams	3	3	3
Sawed beams		4	
Split-tensile strength			
6-in. cylinders		3	
4-in. cores		3	
Modulus of elasticity			
6-in. cylinders		3	
4-in. cores		3	
Fatigue testing			
Molded beams			
Sawed beams			5[b]

[a]Numbers of specimens tested are for each RCC mix/test panel.

[b]Fatigue testing was performed at an age of about 7 months.

TABLE 6 SUMMARY OF TEST RESULTS

Test	Mix A	Mix B	Mix C	Mix D
Compressive strength (psi)				
4-in. cores at 7 days	3,050	3,180	3,610	1,800
6-in. cylinder at 7 days	3,720	2,970	4,010	2,250
4-in. cores at 28 days	3,820	3,660	4,390	2,480
6-in. cylinder at 28 days	4,440	4,010	4,820	3,720
4-in. cores at 90 days	4,280	3,560	4,620	3,500
6-in. cylinder at 90 days	4,620	4,280	5,970	4,260
Flexural strength (psi)				
Sawed beams at 28 days	670	595	625	480
Molded beams at 28 days	705	600	490	490
Sawed beams at 7 months	685	770	740	585
Molded beams at 9 months	755	700	725	700
Split-tensile strength (psi)				
4-in. cores at 28 days	610	540	575	450
6-in. cylinder at 28 days	450	390	510	410
Modulus of elasticity (million psi)				
4-in. cores at 28 days	3.65	4.08	4.29	2.77
6-in. cylinder at 28 days	5.02	4.92	4.88	4.70
Pulse velocty (ft/sec)				
4-in. cores at 28 days	15,750	16,410	16,890	16,320
6-in. cylinder at 28 days	15,860	16,260	16,260	16,360
Density (psi)				
4-in. cores	154.8	155.8	156.0	154.8
6-in. cylinders	150.1	153.3	154.8	152.3
Sawed beams	154.8	156.5	156.5	157.2
Molded beams	150.7	153.4	150.8	144.8

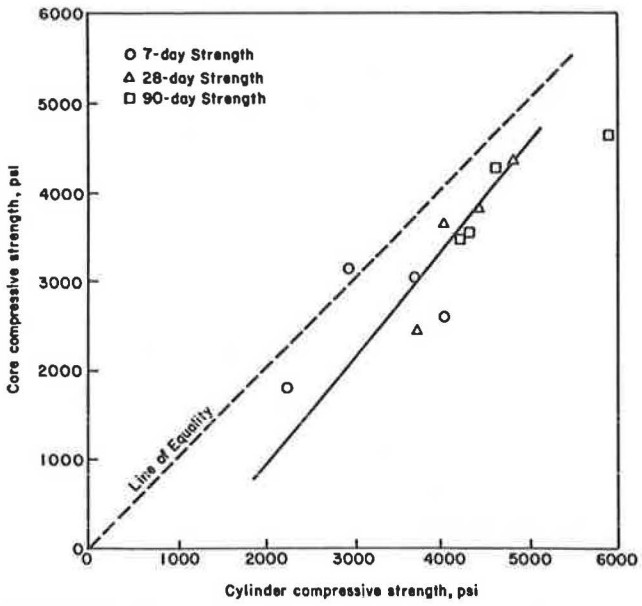

FIGURE 1 Comparison of core and cylinder compressive strengths.

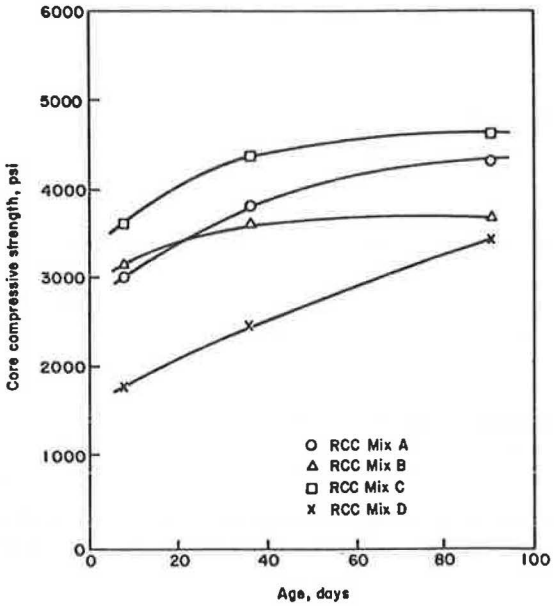

FIGURE 2 Compressive strength development with time (cores).

Flexural Strength Flexural strength measured for sawed beams at 28 days ranged from 480 psi for Mix D to 670 psi for Mix A. Values for molded and sawed beams were generally similar. The relationship between the 28-day flexural strength and the 28-day core compressive strength is shown in Figure 3. The relationship between flexural (sawed beam) and core compressive strengths can be approximated as follows:

RCC Mix A $f_r = 10.8\ (f_c)^{0.5}$

RCC Mix B $f_r = 9.8\ (f_c)^{0.5}$

RCC Mix C $f_r = 9.4\ (f_c)^{0.5}$

RCC Mix D $f_r = 9.6\ (f_c)^{0.5}$

Conventional concrete $f_r = C\ (f_c)^{0.5}$

where

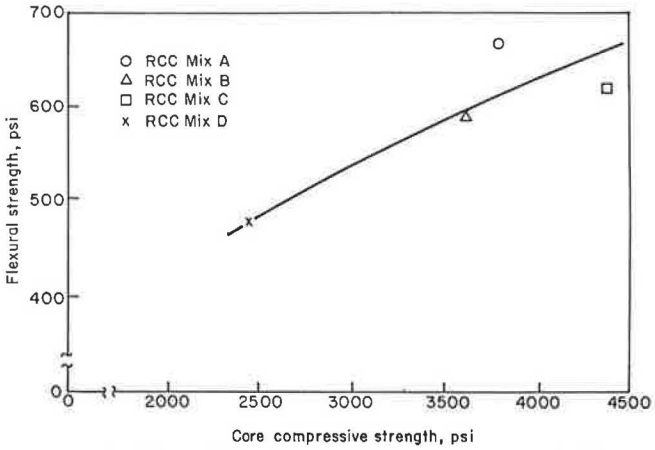

FIGURE 3 Flexural strength versus compressive strength (28-day values of cores).

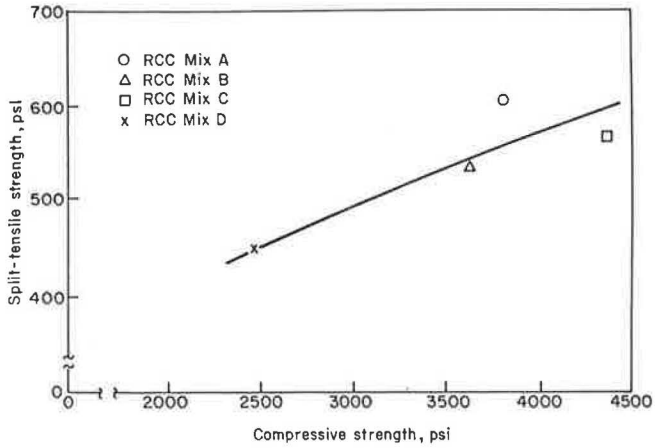

FIGURE 4 Split-tensile strength versus compressive strength (cores).

f_r = average flexural strength of sawed beams at 28 days (psi),
f_c = average compressive strength of cores at 28 days (psi), and
C = constant = 8.0 to 12.0.

Split-Tensile Strength Split-tensile strength of cores measured at 28 days ranged from 450 psi for Mix D to 610 psi for Mix A. Split-tensile strengths for cores were generally higher than those obtained for molded cylinders. The relationship between split-tensile and compressive strength for cores is shown in Figure 4. The relationships among split-tensile, compressive, and flexural strength can be approximated as follows:

RCC Mix A $f_t = 0.91 f_r = 9.8 (f_c)^{0.5}$
RCC Mix B $f_t = 0.91 f_r = 8.9 (f_c)^{0.5}$
RCC Mix C $f_t = 0.92 f_r = 8.7 (f_c)^{0.5}$
RCC Mix D $f_t = 0.94 f_r = 9.0 (f_c)^{0.5}$

where f_t is average split-tensile strength (psi) of cores at 28 days.

Modulus of Elasticity Measured modulus of elasticity values for cores ranged from 2.77 million psi for Mix D to 4.29 million psi for Mix C. The modulus values measured for cores were generally lower than those measured for cylinders. The relationship between modulus of elasticity and compressive strength for cores is shown in Figure 5 and can be approximated as follows:

RCC Mix A: $E = 59{,}000(f_c)^{0.5}$
RCC Mix B: $E = 67{,}000(f_c)^{0.5}$
RCC Mix C: $E = 65{,}000(f_c)^{0.5}$
Conventional concrete: $E = 57{,}000(f_c)^{0.5}$ (4)

Pulse Velocity Pulse velocity was measured at 28 days for both cores and cylinders. Pulse velocity values ranged from 15,750 to 16,890 ft/sec. For conventional paving concrete, pulse velocity is about 14,000 to 16,000 ft/sec.

Density Densities of cores, cylinders, molded beams, and sawed beams were measured. Densities were generally higher

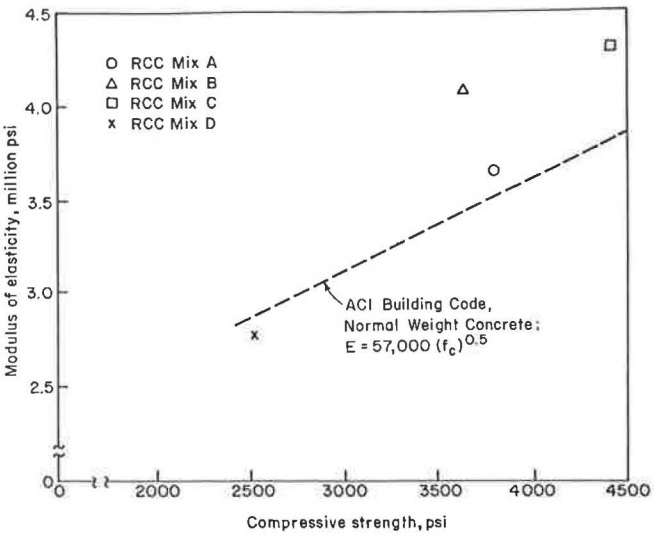

FIGURE 5 Modulus of elasticity versus compressive strength (cores).

for cores and sawed beams than for cylinders and molded beams. Densities of cores and sawed beams were about 1 to 2 pcf higher than those measured at the time of construction by the nuclear density gauge.

Fatigue Behavior Tests were conducted to determine flexural fatigue characteristics of RCC using beam specimens sawed from the test panels. Five beams from each panel were used. Beams were nominally 6 by 6 by 30 in. In general, two tests were performed on a single beam. In addition, beam sections were also used to determine static flexural strength. Fatigue tests were performed at the age of about 7 months.

Repeated load tests were conducted on beam sections supported on an 18-in. span and loaded at third points. Loads were selected to produce applied stress-to-flexural strength ratios ranging from about 0.50 to 0.95. Repeated load was applied with a hydraulic actuator. Loading frequency was maintained at 10 cycles/sec. To prevent impact loading, a minimum static force of 10 percent of maximum applied load was maintained in each load cycle. Testing was automatically terminated when the beam cracked. Each beam was kept in a

moist condition for the duration of the test by means of wet burlap wrapped around the beam and covered with plastic.

Fatigue test results are summarized in Table 7 and shown in Figure 6. Linear regression was used to develop a fatigue curve for the combined results of Mixes A, B, C, and D. The fatigue test results of the RCC mixes are compared in Figure 7 with results from fatigue tests on conventional concrete conducted by Murdoch and Kesler (*5*) and Ballinger (*6*). In addition, the PCA fatigue curve used for design of concrete pavements (*7*) is also shown in Figure 7. The Murdoch-Kesler curve for conventional concrete shown in Figure 7 was drawn so that 95 percent of the test results would fall above the line. The PCA fatigue curve used for pavement design shown in Figure 7 is conservatively set below the Murdoch-Kesler curve.

A design fatigue curve for RCC was developed using a degree of conservatism similar to that used to develop PCA's design fatigue curve for conventional concrete. The design curve for RCC, also shown in Figure 7, is set about 15 percent below the 95 percent curve for RCC. The use of the RCC design curve for thickness design of pavements is discussed in a companion paper by Tayabji and Halpenny in this Record.

TABLE 7 FATIGUE TEST DATA

RCC Mix	Stress Ratio	No. of Load Repetitions to Failure
A	0.59	268,050
	0.61	372,930
	0.79	1,550
	0.84	770
	0.91	1,440
B	0.53	982,460
	0.59	678,270
	0.62	90,300
	0.69	4,590
	0.71	3,000
	0.83	1,620
	0.91	1,270
C	0.50	1,716,560
	0.62	337,580
	0.67	130,450
	0.74	14,140
	0.89	790
D	0.48	3,018,740
	0.72	11,890
	0.80	1,600
	0.85	1,600
	0.91	21,300
	0.96	620

MIX PROPORTIONING OF RCC

A study was conducted to investigate the factors that affect the mix proportioning of RCC. The following factors were investigated.

1. Compaction procedure
   - Vibratory table with a surcharge
   - Modified Proctor (10-lb rammer, 18-in. drop)
2. Maximum size of aggregate
   - 1 1/2 in.
   - 3/4 in.
3. Cement content
   - 3.5 bags per cubic yard
   - 6 bags per cubic yard

The objective of mix proportioning of RCC mixes is to obtain a mix that will provide either maximum density or maximum strength as measured by compressive strength under a compaction effort that closely simulates field vibratory roller compaction effort. The mix proportioning procedure involves development of moisture content-density and moisture content-strength relationships. This procedure closely resembles the approach used to determine the relationship between the moisture content and density of soils and granular materials. For soils and granular materials, the relationship is used to establish the optimum moisture content that will result in maximum compacted density.

Early studies of RCC made use of the Vebe test procedure to establish the optimum moisture content. Preliminary testing at PCA's laboratories indicated that the Vebe test is not very consistent, partly because it is a subjective test. For the PCA study, it was therefore decided to measure compacted density and strength of test specimens compacted by two different procedures. In the first procedure, specimens were

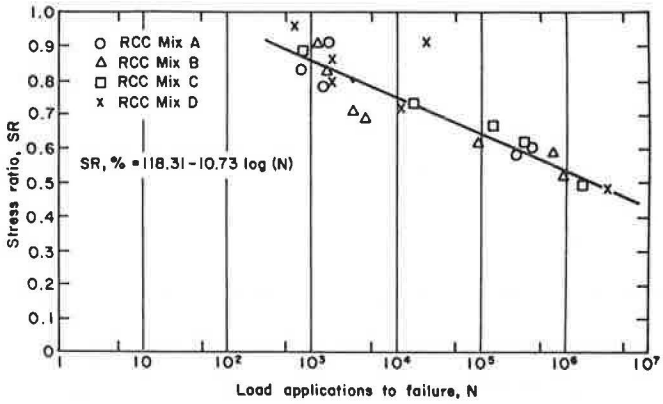

FIGURE 6 Fatigue relationship for RCC.

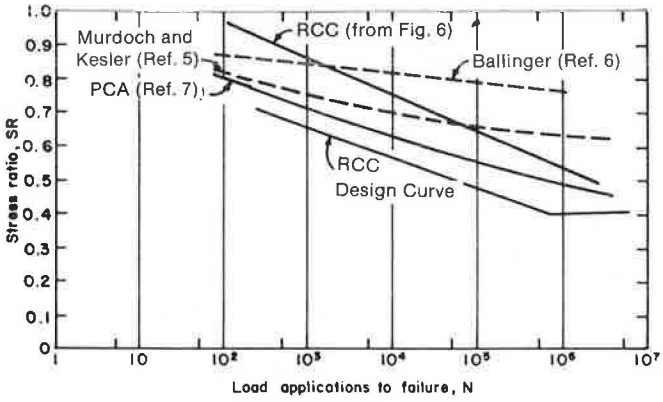

FIGURE 7 Comparison of fatigue relationships of RCC and conventional concrete.

compacted on a vibrating table using a surcharge weight of 27.5 lb for a period of 1 min. The second procedure was the modified Proctor method. For each test procedure, 6-in.-diameter by 12-in.-high cylindrical specimens were prepared using standard steel molds for making concrete specimens.

The modified Proctor method generally followed the procedures of ASTM D 1557-78 (10-lb rammer and 18-in. drop). The ASTM procedure requires use of a mold 4.584 in. high and compaction of the specimen in five equal layers with each layer subjected to 56 blows. In the PCA procedure, the mold was 12 in. high, the specimen was compacted in increments of 2 in., and 122 blows were used per increment. A compactive effort of 122 blows per increment was selected to maintain a compactive effort per unit volume that was the same as that required for the ASTM procedure.

It should be noted that the compactive effort used in preparing laboratory specimens does not have a direct correlation with compaction obtained with different equipment in the field. However, data obtained during construction of the full-scale test panels indicated that densities of specimens compacted on the vibrating table for 1 min were quite close to those measured for the test panels.

The test specimens prepared using the two procedures were used to determine both the compacted density and the 28-day compressive strength.

Test Program

Four RCC mix combinations were selected for the test program:

- Mix Combination P: 1 1/2-in. maximum size aggregate (MSA), 3.5 bags/yd^3 cement;
- Mix Combination Q: 3/4-in. MSA, 3.5 bags/yd^3 cement;
- Mix Combination R: 3/4-in. MSA, 6 bags/yd^3 cement; and
- Mix Combination S: 1 1/2-in. MSA, 6 bags/yd^3 cement.

Coarse and fine aggregates were blended to obtain the desired gradations for each of the two aggregate types. The combined gradations for aggregates with 1 1/2-in. MSA and 3/4-in. MSA are shown in Figure 8.

Mix Proportioning

For each mix combination, mixes were prepared at four different moisture contents. The procedure used was to determine the required amount of coarse and fine aggregate and cement to be used for each mix combination and then to add different amounts of water to each of the four mixes used for each mix combination. Details of the mix proportions are given in Tables 8-11 for Mix Combinations P, Q, R, and S, respectively. Batched total moisture content ranged from 4.3 to 7.5 percent.

Each mix was batched to provide about 1.8 ft^3 of material. Mixing was done in a laboratory paddle mixer. As soon as mixing was completed, a small sample was obtained and oven dried to determine the total moisture content of the mixed material.

Test Specimen Fabrication

For each mix, four specimens were compacted using the vibrating table and a surcharge of 27 1/2 lb and four specimens were compacted using the modified Proctor procedure. Each specimen was weighed after compaction. Specimens were retained in the steel mold for 1 day and then

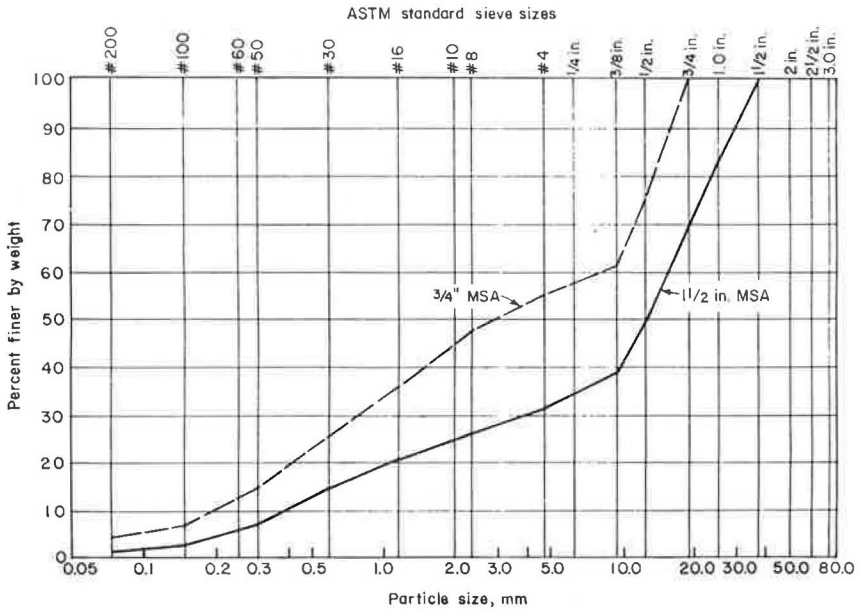

FIGURE 8 Gradations of aggregates with 1 1/2-in. and 3/4-in. MSA.

TABLE 8 PROPORTIONS FOR MIX COMBINATION P (1 1/2-in. MSA, 3.5 BAGS CEMENT)

	Mix Designation			
	4	5	6	7
Proportions (lb/yd^3 air free)				
Aggregate (SSD)	3,888	3,836	3,950	3,922
Cement	326	322	331	329
Water	133	154	108	120
Total	4,347	4,312	4,389	4,371
Air-free unit weight (lb/ft^3)	161.0	159.8	162.6	161.9
Water-to-cement ratio (by weight)	0.41	0.48	0.33	0.36
As-batched total moisture content (%)	4.9	5.5	4.3	4.6

NOTE: Absorption coefficient of aggregate = 1.74 percent. SSD = saturated surface dry.

TABLE 9 PROPORTIONS FOR MIX COMBINATION Q (3/4-in. MSA, 3.5 BAGS CEMENT)

	Mix Designation			
	8	9	10	11
Proportions (lb/yd^3 air free)				
Aggregate (SSD)	3,885	3,758	3,658	3,819
Cement	336	322	316	330
Water	125	175	216	151
Total	4,346	4,258	4,190	4,300
Air-free unit weight (lb/ft^3)	161.0	157.8	155.2	159.3
Water-to-cement ratio (by weight)	0.37	0.54	0.68	0.46
As-batched total moisture content (%)	5.0	6.4	7.5	5.7

NOTE: Absorption coefficient of aggregate = 1.74 percent. SSD = saturated surface dry.

TABLE 10 PROPORTIONS FOR MIX COMBINATION R (3/4-in. MSA, 6 BAGS CEMENT)

	Mix Designation			
	12	13	14	15
Proportions (lb/yd^3 air free)				
Aggregate (SSD)	3,452	3,548	3,499	3,406
Cement	552	568	560	545
Water	219	178	199	239
Total	4,223	4,294	4,258	4,190
Air-free unit weight (lb/ft^3)	156.4	159.1	157.7	155.1
Water-to-cement ratio (by weight)	0.40	0.32	0.36	0.44
As-batched total moisture content (%)	7.0	5.8	6.4	7.5

NOTE: Absorption coefficient of aggregate = 1.74 percent. SSD = saturated surface dry.

TABLE 11 PROPORTIONS FOR MIX COMBINATION S (1 1/2-in. MSA, 6 BAGS CEMENT)

	Mix Designation			
	16	17	18	19
Proportions (lb/yd^3 air free)				
Aggregate (SSD)	3,551	3,429	3,509	3,469
Cement	560	541	554	547
Water	181	233	199	216
Total	4,292	4,203	4,262	4,232
Air-free unit weight (lb/ft^3)	159.0	155.7	157.9	156.8
Water-to-cement ratio (by weight)	0.32	0.43	0.36	0.40
As-batched total moisture content (%)	5.8	7.3	6.3	6.8

NOTE: Absorption coefficient of aggregate = 1.74 percent. SSD = saturated surface dry.

transferred to a moist-curing chamber and cured there until the day of test. Specimens were tested for compressive strength at 28 days. Specimen height generally was 12 in. However, some of the specimens compacted on the vibrating table were slightly shorter than 12 in.

Test Results

Test results for each mix are given in Table 12. Also included in Table 12 are values for both the as-batched total moisture content and the measured total moisture content. The measured total moisture content was generally lower than the as-batched moisture content. This difference ranged from about 0.1 to about 1.4 percent. The variation is attributed primarily to the problem of obtaining representative samples of the mix for oven drying. Inclusion of larger amounts of large-sized aggregate particles can significantly affect the value of the measured moisture content.

The moisture content-density and moisture content-strength relationships are shown in Figures 9-12. These relationships are shown using the as-batched moisture contents.

Test results follow.

1. Specimens compacted on the vibrating table had lower 28-day compressive strengths than specimens compacted using the modified Proctor procedure.
2. For both compaction procedures used, a distinct moisture content-strength relationship was obtained from which the optimum moisture content for maximum strength could be established.
3. The modified Proctor procedure did not provide a distinct relationship between either dry or wet density and moisture content. It appears that, within the narrow range of moisture contents used, the modified Proctor procedure could not discriminate between "dry" and "wet" mixes. On the other hand, the vibrating table compaction procedure did result in reasonably distinct moisture content and density relationships from which it was possible to identify an optimum moisture content that would result in maximum wet or dry density.
4. For the mix combinations used, the optimum as-batched total moisture content values given in Table 13 were obtained. A lower optimum moisture content was obtained for mix combinations with lower cement contents. Also, a lower optimum moisture content was obtained for mix combinations with the 1 1/2-in. MSA.
5. Specimens prepared using the vibrating table produced significantly lower densities and strengths at lower moisture contents.

SUMMARY

Results of an investigation conducted to develop engineering data for the design of RCC have been presented. It is clear that the engineering behavior of RCC is similar to that of conventional normal-weight concrete. Test results for RCC made with 243 to 285 lb/yd^3 of cement show that RCC is capable of providing relatively high-strength concrete.

On the basis of test results, it is recommended that RCC be treated much like conventional concrete when designing thickness of a pavement. Thus existing thickness design procedures used for concrete pavements are considered applicable to the design of RCC pavements when used in conjunction with the design RCC fatigue curve.

TABLE 12 TEST RESULTS

Mix Type	Mix No.	Total Moisture Content (%)		Vibrating Table			Modified Proctor		
		Theoretical	Measured	Wet Density (pcf)	Dry Density (pcf)	f_c^a (psi)	Wet Density (pcf)	Dry Density (pcf)	f_c^a (psi)
P									
(1 1/2-in.	4	4.9	4.8	155.3	148.2	5,000	158.0	150.8	5,770
MSA, 3.5	5	5.5	6.7	157.3	147.4	3,770	157.4	147.5	4,420
bags	6	4.3	3.2	140.0	135.7	2,170	156.7	151.8	4,290
cement)	7	4.6	4.4	154.6	148.1	4,930	158.8	152.1	5,320
Q									
(3/4-in. MSA,	8	5.0	4.8	138.0	131.7	2,020	152.0	145.0	3,450
3.5 bags	9	6.4	5.6	151.1	143.1	3,920	154.5	146.3	4,310
cement)	10	7.5	6.8	151.3	141.7	3,170	153.9	144.1	3,700
	11	5.7	5.9	151.8	143.3	3,760	156.0	147.3	4,500
R									
(3/4-in. MSA,	12	7.0	6.0	144.8	140.4	6,200	155.9	147.1	7,320
6 bags	13	5.8	4.8	138.9	132.5	4,680	156.4	149.2	6,670
cement)	14	6.4	5.4	148.4	140.8	5,640	156.3	148.3	6,900
	15	7.5	6.4	150.5	141.4	6,110	156.0	146.6	6,700
S									
(1 1/2-in.	16	5.8	4.7	156.2	149.2	6,000	160.0	152.8	7,050
MSA, 6	17	7.3	6.3	155.9	145.3	6,430	156.4	145.8	6,740
bags	18	6.3	5.2	144.9	137.7	4,760	158.1	150.3	6,310
cement)	19	6.8	5.4	155.0	147.1	6,230	157.4	149.3	7,090

[a]Measured at 28 days of age.

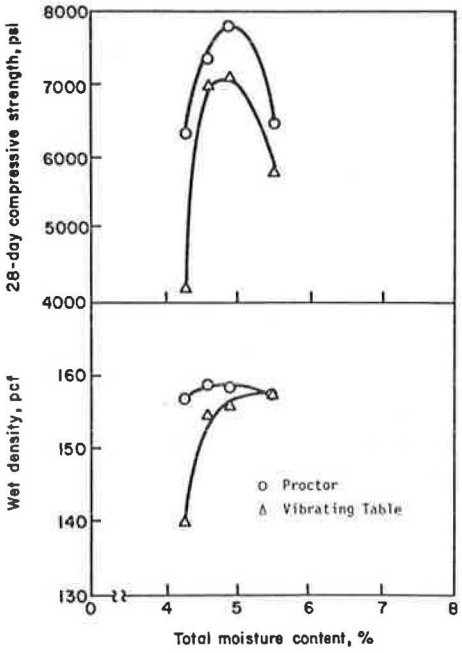

FIGURE 9 Moisture-density-strength relationship for RCC Mix P.

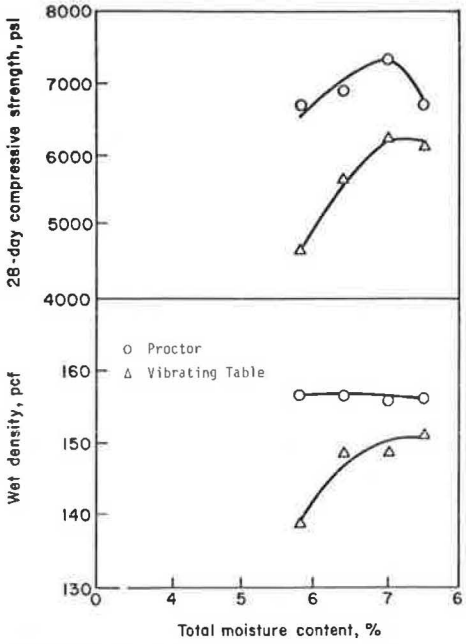

FIGURE 11 Moisture-density-strength relationship for RCC Mix R.

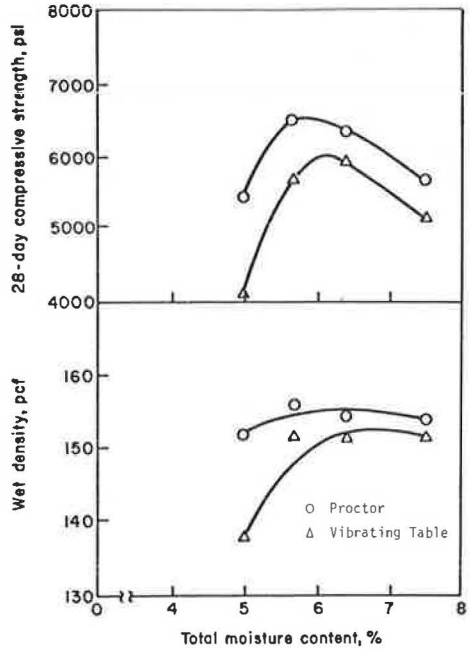

FIGURE 10 Moisture-density-strength relationship for RCC Mix Q.

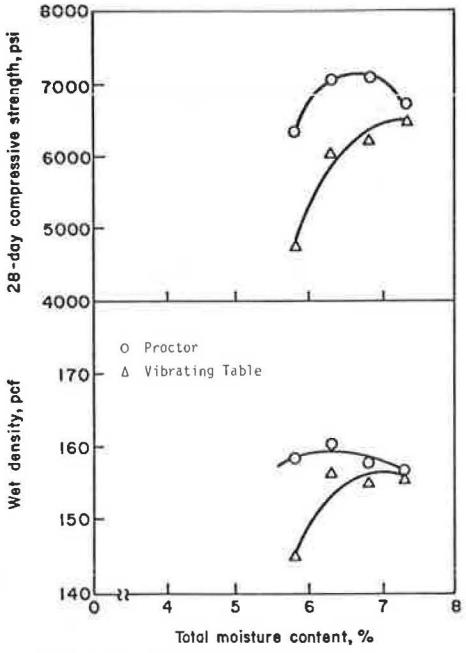

FIGURE 12 Moisture-density-strength relationship for RCC Mix S.

TABLE 13 OPTIMUM AS-BATCHED TOTAL MOISTURE CONTENT

Mix Combination	Optimum Moisture Content (%)		
	DVT	SVT	SP
P (1 1/2-in. MSA, 3.5 bags cement)	5.0	4.8	5.0
Q (3/4-in. MSA, 3.5 bags cement)	6.5	6.0	6.0
R (3/4-in. MSA, 6 bags cement)	7.3	7.2	7.0
S (1 1/2-in. MSA, 6 bags cement)	7.0	7.0	6.5

Note: DVT = Based on density and vibrating table compaction. SVT = Based on strength and vibrating table compaction. SP = Based on strength and modified Proctor compaction.

ACKNOWLEDGMENTS

Work was conducted by the Construction Technology Laboratories, Inc., under the direction of W. G. Corley, vice-president, and B. E. Colley, director, Transportation Development Department.

REFERENCES

1. S. D. Tayabji, P. J. Nussbaum, and A. T. Ciolko. Evaluation of Heavily Loaded Cement-Stabilized Bases. In *Transportation Research Record 839,* TRB, National Research Council, Washington, D.C., 1982, pp. 6-11.
2. R. W. Piggott. Roller-Compacted Concrete for Heavy Duty Pavements—Past Performance, Recent Projects, and Recommended Construction Methods. In *Transportation Research Record 1062,* TRB, National Research Council, Washington, D.C., 1986, pp. 7-13.
3. *Manual of Concrete Practice.* American Concrete Institute, Detroit, Mich., 1985, ACI 207.5R-80: Roller Compacted Concrete.
4. *Manual of Concrete Practice.* American Concrete Institute, Detroit, Mich., 1985, ACI 318-83: Building Code Requirements for Reinforced Concrete.
5. J. W. Murdoch and C. E. Kesler. Effect of Range of Stress on Fatigue Strength of Plain Concrete Beams. *Journal of the American Concrete Institute,* Vol. 30, No. 2, Aug. 1958.
6. C. A. Ballinger. Cumulative Fatigue Damage Characteristics of Plain Concrete. In *Highway Research Record 370,* HRB, National Research Council, Washington, D.C., 1971, pp. 48-60.
7. R. G. Packard. *Thickness Design of Concrete Highway and Street Pavements.* Publication EB109. Portland Cement Association, Skokie, Ill., 1984.

Publication of this paper sponsored by Committees on Rigid Pavement Design, on Rigid Pavement Construction and Rehabilitation, and on Pavement Rehabilitation.

Field Analysis of Rutting in Overlays of Concrete Interstate Pavements in Illinois

SAMUEL H. CARPENTER AND LINN ENOCKSON

Thirty-two overlay projects placed over portland cement concrete pavements were surveyed for the initial development of a comprehensive statewide pavement data base of which these overlay projects would be part. Ninety-two different uniform sections were visually surveyed to obtain performance data on the overlay projects. Design and construction data were collected for inclusion in the data base. The data were analyzed to develop regression relations between rutting and mixture properties of the asphalt concrete overlays. The analysis clearly shows the importance of material properties to the development of rutting, particularly the gradation parameters. Eleven of the projects were cored for structural testing in the laboratory. The structural tests clearly show that the resilient modulus and indirect tensile strength bear a strong relationship to the rutting that develops in the overlay during its life. The analysis in this paper clearly shows how a statistically sound examination of pavement performance can furnish data for an analysis that provides information that can be used to alter mix design and construction practices to address a specific problem. In this paper it is shown that permanent deformation can be controlled through proper material control; further, if the allowable limits on variability of the mixture coming out of the plant can be altered, performance can be altered. A judicious selection of median values and tighter plant control can reduce rutting potential.

The goal of the research project, part of which is presented here, is to examine the structural characterization of bituminous mixes used as overlays on concrete pavements subjected to heavy traffic. To develop a full and true characterization of material performance it is necessary to be able to detail the actual performance of that material in service. Theoretical considerations, which show that asphalt concrete mixtures used as overlays of concrete pavements can be subjected to more severe shear deformation than the same mixture placed over a flexible pavement, were presented previously (*1*). The initial report indicates that some simple material properties determined in the laboratory could possibly be used to indicate the potential for rutting if the tests were performed properly to simulate actual pavement conditions. For these laboratory tests to be meaningful, they must be related to the actual performance of the material on the pavement.

The ability of pavement survey data to establish statistically valid relationships among performance, pavement conditions, and material properties has been established in several recent studies, most effectively in the COPES study (*2*). The COPES project also developed requirements for data collection and preparation that produce a data base with statistically valid data capable of furnishing reliable relationships that can be used to study design changes.

Department of Civil Engineering, University of Illinois, Urbana, Ill. 61801.

HISTORICAL BACKGROUND

At the time this project was being prepared for the Federal Highway Administration in 1981, the Illinois Department of Transportation was considering a survey of their overlaid Interstate pavements because of premature deformation problems. It was decided at that time to coordinate the two studies in order that the data developed would be of benefit to both organizations. Work began to develop the framework for a comprehensive data schema, collection procedure, and analysis procedures. This initial study developed into a comprehensive data base for the state known as the Illinois Pavement Feedback Information System (IPFS). The data collected for this FHWA study formed the basis for the information contained in that study for the initial overlay sections.

SCOPE

The data contained in the data base can be analyzed with suitable statistical procedures to develop relationships among material properties of the bituminous mixtures, the design properties of the overlay, possible construction differences, and the performance of the pavement as detailed by the distress parameters collected during condition surveys of the pavement. Because the focus of this study is on the stability of mixes used as overlays, the performance predictions presented here will concentrate principally on permanent deformation.

Statistical relationships between the permanent deformation developing in any particular mixture and the properties recorded in the data base should relate to properties obtained in a laboratory analysis. Laboratory tests conducted on cores taken from representative overlay sections around the state will also be discussed. It is essential to have laboratory procedures, used to predict the performance potential of a mixture, that logically relate to performance and the mechanism causing the deterioration in the field.

DEVELOPMENT OF DATA BASE

Data Base

A data base is a computerized storage area containing all of the variables used to describe the pavements of interest. The data base used in this study was taken from that used in the NCHRP COPES study (*2*) for rigid pavements that has proven successful throughout the United States and has been adopted for implementation by several states (Pennsylvania, Illinois, and Minnesota). Modifications were made to the data base structure for this project to include the overlay over the existing concrete pavement and its properties. This new section allows separate data on the binder and surface courses to be input to determine the influence of different materials on overall performance.

There are 32 overlay projects and 92 cases in this study. This means that there are approximately 3 cases, or uniform sections, per overlay project. Some had more or fewer uniform sections, depending on the overall length of the project. Material on each case in a project is placed in a separate file folder that is labeled with the identifying project identification and uniform section code.

Design Data Sheets

The design sheets contain all of the information about the case that should be obtainable from the state or district headquarters or from other sources of information about the design and construction of the pavement. This information should not require any revisions once it has been collected and stored in the computer.

Field Data Sheets

The field data sheets contain information that the survey team gathers at each project site.

The section added to the collection sheets, which is significantly different from the COPES collection sheets, is the Bituminous Overlay Design Data. These sheets contain all of the information about the overlay design, mix properties, and asphalt cement properties. Subsequent overlays can be added to the data base through the use of this section.

Data Collection

The data in this study were gathered by the Illinois Department of Transportation. The data were submitted to the project researchers on standard data sheets. Previous studies have indicated that 3 percent sampling can provide a statistically valid indication of the condition of the pavements in a state (*3*). For this study, the pavements under analysis were restricted to Interstate concrete pavements with asphalt concrete overlays. The selection process produced 92 cases across the state of Illinois that are shown in Figure 1. These cases are the "uniform sections" of each pavement.

When any characteristic of a pavement changes, a new uniform section should be selected for inclusion in the data base. The average uniform section length in this study is 3.5 mi. Each uniform section is divided into sample units 600 ft in length. In general, one sample unit is selected for data collection for each mile of the uniform section. The location of the sample units within the uniform section is randomly selected.

The design data from the original pavement construction were obtained from the headquarters office of the Illinois Department of Transportation in Springfield. The information from their historical records is recorded on the design data sheets and referred to as the historical data.

ANALYSIS OF DATA BASE INFORMATION

Preparing the Collected Data

Although most of the raw data could be transcribed directly from the collection sheets to the computer, other data required manipulation. Some data required calculations and estimations to be made by the research group before final entries in the data base could be made. One area that required outside input was the environmental data. The temperature and precipitation values were taken from standard climatic charts. The Freezing Index was obtained from a standard map. The temperature and precipitation values were taken from data for the U.S. Geological Survey weather station nearest each pavement. The other area that required computations by the research staff was Sheet 21, Traffic Volume Data. The traffic values [average daily traffic and average daily truck traffic (ADT and ADTT)] were taken from Illinois DOT traffic maps. The left and right lane distributions for trucks were obtained from relationships derived in previous studies (*2*).

Traffic had to be estimated for the opening of a route if no maps were published that year. It also had to be estimated for 1982, the year the distress surveys were made. Because of changes in recording total commercial traffic, estimates were made for the years 1977-1979 when necessary.

Inventory of Overlaid Interstate Pavements

A major function of the data base is to produce reports that indicate the condition of the pavements in the data base and the types of pavements that are available for analysis. This form of investigation should be done before any statistical analysis to show any distinct groupings of data that should be analyzed separately before being combined into one complete analysis. Examples of this would be thickness; traffic levels; climatic area in the state; and construction differences such as two or three layers of different materials in level binders, binders, and surface mixtures.

Another reason for the inventory study is to establish the range of variables present in the pavement network being examined. Much information can be gained from a study of the average, maximum, and minimum values that can be

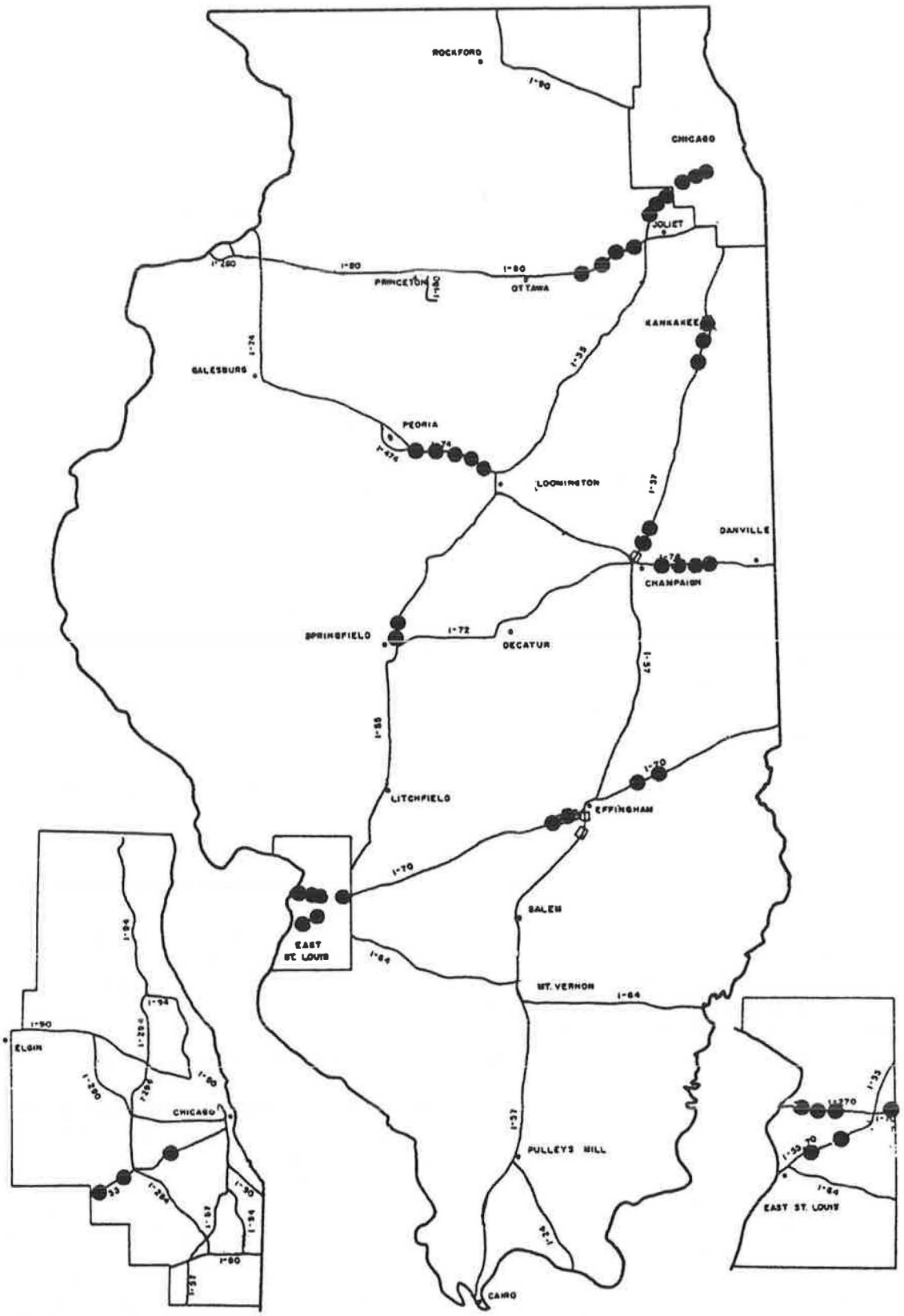

FIGURE 1 Locations of overlay surveys.

found in a state. This analysis shows what variables exist in the field and the variability associated with each factor. Extreme minimum or maximum values should indicate where potential problems may exist. The values of some important variables extracted from the overlay data base are given in Table 1.

TABLE 1 EXAMPLE OF PROPERTIES AND THEIR STATEWIDE VARIABILITY

Property	Average	Maximum	Minimum
Thickness	4.04	8.00	2.6
Level Binder Thickness	1.82	5.0	1.0
Binder Thickness	0.96	2.0	0.0
Surface Thickness	1.27	1.7	0.6
Binder Stability	2154	2908	1567
Binder Flow	11.3	20.4	3.4
Binder Air Voids	2.2	2.4	0.2
Surface Stability	2292	3210	1515
Surface Flow	9.7	13.2	5.1
Surface Air Voids	2.5	4.1	1.1
18k ESALx10^6	3.1	9.5	0.0
Average Rut Depth	0.2	0.48	0.03
Gradation Hump No. 40 Sieve	3.3	13.0	-2.7

Although these values show some significant variation throughout the state, they cannot show the total picture of the influence of the individual variables on the development of rut depth. The numbers in Table 1 do not indicate any influence geographic location may exert on the individual overlay or show whether there may be a pattern of thicknesses that varies from one part of the state to another. Nor does this simple presentation show any climatic influence. Further breakdown of these data is required to show these relationships. This breakdown is typically done with statistical regression techniques.

Examination of the numbers in Table 1 poses some interesting questions, which cannot be answered from a visual analysis, to be investigated later. One question that can be asked is, does rutting occur more when air voids are lower or are air voids even important? There is potential for some quite low air voids in the mixtures used in Illinois during the period being studied. Does more rutting occur in mixes the flow of which is higher, or is there a corresponding change in another mix parameter that reduces total rutting? Does the hump in the gradation curve on the No. 40 sieve as plotted on the FHWA 0.45 power curve really produce increased rutting as is surmised in the literature (*4*)?

These questions can only be answered through a comprehensive statistical regression analysis of the entire data base.

Regression Analysis

To examine the interaction of the variables, a stepwise multiple linear regression was performed on the data base using the Statistical Package for the Social Sciences (*5*). The data base file contained 163 independent variables. Preliminary regression runs were performed to examine correlations between the variables and rut depth. This preliminary analysis indicated the variables that had no relationship with rut depth and could be eliminated. Other variables were eliminated because they contained a significant number of missing values, which reduced the number of cases for the final comparison. There were 95 to 100 variables in the final group used for the general regression, which resulted in 52 out of a possible 80 cases being included in the general analysis.

As anticipated, the rutting in the right lane wheelpaths showed better correlation (higher R^2-values) with the material properties. This is due to the higher traffic in the right lane, which produces more rutting and activates more of the mixture's internal properties that influence rutting. Regression equations were developed initially from a linear regression analysis and later from a nonlinear procedure that takes into account any curvilinear relationship with material properties.

The regression package does not preselect the variables to relate to rutting. The variable that has the highest correlation with the rut depth in the travel lane is automatically selected first by the program. The program subsequently selects the variable that shows the next highest correlation with rut depth. This selection process continues until there is no further improvement in the goodness of fit between the equation and the data. The initial linear equation is

$$RUTR = -0.004671(40 + 80) - 0.0002597(SSTAB) + 0.1032(DIFFS40) + 0.1125(AVEHOT)$$

where

$RUTR$ = average rutting for the travel lane (in.);
40 + 80 = percentage passing the No. 40 sieve and retained on the No. 80 sieve for the surface mixture;
$SSTAB$ = Marshall stability (lb) of the surface mixture;
$DIFFS40$ = hump in the gradation on the No. 40 sieve when plotted on the FHWA 0.45 power gradation curve for the surface mixture (%); and
$AVEHOT$ = average monthly temperature for June, July, and August at the location of the overlay.

The R^2 correlation coefficient for this equation was 0.82 based on 52 cases. The standard error of estimate of the equation was 0.3. These statistics are quite good for equations derived from field data (previous studies have typically developed R^2-values on the order of 0.5 for pavement studies).

Although this relationship by itself is not bad, the linear analyses of the variables in the data base do not accurately indicate such variables as thickness, traffic, and age of the overlay. In addition, better representations of rut depth and traffic could be developed. A thick pavement surface will develop more rutting than a thin surface, but the amount of permanent strain may be the same in both. An overlay that

gets a large amount of traffic in 1 year may have a substantial amount of loadings placed on the overlay during the colder periods of the year and will develop less rutting than a similar overlay that receives the same traffic over a 3- to 4-year period during which there are a greater number of months with high temperatures.

To better include the nonlinear relationships in the data, the data were transformed with the best-fit nonlinear function for that data element. The transformed variables were placed in the data base along with the standard linear variables, and another regression was performed. The resulting equation includes variables that give a truer picture of how they interact to alter rutting development. The nonlinear analysis of the entire data base allowing modified variables provided the following relationship:

$$RUT = -0.040930187(40 + 80)^{1.0849} - 0.0002569715\,(STAB) + 0.083705(DIFFS40) + 0.0523817(AVEHOT) + 0.313578(TCUMRR)^{0.045565} - 1.127458(-200)^{-1.24927} + .00041937(D) + 0.0106828(RDen)$$

where

RUT	=	rut depth (in.);
$40 + 80$	=	percentage passing the No. 40 sieve and retained on the No. 80 sieve in the surface mixture;
$STAB$	=	Marshall stability of the surface mixture;
$DIFFS40$	=	hump in the FHWA 0.45 power gradation curve on the No. 40 sieve in the surface;
$AVEHOT$	=	average of the maximum monthly temperatures during June, July, and August;
$TCUMRR$	=	total 18-kip equivalent standard axle loads (ESALs) applied to the overlay in the right lane;
-200	=	minus No. 200 material in the binder;
D	=	maximum theoretical density (lb/ft^3) of the surface mixture; and
$RDen$	=	relative density of the surface mixture (%).

The R^2-value for this regression equation is 0.89, the standard deviation is 0.04, and the coefficient of variation is 16.1 percent.

When a regression equation is developed, the variables in the equation must first be examined to determine if they relate to the dependent variable in a logical manner. The influence of the variables entering into the prediction equation is shown in Figure 2. The variable relationships tend to support commonly held beliefs about their influence on rutting. As stability increases, rutting decreases. As summer temperatures increase, rutting increases. Although the relationship with relative density may be contrary to current thinking, as relative density increases rutting increases, the average relative density may already be at the level desirable for minimal rutting. Thus the variability seen in the survey data could justify a decrease in air voids producing a minor increase in rutting as shown in the figures. By far the most influential variable in the equation appears to be the hump in the gradation on the No. 40 sieve in the FHWA 0.45 power gradation chart, which shows a dramatic influence on rutting. This variable has been pointed out by many engineers as a prime contributor to an unstable mixture. This value is determined on a plot of the gradation on 0.45 power paper. A line is extended from the origin to the No. 4 sieve data point. The difference between this straight line and the gradation at the No. 40 sieve is the hump value.

Mix Variability

An important use of any regression equation developed to describe behavior of a pavement is the examination of material properties and how they affect the development of distress in the pavement. The ability to study individual materials provides the opportunity to study variability throughout the state and quantify the impact of specific material properties and their variability on pavement life as well as quantify what certain agencies could do to reduce the potential for distress. Table 2 gives the statewide averages and standard deviations for the variables in the regression equation.

In the equation developed here the influence of gradation on the mixture's ability to resist rutting is evident. Although stability and temperature have a definite effect, as does the relative density of the surface, the gradation parameters show the largest influence, given the variability of the parameters across the state. If a complete survey of the state were made, a

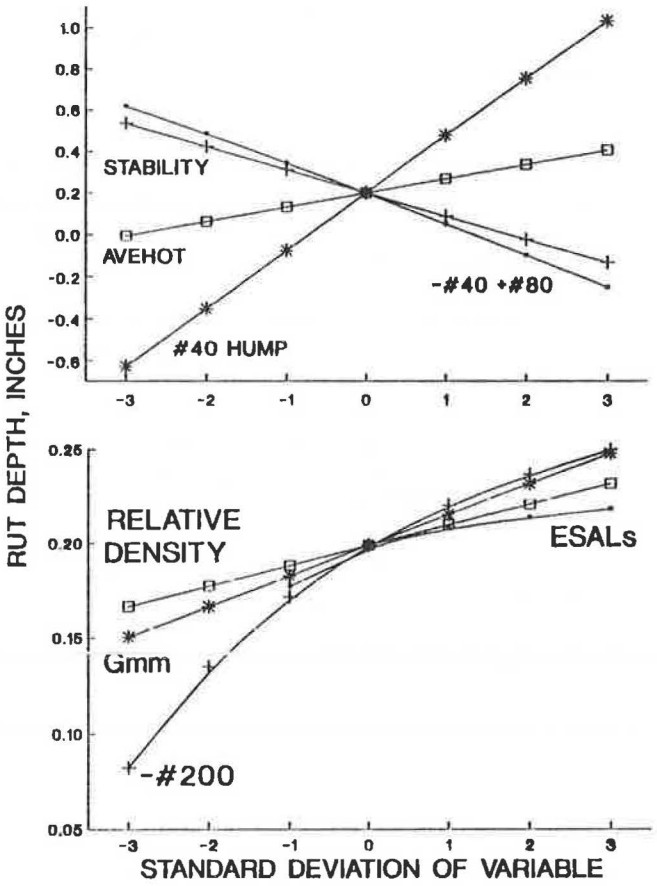

FIGURE 2 Influence of property variability on rutting.

TABLE 2 STATEWIDE VALUES FOR PARAMETERS IN THE REGRESSION EQUATION

Variable	Average	Standard Deviation
40+80	10.6	2.7
SSTAB	2292	435
DIFFS40	3.3	3.3
AVEHOT	22.2	1.3
TCUMRR	3.1	2.4
-200	4.8	0.57
D	143.1	38.4
RDen	96.8	1.0
Rut Depth	0.20	0.11

more detailed analysis could be performed to develop individual regression relationships for each district in the state. This would reflect the construction practices and materials used in the individual districts, which may be highly variable. Because of the limited number of projects in this survey it is more appropriate to examine only the magnitude of each parameter and the variability of that parameter within the district for comparison between districts. This analysis can provide insight into reasons for rutting being higher or lower in any particular district. The mean and standard deviations of the variables in the regression equation for each district in the survey are given in Table 3.

The data in Table 3 indicate which districts have the potential to reduce rutting by altering the mean value of a specific parameter. For example, District 1 could reduce the mean value of the *DIFFS*40 variable and reduce the potential for rutting. Likewise, a material variable with a high standard deviation is a candidate for improvement through more control. By lowering the variability, the number of projects constructed with a high potential for rutting will be reduced.

Figures 3-6 show the differences in rutting in each district as a function of the variability about the mean for several of the variables. Variables such as temperature cannot be altered, but the regression equation shows where more stringent gradation controls can reduce the potential for rutting. Certain increased expenses for extra gradation or mixture control may be justified by prolonged overlay life.

Regression analyses such as this also provide performance data that can be used to evaluate specific mix design properties to show where specific improvements can be made. As part of its new Interstate overlay mix, IDOT eliminated the hump in the gradation on the No. 40 sieve, which, from this analysis, indicates that an improvement in rutting resistance should be realized.

LABORATORY ANALYSIS

Cores were taken from 11 of the 32 overlay projects surveyed. These cores were brought to the laboratory for further analysis to verify any correlation between structural testing and rutting performance. The projects that were sampled are given in Table 4. Six cores were taken between the wheelpaths at each location for testing. Each core was composed of several layers of surface and binder, depending on the construction history of the project. The thicknesses obtained from direct measurement are given in Table 5.

These pavements represent different designs and come from different climatic zones within Illinois, as shown in Figure 7. Table 6 gives the survey data from the data base for each sample unit from which a core was taken and the predicted rutting from the regression equation. Several cores were taken from new construction and therefore do not have data in the data base.

The cores were separated into surface and binder layers for structural testing of the individual layers. Resilient modulus testing was conducted at 40° F, 72° F, and 100° F. Indirect tensile testing was conducted at 72° F under standard conditions. Three cores were tested at each temperature. For the diametral resilient modulus, each core was tested twice. The results for indirect tensile strength are given in Table 7. The diametral resilient modulus values obtained from the testing are given in Table 8.

Stiffness and tensile strength can be related directly to rut depth in the pavement using the rut depth measurements from the data base, but a more suitable parameter to indicate the development of rutting, including the effect of traffic, would be percentage of permanent strain per level of axle load application (rut/thickness/ESAL). This can account, to some extent, for the different ages of the overlay mixtures and the different levels of traffic that have been placed on the

TABLE 3 DISTRICT AVERAGES AND STANDARD DEVIATIONS OF VARIABLES IN THE REGRESSION EQUATION

Variable	Average	Std Dev	Average	Std Dev	Average	Std Dev	Average	Std Dev
	District 1		District 3		District 5		District 8	
40+80	12.5	1.6	12.03	1.73	10.8	0.31	7.27	1.08
SSTAB	2289	354	2268	389	1999	138	2343	641
DIFFS40	5.54	1.65	4.35	1.25	2.91	1.05	-0.62	1.2
AVEHOT	22.3	1.22	22.8	0.34	23.3	0.52	25.7	0.0
TCUMRR	5.69	1.71	3.02	1.96	1.85	0.24	2.65	1.76
-200	4.65	0.47	4.35	0.41	4.57	0.10	4.72	0.71
D	154.3	2.2	153.4	2.14	-	-	150.9	4.5
RDen	96.79	1.10	96.68	0.97	97.47	0.41	96.19	0.79
Rut	0.29	0.10	0.22	0.08	0.26	0.11	0.18	0.08

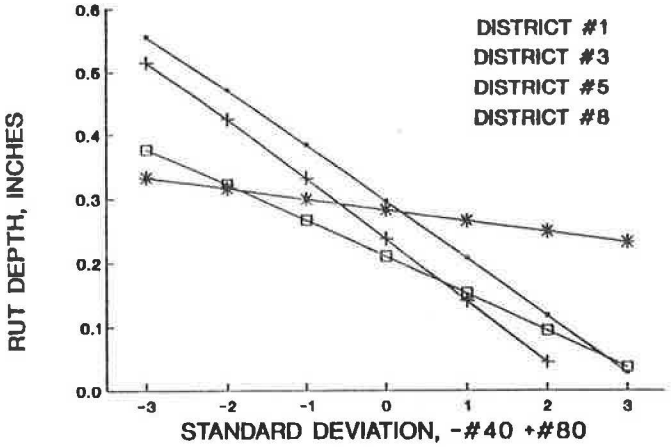

FIGURE 3 Influence of variability in the amount passing the No. 40 and retained on the No. 80 sieve for each district.

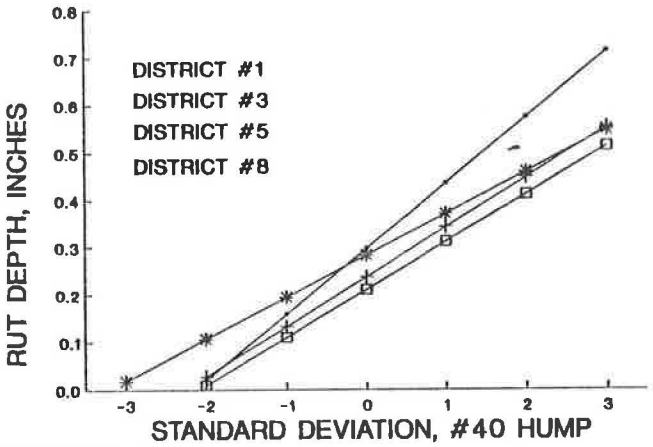

FIGURE 5 Influence of variability in the 0.45 power curve hump on the No. 40 sieve on rutting in each district.

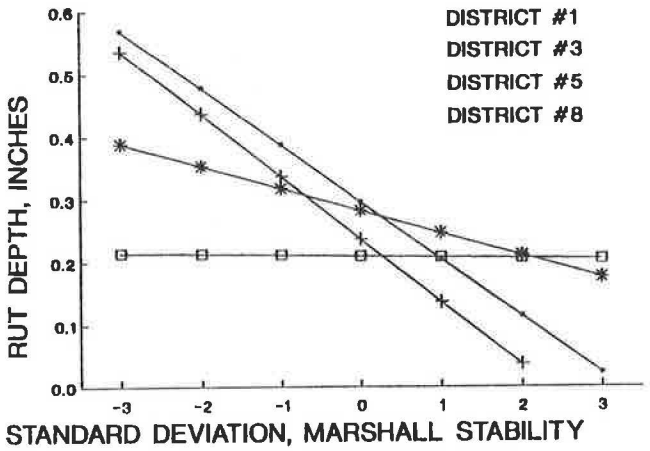

FIGURE 4 Influence of variability in the Marshall stability of the surface layer on rutting in each district.

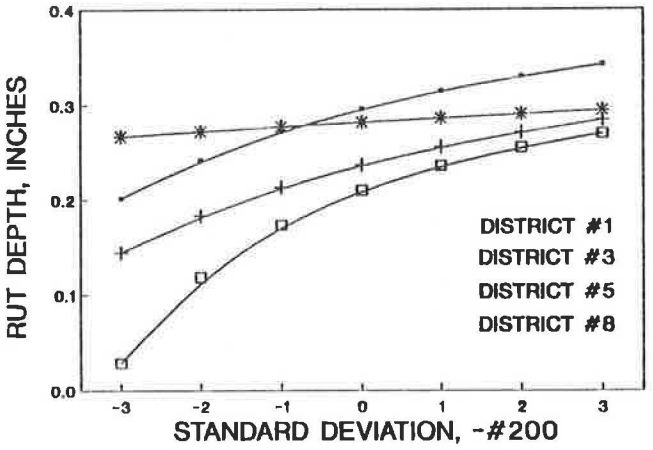

FIGURE 6 Influence of variability of the percentage of the binder mix passing the No. 200 sieve on rutting in each district.

TABLE 4 CORES TAKEN FROM OVERLAY PROJECTS FOR LABORATORY ANALYSIS

Core Sequence	District	Highway	Contract No.
1	1	I 55	30861
4	8	I 270	33348
5	8	I 70	33347
7	7	I 70	26040
10	5	I 57	33123
11	1	I 80	34444
13	3	I 80	34187
16	1	I 55	29437
17*	5	I 70	34174
20*	5	I 70	35824
21*	5	I 70	35824

* = data not in data base, just constructed.

TABLE 5 LAYER THICKNESSES OF OVERLAY CORES

Core Sequence	Surface	Binder	Age, years
1	2.5	3.0	11
4	0.75	2.25	1
5	1.0	1.0	2
7 Combo*	1.0, 1.0	4.0, 3.5	1, 13
10	1.0	4.2	2
11	1.6	2.7	4
13	1.5	3.2	1
16	1.5	4.0	6
17	1.0	3.9	0
20	1.3	2.0	0
21	1.0	2.7	0

* = two overlays, respectively.

overlay. This parameter is the permanent strain (rut depth/thickness) divided by the 18-kip ESALs, in millions, that have trafficked the overlay since placement. This conversion produces the rutting variable, permanent strain/ESAL, given in Table 9.

The laboratory structural tests show a clear relationship to the development of rutting in an overlay of a concrete pavement. Figure 8 shows average tensile strength of the surface-binder combination versus rate of rutting. Below an average tensile strength of approximately 150 psi, the rate of rut development increases dramatically. The two extreme points with high strengths and high rutting levels are also the oldest pavements. This shows the influence of age on the stiffening of the asphalt mixture and also hints at problems in testing pavement materials placed at different times with possibly different mix criteria. The older mixes may have been constructed with materials that produce low tensile strengths, which over the years have reached the high value shown in Figure 8. The relationship of age and tensile strength is seen in Figure 9, which clearly shows an influence of age on structural properties of the mix.

A similar relationship exists between the diametral resilient modulus and the rate of rutting. This is shown in Figure 10 for

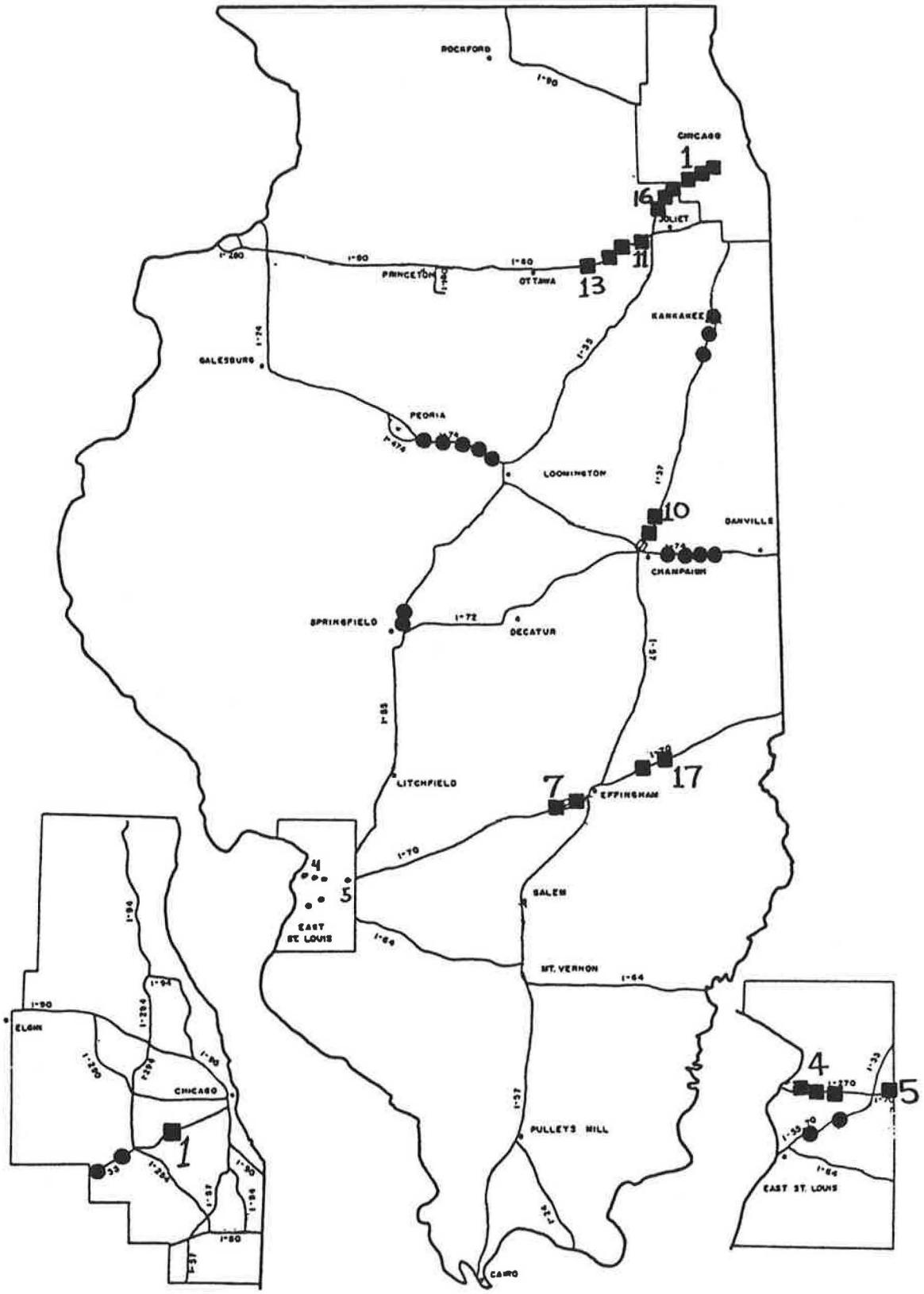

FIGURE 7 Location of overlay projects with the core sequence numbers indicated by squares.

the average diametral resilient modulus of the surface and binder mixtures.

The relationships among these structural parameters, rutting, and age are important because rutting is most likely to develop during the initial years of the life of mixes. When the problem is premature deformation, the initial years are

TABLE 6 MIXTURE PARAMETERS FROM THE DATA BASE

Core Sequence	CASE-NO	AGE	-200	40+80	SSTAB	D	RDen	TCUMRR	RUTR
1	14	10.5	4.9	11.9	2036.	152.3	95.5	7.93	.23
16	15	6.0	4.5	13.8	2386.	155.4	97.6	5.65	.31
11	24	1.67	4.3	10.2	3210.	149.8	95.0	1.77	.03
	25	4.67	4.9	14.7	-0	-0	-0	2.89	.19
13	44	.92	5.7	-0	-0	-0	-0	.49	.07
10	50	1.67	-0	-0	2830.	-0	-0	2.23	.13
	51	1.67	-0	-0	2830.	-0	-0	2.21	.25
7	70	.92	3.9	8.6	1819.	155.4	96.4	4.43	.32
5	82	1.83	5.5	-0	-0	-0	-0	2.30	.10
4	87	0.92	5.6	6.0	2847.	147.3	94.9	1.20	.14
	89	0.92	5.6	6.0	2847.	147.3	94.9	1.20	.09

Where the variables are as defined previously.

TABLE 7 INDIRECT TENSILE STRENGTH FOR OVERLAY CORES

Core Sequence		Surface	Binder
1		284	205
4		136	130
5		124	121
7	new	210	164
	old	186	176
10		207	241
11		192	224
13		127	201
16		285	300

TABLE 8 DIAMETRAL RESILIENT MODULUS OF OVERLAY CORES

Core Sequence		Layer	Stiffness, psi x 10^6 40°F	72°F	100°F
1		Surf	3.21	1.01	.274
		Binder	2.93	1.14	.38
4		Surf	1.62	.797	.178
		binder	2.09	.723	.143
5		Surf	1.73	.822	.198
		Binder	1.65	.89	.25
7	New	Surf	3.84	1.99	.80
	Old	Surf	3.99	1.51	.308
	New	Binder	2.96	.902	.166
	Old	Binder	3.18	1.71	.445
10		Surf	2.73	1.15	.196
		Binder	2.9	1.15	
11		Surf	3.42	1.46	.652
		Binder		1.09	.262
13		Surf	2.43	.847	.686
		Binder		.919	.116
16		Surf	3.34	1.38	.392
		binder	2.87	1.33	.319
20		Surf	2.94	1.25	.346
		Binder	2.95	1.3	.357

TABLE 9 RUTTING PARAMETER FOR COMPARISON WITH STRUCTURAL PROPERTIES

Core Sequence	Strain/ESAL x10-08	Rut Depth
1	0.58	0.23
4	3.30	0.12
5	2.17	0.10
7	0.76	0.32
10	1.64	0.19
11	1.10	0.11
13	3.04	0.07
16	1.00	0.31

even more critical to the performance of the overlay. The relationships clearly show that, during the first 2 to 3 years, stiffness and tensile strength are direct indicators of the rate at which rutting may be expected to develop. To determine the precise relationship between rutting and stiffness or tensile strength over longer times it will be necessary to collect more data in the future from these same sections and repeat the analysis to determine the exact influence of age on changes in material properties.

RESULTS AND CONCLUSIONS

The work presented here is part of a study to establish field and laboratory data indicating factors that may be crucial to the development of rutting or premature deformation, or both, in asphalt concrete overlays of portland cement concrete pavements. Although this study of materials was confined to Illinois, the methodology used to establish these relationships can be implemented without a great deal of expenditure and actually represents the concept behind the long-term pavement performance studies now being initiated as part of the Strategic Highway Research Program. The results indicate that a state can survey its pavements and study material properties that contribute to a specific problem. The field survey and data base development have been implemented in Illinois with the development of the Illinois Pavement Feedback System, which will contain a comprehensive data base of the entire system of pavements in the state (*6*).

Analysis of the field data indicates that the majority of problems in Illinois can be attributed to material properties in the gradation of the mixture. Although temperature and traffic have an impact on rutting, as expected, the properties of the component materials demonstrated the most critical relationship with rutting. The impact of these material parameters is not unexpected. The "tender mix" phenomenon associated with the hump in the 0.45 power gradation chart has long been recognized as contributing to rutting. The predominant influence of the percentage passing the No. 40 sieve and retained on the No. 80 sieve on rutting is a result that, although not contrary to experience, was not expected to come out as strongly as it did.

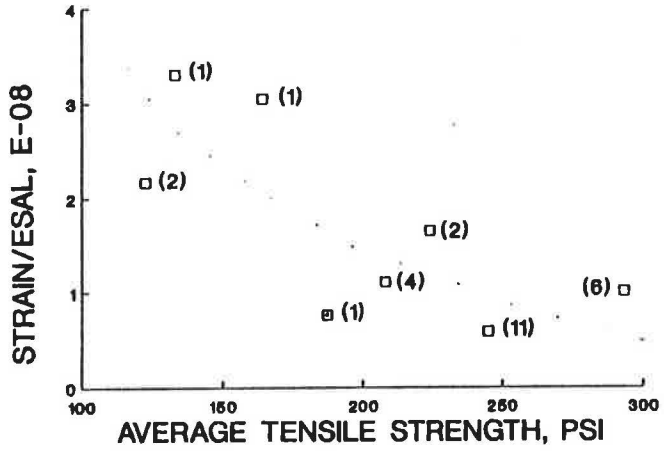

FIGURE 8 Average tensile strength of overlay related to rutting (age in parentheses).

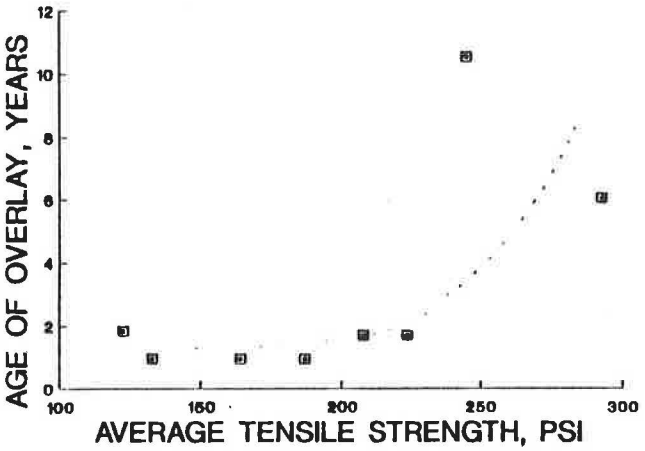

FIGURE 9 Relationship between tensile strength and age of overlay.

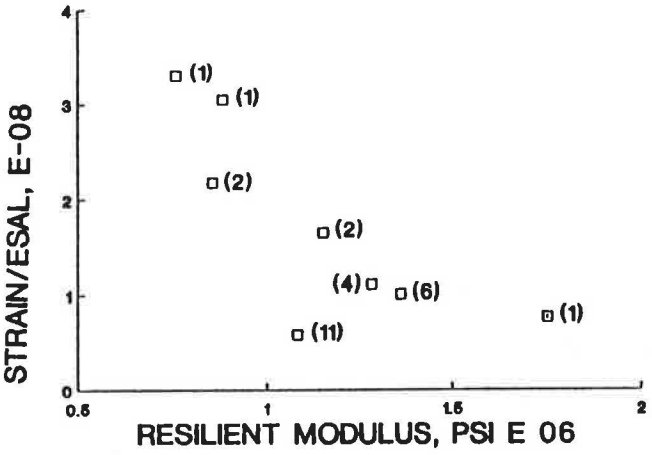

FIGURE 10 Relationship of resilient modulus to rutting.

An important factor that emerges from the analysis is that normal variability in gradation occurring across a state can produce a significant change in the rutting that develops in the overlay. Studies such as this one can show where changing one variable or exercising extra control during construction can reduce the occurrence of distress. Data such as these will have future use in establishing life values for quality assurance specifications, which must be based on material variability. Laboratory testing has shown only inconsistent tendencies relating laboratory structural tests of material properties to rutting or other distress that decreases the life of a pavement. Field testing of actual pavements with samples taken for laboratory analysis provides a better indication of performance. The data developed in this study clearly indicate where variability can be controlled to alter the rutting life of an overlay.

The close relationship between a structural property of individual lifts and age may indicate that aging does indeed alter more than the surface layer of the mix. Whether this is "aging" wherein chemical alterations are taking place or a thixotropic hardening over time is an academic question. That changes occur, over time in all layers, and provide an increased resistance to rutting is the important consideration. It is important to develop a historical time sequence to establish a minimum tensile strength in the mix at the time of construction that may be required to resist rutting in the initial years of the life of the overlay until the hardening develops sufficiently to provide significant strength to resist rutting. This must be balanced against cracking and other distress that may increase as a mix becomes harder.

The problem of premature deformation in overlays of Interstate concrete pavements in Illinois led to the formation of a Task Force on Rutting and Durability to address and recommend changes to eliminate premature deformation. The relationships established in this study were presented to the task force and served to reinforce the recommendations the task force was formulating. Gradations were altered to ensure that the hump in the gradation was not allowed to occur again. The amount of material in the No. 40 to No. 80 sieve range was also changed by this alteration to further reduce the potential for rutting. Additional recommendations addressed control on density and air voids and voids in mineral aggregate during construction.

This study clearly demonstrates the usefulness of field distress surveys for establishing relationships between material properties and mixture performance. Such surveys can be accomplished without great expense and can provide a source of information for future use in evaluating pavement performance when unforeseen problems arise.

ACKNOWLEDGMENTS

This paper was prepared as part of the study entitled Structural Characterization of Bituminous Mixes Used as Overlays on Heavily Trafficked Concrete Pavements undertaken by the Department of Civil Engineering, in the Engineering Experiment Station, University of Illinois at Urbana-Champaign. The study was funded by the Federal Highway Administration, U.S. Department of Transporta-

tion, as a part of the Department of Transportation's Program of University Research. The authors would like to extend their appreciation to all who provided data for this study.

REFERENCES

1. S. H. Carpenter and T. J. Freeman. *An Analytical Study of Bituminous Mixtures Used as Overlays on Concrete Pavements.* Interim Report. FHWA, U.S. Department of Transportation, Jan. 1984.
2. M. I. Darter, J. M. Becker, M. B. Snyder, and R. E. Smith. *NCHRP Report 277: Portland Cement Concrete Pavement Evaluation System—COPES.* TRB, National Research Council, Washington, D.C., 1985.
3. J. P. Mahoney. Measuring Pavement Performance by Using Statistical Sampling Techniques. In *Transportation Research Record 715,* TRB, National Research Council, Washington, D.C., 1979, pp. 45-52.
4. V. Marker. *Tender Mixes: The Causes and Prevention.* Information Series 168. The Asphalt Institute, College Park, Md., June 1977.
5. C. H. Hull and N. H. Nie. *SPSS Update 7-9, New Procedures and Facilities for Releases 7-9.* McGraw Hill Book Company, New York, 1981.
6. M. B. Snyder et al. *Illinois Pavement Feedback Data System.* Draft Report. Illinois Highway Research Project Advisory Committee, Illinois Department of Transportation, Springfield, Sept. 1984.

Publication of this paper sponsored by Committee on Flexible Pavement Design.

Dynamic Response of Paving Materials

JORGE B. SOUSA AND CARL L. MONISMITH

Equipment developed to determine the dynamic properties of paving materials in axial and torsional loading is described. Dynamic properties were determined by the excitation of hollow cylindrical specimens using two independent sinusoidal loads with frequencies up to 30 Hz. An IBM PC/AT equipped with a Metrabyte DASH16 data acquisition board was used to directly control two MTS hydraulic servorams. Menu-driven software was developed, taking advantage of direct memory access channels, so that data acquisition, wave form generation, and closed-loop control could take place simultaneously at rates above 5,000 samples/sec/channel. To convert raw data into graphs and parameters representative of dynamic material properties, a postprocessing menu-driven program was also developed. Dynamic properties of an asphalt concrete, a uniform sand, and a silty clay are presented. For the asphalt concrete, dynamic moduli in axial loading, dynamic shear moduli, internal damping determined in both axial and shear loading, and dynamic Poisson's ratios are presented for tests conducted at temperatures ranging from 11° C to 40° C. For the uniform sand and silty clay, dynamic shear moduli and internal damping as a function of stress state, magnitude of shear strain, and frequency of loading are presented.

Assessing the response of pavement systems to dynamic loads requires knowledge of the applied load spectrum, solutions for representations of pavement systems that permit inclusion of dynamic effects, and measures of the dynamic response of materials that make up pavement systems (*1*).

Recent developments in microcomputers, such as increased speed and memory capabilities, have opened new avenues for data acquisition, process and equipment control, automation, and data analysis for the definition of requisite dynamic properties of pavement materials. A new testing system that uses the capabilities of microcomputers to define these properties is described.

With the system, specimens can be tested as hollow or solid cylinders subjected to axial, torsional, or combined axial and torsional loads at frequencies up to 30 Hz.

Although the primary purpose of this paper is to describe the computer-controlled dynamic testing equipment, results are presented for the elastic and damping characteristics of an asphalt concrete tested over a range of temperatures and for a sand tested over a range of stress conditions. Both materials were tested as hollow cylinders 9 in. (22.8 cm) outside diameter and 18 in. (45.7 cm) high with a wall thickness of 1 in. (2.54 cm). These materials were subjected to axial and torsional stresses permitting the dynamic response of both materials to be defined in compression and shear.

Department of Civil Engineering and Institute of Transportation Studies, University of California, Berkeley, Calif. 94720.

DYNAMIC LOADING SYSTEM

The test apparatus, termed herein the Dynamic Loading System (DLS), was designed to test hollow cylinders in both torsional and axial loading to attempt to simulate the three-dimensional stress states that occur in pavement materials in situ when subjected to moving dynamic loads. The torsional and axial loads can be applied either independently or simultaneously, which makes possible the rotation of the principal stress axes to follow predefined stress paths. Loads can be applied at frequencies up to 30 Hz, which appear to cover the range of frequencies that might result from loads of trucks operating on rough pavements (*2*).

Advances in microcomputer technology provided a relatively inexpensive way to develop an apparatus in which the accuracy and power of feedback closed-loop control hydraulic systems are combined with the flexibility, automation, and speed capabilities of digital equipment (*3*).

Description of Apparatus

Specimen Dimensions and Pressure Chamber

An axonometric view of the hollow cylindrical specimen and the adjacent apparatus is shown in Figure 1. The hollow cylindrical specimen is 18 in. (45.7 cm) high with a 9-in. (22.8-cm) external diameter and a wall 1 in. (2.54 cm) thick. The specimen is contained between a membrane and cap and base rings made of hard anodized aluminum. A top plate can be placed between the load cell and the cap ring when different interior and exterior confining pressures are required. The apparatus can also be used with solid cylindrical specimens 9 in. in diameter and 18 in. high.

Temperature Control

Temperature control is achieved by circulating the pressurized air contained within the cell through a copper serpentine located in the interior of an insulated box. Heat is transferred to and from the serpentine by heating and cooling systems controlled and monitored by a temperature-sensitive sensor. The feedback sensor is placed inside the return pressure line near the top chamber plate.

Slippage-Free Surfaces

To ensure adequate load transfer between the specimen and the cap and base rings, eight 0.5-in. (1.27-cm) lugs are

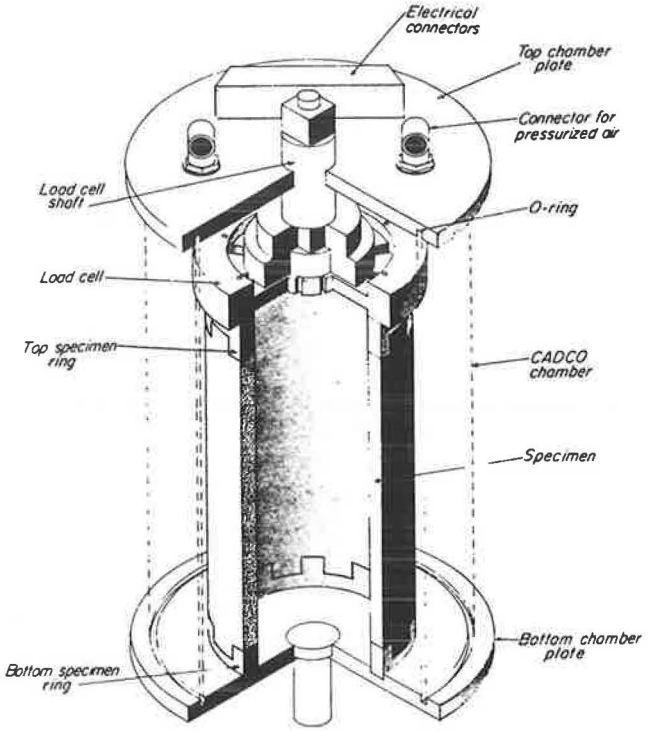

FIGURE 1 Axonometric view of pressure chamber, specimen, and load cell.

mounted on the rings. Under certain loading conditions, other additional means of load transfer to the specimen are not required. However, if complete reversal of torsional stress or axial traction, or both, is required, epoxy adhesive or hydrastone must be used.

Deformation Measurements

Measurements of specimen deformation are made using linear variable differential transformers (LVDTs). The LVDTs used are in constant contact, due to spring-loaded gauging heads, with a target mounted on the specimen. The target can be positioned anywhere on the specimen by using either fastening screws or clamping rings surrounding the specimen, which eliminates possible errors due to end effects.

Loading System

The DLS was designed so that the loaders could be mounted on a heavily reinforced frame beneath which the specimen is placed. Vertical loads are applied by a vertically mounted 10-kip MTS servoram with a 6-in. stroke. Torsional loads are applied by a horizontally mounted 6-in. stroke, 2-kip MTS servoram. The latter, when connected to a torque arm 7 in. (17.78 cm) in length, provides up to a 14-kip/in. torsional moment to the center shaft (Figure 2).

A Rotolin linear and rotary ball bearing with a total linear travel of 1 in. allows the coupling of both loads through the same shaft. Decoupling of the vertical movement of the torque arm from the horizontal movement of the horizontal

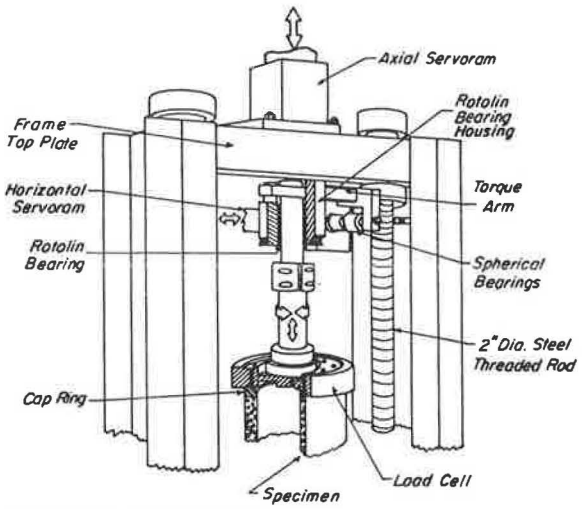

FIGURE 2 Loading system.

servoram is made possible by two spherical bearings that limit the angle of the torque to ± 15 degrees.

A wheel-shaped load cell was constructed with eight spokes, each in the form of a rectangular prism. Each of the spokes is assumed to behave as a beam. Vertical and torsional loads can be measured independently because strain gauges are mounted on the centerlines of alternate faces of the beams.

Data Acquisition and Equipment Control

The development of the DLS required that tasks like wave form generation, data acquisition, equipment control, and data processing be accomplished almost simultaneously. To successfully perform them, a microcomputer (IBM PC/AT) was used with a data acquisition board from Metrabyte and a signal-conditioning interface. Figure 3 shows schematically how the elements of the apparatus are interconnected.

Hardware

Digital to analog and analog to digital conversions are performed by Metrabyte's DASH16 expansion board. To interface servovalves, strain gauges, and LVDTs to the Metrabyte board, two electronic devices were built. One, a board (Data Acquisition Interface Card) occupying one of the slots of the IBM PC/AT, provides software-selectable amplification gains for eight channels and software-selectable analog hardware offsets for four of the eight channels; the other, an A/C Signal-Conditioning Unit, provides the excitation for the load cells or the LVDTs, or both, in eight channels and transforms the voltage output of the two D/A channels into current, varying between ± 15 mA, that drives the servovalves.

Software

The software is written in compiled BASIC version 3.0 with

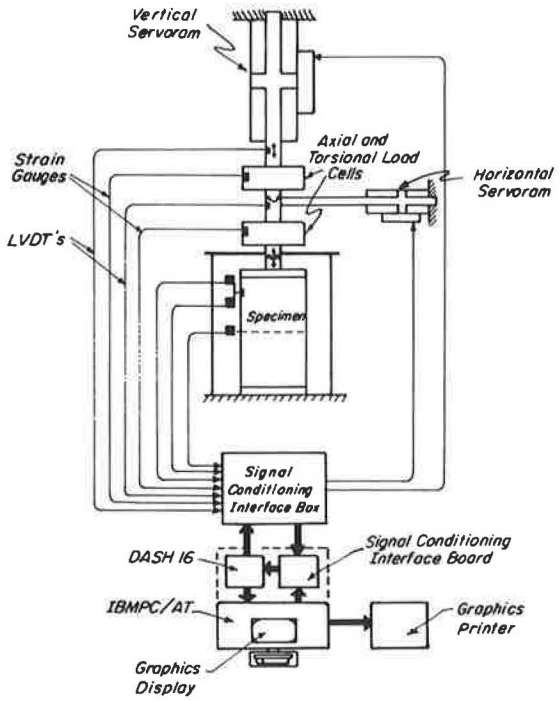

FIGURE 3 Data acquisition and control scheme.

ASSEMBLER subroutine calls addressing specific components or requesting specific tasks, or both. While data are being collected, two servorams must apply independent and synchronized sinusoidal forces, with frequencies of up to 30 Hz, to the specimen. For higher accuracy in test results, feedback closed control loops and high signal resolution are required. Because several types of tests can be performed sequentially on a single specimen, rapid adjustment of signal ranges and rapid change of feedback channels are necessary, forcing the adoption of software-programmable gains and software-programmable analog voltage offsets.

Furthermore, feedback closed-loop control is accurate because the desired signal (COMMAND) is compared with the signal obtained at the probe (FEEDBACK), and an error signal is sent to the servovalves to make any necessary adjustments. When analog equipment is used in feedback closed-loop controls, the time needed to read the feedback signal, compare it with a command value, send out the error value, and reread the feedback value is almost zero [i.e., the rate (number of closed loops/time) is almost infinite]. However, when using digital equipment, time is involved in

1. Converting the feedback signal from analog to digital,
2. Computing the command value,
3. Determining the error signal, and
4. Converting the error signal from digital to analog.

The rate is, therefore, a finite number that must be kept sufficiently high in order to provide complete control of the servorams. To accomplish this, command waves may be generated before testing, provided they are either periodic or of short duration. This frees the computer's central processing unit (CPU) from performing wave generation during testing. If the data acquisition components responsible for feedback data input are CPU independent, taking advantage of direct memory access (DMA) channels, error signal evaluation and output are the only tasks that must be executed during testing.

The menu-driven programs (SETUP, WAVGEN, and DACTEST) were developed so that these requirements could be fulfilled. These programs are described in the following subsections.

SETUP This program prompts the user to input the proper conversion factors, amplification gains, and analog hardware offsets for each of the eight input channels in order to convert input voltage from the probes into engineering units. The set of all of these values constitutes a configuration file. When a specific configuration is required, the program retrieves the file from the hard disk, addresses the data acquisition interface card, and sets the required amplification gain and analog offset for each channel.

WAVGEN This program creates and saves an array containing the values of command waves to be used by DACTEST. To define the waves, the following information is requested:

1. Configuration file name.
2. Feedback channel number of each of the servorams. Both of the servorams can be controlled with the feedback from any of the eight available channels. Stress or strain closed-loop control is initiated simply by selecting the correct feedback channel.
3. Frequency, amplitude, phase angle, wave form, and gain for each of the command waves. The software can perform feedback closed-loop control at a rate of 5,000 points/sec/servoram. Therefore, a 1-Hz sine wave would be defined by 5,000 points, but a 50-Hz wave would be defined by 100 points.
4. Definition of data acquisition schedules. To accurately perform closed-loop control, very high rates of data acquisition are necessary. However, for data analysis a smaller number of conversions is needed. Saving all of the data points would not only be next to impossible but inefficient. The data acquisition schedule tells the computer which periods to save for later analysis.

This information is saved in a test-type file. Several types of tests can be created and saved by several runs of WAVGEN.

DACTEST A testing sequence can consist of a series of different or identical tests, or even a single test, defined by the name of the file created by WAVGEN. For each test within the sequence, the program requests a name for the file in which the resultant data are to be stored.

Every 1/5000 sec DASH16, from its DMA controllers, updates 16 computer memory bytes (two for each input channel) with a digital value corresponding to the voltage present in each of the eight channels. This allows values present in the probes to be placed directly in memory (with only a 1/5000-sec delay) without spending CPU time. Control of the servorams is maintained by sending the difference between the feedback values and the command

values, multiplied by a constant (GAIN), to the D/A channels of the DASH16 board. GAIN depends on the stiffness of the specimen, the oil pressure, the stiffness of the frame, and the frequency and amplitude of the loads. This constant is automatically adjusted by the software for each situation.

After completion of each individual test, data are retrieved from random access memory and stored on the hard disk (for each test 64 Kb of data can be collected). This is accomplished while simultaneously maintaining control of the servorams.

Data Analysis

Data analysis for this type of testing is lengthy. Accordingly, two postprocessor programs (OPTMZER and ANALYSR) were developed to convert data obtained during a testing sequence into material properties.

OPTMZER

Data produced by DACTEST during a testing sequence are stored in a macrofile. OPTMZER reads the macrofile and creates a number of files equivalent to the number of tests in the testing sequence. For each of the tests, it also creates a file containing the values of the amplitude, mean, and phase angle of the individual sinusoidal waves from each channel and in each period. These values are statistically obtained by the method of least squares. The information is converted and stored in engineering units, taking into consideration the amplification factor and the analog offset used during testing.

ANALYSR

Programs for data analysis derive their productiveness from the specificity of their function. ANALYSR is specifically designed to interpret data from dynamic tests retrieved with DACTEST. The program's menu-driven construction makes it user friendly.

Most pavement materials at low strain levels exhibit response characteristics that can be approximately described by linear viscoelastic models. To determine the dynamic properties of a material (complex modulus and internal damping), a testing sequence based on stress- or strain-controlled sinusoidal excitation was used.

If a sinusoidal force [$P = P_o \sin(\omega t)$] is applied to a specimen composed of an ideal massless linear viscoelastic material, the deformation response will be sinusoidal and at the same frequency, but it will lag by a phase angle (δ) as given by the following expression:

$$X = X_o \sin(\omega t - \delta) \tag{1}$$

At each instant the relationship between P and X of the specimen is therefore a function of P_o/X_o and δ. It can be shown that if

$$P = P_o \exp(i\omega t)$$

then

$$X = X_o \exp[i(\omega t - \delta)]$$

$$P/X = P_o/X_o \exp(i\delta) = k_s' + ik_s'' = k_s^*$$

$$P_o/X_o = | k_s'^2 + k_s''^2 |^{1/2} = | k_s^* |$$

$$\tan \delta = k_s''/k_s'$$

where k represents a modulus determined in axial or shear loading.

For engineering applications, it is convenient to express the axial dynamic modulus as

$$E^* = E(1 + 2\beta_a i) \tag{2}$$

and the dynamic shear modulus as

$$G^* = G(1 + 2\beta_s i) \tag{3}$$

where β_a and β_s are measures of internal damping under axial and shear loadings, respectively. It should also be noted that

$$\beta = \tan \delta/2 \tag{4}$$

Thus the internal damping of an ideal massless viscoelastic material can be directly derived from the phase angle (δ) (between the sinusoidal forces and the sinusoidal displacements at the top of the specimen) and the stiffness modulus (from the ratio of the amplitudes).

However, materials are not massless and some exhibit damping behavior with nonelliptical stress-strain loops dependent on the strain level. The program makes the necessary adjustments incorporating corrections for the mass of the specimen and load cell and corrections for nonlinear viscous materials.

SPECIMEN PREPARATION

Specimen Mold

To prepare hollow cylindrical specimens, a typical unit consisting of inner and outer molds is required (Figure 4). The outer mold is a hard anodized aluminum cylinder that has been divided in half. After the two half cylinders have been secured, the tube can be fastened to the bottom plate. The inner mold, designed to be inwardly collapsible, can be removed without imposing stress on the specimens. When asphalt specimens are compacted, stainless steel sleeves are used to protect the mold from abrasive action by the aggregate. Vacuum grooves are provided on the inside wall of the outer mold and on the outside wall of the inner mold to keep in position a 0.020-in.-thick latex membrane that is used when fabricating fine-grained soil and sand specimens.

Compacting Equipment and Procedure

For the fabrication of hollow cylindrical specimens with materials requiring kneading compaction, special compaction

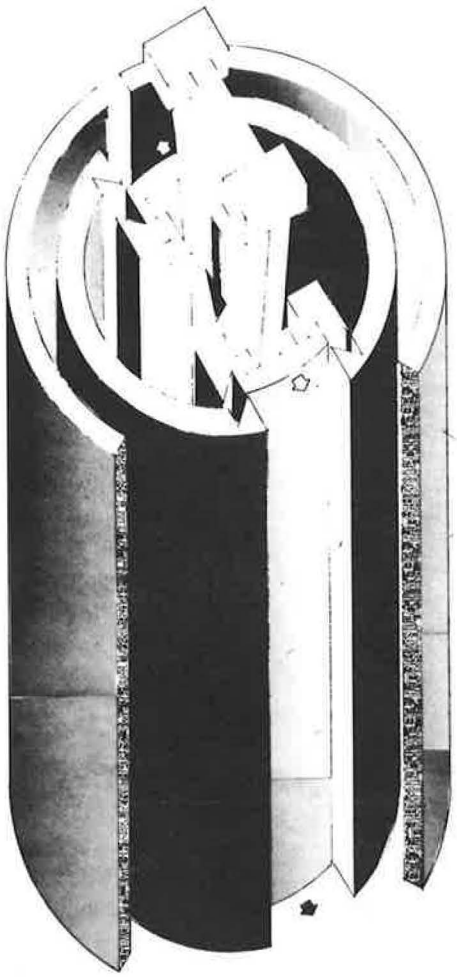

FIGURE 4 Molds for hollow cylindrical specimens.

feet were developed to fit into the 1-in. space between the inner and outer molds. Figure 5 shows the compaction feet and the driving mechanism. The compaction feet contain both strain gauges to measure the force and heating cartridges that provide heat to the 2.35-in.^{2} hardened steel feet. The back and forth movement of the horizontal servoram is converted into intermittent rotation of a driving screw by means of an indexing clutch. The mold is fastened to the driving screw and thus rotates intermittently, sliding over a Teflon sheet. Both servorams are controlled by a computer program called COMPACT. Unlike those of other kneading compactors, the inputs for this program are (*a*) specimen density, (*b*) mass of an individual batch of material, and (*c*) compaction pressure. The number of tamps of the compaction feet is dependent on the required density for each batch.

DYNAMIC PROPERTIES OF AN ASPHALT CONCRETE PAVING MIXTURE

Material and Specimen Preparation

A dense-graded asphalt concrete with granite aggregate (from Watsonville, California) was used in this study. The gradation of the aggregate conforms to the state of California

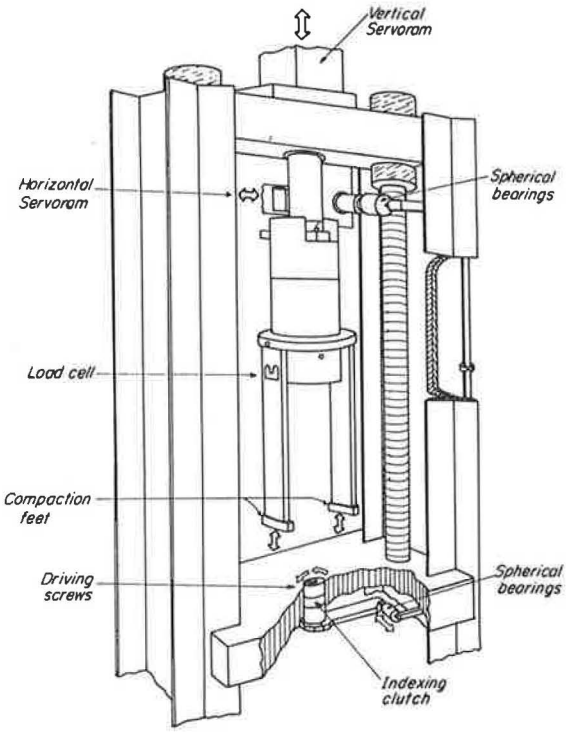

FIGURE 5 Compaction equipment.

specifications for Type B mixtures (Figure 6). The asphalt cement used was an AR-4000 produced by Chevron. An asphalt content of 5.5 percent by weight of aggregate was selected. Specimens were prepared using the DLS in its compaction mode with a required specific gravity of 2.49, compaction measure of 350 psi, and compaction time (duration of each tamp) of 4 sec.

The specimen, weighing 40 lb, was compacted using 17 batches. The first batch weighed 6 lb, the last 4 lb, and the others 2 lb each. The final layer was compacted with a static load of 40,000 lb, which was applied for 20 min; this permitted placement and leveling of the top ring (with lugs). For the specimens tested thus far, the specific gravity actually obtained was 2.44. Although visual inspection showed that the procedure produced specimens of uniform density, the

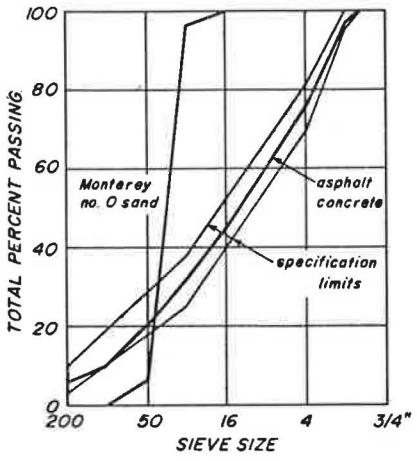

FIGURE 6 Gradations for asphalt concrete aggregate and sand.

desired density of 2.49 was not achieved because of deformation of the frame, the compaction feet, the mold, and the specimen while the compaction load was applied. This caused errors in the readings of the heights of the batches. This disparity can be corrected, however, by requesting a proportionally higher density.

Test Procedures and Results

Several vertical and torsional sinusoidal loads were applied to the specimen at three different temperatures (11°C, 25°C, and 40°C). At 11°C the vertical sinusoidal compression stress had a mean value of 40 psi and amplitude of 70 psi; the torsional sinusoidal loads produced shear stresses with a mean value of 12 psi and an amplitude of 20 psi. At 25°C and 40°C the axial values were 25 and 40 psi and shear stresses were 4 and 6 psi, respectively. At each temperature level the frequency of the sinusoidal loads was varied between 0.5 and 20 Hz (i.e., 0.5, 1.0, 5.0, 10, 15, and 20 Hz). A total of 200 loading cycles were applied at each frequency. (At 0.5 Hz, 60 cycles were applied, and, at 1.0 Hz, 100 cycles were applied.) All tests were performed under stress control (feedback from the load cells) with LVDTs placed 2.5 in. from the ends of the specimens. Each specimen was initially tested at 11°C, then at 25°C and at 40°C. This sequence was repeated three times. A specimen was maintained at each temperature level for at least 3 hr before testing. Vertical vibratory loads (20 to 0.5 Hz) were applied first, then torsional vibrations (20 to 0.5 Hz). This sequence was repeated twice at each temperature.

The effect of temperature and frequency on the variation of the dynamic modulus (E^*) and the dynamic shear modulus of G^* is shown in Figure 7. Repeatability of the results after various tests have been performed indicates that the dynamic properties of the specimen are not influenced by previous testing frequencies and temperatures. Thus several different tests can be performed on the same specimen using various frequencies, temperatures, load applications, and levels of stress without changing the data significantly. The stiffness moduli exhibit, however, strong dependence on frequency and temperature.

From stress-strain hysteresis loops the internal damping can be determined. Figure 8 shows a typical loop obtained at 1 Hz and 40°C. The effect of temperature and frequency on the values of internal damping, measured under vertical loading, and those measured under torsional loading is plotted in Figure 9. It is interesting to note that the difference increases with temperature. Temperature and frequency effects are particularly noticeable in the values of the dynamic Poisson's ratio [$\nu^* = E^*/(2.G^*) - 1$] shown in Figure 10. Similar results are reported elsewhere (*4*).

DYNAMIC PROPERTIES OF A SAND

Material and Specimen Preparation

The sand used for this study was a dry, cohesionless, uniformly graded Monterey sand No. 0 with a D_{50} of 0.5 mm (Figure 6), a minimum dry density of 88 lb/ft^3, and a

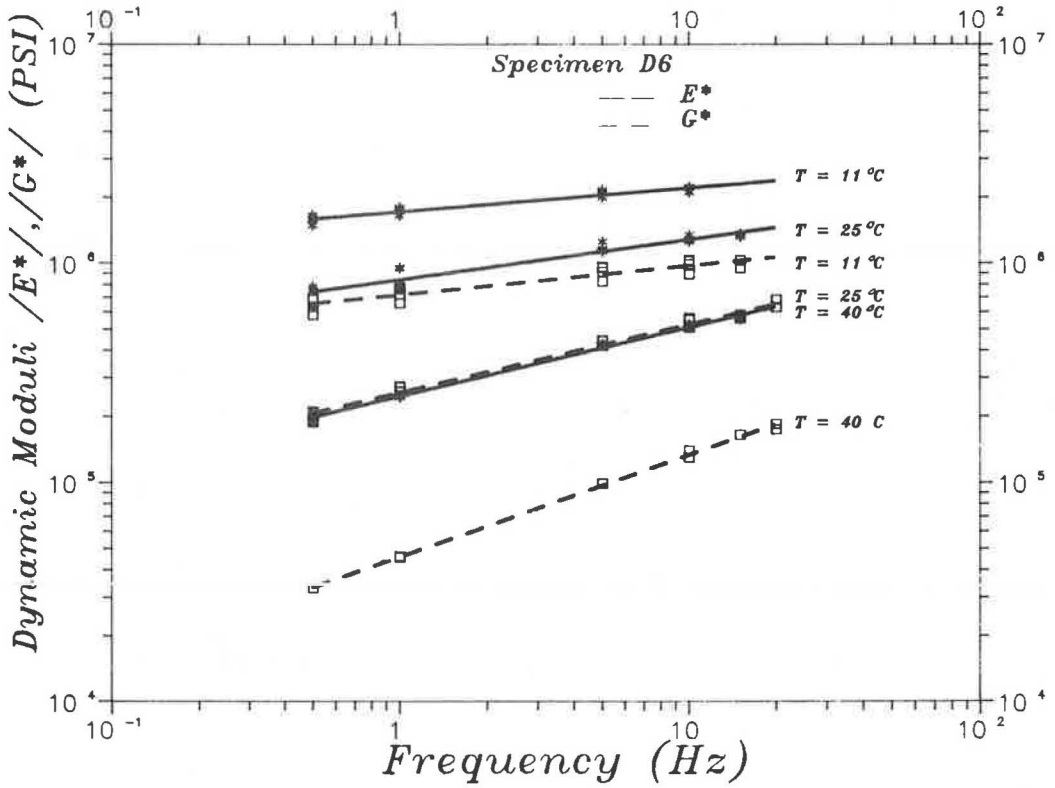

FIGURE 7 Influence of frequency and temperature on the dynamic moduli of an asphalt concrete in compression and shear.

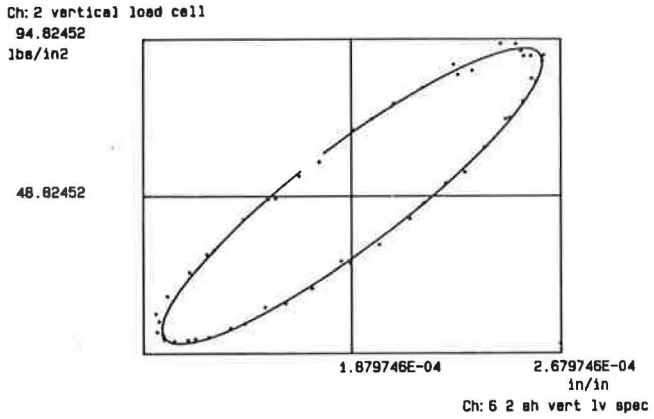

FIGURE 8 Hysteresis loop for an asphalt concrete mixture.

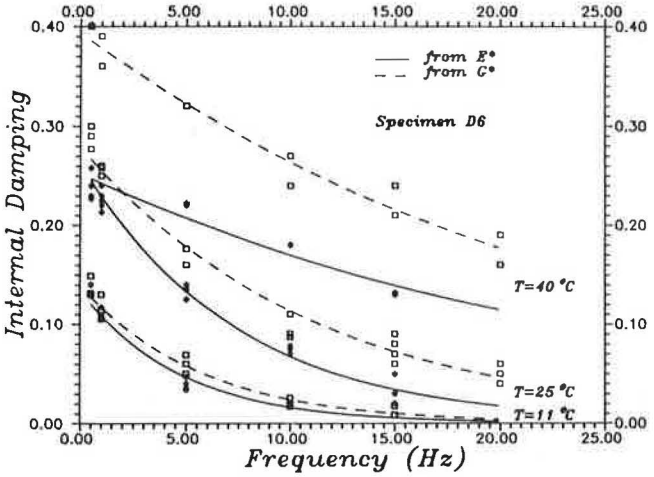

FIGURE 9 Influence of temperature and frequency on the damping characteristics of an asphalt concrete.

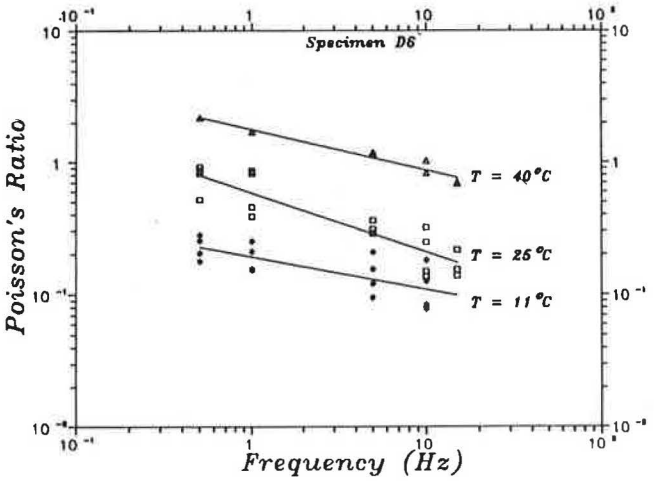

FIGURE 10 Influence of temperature and frequency on Poisson's ratio, asphalt concrete.

maximum dry density of 105 lb/ft^3. For this specimen a relative density of 90 percent was obtained using a vibrating table.

To fabricate the specimen, the sand was confined by a latex rubber membrane 0.020 in. thick and U-shaped in cross section. Holes in the bottom of the membrane allow the bottom ring to be securely attached to the bottom plate and also permit vacuum to be applied through porous stones placed in the ring. When the sample was nearly completed, the top ring was set in place. While the mold continued to vibrate, additional sand was poured through holes in the top ring to achieve the desired density even between the lugs. On completion, the membrane was rolled over the top ring and sealed with O-rings. A vacuum was then applied to the specimen and the mold was removed. Visual inspection indicated that this method produced a sample of uniform shape and density.

Testing Procedures and Results

In a series of tests, the influence of the mean effective stress frequency and strain level on the dynamic shear was investigated. At each strain level (0.01, 0.1, and 1 percent) tests were conducted at three different levels of effective mean stress (26, 20, and 16 in. Hg). The tests were performed under torsional strain control and vertical stress control.

Figure 11 shows a comparison of dynamic shear modulus (G^*) with the shear strain (percentage) for three different mean confining stresses. The mean stress was measured in inches of mercury and corresponds to the level of vacuum applied to the specimen. All tests were performed under no axial load. It was further determined that no relationship exists (for the sand tested) between dynamic shear modulus and frequency over the range of 0.5 to 10 Hz. This is shown in Figure 12 for the range of frequencies and at different stress and strain levels.

Internal damping was computed from stress-strain hysteresis loops (Figure 13). The resulting values were plotted against the shear strain in Figure 14. From the data it can be inferred that an increase in the magnitude of the shear strain results in an increase in the internal damping. However, the scattering of the data implies some frequency effects.

Figure 15 shows the effect of frequency at different stress and strain levels on the internal damping. The results suggest that the effect of frequency on internal damping varies differently with different levels of stress and that damping is not affected by the mean stress level.

All of the data reported were obtained from tests on a single specimen. The final test on the same specimen was conducted at a very high level of strain, 7.5 percent, and resulted in the destruction of the specimen. Figure 16 shows the deformation that occurred during testing. Channel 0 shows axial displacements and Channel 1 torsional displacement. The path of Channel 1 shows that the software automatically adjusted the gain until the desired amplitude was reached. It is significant that initially the specimen contracted and then the specimen dilated until testing was stopped. Because there was no pore fluid, dilation of the sample resulted in plastic strain softening of the specimen in distinct banded areas. Visual inspection showed the formation of helical deformation lines on the sample. Formation of these bands indicates that the material was failing in these regions according to the Mohr-Coulomb hypothesis.

The findings in this series of tests are consistent with the results reported by Seed and Idriss (*5*).

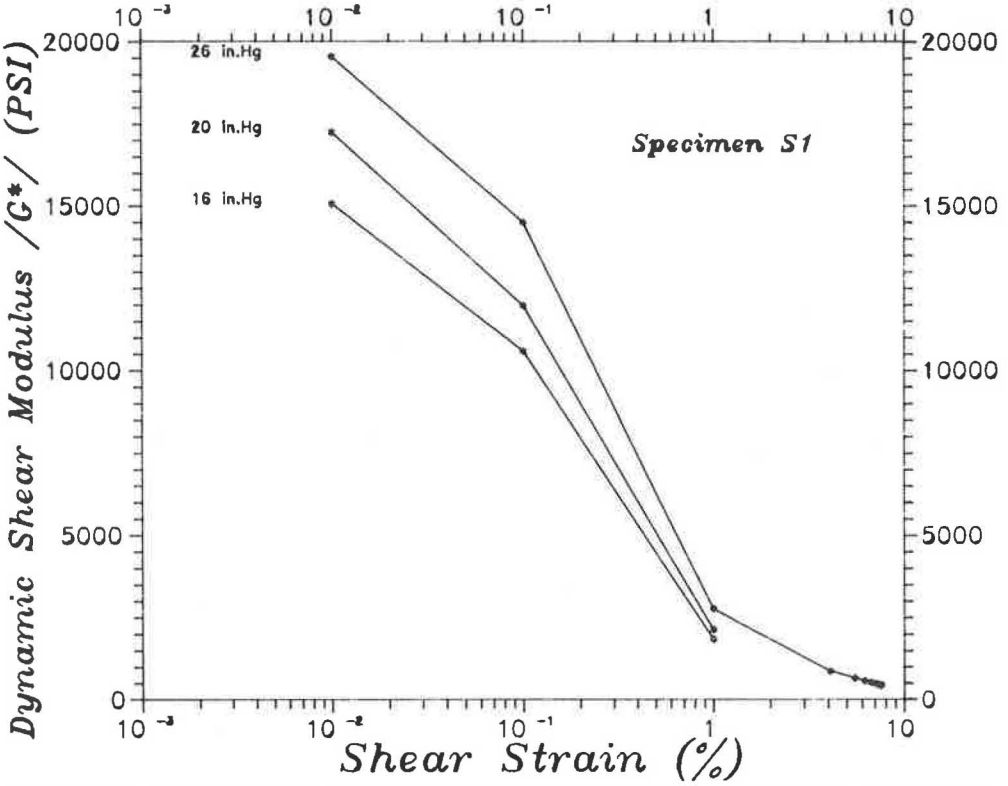

FIGURE 11 Relationship between dynamic shear modulus and shear strain for a range of confining pressures: Monterey sand, 90 percent relative density.

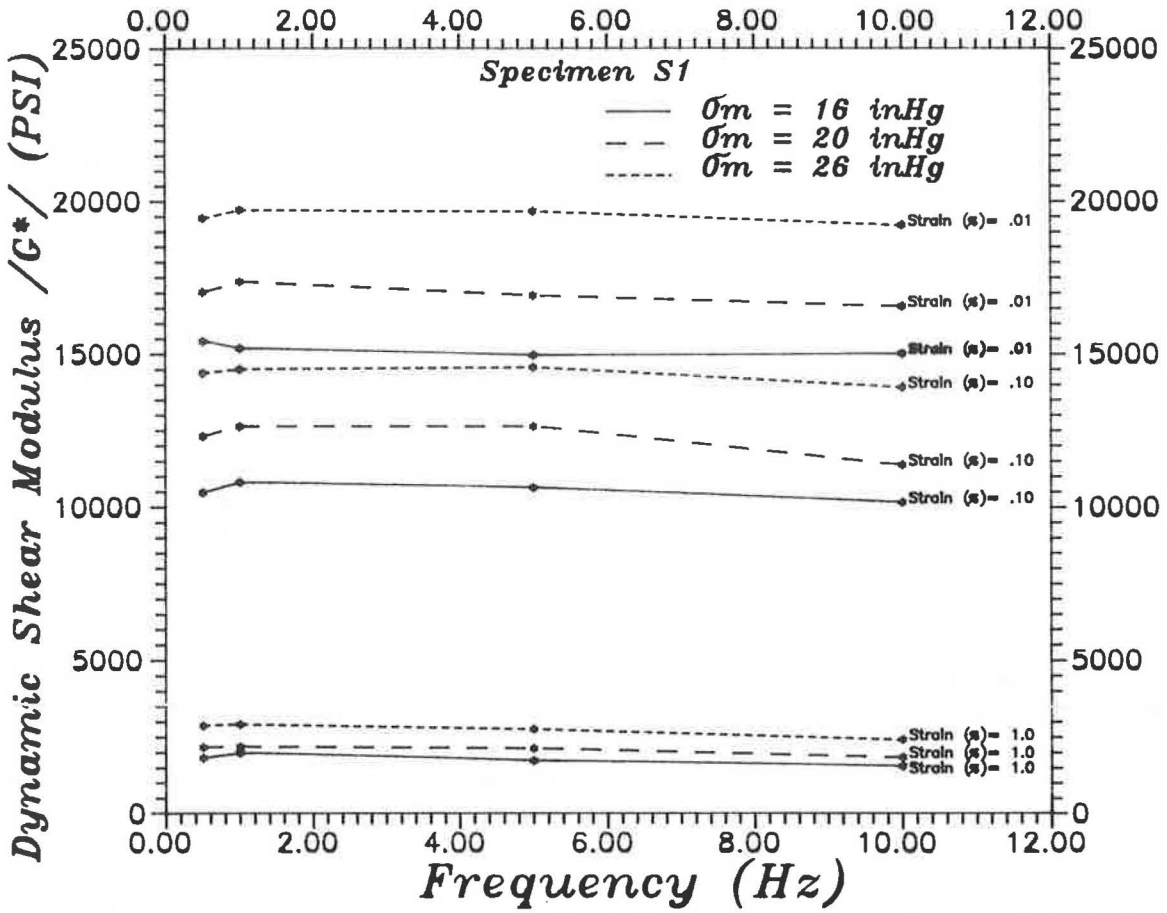

FIGURE 12 Relationship between dynamic shear modulus and frequency: Monterey sand, 90 percent relative density.

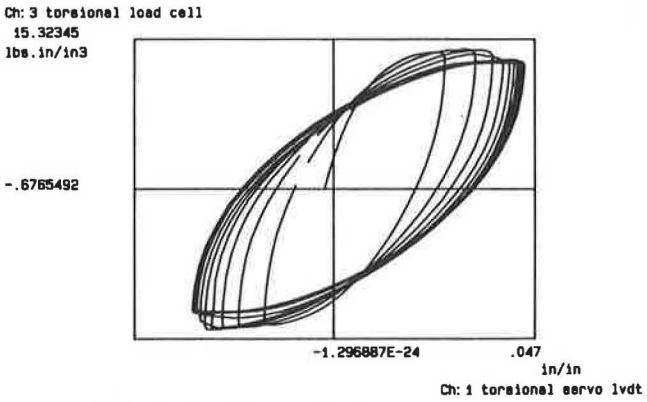

FIGURE 13 Hysteresis loops: Monterey sand, 90 percent relative density, frequency of loading 0.5 Hz.

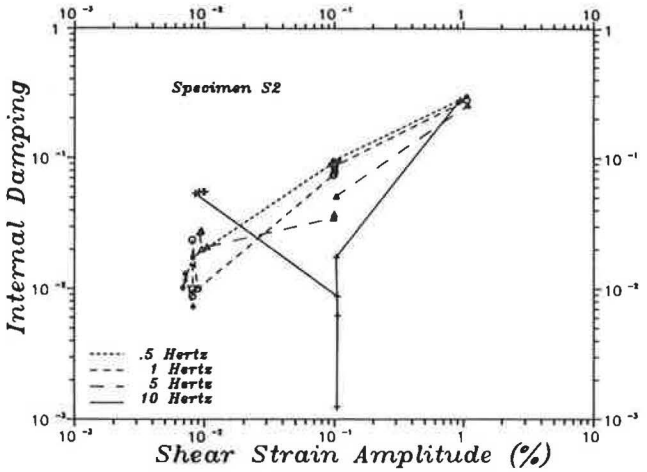

FIGURE 14 Internal damping versus shear strain: Monterey sand, 90 percent relative compaction.

DYNAMIC PROPERTIES OF A SILTY CLAY

Material and Specimen Preparation

A silty clay from Vicksburg, Mississippi (material supplied by the Geotechnical Laboratory of the U.S. Army Corps of Engineers Waterways Experiment Station), was used for this portion of the investigation (liquid limit = 35, plasticity index = 13). A compaction procedure similar to that for the asphalt concrete was used. The compactive effort selected was approximately equivalent to that used in the modified AASHTO (T 180) compaction test. For the specimen the data of which are reported herein, the resulting dry density was 116 lb/ft^3 (1858 kg/m^3) and the molding water content was 14 percent.

The specimen, weighing 35 lb (15.9 kg), was compacted using 17 batches; the initial batch weighed 5.5 lb (2.5 kg), the final 3.25 lb (1.48 kg), and the intermediate ones 1.75 lb (0.80 kg) each. After kneading compaction, the specimen was subjected to a static leveling load of 25,000 lb (111.2 kN). To ensure a smooth-surfaced specimen, the compaction mold was lined with a Teflon sleeve.

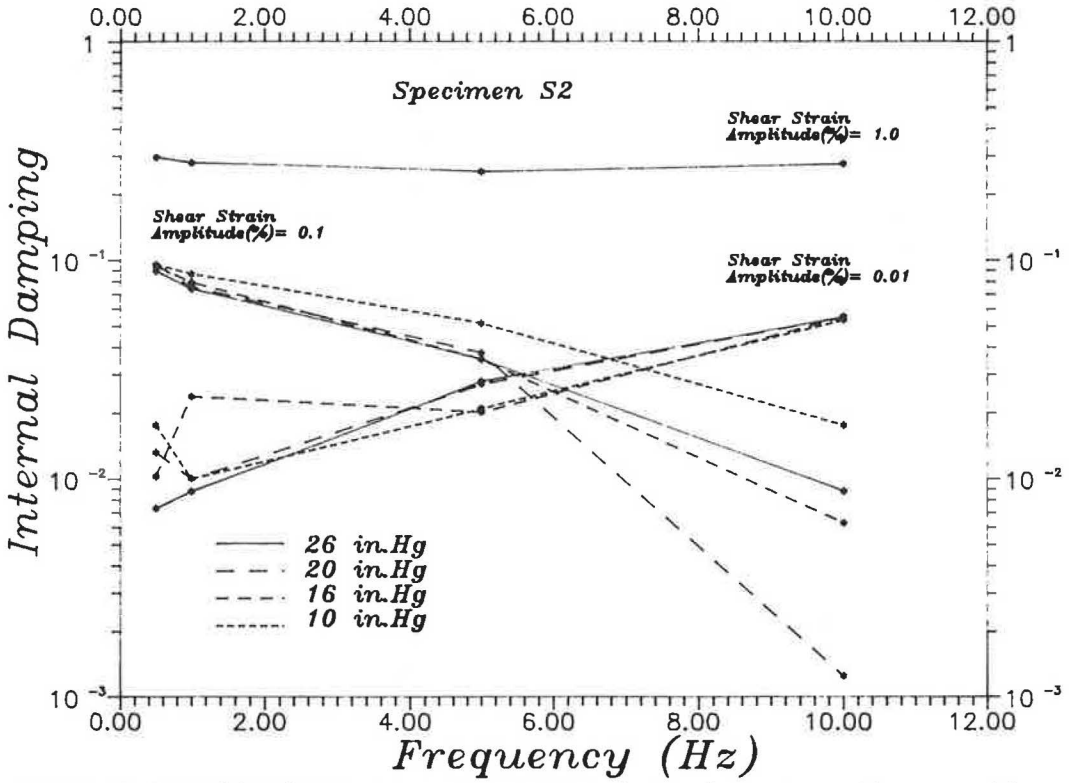

FIGURE 15 Internal damping versus frequency over a range of values of mean stress and for a range of shear strains: Monterey sand, 90 percent relative density.

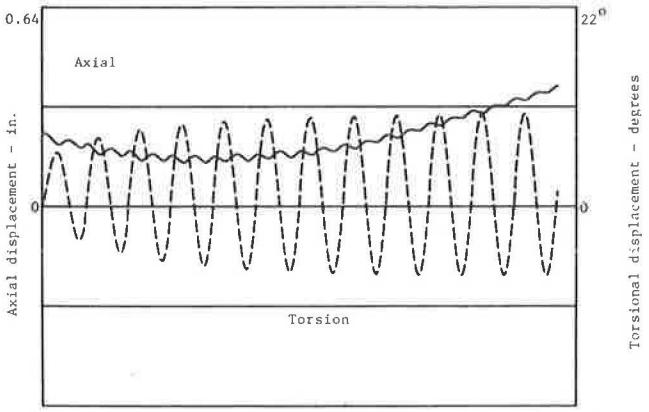

FIGURE 16 Displacement occurring during testing of Monterey sand at 7.5 shear strain.

Testing Procedures and Results

The specimen was tested at three strain levels (0.01, 0.1, and 1.0 percent), four frequency levels (0.5, 1.0, 5.0, and 10 Hz), and four levels of confining pressure (29, 20, 11, and again 29 in. Hg). Confining pressure was applied through vacuum for at least 10 hr before testing. During testing, approximately 30 sinusoidal load cycles were applied at each level.

Figure 17 shows the effect of shear strain amplitude and confining stress on dynamic shear modulus. To obtain these results, the confining pressure was changed at each strain level; this was done to mitigate the effects on the results of damage that might occur at higher strain levels. Repeatability of results at 29 in. Hg after several cycles were applied at 20 and 11 in. Hg indicates that the number of load applications (though applied at lower confining pressures and over a range of frequencies) does not significantly alter the dynamic shear modulus values.

Frequency effects on shear modulus are negligible for this particular specimen, as seen in Figure 18.

When the specimen was tested at a strain level of 1.0 percent, the lugs induced cracking. Although this phenomenon was not observed in tests on the asphalt concrete or sand, it does suggest that the lugs should not be used for relatively brittle materials (this clay compacted to a relatively high density and at a water content slightly to the left of the line of optimums). Instead, the rings should be bonded to the specimen with an adhesive.

The effect of confining stress, frequency, and strain amplitude on damping was also evaluated. A typical hysteresis loop is shown in Figure 19. The data shown in Figure 20 suggest that internal damping increases with increase in shear strain amplitude but is little affected by confining pressure. The scattering of data is thought to be due to the frequency effects. Figure 21 shows the variation of internal damping with frequency at each strain level. From these data, it can be inferred that the frequency effect is similar at each strain level because the slopes of the lines are similar.

SUMMARY AND CONCLUSIONS

The DLS described herein and used to determine the dynamic properties for three pavement materials illustrates microcomputer capabilities in a research environment. Beyond the economic advantage of replacing expensive equipment (i.e., strip chart recorders, function generators, and closed-loop controllers) microcomputers present (*a*) the added advantage of eliminating the need for time-consuming data reduction and (*b*) the ability to control several processes involving different pieces of equipment simultaneously. The ability to control the values of three principal axes of stress or strain over a representative range of frequencies and temperatures provides a valuable tool for determining material properties.

Results of the test program for the asphalt concrete illustrate the dependence of the stiffness and damping characteristics of the mixture on frequency, temperature, and mode of loading.

Some nonlinearities are apparent in the response characteristics of this asphalt concrete. This is evidenced, for

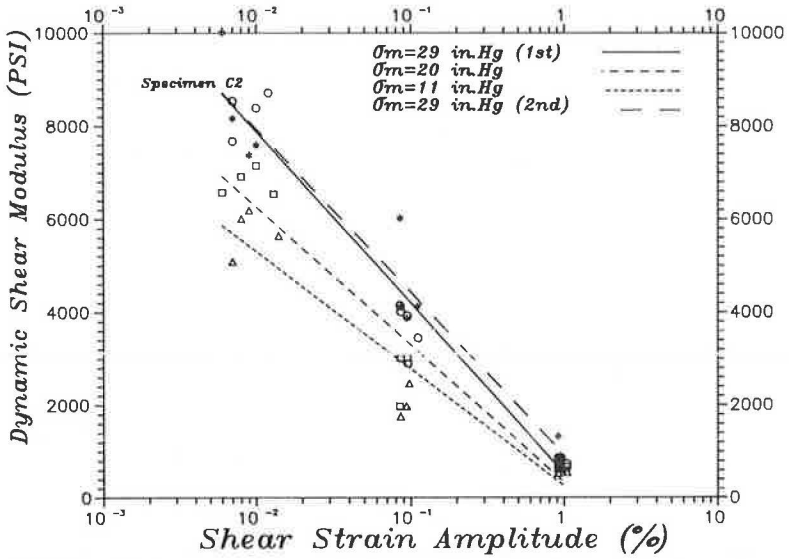

FIGURE 17 Influence of shear strain amplitude on the dynamic shear modulus of a silty clay specimen at three different confining pressures.

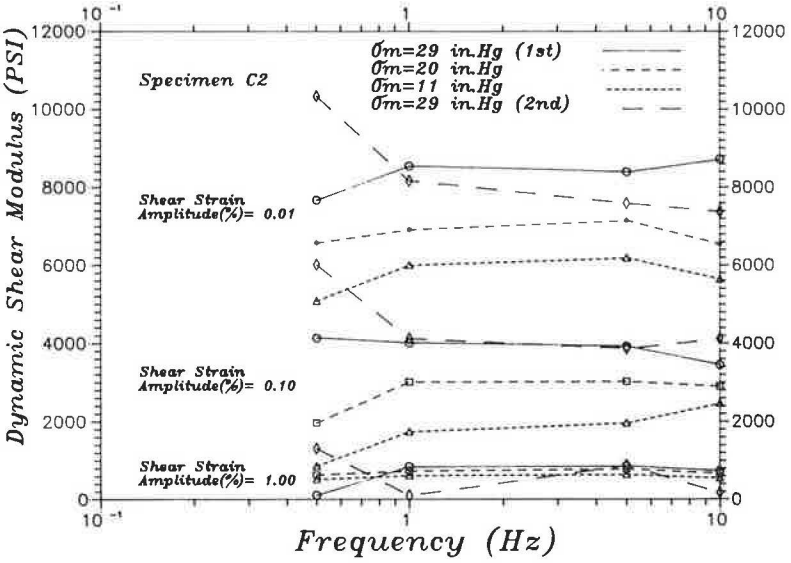

FIGURE 18 Influence of frequency loading on dynamic shear modulus.

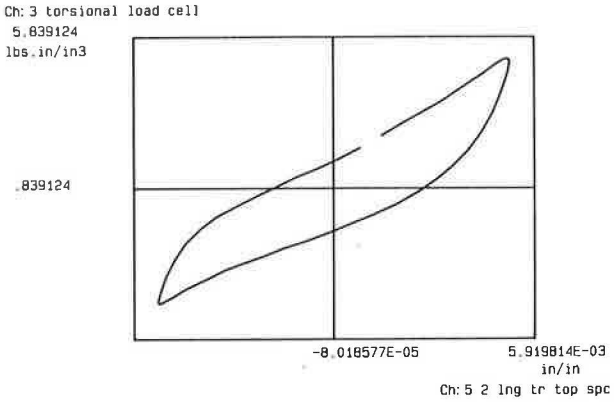

FIGURE 19 Typical hysteresis loop for Vicksburg silty clay at 1 Hz and a strain amplitude of 1 percent.

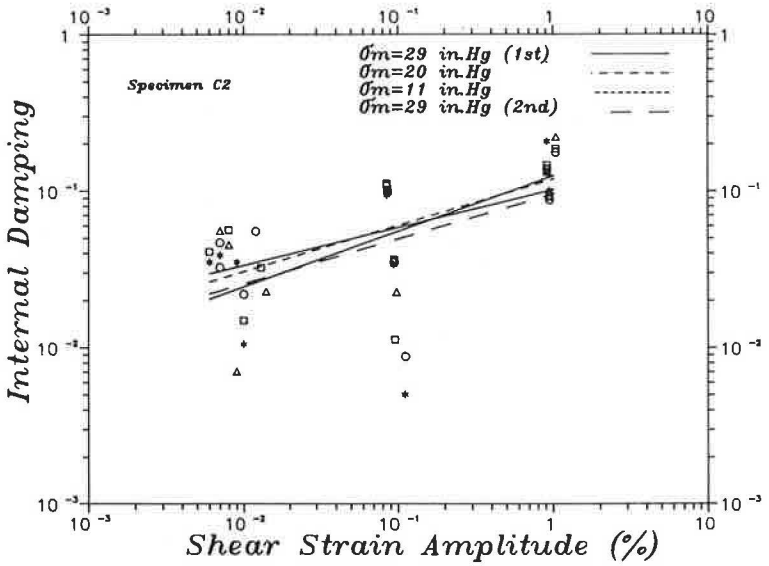

FIGURE 20 Variation of internal damping as a function of strain level for a silty clay.

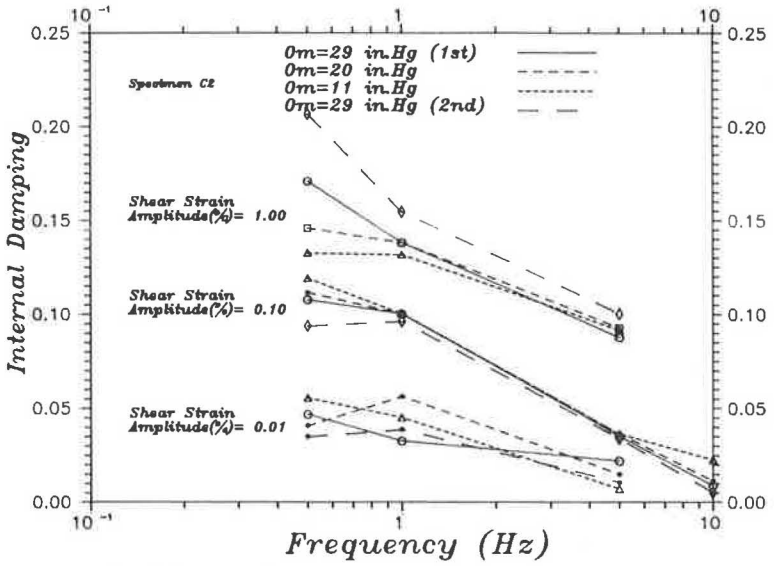

FIGURE 21 Influence of load frequency on internal damping at different strain levels for Vicksburg silty clay.

example, by changes in values for internal damping computed from the stiffness moduli (E^* and G^*). As the differences in damping determined in the axial and shear modes of loading increase, computed Poisson's ratios exceed 0.5 indicating some volume increase—most likely in the shear mode of loading.

This investigation also considered the effect of frequency, confining pressure, and strain level on the dynamic shear modulus and the internal damping characteristics of sand and silty clay. The data clearly indicate that frequency has no influence on the dynamic shear modulus of either clay or sand specimens (within the ranges tested). Frequency does, however, have a marked effect on the internal damping of both materials. For the sand studied, it was observed that frequency effects vary with strain level whereas, for silty clay, the effects were identical at all strain levels.

Dynamic moduli so obtained can be used to determine the stresses, strains, and deflections in pavement systems for moving vehicles, provided the time histories of the loads are available. This is possible, using a computer code, SAPSI, recently developed by S. S. Chen and J. Lysmer. Work by Sousa (*6*) contains an illustration of such an approach.

ACKNOWLEDGMENTS

Partial funding for this project was provided by the Transportation Laboratory of the State of California Department of Transportation, International Business Machines, and the Institute of Transportation Studies. The authors wish to express their appreciation for the contribution provided by Manuel Bronstein during the initial development of the ASSEMBLER code and by Paul Gross for the design and construction of all electronic interfaces. Phyllis De Fabio typed the manuscript.

REFERENCES

1. J. L. Lysmer, C. L. Monismith, J. B. Sousa, and S. S. Chen. *Pavement Response to Dynamic Loads.* Transportation Laboratory, State of California Department of Transportation, University of California, Berkeley, Oct. 1985.
2. T. D. Gillespie et al. *Influence of Size and Weight Variables on the Stability and Control Properties of Heavy Trucks.* Report UMTRI-83-10/2. University of Michigan, Ann Arbor, April 1983.
3. N. Sitar and Y. D. Wang. Cyclic Test Control and Data Acquisition Using a Microcomputer. *Proc., Second National Conference on Microcomputers in Civil Engineering*, Orlando, Fla., 1984, pp. 6-8.
4. J. F. Hills and W. Heukelom. The Modulus and Poisson's Ratio of Asphalt Mixes. *Journal of the Institute of Petroleum*, Vol. 55, No. 541, Jan. 1969.
5. H. B. Seed and I. M. Idriss. *Soil Moduli and Damping Factors for Dynamic Response Analysis.* Report EERC 70-10. University of California, Berkeley, Dec. 1970.
6. J. Sousa. *Dynamic Properties of Pavement Materials.* Ph.D. dissertation. University of California, Berkeley, Nov. 1986.

Publication of this paper sponsored by Committee on Flexible Pavement Design.

Analysis of Axle Loads and Axle Types for the Evaluation of Load Limits on Flexible Pavements

EMMANUEL G. FERNANDO, DAVID R. LUHR, AND HARI N. SAXENA

The Commonwealth of Pennsylvania is responsible for 44,000 mi of roads, the majority of which have pavements with limited structural capacity. The state has the authority to restrict axle loads on its roads if it is believed that those axle loads would result in excessive damage to the pavement structure. Consequently, a procedure for establishing axle load restrictions is necessary. As part of the development of a framework for load limit analysis, an evaluation was made of the sensitivity of pavement response and predicted performance to variations in loads, layer moduli, and layer thicknesses. To evaluate the effect of axle loads under a variety of conditions, a theoretical elastic layer analysis was conducted that considered various load magnitudes and configurations for different pavement thicknesses and material properties. It was found that axle configuration (single-, tandem-, and triple-axle assemblies) did not significantly affect theoretical pavement response, provided that the load per tire remained the same. In addition, a comparison of predictions from various performance models indicated that the sensitivity of predicted performance to the design variables considered can vary depending on the performance model and failure criteria used. Equivalence factors calculated for a broad range of pavement structures were also examined. It was found that AASHTO equivalence factors do not vary significantly with different pavement structures. Consequently, the use of these equivalence factors for evaluating the effects of alternative load limit policies is not advisable.

Low-volume roads make up the greater part of most road networks in the world, including in the United States where the Interstate highway system makes up less than 2 percent of total road mileage. Much of the roadway network in this country is composed of thin, flexible pavement structures that are intended to carry low volumes of traffic. In Pennsylvania these are termed Type D (collector) and Type E (local) roads.

Every state has a specified maximum legal load limit for a single axle, for a tandem axle, and for maximum gross vehicle weight (GVW). Often, however, low-volume roads do not have adequate structural capacity to carry axle loads at the legal load limit for all, or part, of the year. In the spring when the ground is thawing, these pavements have significantly reduced bearing capacity, and often the expense of importing non-frost-susceptible materials is prohibitive. To deal with this problem, some legal codes allow the posting of load limits below the state's legal maximum.

The Commonwealth of Pennsylvania has 44,000 mi of roads under its jurisdiction. About two-thirds of these are low-volume roads that, in other states, would be the responsibility of local governments. Because a majority of these low-volume roads have pavements with limited structural capacity, the state has the authority to restrict axle loads if it is believed that those axle loads would result in excessive damage to the pavement structure. In Pennsylvania, the establishment of load restrictions below the legal load limit is authorized by Section 4902 of the Motor Vehicle Code (*1*). Under this law, commonwealth and local authorities may impose restrictions on the weight or size of vehicles allowed to operate on a particular route whenever it is determined that, without such restrictions, excessive damage may occur to the road. This load limit specification is based on GVW and was selected on the basis of engineering judgment and experience.

The posting of load limits on the basis of GVW poses a fundamental problem. The load from the vehicle is transmitted through the axle tires, and the load applied by each tire depends on the number of tires per axle. Tandem and triple axles have more tires than do single axles, so they can carry a heavier load while putting the same stress on the pavement as a lighter-loaded single axle. Because pavement performance is related more accurately to axle loads and axle types than to GVW, the posting of load limits on flexible pavements should be based on a maximum load for a given axle type.

To determine the appropriate load restrictions for various axle types and pavement conditions, it is important to evaluate how predicted performance varies with different axle loads and axle configurations and with various pavement layer thicknesses and material properties. In this paper the effects of these design variables on calculated pavement response and predicted pavement performance are examined. The results of the analysis were important in the development of a procedure for determining load restrictions in Pennsylvania.

ANALYSIS OF AXLE LOADS AND AXLE TYPES

The analysis of axle loads and axle types was conducted by examining theoretical solutions of a linear elastic pavement analysis computer program called BISAR (*2*). A three-layer

E. G. Fernando and D. R. Luhr, Department of Civil Engineering, Pennsylvania State University, University Park, Pa. 16802. H. N. Saxena, Public Works Department, Jaipur, India.

pavement structure (surface, base, and subgrade) was selected for the analysis because it is representative of typical pavements on low-volume roads in Pennsylvania. Three different levels (associated with low, medium, and high values) were chosen for various pavement parameters (surface thickness, surface modulus, base thickness, base modulus, and subgrade modulus). Because of the importance of load magnitude in this study, five different levels were selected for this variable. The values chosen for the different factor levels (Table 1) represent a broad range of pavement and loading conditions.

The possible combinations of all values of all factors result in $3^5 \times 5$, or 1,215, observations for each axle configuration included in the study. For all of these combinations, pavement deflections, horizontal strain at the bottom of the asphalt concrete layer, and vertical strain at the top of the subgrade were calculated. These pavement response parameters are commonly used for predicting pavement performance, and it was therefore important to evaluate how they are affected by the different variables included in the study. In the discussion that follows, the findings from the analysis are presented. The discussion has been limited to subgrade strain because this pavement response parameter has been strongly related to pavement performance. The trends observed for the other pavement response parameters were found to be similar to those for subgrade strain, and they are therefore not reported separately.

Effect of Variables on Pavement Response

Plots are shown in Figures 1-3 of maximum vertical subgrade strain versus load per tire for the three axle configurations (single, tandem, and triple) for cases in which the layer moduli and thicknesses are fixed at the low, middle, and high levels selected for these variables (Table 1). These plots indicate that an increase in load results in an increase in subgrade strain, as would be expected. The significant observation is that the plots for the three different axle configurations are almost identical in both shape and magnitude. This indicates that, theoretically, similar pavement response will occur with different axle configurations as long as the load per tire is constant.

To study the effect of axle configuration on subgrade strain along the direction of vehicle movement (longitudinal direc-

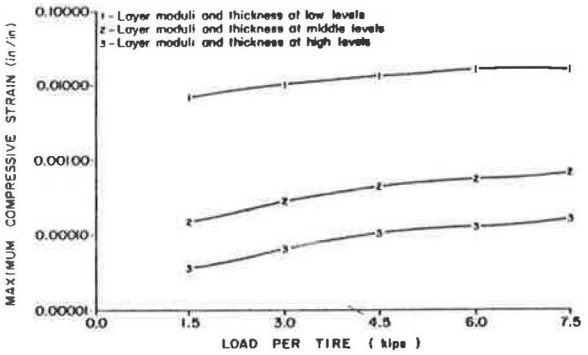

FIGURE 1 Maximum subgrade compressive strain versus load per tire for a single-axle configuration.

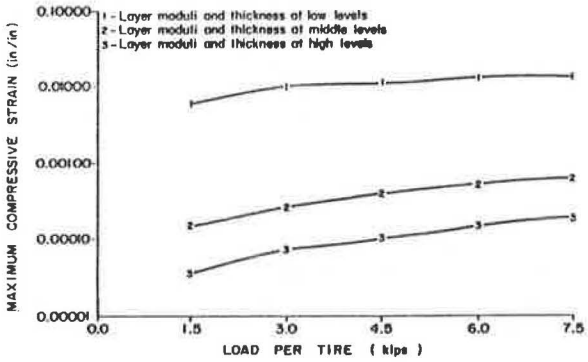

FIGURE 2 Maximum subgrade compressive strain versus load per tire for a tandem-axle configuration.

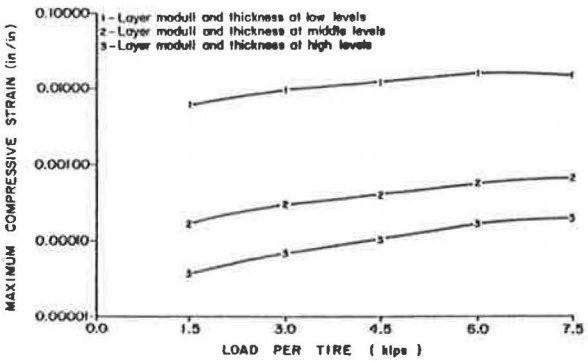

FIGURE 3 Maximum subgrade compressive strain versus load per tire for a triple-axle configuration.

TABLE 1 LEVELS OF VARIABLES USED IN THE STUDY

Variable	Level	Unit
Load (all dual tires)		
Single axle	6; 12; 18; 24; 30	Kips
Tandem axle	12; 24; 36; 48; 60	Kips
Triple axle	18; 36; 54; 72; 90	Kips
Surface thickness ($T1$)	1; 5.5; 10	Inches
Surface modulus ($E1$)	80×10^3; 540×10^3; $1{,}000 \times 10^3$	psi
Granular base thickness ($T2$)	3; 9; 15	Inches
Granular base modulus ($E2$)	10×10^3; 40×10^3; 70×10^3	psi
Subgrade modulus ($E3$)	3×10^3; 10×10^3; 17×10^3	psi

tion), plots of subgrade strain versus longitudinal position for 18-kip single, 36-kip tandem, and 54-kip triple axles were drawn using the same scale. The plots that resulted when all factors were at middle levels are shown in Figures 4-6. The plots indicate that the distribution of the subgrade strain along the longitudinal direction is different for the three axles. Although there is one cycle of strain for the single-axle configuration, there are two cycles of strain for the tandem-axle and three cycles of strain for the triple-axle configurations.

These plots suggest that the damaging effect of axle configurations may be different, although the magnitude of the maximum subgrade compressive strain is the same for all three cases. The triple axle may be more damaging than the single or tandem axle because it causes more cycles of strain in the pavement. Similarly, the effect of a tandem-axle load may be more damaging than that of a single-axle load. To evaluate this factor more closely, an analysis was performed on data collected at the AASHO Road Test.

The AASHTO design procedure is one of the most widely used methods for designing flexible pavements. The procedure is based on the results of the extensive AASHO Road Test conducted in Ottawa, Illinois, from 1958 to 1960. The road test site contained six main loops, of which Loop 3 had traffic loads of 12-kip single axles and 24-kip tandem axles, respectively, on two separate lanes (*3*). These are the only data from the road test for single and tandem axles carrying the same load per tire on identical pavement sections.

Plots of performance data from Loop 3, for 24-kip tandem axles versus 12-kip single axles, are shown in Figures 7 and 8. The data points are scattered along the line of equality, indicating that the two axle configurations caused similar pavement performance. To provide a measure of the variation in the observed performance, a root-mean-square (RMS) statistic was calculated as follows:

$$RMS = \left[\frac{\sum_{i=1}^{n} (\log_{10} N_{12} - \log_{10} N_{24})^2}{n} \right]^{1/2} \quad (1)$$

where

$\log_{10} N_{12}$ = logarithm of the number of 12-kip single-axle load applications before failure,

$\log_{10} N_{24}$ = logarithm of the number of 24-kip tandem-axle load applications before failure, and

n = number of pairs of identical pavement sections.

For terminal serviceability indices of 1.5 and 2.5, the RMS statistics were calculated to be 0.19 and 0.20, respectively. Similarly, RMS statistics were calculated for the replicate sections at the AASHO Road Test and were found to have values of 0.15 and 0.16 for terminal serviceability indices of 1.5 and 2.5, respectively. Because the RMS statistics calculated for the Loop 3 sections are close to those for the replicates, it is unlikely that significant variations in observed pavement performance can be attributed to the difference in axle configurations. This provides some measure of plausibility to the theoretical inference that different axle configurations will cause no significant variations in pavement performance provided that the load per tire is constant for all axle configurations.

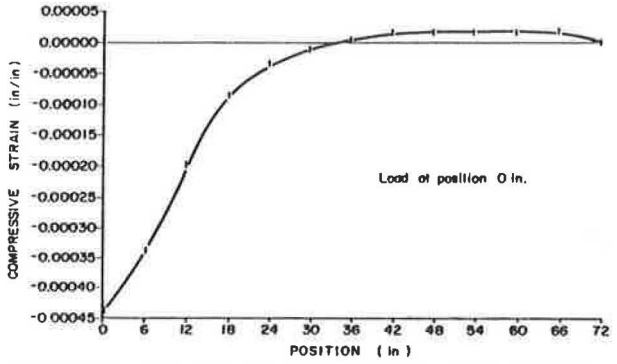

FIGURE 4 Subgrade compressive strain versus position, with factors at middle levels, for an 18-kip single-axle load.

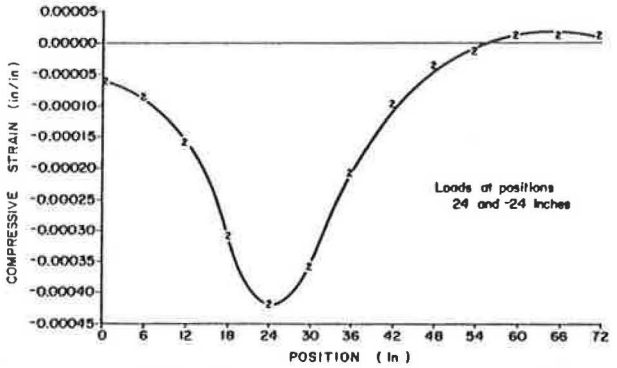

FIGURE 5 Subgrade compressive strain versus position, with factors at middle levels, for a 36-kip tandem-axle load.

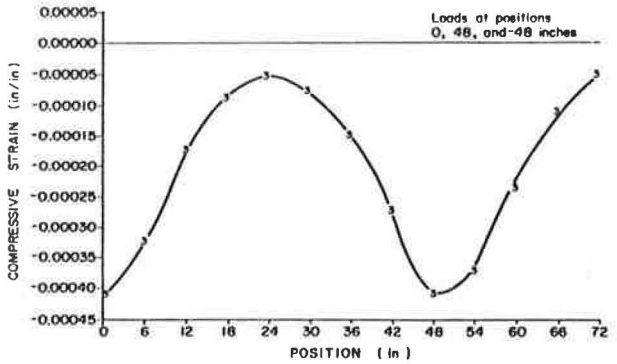

FIGURE 6 Subgrade compressive strain versus position, with factors at middle levels, for a 54-kip triple-axle load.

One possible explanation of the similar pavement performance resulting from 12-kip single-axle loads and 24-kip tandem-axle loads, even though Figures 4 and 5 indicate that the tandem axle causes two strain cycles versus one strain cycle for the single axle, is that the theoretical strain basins are calculated assuming static loading conditions. Under dynamic loading conditions the pavement stiffness will be higher, and there will be a smaller difference between the strain basins caused by single- and tandem-axle configurations.

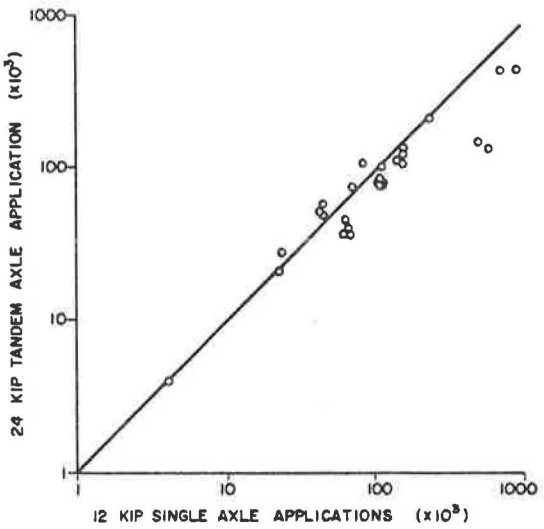

FIGURE 7 Comparison of the performance of identical pavement sections subjected to 12-kip single-axle and 24-kip tandem-axle loadings [weighted axle applications to present serviceability index (PSI) = 1.5].

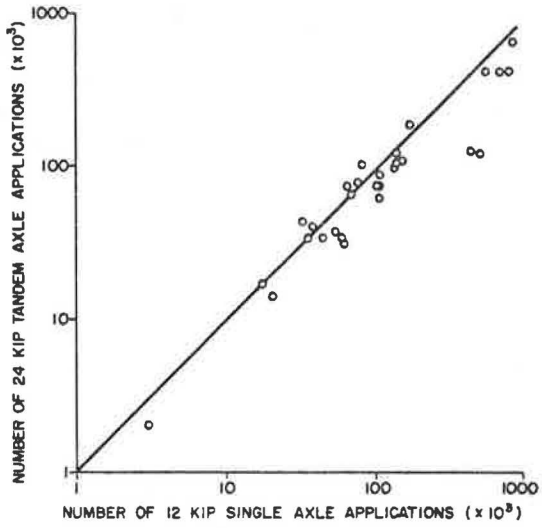

FIGURE 8 Comparison of the performance of identical pavement sections subjected to 12-kip single-axle and 24-kip tandem-axle loadings (weighted axle applications to PSI = 2.5).

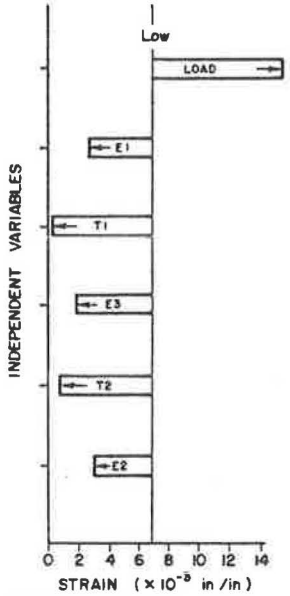

FIGURE 9 Change in subgrade strain when each factor is varied from low to high levels, with all other factors at low levels.

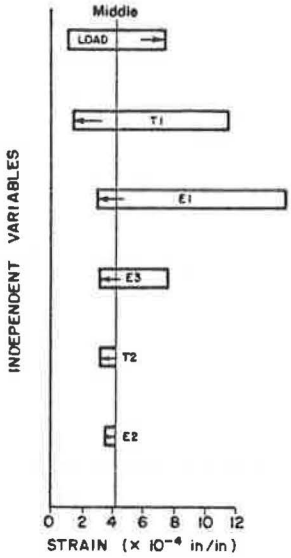

FIGURE 10 Change in subgrade strain when each factor is varied from low to high levels, with all other factors at middle levels.

In addition to the study of the effects of axle load and axle configuration, an evaluation was made of the effects of layer moduli and thicknesses on calculated pavement response. For this evaluation, each of the independent variables considered was varied from low to high levels, while the other independent variables were kept at low, middle, and high levels successively. Figures 9-11 show the effect of the six independent variables on the calculated value of subgrade compressive strain. The arrows in the boxes indicate whether the variable in question had a positive (pointing right) or negative (pointing left) effect on maximum subgrade strain.

The levels selected for the pavement parameters cover a wide practical range. The vertical line indicates the value when all variables are held at one level. These figures give a good indication of how sensitive the dependent variable (subgrade strain) is to the variation of any one of the independent variables.

It can be seen that at low levels pavement response is highly sensitive to load, surface thickness, and base thickness. It can therefore be inferred that, for pavements with weak materials and on poor subgrade, subgrade strain can be reduced by increasing the thickness of the surface and the base layers. At

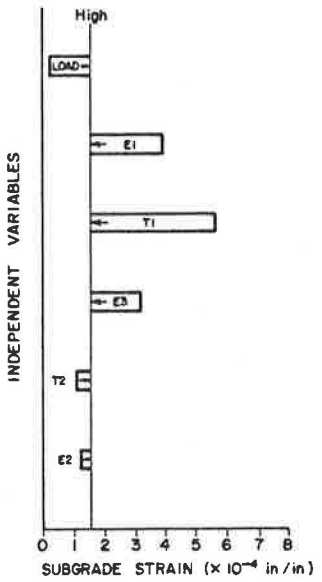

FIGURE 11 Change in subgrade strain when each factor is varied from low to high levels, with all other factors at high levels.

the middle and high levels, pavement response is quite sensitive to load, surface thickness, and surface modulus. For these pavements the subgrade strain can be reduced by increasing the thickness and improving the quality of the surface. At the middle and high levels, pavement response is not particularly sensitive to base thickness and base modulus. Subgrade modulus affects pavement response at all levels.

Effects of Variables on Predicted Pavement Performance

In addition to evaluating the sensitivity of pavement response to axle loads, axle configurations, layer moduli, and layer thicknesses, the sensitivity of predicted pavement performance to these design variables was examined. Even though pavement response is correlated with pavement performance, the relationship between these two variables is usually nonlinear, and it is therefore important to evaluate the sensitivity of predicted pavement performance separately. For this evaluation, performance estimates were calculated using several existing models in order to determine whether the effects of the design variables vary depending on the performance model used. The prediction equations selected for this study were (*a*) the simplified rational pavement design (SRPD) performance equation developed by Luhr (*4*); (*b*) the Shell performance models based on subgrade and asphalt strain criteria (*5, 6*); (*c*) the fatigue relationship developed by ARE for FHWA (*7*); and (*d*) the performance model developed for the Pennsylvania load limit analysis procedure (*8*). All of these models use multilayer linear elastic theory for evaluating pavement response parameters used in predicting pavement performance.

Figure 12 shows a summary of the performance prediction equations considered for this particular study. The fatigue relationships developed by Shell for pavement design

A. SRPD model:

$$\log_{10} N_x = 2.15122 - 597.662\ (\varepsilon_{sg}) - 1.32967 \log_{10}(\varepsilon_{sg}) + \log_{10}[(PSI_i - TSI)/2.7]^{1/2}$$

where

N_x = number of weighted applications of axle load x before pavement reaches a specified terminal serviceability index (TSI),
ε_{sg} = subgrade compressive strain due to axle load x,
PSI_i = initial present serviceability index of pavement, and
TSI = terminal serviceability index.

B. Shell model based on subgrade strain:

$$\varepsilon_{sg} = 0.028\ N^{-0.25}$$

where ε_{sg} is permissible compressive strain in subgrade and N is number of strain repetitions.

C. ARE model:

$$W_{18} = 9.73 \times 10^{-15}\ (1/\varepsilon_t)^{5.16}$$

where W_{18} is weighted 18-kip applications before Class 2 cracking and ε_t is tensile strain at the bottom of the asphalt surface layer.

D. Performance model for Pennsylvania load limit analysis procedure:

$$\log_{10} N_x = 4.508 - 436.992\ (\varepsilon_{sg}) + 0.092\ (H_2 + H_3) + 0.141\ (PSI_i * TSI) - 0.014\ [TSI(H_1 + H_2 + H_3)] + 3.382 \log_{10}(H_1 + H_2) - 0.319 \log_{10}[(PSI_i * H_2) + 1] - 1.987 \log_{10}(TSI * H_1) - 0.299 H_2 - 0.00018P + 0.041\ (H_1 * H_2)$$

where

N_x = number of applications of axle load x,
ε_{sg} = maximum subgrade vertical strain,
H_1 = surface layer thickness (inches),
H_2 = base layer thickness (inches),
H_3 = subbase layer thickness (inches),
PSI_i = current present serviceability index,
TSI = terminal serviceability index, and
P = load per tire (lb).

FIGURE 12 Performance models used in the sensitivity analysis.

purposes are shown in Figure 13. Two sets of fatigue curves for two different asphalt fatigue characteristics ($F1$ and $F2$), are shown in the figure. As a general guide, the $F1$ curves are indicative of the fatigue characteristics of asphalt mixes with moderate bitumen and voids content, and the $F2$ curves characterize the fatigue performance of mixes with relatively higher voids content (*6*).

Strain data generated in the sensitivity analysis of pavement response were used in the selected performance models to determine performance estimates for various combinations of the independent variables included in the study. The independent variables considered were load, surface modulus ($E1$), base modulus ($E2$), subgrade modulus ($E3$), surface thickness ($T1$), and base thickness ($T2$). Only one type of axle configuration (single axle) was considered because the results presented previously indicated that this factor has no significant effect as long as the load per tire is constant.

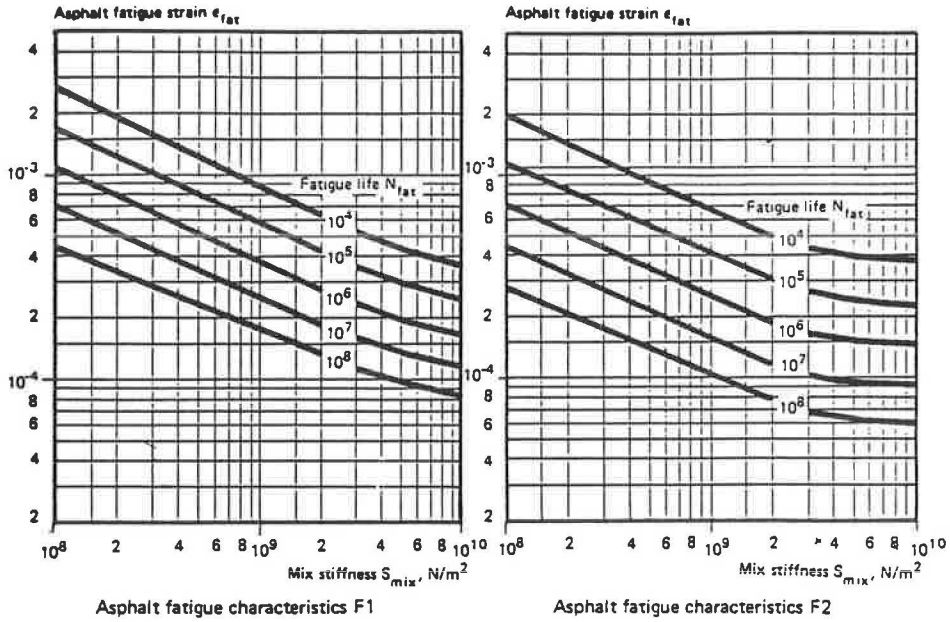

FIGURE 13 Shell fatigue relationships for flexible pavement design (*6*).

As was the case in the sensitivity analysis for pavement response, each of the independent variables considered was varied from low to high levels while the other independent variables were kept at one level (low, middle, or high). Figures 14-18 show the effect of each of the six independent variables on the performance estimates calculated from the prediction equations. Each figure shows the change in the predicted number of applications to failure when each independent variable is varied from low to high levels while all other variables are kept at middle levels. The vertical line in each of the figures indicates the value for predicted performance when all variables are held at middle levels. The bar charts give a fairly good indication of the sensitivity of predicted pavement performance to variations in any one of the independent variables for an average set of conditions.

From the figures, it can be observed that predicted pavement performance is quite sensitive to load; to surface thickness; and, to a lesser degree, to the surface modulus and the subgrade modulus. The effect of the base modulus is relatively small for performance models based on subgrade strain, but it is relatively significant for performance models based on asphalt tensile strain. In addition, the effect of base thickness is minor for performance models based on subgrade strain, with the possible exception of the prediction equation developed for the Pennsylvania load limit analysis procedure. The results therefore indicate that the sensitivity of predicted performance to the different independent variables can vary according to the model used. In addition, performance predictions are also affected by performance criteria. For the conditions considered, the predicted number of applications to failure using asphalt strain are less than for those performance models based on subgrade strain. It should be recognized, however, that the subgrade strain models may govern in other cases. Consequently, for the development of a load limit analysis procedure, it may be important to consider different performance criteria in order to determine the appropriate load restrictions for different pavement structures.

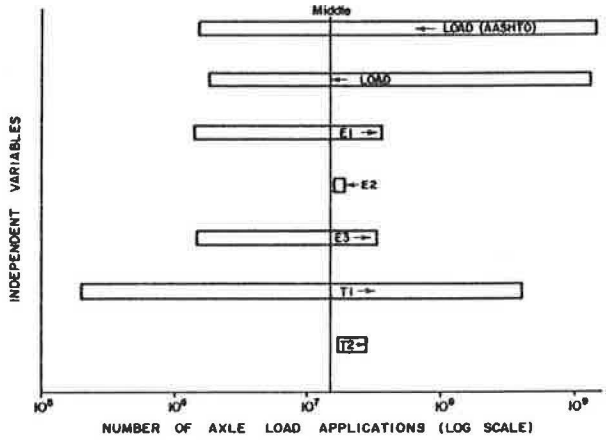

FIGURE 14 Change in applications to failure when each factor is varied from low to high levels, with all other factors at middle levels (Shell model based on subgrade strain).

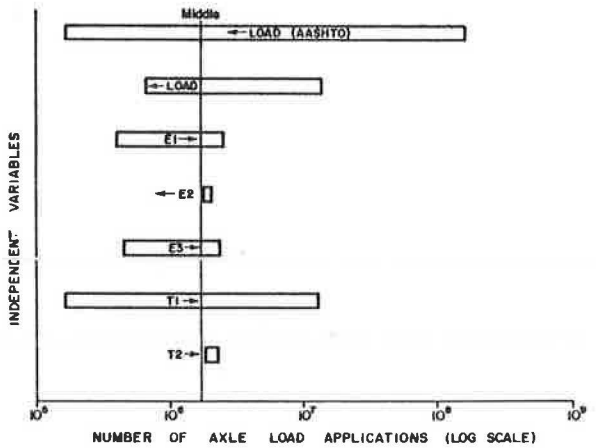

FIGURE 15 Change in applications to failure when each factor is varied from low to high levels, with all other factors at middle levels (SRPD model).

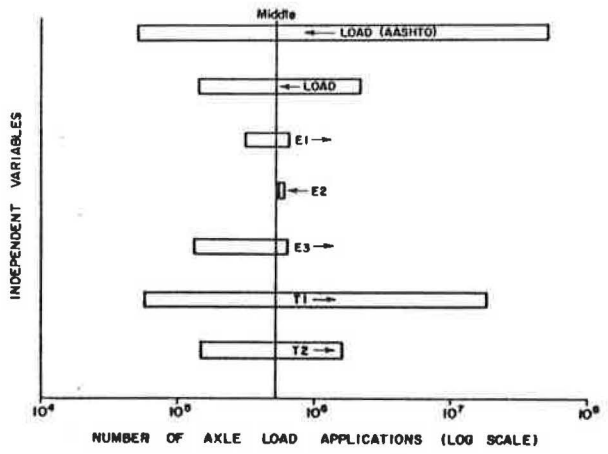

FIGURE 16 Change in applications to failure when each factor is varied from low to high levels, with all other factors at middle levels (Pennsylvania load limit performance equation).

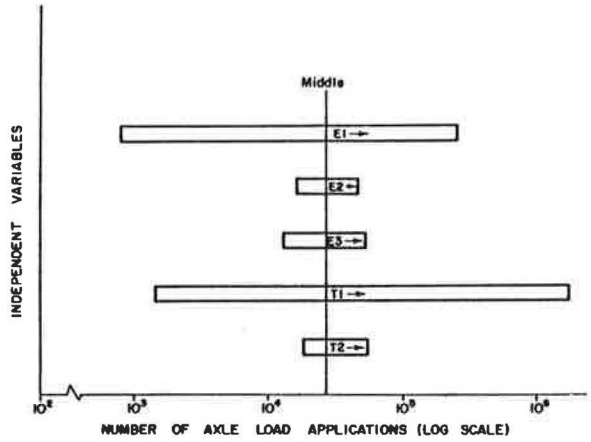

FIGURE 17 Change in applications to failure when each factor is varied from low to high levels, with all other factors at middle levels (ARE model).

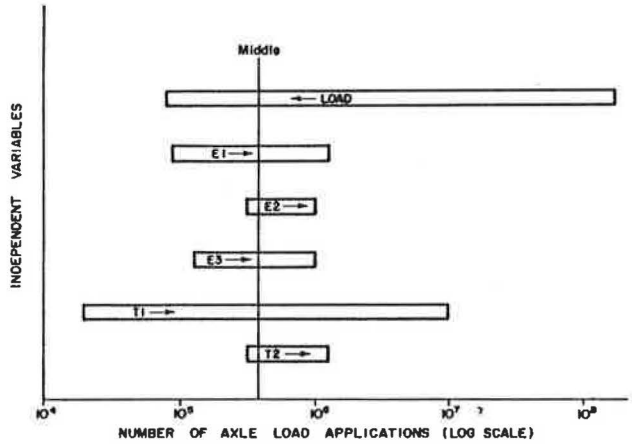

FIGURE 18 Change in applications to failure when each factor is varied from low to high levels, with all other factors at middle levels (Shell fatigue performance relationships).

EVALUATION OF AXLE LOAD EQUIVALENCE FACTORS

Figures 14-16 also show the sensitivity of performance predictions to load when AASHTO equivalence factors are used to determine the predicted number of applications to failure. As mentioned previously, the vertical line in each figure shows the value for the predicted number of allowable load applications when all variables considered are at middle levels. Inasmuch as an 18,000-lb axle load represents the middle level for the load factor at the single-axle configuration (Table 1), the vertical line also indicates the predicted number of allowable 18-kip applications. By using the AASHTO equivalence factor for 6-kip and 30-kip single-axle loadings, the equivalent number of 6-kip and 30-kip load applications corresponding to the predicted number of allowable 18-kip applications can be determined. The use of AASHTO equivalence factors with the performance predictions from models based on subgrade strain is appropriate because all three models (i.e., Shell, SRPD, Pennsylvania load limit equation) were developed from AASHO Road Test data using Present Service Index (PSI) as the performance criterion. The horizontal bars [labeled "LOAD (AASHTO)"] at the top of Figures 14-16 show the effect of load on predicted performance as determined from the AASHTO equivalence factors.

It may be observed from Figure 14 that, for the case in which factors are at middle levels, the performance predictions from the Shell model based on subgrade strain agree reasonably well with the predictions using the AASHTO equivalence factors. In contrast, the predictions from the other two performance models based on subgrade strain show significant differences (Figures 15 and 16). For these models, the predicted number of 6-kip applications to failure is much less than that determined using the AASHTO equivalence factor for a 6-kip single-axle loading. However, the predicted number of allowable 30-kip applications is greater than that determined using the appropriate equivalence factor that, for a 30-kip single-axle loading, has a mean value of about 9.0 for a range of structural numbers.

The AASHTO equivalence factors, calculated from the AASHTO performance equation, do not vary significantly with structural number. This is seen in Table 2, which gives the means and the standard deviations of calculated equivalence factors for a range of structural numbers from 1.0 to 6.0. In contrast, the equivalence factors calculated from observed AASHTO performance data show much more variability, as shown in Figure 19. The equivalence factors based on observed data were determined by analyzing identical pavement sections that carried different loads at the AASHO Road Test. For any particular pavement structure, equivalence factors were calculated using the following equation:

$$e_x = \frac{N_{18}}{N_x} \tag{2}$$

where

TABLE 2 MEANS AND STANDARD DEVIATIONS OF EQUIVALENCE FACTORS CALCULATED FROM AASHTO PERFORMANCE EQUATION

	Terminal Serviceability Index			
	2.0		2.5	
Single-Axle Load (kips)	Mean	Standard Deviation	Mean	Standard Deviation
6	0.01	0.001	0.01	0.003
12	0.18	0.008	0.20	0.019
24	3.48	0.125	3.20	0.262
30	9.28	0.620	8.07	1.240

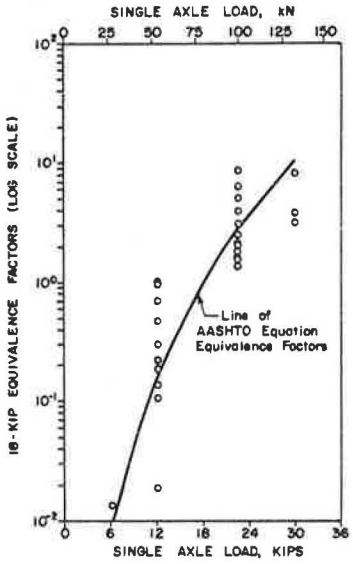

FIGURE 19 Measured and AASHTO-calculated 18-kip equivalence factors for single-axle loads.

e_x = equivalence factor for axle load x,
N_{18} = number of 18-kip applications required for a particular pavement structure to reach a specified value or PSI, and
N_x = number of applications of load x required for the pavement structure to reach the same value of PSI.

The means and standard deviations of equivalence factors determined from observed data for 6-, 12-, 22.4-, and 30-kip single-axle loads are given in Table 3.

To evaluate the sensitivity of performance predictions to a wide range of pavement designs, 18-kip equivalence factors for 6-, 12-, 24-, and 30-kip single-axle loadings were calculated for each combination of layer moduli and thicknesses included in the load limit factorial study. Inasmuch as comparisons are being made relative to AASHTO equivalence factors, the performance equations based on subgrade strain were used in the calculations. As mentioned previously, these models were developed using AASHO Road Test data with PSI as the performance criterion. Table 4 gives the means and standard deviations of the equivalence factors obtained.

It may be observed from the table that the variability in the calculated equivalence factors from the performance models based on subgrade strain is greater than the variability found in the equivalence factors determined using the AASHTO performance equation (Table 2). However, it should be recognized that the statistics presented are for a broad range of pavement designs, and the variability obtained simply reflects the sensitivity of the performance predictions to different designs. That AASHTO equivalence factors show relatively small variations for a range of structural numbers indicates that the AASHTO equivalence factors are not as sensitive to different pavement designs as are those from the other performance models considered. For a terminal serviceability index of 1.5, and for any given axle loading, the AASHTO equivalence factors do not vary with structural number, as determined from the following equations used to calculate AASHTO equivalence factors (*9*):

$$\log_{10}\frac{W_{t_x}}{W_{t_{18}}} = 4.79 * \log_{10}(18 + 1) - 4.79 * \log_{10}(L_x + L_2) + 4.33 * \log_{10}L_2 + \frac{G_t}{\beta_x} - \frac{G_t}{\beta_{18}} \quad (3)$$

$$G_t = \log_{10}\left[\frac{4.2 - p_t}{4.2 - 1.5}\right] \quad (4)$$

$$\beta = 0.40 + \frac{0.081 * (L_x + L_2)^{3.23}}{(SN + 1)^{5.19} * L_2^{3.23}} \quad (5)$$

where

L_x = load on one single-axle or one tandem-axle set (kips),
L_2 = axle code (1 for single axle and 2 for tandem axle),

TABLE 3 MEANS AND STANDARD DEVIATIONS OF EQUIVALENCE FACTORS DETERMINED FROM OBSERVED AASHO ROAD TEST DATA

	Terminal Serviceability Index			
	2.0		2.5	
Single-Axle Load (kips)	Mean	Standard Deviation	Mean	Standard Deviation
6	0.01		0.01	
12	0.43	0.36	0.40	0.35
22.4	3.81	3.47	4.03	2.86
30	4.66	2.02	6.23	3.01

TABLE 4 MEANS AND STANDARD DEVIATIONS OF EQUIVALENCE FACTORS DETERMINED FROM PERFORMANCE MODELS BASED ON SUBGRADE STRAIN

	Single-Axle-Load (kips)							
	6		12		24		30	
Performance Model	Mean	Standard Deviation	Mean	Standard Deviation	Mean	Standard Deviation	Mean	Standard Deviation
SRPD	0.14	0.06	0.45	0.12	2.11	1.23	4.79	7.38
Shell	0.02	0.02	0.24	0.07	2.81	0.43	6.27	1.55
Pennsylvania load limit equation	0.19	0.07	0.43	0.10	2.48	1.00	6.59	6.63

SN = structural number,
p_t = terminal serviceability, and
β_{18} = value of β_x when L_x is equal to 18 and L_2 is equal to 1.

From Equation 3, it is seen that, for a terminal serviceability index of 1.5, G_t becomes zero and the equivalence factor calculated from Equation 2 becomes only a function of axle load magnitude and axle configuration. This would indicate that the equivalence between an 18-kip single-axle load and any other axle load (L_x) for a terminal serviceability index of 1.5 would be the same for any pavement structure. However, no field data exist to support this conclusion, and as indicated in Figure 19, there is a wide range in the observed AASHTO equivalence factors for the axle loads considered in the AASHO Road Test. Consequently, in view of the relative insensitivity of AASHTO equivalence factors to variations in pavement structure, it would be difficult to justify their use for comparing the effects of different axle loads in the evaluation of alternative load limit policies.

SUMMARY AND CONCLUSIONS

The Commonwealth of Pennsylvania has 44,000 mi of roads under its jurisdiction. About two-thirds of these are low-volume roads that, in other states, would be the responsibility of local governments. Because a majority of these low-volume roads have pavements with limited structural capacity, the state has the authority to restrict axle loads if it is believed that those axle loads would result in excessive damage to the pavement structure. A procedure for posting load limits is therefore necessary.

As part of the development of a framework for load limit analysis, an evaluation of the sensitivity of pavement response and predicted performance to different design variables was conducted with a view to establishing guidelines for the development of a procedure for load limit analysis. To evaluate the effect of axle loads under a variety of conditions, a theoretical evaluation was conducted that considered various load magnitudes and configurations for different pavement thicknesses and material properties.

The following conclusions, based on the results of this study, are drawn with regard to load limits for flexible pavements:

1. It was found that axle configuration (i.e., single-, tandem-, and triple-axle assemblies) did not significantly affect pavement response, provided that the load per tire remained the same. Because pavement response is correlated with pavement performance, it can be inferred that axle configuration will not have a significant effect on performance as long as the load per tire is constant. Performance data from the AASHO Road Test tend to confirm this theoretical inference. In view of this finding, the determination of load limits based on load per tire is recommended.
2. The results of the analysis show that the sensitivity of predicted performance to the different design variables

considered in the study can vary for different performance models. Consequently, it is important to evaluate the performance model selected or developed for a load limit analysis procedure in order to determine whether the sensitivity of the model predictions to the design variables is consistent with observed performance data. In addition, it may be important to consider different performance criteria because the critical mode of pavement failure will vary for different pavement structures.

3. An evaluation of the sensitivity of predicted performance to different pavement designs was made by calculating 18-kip equivalence factors for a broad range of pavement structures using different performance models. It was found that calculated AASHTO equivalence factors do not vary significantly for different pavement designs. In contrast, equivalence factors determined from observed AASHO Road Test data, and from the other performance models considered, showed a much wider variation for the range of pavement designs investigated. In view of the relative insensitivity of AASHTO equivalence factors to variations in pavement structure, it would be difficult to justify their use in a load limit analysis procedure for evaluating the effects of different load limit policies. In addition, the equivalence factors calculated from the Pennsylvania load limit procedure are more in agreement with AASHO Road Test data than the AASHTO equivalence factors.

ACKNOWLEDGMENT

This paper is based on results of a project sponsored by the Pennsylvania Department of Transportation and the Federal Highway Administration, U.S. Department of Transportation.

REFERENCES

1. *Maintenance Manual.* Pennsylvania Department of Transportation, Harrisburg, 1985, Chapter 15: Weight Restrictions on Highways (Posted Highways).
2. D. L. De Jong, M. G. F. Peutz, and A. R. Korswagen. *Computer Program BISAR.* External Report. Koninklijke/Shell-Laboratorium, Amsterdam, The Netherlands, 1973.
3. *Special Report 61E: The AASHO Road Test: Report 5—Pavement Research.* HRB, National Research Council, Washington, D.C., 1962.
4. D. R. Luhr, B. F. McCullough, and A. Pelzner. Simplified Rational Pavement Design Procedure for Low-Volume Roads. In *Transportation Research Record 898,* TRB, National Research Council, Washington, D.C., 1983, pp. 202-206.
5. A. I. M. Claessen, J. M. Edwards, P. Sommer, and P. Uge. Asphalt Pavement Design—The Shell Method. *Proc., Fourth International Conference on Structural Design of Asphalt Pavements,* University of Michigan, Ann Arbor, 1977, Vol. 1, pp. 39-74.
6. *Shell Pavement Design Manual: Asphalt Pavements and Overlays for Road Traffic.* Shell International Petroleum Co., London, England, 1978.
7. Austin Research Engineers. *Asphalt Concrete Overlays of Flexible Pavements: Vol. 1—Development of New Design Criteria.* Report FHWA-RD-75-75. FHWA, U.S. Department of Transportation, 1975.
8. E. G. Fernando, D. R. Luhr, and H. N. Saxena. *Development of Guidelines for Posting Load Limits on Pavements.* PTI Report 8525. Pennsylvania Transportation Institute, University Park, 1985.
9. *Guide for Design of Pavement Structures.* American Association of State Highway and Transportation Officials, Washington, D.C., 1986.

Publication of this paper sponsored by Committee on Flexible Pavement Design.

Reliability of the Flexible Pavement Design Model

JOHN C. POTTER

The design of flexible pavements by the U.S. Army Corps of Engineers is currently based on the California bearing ratio (CBR) curve. The CBR curve is empirical, and the current design approach is deterministic. A probabilistic approach, providing more reliable designs at potentially lower costs, can be developed from the current design procedure if the reliability of the CBR curve is known. This study was undertaken to establish the reliability of the current CBR-based flexible pavement design model using existing data from accelerated traffic tests. The reliability of the design model was found to be about 50 percent, excluding the effects of conservative estimates of the design parameters.

The design of flexible pavements by the U.S. Corps of Engineers is currently based on the California bearing ratio (CBR) equation that was formulated in the 1950s, and extended in the 1970s, on the basis of the results of numerous full-scale accelerated traffic tests. These tests involved full-scale load carts operated on various test section pavements. Both highway vehicles and aircraft landing gears, with a wide variety of contact areas and tire pressures, were represented by the various load cart configurations. The test sections consisted of flexible pavements with many different thicknesses built on subgrades that had a wide range of strengths. The CBR equation is empirical and the design approach is deterministic. A unique pavement system based on a unique set of variables is designed. On the other hand, the design process can be approached probabilistically. This type of approach would allow the design engineer to account for uncertainty in the design variables and to accommodate material variability. The engineer can also ensure a low probability of premature failure, which is to say, a high reliability. Lower costs may be realized by reducing over-conservatism in design in the form of excess wearing course, base, or subbase thickness or by reducing unrealistic estimates of pavement service life. The first step in implementing a probabilistic approach is to establish the accuracy or reliability of the basic design model as a predictor of pavement performance. This reliability is expressed in terms of the probability that the design model will correctly predict the performance of a particular pavement, given a particular set of design variables. However, because the CBR equation is based on a curve fit to the data using subjective engineering judgment, the reliability of this fit is uncertain. This constitutes a serious problem in implementing probabilistic methods in current U.S. Army pavement design procedures.

U.S. Army Engineer Waterways Experiment Station, P.O. Box 631, Vicksburg, Miss. 39180-0631.

REVIEW

The evolution of the flexible pavement design model can be traced through various references that describe the development of the CBR curve. The basic formulation is described in several U.S. Army Engineer Waterways Experiment Station (WES) technical memoranda (*1-3*), technical reports (*4, 5*), a miscellaneous paper (*6*), and instruction reports (*7, 8*) and work by others (*9*). The expansion of the CBR equation to include a term for a particular number of tires in a group is documented by Cooksey and Ladd (*10*) and Ahlvin et al. (*11*). This latter work also included the data generated by accelerated traffic tests with multiple-wheel loads in the late 1960s and early 1970s.

In its current form, the CBR equation is

$$t = \alpha\{A[(p/8.1\ CBR) - (1/\pi)]\}^{1/2} \quad \text{for } CBR/p < 0.22 \tag{1}$$

where

t = pavement thickness (in.),
α = load repetition factor for particular tire group size as a function of traffic volume (discussed later),
A = contact area of one tire (in.^{2}),
p = equivalent single-wheel tire pressure (psi), and
CBR = strength of supporting material.

The curve has a graphic modification that can be described by the quadratic

$$t = \alpha(A\{0.05 - 0.35187 \log(CBR/p) + 0.51492\,[\log(CBR/p)]^2\})^{1/2} \quad \text{for } CBR/p \geq 0.22 \tag{2}$$

The CBR relationship has traditionally been depicted as in Figure 1 (*5*). These plots are characterized by large data scatter. This has been attributed to the effects of variations in the coverages required to produce failure. Here, failure is defined as attaining a maximum rut depth of 1 in., and a coverage is defined as a sufficient number of passes of the design vehicle to cover the entire traffic lane with at least one

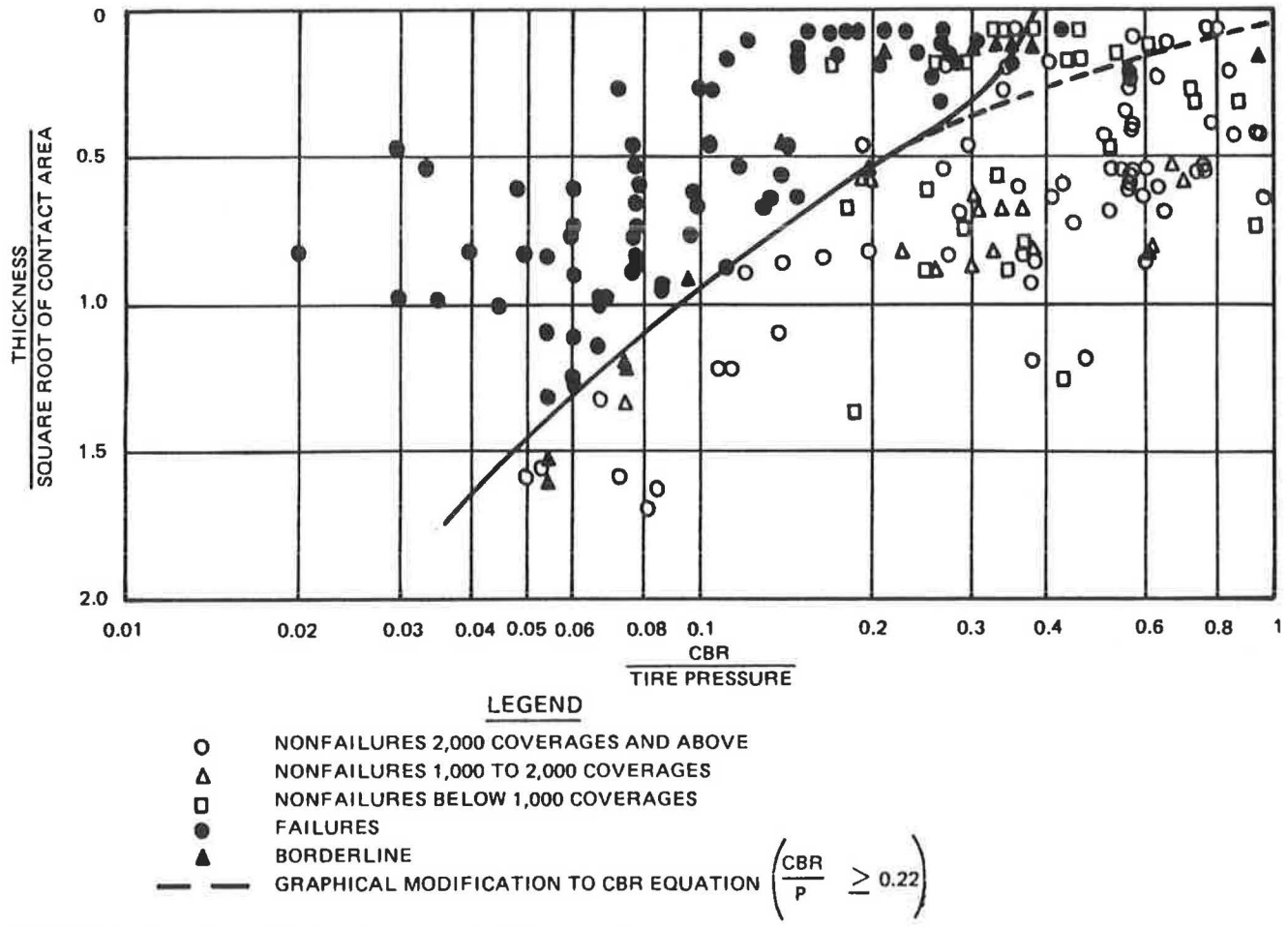

FIGURE 1 Curve from CBR formula compared with behavior data.

wheel load. Because the curve in Figure 1 passes essentially below and to the right of the failure data, it could be argued that the CBR relation is a conservative bound on actual behavior. However, plots such as Figure 1 are misleading in this respect. As noted in Technical Report 3-495 (*5*), the failure points that fall above and to the left of the curve are for coverage levels below 5,000. A review of the tabulated data in Technical Report 3-495 reveals that none of the "failures" shown in Figure 1 are for coverage levels above 5,000. Thus the appropriate conclusion is that the curve in Figure 1 represents the bound for failures (that is, the limit for satisfactory performance) occurring at coverage levels less than 5,000. From the position of the curve with respect to the coverage data, it would appear reasonable that the curve might also be close to the best fit for failure at 5,000 coverages. Variations in traffic volume were considered by adjusting the design thickness by an *f*-factor equal to 0.15 + 0.23 log *C*, where *C* is the total number of coverages of the design vehicle gear (*6*).

Ahlvin et al. (*11*) published an alternate CBR equation resulting from their best fit of a cubic equation to Equations 1 and 2. This equation is

$$t = \alpha(A^{1/2})\{-0.0481 - 1.1562 \log(CBR/p) - 0.6414[\log(CBR/p)]^2 - 0.4730[\log(CBR/p)]^3\} \quad (3)$$

The associated load repetition factor (α) curves, shown in Figure 2, were developed from the data in Table 1. This relationship allows consideration of variations in pass level, gear configuration, and vehicle wander. Here, pass level is defined as the number of movements (passes) of the design vehicle gear past a given point on the pavement. Such considerations are not possible with the basic relationship shown in Figure 1. The data were analyzed separately and weighted on the basis of differences in individual test objectives, failure criteria, methods of determining strength, frequency of field observations and measurements, construction techniques and materials, and methods of applying traffic. This reduced the effects of data scatter and is discussed in some detail by Ahlvin et al. (*11*).

As shown in Figure 3, the CBR curve (Equations 1 and 2) is essentially the same as the regression equation (Equation 3). This implies that the reliability of the two functions is equivalent. The U.S. Corps of Engineers uses these two relationships interchangeably (*8*).

In Technical Report 3-495 (*5*), the effect of multiple-wheel gears was recognized and the multiple-wheel data were reduced to equivalent single-wheel loads (ESWLs) for plotting on Figure 1. The technique for using elastic layer theory to compute the ESWL is described in detail by Ahlvin et al. (*11*). The equivalent single-wheel tire pressure (p) is obtained by dividing the ESWL by the contact area (A) of one tire. Later, Ahlvin et al. (*11*) developed the load repetition (α) factor

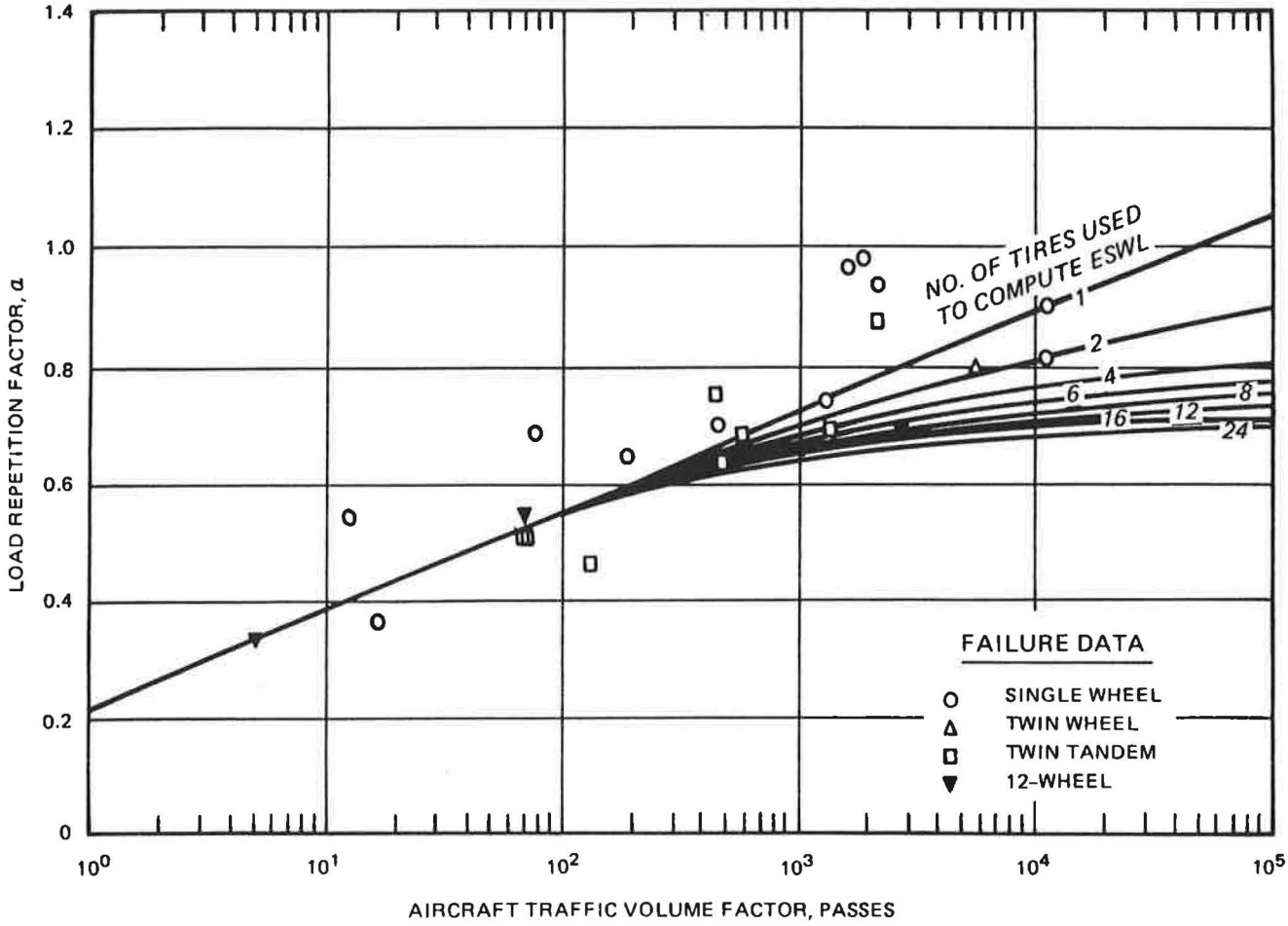

FIGURE 2 Composite plot of load repetitions factor versus passes, after Ahlvin et al. (*11*).

TABLE 1 SELECTED CBR FAILURE DATA

Reference	Gear Type	p(psi)	A(in.^{2})	t(in.)	CBR	C	α	t_{CBR} (in.)	t/t_{CBR}
12	Single	133.2	1,501	39.0	6.0	150	0.645	38.9	1.0025
		133.2	1,501	44.0	9.0	1,700	0.855	40.7	1.0811
		133.2	1,501	18.0	16.0	10	0.405	13.2	1.3616
		133.2	1,501	20.5	18.0	60	0.565	16.9	1.2135
		133.2	1,501	23.5	15.5	360	0.720	24.0	0.9774
		133.2	1,501	30.0	17.5	1,500	0.845	25.8	1.1622
		133.2	1,501	49.0	8.0	1,300	0.830	42.4	1.1559
13	Single	60.0	250	10.0	8.0	3,760	0.915	11.3	0.8867
		60.0	250	10.0	9.0	3,760	0.915	10.3	0.9729
11	Single	175.4	285	15.0	3.7	6	0.350	13.9	1.0790
		175.4	285	24.0	4.4	200	0.670	24.3	0.9889
		105.3	285	15.0	3.7	120	0.625	18.9	0.7955
14	B-29	126.7	330	10.0	20.0	2,000	0.805	10.0	1.0043
	B-36	241.6	262	14.0	16.0	1,000	0.710	14.3	0.9798
15	B-36	318.7	150	16.0	12.0	312	0.645	13.6	1.1772
		318.7	150	16.0	5.0	90	0.565	19.0	0.8415
		318.7	150	16.0	15.0	1,500	0.730	13.6	1.1789
11	B-747	430.3	290	33.0	3.8	40	0.510	32.1	1.0279
		430.3	290	33.0	4.0	40	0.510	31.3	1.0553
		496.6	290	41.0	4.0	280	0.640	42.2	0.9711
11	C-5A	218.5	285	15.0	3.7	8	0.345	15.4	0.9753
		272.8	285	24.0	4.4	104	0.550	25.2	0.9542
		330.9	285	33.0	3.8	1,500	0.670	36.5	0.9032
		330.9	285	33.0	4.0	1,500	0.670	35.6	0.9274

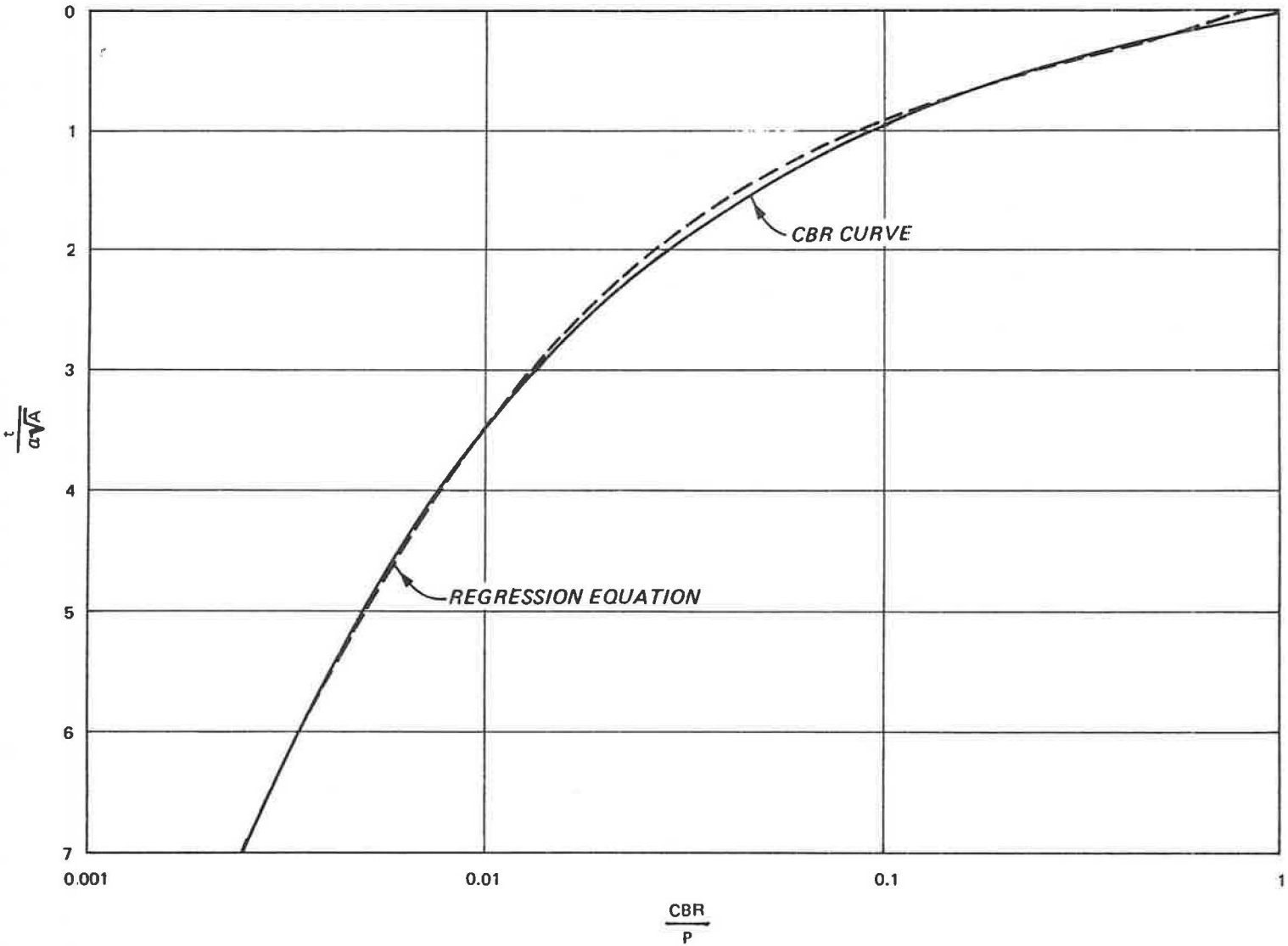

FIGURE 3 Comparison of the CBR curve and the regression equation (*11*).

shown in Equations 1, 2, and 3 to better account for the effects of multiple-wheel loading and to account for variations in traffic volume. Cooksey and Ladd (*10*) developed the α-factor curves shown in Figure 4 in terms of coverages. This is the form currently used by the Corps of Engineers, with Equations 1 and 2 or Equation 3. Because little full-scale accelerated traffic testing has been done since the multiple-wheel, heavy-gear load tests reported by Ahlvin et al. (*11*), these relationships consider essentially all available data.

The α-factor curves developed by Cooksey and Ladd (*10*) are based on the data in Table 1 plus the additional data given in Table 2. Of all available data, only the data in Tables 1 and 2 resulted from subgrade failures, consisted of only one loading condition or intensity, and represented pavements made of accepted construction materials. Only subgrade failures were considered because the thickness design procedure is based on protecting the subgrade from failure. Only those failures produced by one loading condition were considered to eliminate uncertainty introduced by assumptions about the effects of mixed traffic. The design of pavements for different coverage levels is done by changing thickness requirements instead of material requirements. Therefore only data from failures on material meeting quality standards were used.

ANALYSIS

A design thickness (t_{CBR}) can be computed from the CBR equation for each data point in Tables 1 and 2. For example, the first line in Table 1 is from a test section on a 6 CBR subgrade, subjected to 150 coverages of a 133.2-psi, 1,501-in.^{2} single-wheel load. From Figure 4, the α-factor is 0.645. The design thickness calculated using Equation 1 is 38.9 in. This design thickness can then be compared with the actual test section thickness (t) as shown in Figure 5 for all of the data. Note that all points lie close to the line of equality.

The ratio of the actual test section thickness to the design thickness can be used as a measure of correlation. In the previous example, the thickness ratio is 1.0025, meaning that the actual thickness was 0.25 percent greater than that predicted by the CBR equation. The value of this ratio, in general, can be viewed as a random variable, with the ratios tabulated in Tables 1 and 2 being samples from the population. The 28 thickness ratios in Tables 1 and 2 have a mean value (average) (μ) of 1.0053. The standard deviation (σ) is 0.1497.

The reliability of the CBR equation is the probability (P) that the actual test section thickness (t) is less than the design thickness (t_{CBR}). That is,

$$\text{Reliability} = \text{Probability}\ (t \leq t_{CBR}) = P\ [(t/t_{CBR}) \leq 1] \quad (4)$$

Assuming a normal distribution for the ratio of the thickness,

$$\text{Reliability} = \Phi(1 - \mu/\sigma) = \Phi(-0.035) = 48.6 \text{ percent} \quad (5)$$

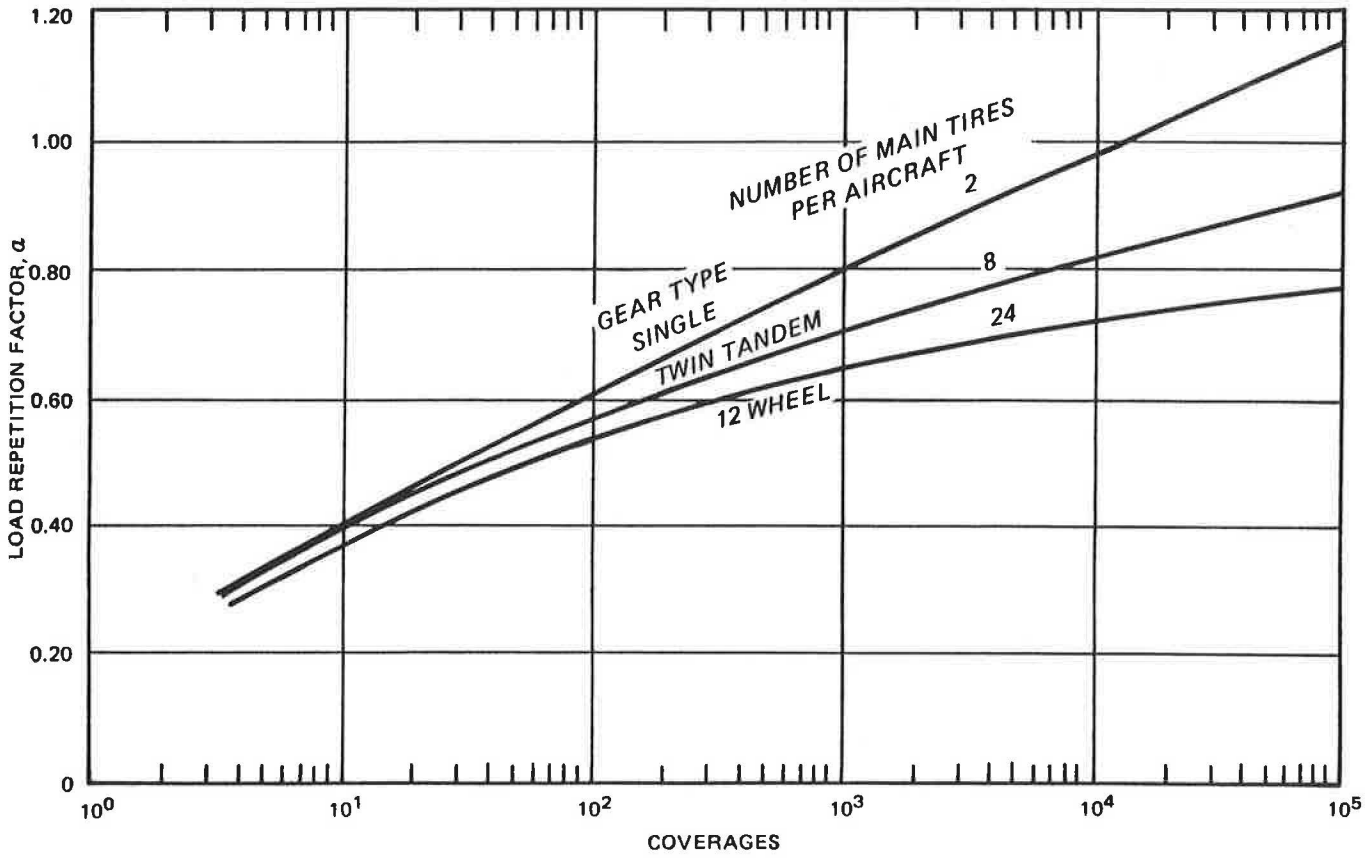

FIGURE 4 Flexible pavement thickness adjustment curves for various landing gears, after Cooksey and Ladd (*10*).

TABLE 2 ADDITIONAL CBR FAILURE DATA

Reference	Gear Type	p(psi)	A(in.^{2})	t(in.)	CBR	C	α	t_{CBR} (in.)	t/t_{CBR}
15	Single	200.0	150	12.0	14.0	216	0.680	10.0	1.1985
		200.0	150	12.0	7.0	178	0.665	14.6	0.8225
		200.0	150	12.0	6.0	203	0.675	16.1	0.7449
16	Single	109.9	91	5.0	6.0	40	0.530	7.0	0.7095

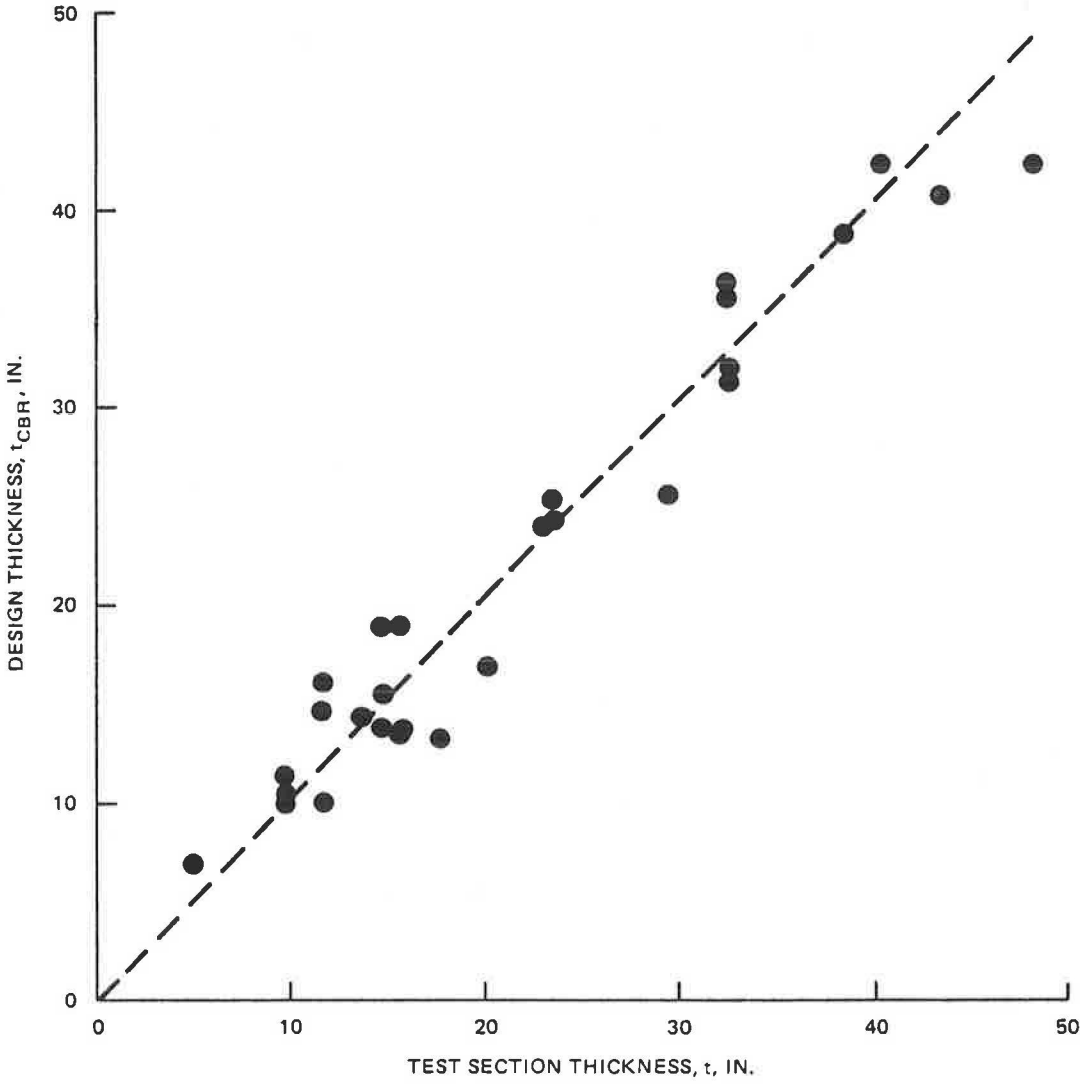

FIGURE 5 Test section thickness versus design thickness.

Because neither of the thicknesses nor their ratio can be negative, the ratio could be log normally distributed. In this case,

$$\text{Reliability} = \Phi(0 - \ln\{\mu/[1 + (\sigma^2/\mu^2)]^{1/2}\}/\{\ln[1 + (\sigma^2/\mu^2)]\}^{1/2}) = \Phi(0.038)$$
$$= 51.5 \text{ percent} \quad (6)$$

Finally, a beta distribution could be fitted to the data, using two other data statistics. The skewness of the data (β_1) (third moment about the mean) is 0.1416 and the kurtosis (β_2) (fourth moment about the mean) is 2.76. The beta distribution fitting these statistics has an alpha value of 7.14 and a beta value of 10.38. The minimum and maximum values of the variate are 0.432 and 1.806, respectively. For this distribution the reliability is

$$\text{Reliability} = P[(t/t_{CBR}) \leq 1] = 49.3 \text{ percent} \quad (7)$$

CONCLUSIONS

The reliability of the U.S. Corps of Engineers flexible pavement design model is about 50 percent. This flexible pavement design model will therefore provide very nearly the best estimate or expected value of the pavement thickness required for the given design parameters, including the

required service life. On the average, about one-half of all pavements designed using this model will fail before the design service life is reached and one-half will continue to perform beyond their design service life.

This reliability statement does not include the difference between the performance of the accelerated traffic test sections and the long-term performance of actual in-service pavements. Also not included are the effects of conservative estimates ("design" values) for the parameters for material strength (CBR), traffic load (p), and traffic intensity (α). Because the soaked CBR or the 15th percentile of the field CBR-values is often used for conservative design, for example, the reliability of the resulting pavement is much greater than 50 percent. This is consistent with the findings of long-term studies of in-service pavements: more than 50 percent are performing beyond their design life. Quantifying the effects on reliability of choosing conservative design values or of uncertainty in the true values of the design parameters is the subject of follow-on work at the Waterways Experiment Station (in publication) by Y. T. Chou.

ACKNOWLEDGMENT

The author is grateful to the U.S. Army Corps of Engineers Waterways Experiment Station for administrative support as well as permission to publish this paper. The views of the author do not purport to reflect the position of the Department of the Army or the Department of Defense.

REFERENCES

1. *Investigation of the Design and Control of Asphalt Paving Mixtures.* Technical Memorandum 3-254, Vol. 1. U.S. Army Engineer Waterways Experiment Station, Vicksburg, Miss., 1948.
2. *Investigation of Pressures and Deflections for Flexible Pavements: Homogeneous Clayey-Silt Test Section.* Technical Memorandum 3-323, Report 1. U.S. Army Engineer Waterways Experiment Station, Vicksburg, Miss., 1951.
3. *Design of Flexible Airfield Pavements for Multiple-Wheel Landing Gear Assemblies, Report No. 2, Analysis of Existing Data.* Technical Memorandum 3-349. U.S. Army Engineer Waterways Experiment Station, Vicksburg, Miss., 1955.
4. *Mathematic Expression of the CBR Relations.* Technical Report 3-441. U.S. Army Engineer Waterways Experiment Station, Vicksburg, Miss., 1956.
5. *Combined CBR Criteria.* Technical Report 3-495. U.S. Army Engineer Waterways Experiment Station, Vicksburg, Miss., 1959.
6. *Collection of Letter Reports on Flexible Pavement Design Curves.* Miscellaneous Paper 4-61. U.S. Army Engineer Waterways Experiment Station, Vicksburg, Miss., 1951.
7. *Developing a Set of CBR Design Curves.* Instruction Report 4. U.S. Army Engineer Waterways Experiment Station, Vicksburg, Miss., 1959.
8. A. T. Pereira. *Procedures for Development of CBR Design Curves.* Instruction Report S-77-1. U.S. Army Engineer Waterways Experiment Station, Vicksburg, Miss., 1977.
9. R. E. Kerkhoven and G. M. Dorman. *Some Consideration on the California Bearing Ratio Method for the Design of Flexible Pavements.* Shell Research Center, London, England, 1953.
10. D. L. Cooksey and D. M. Ladd. *Pavement Design for Various Levels of Traffic Volume.* Technical Report AFWL-TR-70-133. Air Force Weapons Laboratory, Kirtland Air Force Base, N. Mex., 1971.
11. R. G. Ahlvin, H. H. Ulery, Jr., R. L. Hutchinson, and J. L. Rice. *Multiple-Wheel Heavy Gear Load Pavement Tests,* Vol. 1: *Basic Report.* Technical Report S-71-17. U.S. Army Engineer Waterways Experiment Station, Vicksburg, Miss., 1971.
12. O. J. Porter and Company, Consulting Engineers. *Accelerated Traffic Test at Stockton Airfield, Stockton, California (Stockton Test 2).* U.S. Army Engineer District, Sacramento, Calif., 1948.
13. *Flexible Pavement Behavior Studies.* Interim Report 2. U.S. Army Engineer Waterways Experiment Station, Vicksburg, Miss., 1947.
14. *Design of Flexible Airfield Pavements for Multiple-Wheel Landing Gear Assemblies, Test Section with Lean Clay Subgrade.* Technical Memorandum 3-349, Report 1. U.S. Army Engineer Waterways Experiment Station, Vicksburg, Miss., 1952.
15. *Investigation of Effects of Traffic with High-Pressure Tires on Asphalt Pavements.* Technical Memorandum 3-312. U.S. Army Engineer Waterways Experiment Station, Vicksburg, Miss., 1950.
16. *A Limited Study of Effects of Mixed Traffic on Flexible Pavements.* Technical Report 3-587. U.S. Army Engineer Waterways Experiment Station, Vicksburg, Miss., 1962.

Publication of this paper sponsored by Committee on Flexible Pavement Design.

Analytical Evaluation of Variables Affecting Surface Wave Testing of Pavements

IGNACIO SANCHEZ-SALINERO, JOSE M. ROESSET, KO-YOUNG SHAO, KENNETH H. STOKOE II, AND GLENN J. RIX

Spectral-Analysis-of-Surface-Waves (SASW) is a promising nondestructive technique for evaluating the mechanical properties of pavement systems and soil deposits. In applying the technique, it is assumed that only plane Rayleigh waves are generated by the source. In reality, when an impulse is applied at the top of a layered system, body waves (shear and compression waves) and other types of surface waves are produced along with Rayleigh waves. In this paper, the dispersion curves (frequency or wavelength versus phase velocity) obtained by assuming only plane Rayleigh waves are compared with dispersion curves obtained when all types of waves are considered. Several cases with different types of layering are studied, and emphasis is placed on typical pavement systems. It is found that the receiver arrangement can significantly influence the dispersion curve and, hence, the resulting modulus profile. For a typical SASW setup in which the distance from the source to the first receiver is kept equal to the distance between the two receivers, wavelengths considered during analysis of the field data should be equal to or less than one-half of the distance between receivers. If this filtering of low frequencies is not performed, the assumption that only plane Rayleigh waves propagate through the medium can lead to errors when backcalculating physical properties from the dispersion curve.

Spectral-Analysis-of-Surface-Waves (SASW) is a nondestructive technique used to evaluate elastic modulus profiles of soil and pavement systems. The method is a modification of the Steady-State-Rayleigh-Wave method that was introduced in the 1950s for measurement of thicknesses and elastic properties of road pavements and soil deposits (*1-6*). Recently the technique has been improved and simplified by the development of digital dynamic signal analyzers (*7-9*).

In the original technique, a steady-state vibrator acting vertically on the surface of the soil or pavement system produced vibrations of a known frequency that propagated along the surface. A vertically oriented sensor (velocity transducer or accelerometer) was moved progressively away from the vibrator and successive positions were found at which surface motions were in phase with the vibrator. The distance between any two of these successive positions corresponds to one wavelength (λ) of the propagating wave. Because the frequency of vibration (f) was known, the velocity of the wave propagating at that frequency could be calculated as

$$V = \lambda \cdot f \tag{1}$$

By repeating this process for different excitation frequencies, a plot of velocity versus frequency (or wavelength) was obtained. Such a plot is known as a dispersion curve.

Most of the energy generated by a vertically acting, surface vibrator is transmitted to the soil or pavement system in the form of Rayleigh waves (surface waves). Body waves (compression and shear waves) are also generated by this source, but, because body waves attenuate more rapidly than the Rayleigh waves near the surface, it is assumed that at large distances from the source the energy carried by the body waves is insignificant compared with that transmitted by the Rayleigh waves. The dispersion curve obtained is therefore assumed to be a curve of phase velocities of Rayleigh waves versus frequency.

The premise underlying the surface wave method is that the propagation velocity of Rayleigh waves is affected primarily by the properties of the upper part of the soil or pavement. The depth of this upper part "sampled" by the waves depends on the frequency of the waves. It is assumed that the bulk of the Rayleigh wave energy travels through a zone about one wavelength deep. By assuming that the velocity obtained at a particular frequency is representative of the properties at a depth of one-half the wavelength, a plot of Rayleigh wave velocities with depth (rather than wavelength) could be obtained. This hypothesis, used in the early stages of the method, is only a rough approximation because the properties of materials above and below a depth of one-half of a wavelength indeed affect the propagation velocity at that frequency. The assumption is, however, fairly good for materials with moduli varying only slightly and smoothly with depth. Shear wave velocity may be obtained from the Rayleigh wave velocity by assuming a Poisson's ratio. The ratio of Rayleigh wave velocity to shear wave velocity varies from 0.874 for a Poisson's ratio of 0.0 to 0.955 for a Poissons's ratio of 0.5. For most practical applications this ratio can be considered equal to 0.92.

I. Sanchez-Salinero, J. M. Roesset, K. H. Stokoe II, and G. J. Rix, Civil Engineering Department, University of Texas at Austin, Austin, Tex. 78712. Current address for Sanchez-Salinero: GEOCISA, Los Llanos de Jerez, 10, Coslada-Madrid, Spain. K.-Y. Shao, Harza Engineering Co., 150 South Wacker Drive, Chicago, Ill. 60606.

If the density (ρ) and Poisson's ratio (ν) of the material are known, the shear modulus (G) and Young's modulus of elasticity (E) can be obtained as

$$G = \rho v_S^2 \tag{2}$$

$$E = 2G(1 + \nu) \tag{3}$$

and a profile of modulus of elasticity versus depth can then be constructed.

The steady-state process is easy to understand and to perform, but field testing can be quite time consuming. In addition, a rigorous inversion process to backcalculate the elastic properties is required for use with pavement systems because the moduli of pavement systems do not vary smoothly with depth.

With the development of digital electronic equipment in the 1970s, the Rayleigh wave procedure regained popularity. Instead of a steady-state vibrator at a fixed frequency, an impulsive or random noise load is applied at the surface of the soil or pavement. Two vertical receivers located on the surface are used to monitor the wave train generated by the source as it passes by them, as shown in Figure 1. The electrical signals produced by the receivers are digitized and recorded by a dynamic signal analyzer. The time signals recorded are transformed to the frequency domain using a fast Fourier transform algorithm, and the phase difference (ϕ) between the two signals is calculated for each frequency. A travel time (t) between receivers can be obtained for each frequency by

$$t = \phi / 2\pi f \tag{4}$$

where the phase difference (ϕ) is in radians and the frequency (f) is in cycles per second. Because the distance between receivers (d) is known, a velocity is calculated as

$$V = d/t \tag{5}$$

Details of the process can be found elsewhere (*7-10*).

One of the advantages of the SASW method with respect to the Steady-State-Surface-Wave method is that substantially less time is required in the field. Because impulsive or random noise signals contain a very broad range of frequencies, all information needed can be obtained simultaneously.

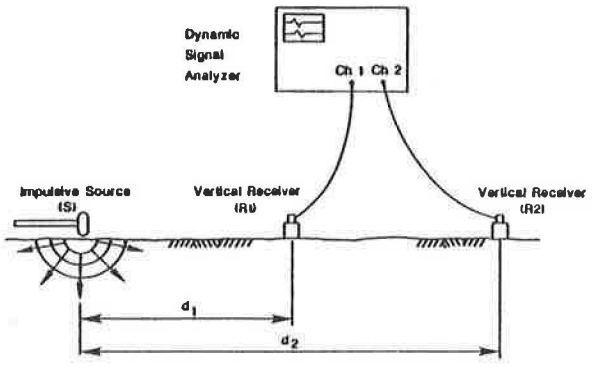

FIGURE 1 Schematic diagram of SASW method.

Another significant improvement of the SASW method is obtained by inverting the dispersion curve. In the inversion process, the elastic properties of the different layers are backcalculated by matching a theoretical dispersion curve to the experimental dispersion curve obtained in the field. An iterative procedure based on forward modeling is given by Nazarian (*10*).

There are still several approximations in the SASW method. That body waves are not considered in the method presents one of the major uncertainties. It is also not clear which arrangement of source and receivers should be used to obtain the best results. To better understand the method, a series of analytical studies that simulate the testing procedure has been performed and is presented herein. The procedures used to calculate plane Rayleigh wave dispersion curves and dispersion curves generated by a point load are presented first. The former method assumes that only Rayleigh waves propagate in the medium whereas the latter method also includes the effect of body waves. Dispersion curves obtained using both methods are then compared. Finally, an alternate method to that suggested by Nazarian (*10*) for backcalculating the elastic properties from a dispersion curve is presented. This alternate method has the advantage of being easily automated.

DISPERSION OF PLANE RAYLEIGH WAVES

The plane Rayleigh wave dispersion curve can be calculated using wave propagation theory. The mathematical model consists of a horizontally layered half-space with properties varying from one layer to another but constant within each layer. The waves are assumed to be propagating in the x-z plane. The differential equations for each layer in terms of displacement potentials can be expressed as

$$\frac{\partial^2 \phi}{\partial t^2} = v_p^2 \left(\frac{\partial^2 \phi}{\partial x^2} + \frac{\partial^2 \phi}{\partial z^2} \right) \tag{6}$$

$$\frac{\partial^2 \psi}{\partial t^2} = v_s^2 \left(\frac{\partial^2 \psi}{\partial x^2} + \frac{\partial^2 \psi}{\partial z^2} \right) \tag{7}$$

where

ϕ and ψ = displacement potentials,

$$v_s^2 = G/\rho, \tag{8}$$

$$v_p^2 = 2G(1 - \nu)/\rho(1 - 2\nu), \tag{9}$$

$G = E/[1(1 + \nu)]$ is the shear modulus of the layer, (10)

ρ = density of the layer, and

ν = Poisson's ratio.

The displacements in the x- and z-directions can be expressed in terms of displacement potentials as

$$u = \frac{\partial \phi}{\partial x} - \frac{\partial \psi}{\partial z}$$, where u is the displacement in the x-direction and (11)

$$w = \frac{\partial \phi}{\partial z} + \frac{\partial \psi}{\partial x}$$, where w is the displacement in the z-direction. (12)

Solutions to Equations 6 and 7 are of the form

$$\phi = (a\, e^{imz} + c\, e^{-imz})\, e^{i(kx-\omega t)} \quad (13)$$

$$\psi = (b\, e^{inz} + d\, e^{-inz})\, e^{i(kx-\omega t)} \quad (14)$$

where ω, k, m, and n are constants satisfying the relations

$$k^2 + m^2 = \omega^2/v_p^2 \quad (15)$$

$$k^2 + n^2 = \omega^2/v_s^2 \quad (16)$$

and where

i = $\sqrt{-1}$
ω = frequency in rad/sec, and
a, b, c, and d = constants of integration.

The quotient of the frequency and the wave number in the x-direction (k) is the phase velocity of the wave in the x-direction:

$$V = \omega/k \quad (17)$$

When the values of m and n are imaginary numbers, Equations 13 and 14 represent waves that propagate in the x-direction and whose amplitude decays in the z-direction. This type of wave is called a Rayleigh wave.

The stresses on a horizontal plane can be expressed in terms of displacements as

$$\tau_{xz} = G\left(\frac{\partial u}{\partial z} + \frac{\partial w}{\partial x}\right) \quad (18)$$

$$\sigma z = 2G\left[\frac{\nu}{1-2\nu}\left(\frac{\partial u}{\partial x} + \frac{\partial w}{\partial z}\right) + \frac{\partial w}{\partial z}\right] \quad (19)$$

By substituting Equations 13 and 14 into Equations 11 and 12 and, subsequently, substituting into Equations 18 and 19, the stresses and displacements at the top of the layer can be expressed in terms of the stresses and displacements at the bottom of the layer after the constants of integration are eliminated. For any layer (j) this relationship can be expressed as

$$\begin{bmatrix} U_h \\ S_h \end{bmatrix}_j = [T]_j \begin{bmatrix} U_o \\ S_o \end{bmatrix}_j \quad (20)$$

where

$$U = \begin{bmatrix} u \\ w \end{bmatrix}$$ and

$$S = \begin{bmatrix} \tau_{xz} \\ \sigma_z \end{bmatrix}$$

and the subscripts h and o indicate bottom and top of layer, respectively. Matrix $[T]$ is called a transfer or propagator matrix because it gives displacements and stresses at the bottom of the layer in terms of displacements and stresses at the top of the layer. Expressions for the elements of matrix $[T]$ can be found elsewhere (*11, 12*).

The compatibility of displacements and stresses at the interface of any two adjacent layers can be written as

$$\begin{bmatrix} U_h \\ S_h \end{bmatrix}_j = \begin{bmatrix} U_o \\ S_o \end{bmatrix}_{j+1} \quad (21)$$

which substituted in Equation 20 results in

$$\begin{bmatrix} U_o \\ S_o \end{bmatrix}_{j+1} = [T]_j \begin{bmatrix} U_o \\ S_o \end{bmatrix}_j \quad (22)$$

If the process is repeated for all of the layers, a relationship can be obtained between the displacements and stresses at the surface of the layered system and those at any depth:

$$\begin{bmatrix} U_o \\ S_o \end{bmatrix}_{n+1} = [T]_n [T]_{n-1} \cdots [T]_1 \begin{bmatrix} U_o \\ S_o \end{bmatrix}_1 \quad (23)$$

If layer $n + 1$ is considered to be a half-space, an equation relating displacements and stresses at the top of the half-space with the amplitudes of the upward and downward propagating waves in the half-space can be written as

$$\begin{bmatrix} U_o \\ S_o \end{bmatrix}_{n+1} = [H]_{n+1} \begin{bmatrix} A \\ B \\ C \\ D \end{bmatrix}_{n+1} \quad (24)$$

where A and B, and C and D, are proportional to the amplitudes of the waves propagating in the downward and upward directions, respectively, in the half-space.

Substituting Equation 24 into Equation 23 results in

$$\begin{bmatrix} A \\ B \\ C \\ D \end{bmatrix}_{n+1} = \left[\begin{array}{c|c} L_{11} & L_{12} \\ \hline L_{21} & L_{22} \end{array}\right] \begin{bmatrix} U_o \\ S_o \end{bmatrix}_1 \tag{25}$$

where matrix $[L]$ is a 4×4 matrix

$$[L] = [H]^{-1}_{n+1} [T]_n [T]_{n-1} \cdots [T]_1 \tag{26}$$

To obtain the natural modes of vibration, no forces are applied at the top of the layered system ($S_{o_1} = 0$) and no waves are assumed to travel upward in the half-space ($C_{n+1} = D_{n+1} = 0$). This leads to the system of equations

$$\begin{bmatrix} A \\ B \\ 0 \\ 0 \end{bmatrix}_{n+1} = \left[\begin{array}{c|c} L_{11} & L_{12} \\ \hline L_{21} & L_{22} \end{array}\right] \begin{bmatrix} U_o \\ 0 \end{bmatrix}_1 \tag{27}$$

To have other than a trivial solution, the determinant of the submatrix L_{21} must be set equal to zero.

$$|L_{21}| = 0 \tag{28}$$

This equation, called the characteristic equation, relates frequency (ω) with phase velocity (V). At any frequency there may be several values of velocity that satisfy this equation. Each value of velocity corresponds to a different mode of propagation and defines a different dispersion curve. A dispersion curve obtained in the field is a combination of different modes of propagation, but it is usually assumed that for shallow sources the major contribution is provided by the first mode.

This procedure was first explained by Thomson (*11*) and Haskell (*12*) and has been the basis of many studies on wave propagation through layered systems in recent years. An alternate method for computing the modes of propagation and dispersion curves can be obtained by using the layer stiffness matrices suggested by Kausel and Roesset (*13*).

Equation 20 can be rearranged so that forces are given in terms of displacements as

$$\begin{bmatrix} S_o \\ S_h \end{bmatrix}_j = [K]_j \begin{bmatrix} U_o \\ U_h \end{bmatrix}_j \tag{29}$$

where $[K]$ is similar to a stiffness matrix. Expressions for the elements of $[K]$ can be found elsewhere (*13*).

By assembling the stiffness matrices of all of the layers (Equation 29), a global stiffness matrix for the complete layered system can be obtained. This global stiffness matrix relates forces per unit area to the displacements at the interfaces between layers. For the half-space, the stiffness matrix directly relates stresses and displacements at the top surface of the half-space.

To calculate the modes of propagation, the determinant of the global stiffness matrix is set equal to zero. This leads to an equation similar to Equation 28.

When the layered system reduces to a uniform half-space, the characteristic equation becomes

$$(2 - V^2/v_s^2)^2 - 4(1 - V^2/v_s^2)^{1/2}(1 - V^2/v_p^2)^{1/2} = 0 \tag{30}$$

where, in this case, v_s and v_p represent the shear and compression wave velocity of the half-space, respectively. This characteristic equation is independent of frequency, indicating that Rayleigh waves are not dispersive when propagating in a uniform half-space.

Dispersion curves for the cases of a soft layer over a stiffer half-space and a stiff layer over a softer half-space are shown in Figures 2 and 3, respectively. The case of the upper soft layer consists of a 10-ft-thick layer with a shear wave velocity of 700 ft/sec, a Poisson's ratio of 0.25, and a mass density of 4 lb-sec^2/ft^4 ($E = 4.90 \times 10^6$ lb/ft^2) overlying a half-space with a shear wave velocity of 1,565 ft/sec, a Poisson's ratio of 0.25, and a mass density of 4 lb-sec^2/ft^4 ($E = 2.45 \times 10^7$ lb/ft^2). It can be observed (Figure 2) that the phase velocity of the Rayleigh wave (V) starts at a value of 1,439 ft/sec for the very low frequencies and decreases to a value of 644 ft/sec at very high frequencies. The first of these velocities (1,439 ft/sec) corresponds to the velocity of a Rayleigh wave in a uniform half-space with the properties of the half-space of the two-layer system, and the second velocity (644 ft/sec) corresponds to that of a Rayleigh wave propagating in a uniform half-space with the properties of the upper layer.

The case of a stiff layer over a softer half-space (Figure 3) presents some complications. At low frequencies ($f < 10$ Hz in the figure), phase velocity increases as frequency increases.

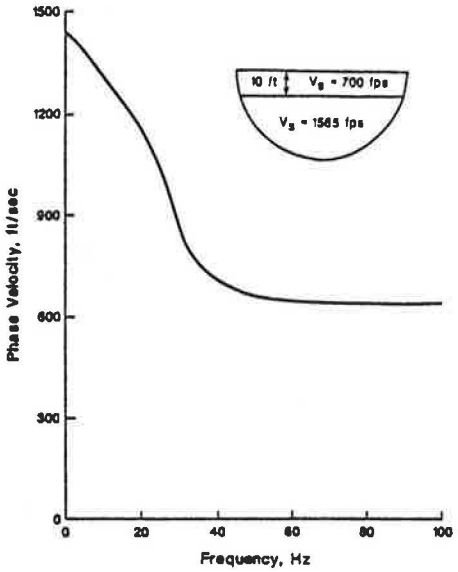

FIGURE 2 Dispersion of plane Rayleigh waves propagating in a layer underlain by a stiffer half-space.

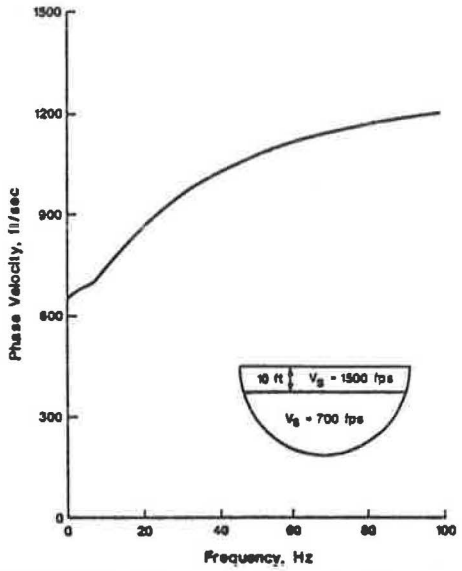

FIGURE 3 Dispersion of plane Rayleigh waves propagating in a layer underlain by a softer half-space.

At some critical frequency ($f \simeq$ 10 Hz in this case) the phase velocity reaches the value of the shear wave velocity in the half-space. For higher frequencies the determinant of Equation 28 becomes complex, and there are no solutions for the phase velocity that satisfy the characteristic equation, indicating that there are no waves of the Rayleigh type (whose amplitude decreases with depth) propagating at frequencies higher than that critical frequency. To obtain a dispersion curve that extends over the entire frequency range, only the real part of the determinant in Equation 28 was considered for the solution of the characteristic equation. The results of this approximation for a layer 10 ft thick with a shear wave velocity of 1,500 ft/sec, a Poisson's ratio of 0.33, and a mass density of 4 lb-sec^2/ft^4 ($E = 2.39 \times 10^7$ lb/ft^2), resting on a half-space with a shear wave velocity of 700 ft/sec, a Poisson's ratio of 0.33, and a density of 4 lb-sec^2/ft^4 ($E = 5.21 \times 10^6$ lb/ft^2), are shown in Figure 3.

DISPERSION CAUSED BY A POINT LOAD

When the SASW technique is used in the field, a transient load is usually applied at a point (or over a small area) on the surface of the pavement or soil deposit. Waves generated by the point load include Rayleigh waves that propagate radially outward from the source along a cylindrical wave front and body waves (shear and compression waves) that propagate outward along a hemispherical wave front. The rate of energy dissipation associated with body waves or the amplitude decrease of body waves is in proportion to the ratio $1/r^2$ along the surface of the layered system, where r is the distance from the source. The amplitude of Rayleigh waves decreases at a rate of $1/r^{1/2}$. In the SASW method it is assumed that because about two-thirds of the energy imparted by the source is transmitted by Rayleigh waves and because these waves attenuate less, the wave train passing by the two receivers is composed primarily of Rayleigh wave components. To study the effect that body wave components might have on the SASW method, dispersion curves caused by a point source were compared with those obtained assuming that only plane Rayleigh waves propagate along the surface.

The formulation used to study the dynamic effects caused by any type of force requires first that the time-history of the specified forces be decomposed into different frequency components (harmonics) using a Fourier series or, more conveniently, a Fourier transform. Results are then obtained for each harmonic and combined via an inverse Fourier transform to obtain the time-history of displacements (Fourier synthesis). For each harmonic (each frequency) the force is expanded in a double Fourier series (or Fourier transform) in the two horizontal directions for cartesian coordinates, or in a Fourier series in the circumferential direction and Hankel transforms in the radial direction for cylindrical coordinates. For each term of these transforms corresponding to a given wave number, the solution can be determined in terms of displacements or stresses by using the global stiffness matrix of the complete layered system as in the approach suggested by Kausel and Roesset (*13*) and outlined in the previous section.

When the solution for each wave number is known, inverse Fourier transforms or Hankel transforms, or both, must be performed to obtain the solution for the specified load distribution. Because the terms of the stiffness matrices of each layer are transcendental functions (complex exponentials), these inverse transforms are very difficult to perform and are done normally by numerical integration. Formulations along these lines have been implemented by Gazetas (*14*) in cartesian coordinates and Apsel (*15*) in cylindrical coordinates. This procedure is particularly convenient when dealing with a uniform half-space or a very small number of layers but extremely expensive when a large number of layers are needed to reproduce the variation of properties with depth.

When the layers are very thin, the transcendental functions representing the variation of displacements with depth can be approximated over each layer by a straight line or any other higher-order polynomial expansion. The solution (displacements and stresses) is then expressed in terms of the exact analytical expression in the two horizontal (or radial and circumferential) directions and in terms of a simpler polynomial expansion in the vertical direction. This approximation leads to much simpler algebraic expressions for the terms of the stiffness matrices of the layers. In addition, when the layered system is underlain by a much stiffer, rocklike material, which can be considered rigid, the wave numbers (eigenvalues) and mode shapes (eigenvectors) of the waves propagating through the layered system can be determined by solving an algebraic eigenvalue problem (*16, 17*). By expressing the solution in terms of these mode shapes (eigenfunction expansion), Kausel (*18*) was able to obtain explicit solutions for the displacements caused by harmonic loads in a layered system. Kausel's formulation is quite efficient from the computational point of view, but the layers must be sufficiently thin to reproduce accurately the variation of the displacements with depth with the linear or higher-order polynomial expansion.

Numerical Implementation

Kausel's formulation was implemented by Shao (*19*) and results from the computer program were compared with those published by Kausel (*18*) with excellent agreement. An approximate formulation for a half-space at the bottom of a layered system was suggested by Hull and Kausel (*20*) and was implemented in the version of the computer program used for the studies presented herein.

Because of the discrete nature of the formulation used, a series of parametric studies was conducted to determine an appropriate mesh size (thickness of the sublayers) to provide an accurate solution. From the results obtained by Shao (*19*) a rule was derived to generate automatically the desired layering. If D is the distance from the point of impact to the point where the displacements are computed, the first depth equal to D is divided into $2N$ sublayers of equal thickness, and the next depth equal to D is divided into N sublayers. N sublayers are then used for the following depth of $2D$, the next depth of $4D$, and so forth. For a nonuniform deposit (such as a pavement) the thickness of each sublayer is the lesser of the value suggested by the rule or the actual physical dimension of the layer. Finally, when the results are to be obtained simultaneously at various points, the smallest value of D controls.

Using this rule, meshes were constructed with values of N equal to 4 (fine mesh), 2 (standard mesh), and 1 (coarse mesh). It was found that the results with the standard mesh were sufficiently accurate for most practical applications. If more accurate results were needed at short distances from the source, a fine mesh was used.

In all cases the thickness of any sublayer should not be greater than 4 to 6 times a reference wavelength. This wavelength can be considered the length of the shear wave in the layer being discretized. Because the wavelength of the shear wave is v_s/f (f being frequency), the maximum thickness of the sublayers varies with each frequency.

Numerical Examples

Dispersion curves were next obtained for a setup similar to that used in the field in an SASW test. The distance from the source to the first receiver was always kept the same as the distance between the two receivers. The load was applied over a circular area with a radius of 1 in. Various frequencies were considered, and for each frequency the distance between the receivers was varied such that the ratio d/λ remained constant. Values of the ratio d/λ (distance divided by the wavelength) of 1/8, 1/4, 1/2, 1, 2, 4, 8, and 16 were used.

A case of a uniform half-space with a shear wave velocity of 700 ft/sec, a density of 4 lb-sec^2/ft^4, and a Poisson's ratio of 0.33 was considered first. The dispersion curves obtained for this case are compared with the one obtained for a plane Rayleigh wave in Figure 4. It can be observed that, at distances from the source of two times the wavelength or more, the dispersion curves for the point load are practically equal to that of a plane Rayleigh wave.

Dispersion curves for the case of a 10-ft-thick soft layer over a stiffer half-space were obtained next. The shear wave velocity of the layer and half-space were 700 and 1,565 ft/sec, respectively. The dispersion curves are shown in Figure 5 and are compared with the dispersion curve obtained for a plane Rayleigh wave. It can be observed that the dispersion curves obtained for distances from the source of two or more times the wavelength are quite similar to that of a plane Rayleigh wave.

Finally, the case of a 10-ft-thick stiff layer (v_s = 1,500 ft/sec) over a softer half-space (v_s = 700 ft/sec) was considered (Figure 6). It is interesting to notice that the dispersion curve

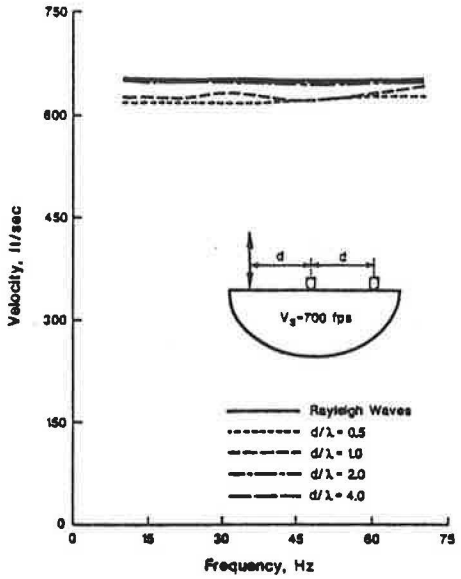

FIGURE 4 Dispersion curves produced by a point load on the surface of a homogeneous half-space compared with the dispersion curve obtained assuming plane Rayleigh waves.

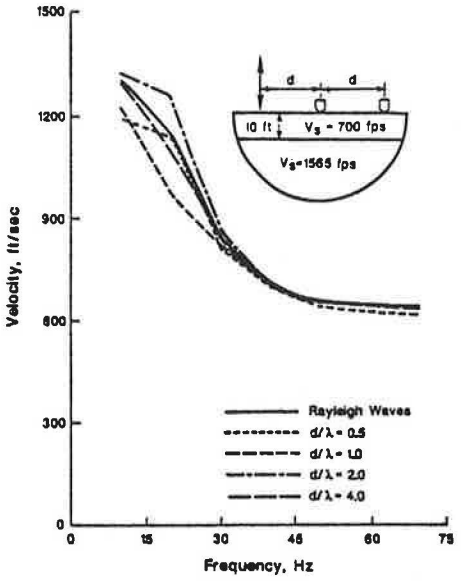

FIGURE 5 Dispersion curves produced by a point load on the surface of a layer underlain by a stiffer half-space compared with the dispersion curve obtained by assuming plane Rayleigh waves.

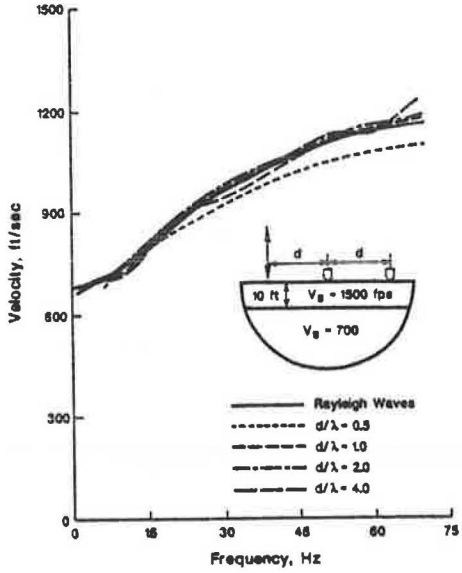

FIGURE 6 Dispersion curves produced by a point load on the surface of a layer underlain by a softer half-space compared with the dispersion curve obtained assuming plane Rayleigh waves.

obtained from the real part of the determinant of Equation 28 for plane Rayleigh waves agrees well with the dispersion curves generated by the point load. At distances from the source of two wavelengths or more the agreement is excellent.

From these comparative studies, it can be concluded that the assumption that only plane Rayleigh waves exist when interpreting the results of an SASW test is best when the distance from the source to the first receiver is of the order of two wavelengths or more.

APPLICATION TO PAVEMENTS

Identification of Mode of Propagation

Application of the SASW method to a three-layer pavement was considered: the first layer (pavement) with a thickness of 2.5 in., a shear wave velocity (v_s) of 1,513 ft/sec, a Poisson's ratio (ν) of 0.35, and a density (ρ) of 4.66 lb-sec^2/ft^4 (modulus of elasticity, $E = 2.88 \times 10^7$ lb/ft^2); the second layer (base) with a thickness of 15 in., V_s = 948 ft/sec, ν = 0.35, and ρ = 4.66 lb-sec^2/ft^4 ($E = 1.13 \times 10^7$ lb/ft^2); and the third layer (subgrade) with v_s = 633 ft/sec, ν = 0.40, and ρ = 3.73 lb-sec^2/ft^4 ($E = 4.18 \times 10^6$ lb/ft^2) and with thickness extending to infinity (a half-space).

The dispersion curve obtained assuming only plane Rayleigh waves is shown in Figure 7 in a semilogarithmic scale. For high frequencies more than one root satisfying the characteristic equation is obtained in the range of phase velocities of interest. It is not immediately apparent which of these roots is the most appropriate.

The dispersion curves resulting from the more accurate analysis, considering a point load at the surface of the pavement, are shown in Figure 8 for various ratios of d/λ (d/λ = 1/4, 1/2, 1, 2, 4), where d is the distance between receivers and λ is the wavelength. It can be observed that the dispersion curves for the different d/λ ratios are nearly identical.

A comparison of the dispersion curves obtained assuming only plane Rayleigh waves with the dispersion curve shown in Figure 8 for d/λ = 4 is shown in Figure 9. The dispersion curve from the point load coincides with the first root of the Rayleigh wave characteristic equation for frequencies below 500 Hz, with the second root for a frequency of 1000 Hz, and with the third root for a frequency of 2000 Hz. To avoid this complication, it was found that if the model for the computation of the Rayleigh wave characteristic equation assumed a uniform half-space beyond a depth of λ, the dispersion curve obtained from the smallest roots of the characteristic equation was the closest to the dispersion curve obtained from the point load at the surface.

Backcalculation of Elastic Properties

When the dispersion curve has been obtained in the field, determination of the elastic moduli requires the solution of an inverse problem. In this work the inversion process adopted consisted of the following steps.

By starting with the results for the highest frequency and assuming a uniform half-space, the apparent wave propagation velocity is assumed to be equal to the Rayleigh wave velocity of the material. Because the results are relatively insensitive to small variations in Poisson's ratio and material density, values of ν = 0.33 and ρ = 3.2 are adopted. It is then possible, from the Rayleigh wave velocity, to compute the shear wave velocity, shear modulus, and Young's modulus of the material.

It is next assumed that these properties, computed assuming only a uniform half-space, are those of a layer with a thickness equal to a factor α times the wavelength λ (values of α of 1/3 to 1 were studied).

By considering the next frequency (second highest) and a profile consisting of a layer with known depth and properties underlain by a half-space, the properties of the half-space that would give a Rayleigh wave velocity equal to the apparent propagation velocity are determined by a search technique. These properties are then assumed to apply from the bottom of the top layer to a depth of $\alpha\lambda$, where λ is the new wavelength.

The procedure is continued, taking successively lower frequencies and proceeding down the profile. At any time, n layers are defined with known thicknesses and material properties and a half-space is assumed to exist below them. The properties of the half-space are determined by a search technique in order to produce a Rayleigh wave velocity equal to the apparent velocity of propagation, and these properties are assumed to apply from the bottom of the nth layer to a depth $\alpha\lambda$.

This first set of computations is quite similar to the direct determination of the dispersion curve for a given profile (a forward problem) and can be performed with relative economy. It should be noticed, however, that when the properties of the underlying half-space have been selected at any step to match the apparent velocity at a given frequency,

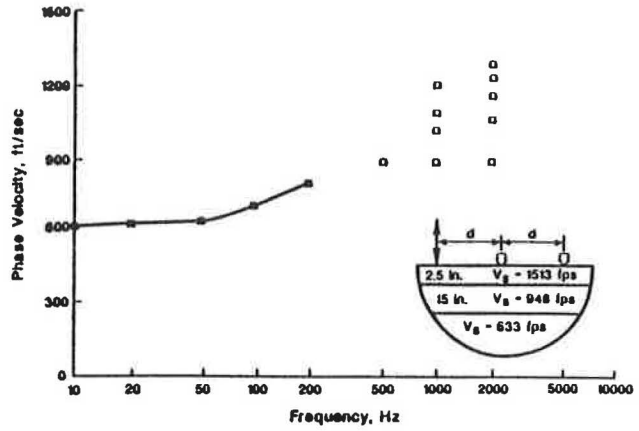

FIGURE 7 Rayleigh wave dispersion of a pavement model.

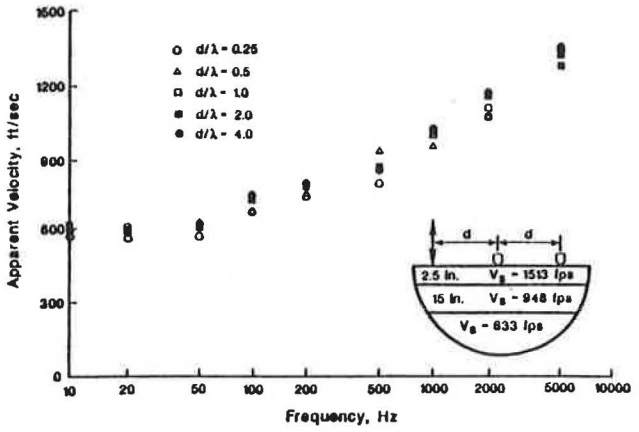

FIGURE 8 Dispersion curves caused by a point load on the surface of a pavement system (obtained with different receiver spacings).

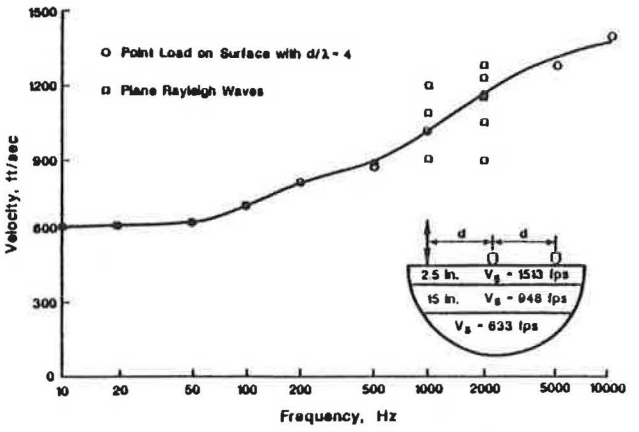

FIGURE 9 Comparison of the dispersion curve produced by a point load on the surface of a pavement with the dispersion curves obtained assuming plane Rayleigh waves.

the resulting profile will no longer match exactly the results at higher frequencies. A correction procedure is therefore necessary. The correction is often performed by considering the complete layered profile obtained after processing all of the frequencies and varying the properties of each layer in order to obtain the best fit.

For pavement systems, if the thicknesses of the layers are known in advance, the correction procedure can be simplified. Only three unknowns (the shear wave velocities of the pavement, base, and subgrade) are considered, and their values are computed using a weighted average of the shear wave velocities of the sublayers contained within the specified layer.

For the case of a half-space, only the first part of the inversion process would be needed. There is no need for correction because the dispersion curve and the properties are independent of frequency and depth. When the suggested inversion program was applied to the results of the uniform half-space studied earlier, a shear wave velocity of 698.7 ft/sec was obtained. The correct result is 700 ft/sec; the difference of 0.2 percent is due to the tolerance in the search technique.

The process was applied next to the dispersion curve calculated for the pavement profile assuming only plane Rayleigh waves. Notice that in this case, because both the computation of the dispersion curve and the inversion procedure are based on the same assumption, comparison of results (original and backcalculated values of the shear wave velocities or elastic moduli) reflects exclusively the errors introduced by the inversion process. Factors influencing the accuracy of the inversion process are the range of frequencies considered, the frequency increment (number of frequencies or points in the dispersion curve), and the value of the parameter α used to define the thickness of the stratum.

Using a maximum frequency of 14 336 Hz, the computed values of the shear wave velocities for the pavement, base, and subgrade estimated with different numbers of points (different frequency increment) are as given in Table 1.

These results were obtained for a value of $\alpha = 1.0$. To get a good approximation of the properties of the pavement, which is very thin, it is necessary to consider very high frequencies. The results improved when higher values were used for the maximum frequency and worsened when lower maximum frequencies were considered.

The results of the inversion process for different values of α (using a maximum frequency of 14 336 Hz and 256 frequencies) are given in Table 2. The agreement appears to be better when using $\alpha = 1$ with maximum errors on the order of 2 percent or less.

To investigate the error in the inversion process created by assuming only a plane Rayleigh wave, the process was applied to the dispersion curves calculated from the more accurate solution of a point load on the surface. This type of dispersion curve should correspond more closely to the values measured experimentally in an SASW test. Notice that in this case the dispersion curve includes the effects of all of the waves generated by the surface load, but the inversion procedure is still based on only plane Rayleigh waves.

The results using the dispersion curve when the two receivers are spaced a distance equal to λ ($d/\lambda = 1$) are given

in Table 3, and those for receivers spaced at a distance 2λ ($d/\lambda = 2$) are given in Table 4.

These results would improve if more frequencies were used. For a distance between receivers of 2λ and a value of $\alpha = 1$, the maximum error is 4 percent (for the shear wave velocity of the base). In all cases the results are generally better for $\alpha = 1$ than for $\alpha = 1/3$.

In practice, the number of frequencies used is normally higher than the number considered in these studies. It is worth noticing that even with $d/\lambda = 1$ and $\alpha = 1/3$ the maximum error, which occurs for the shear wave velocity of the pavement, is only slightly greater than 10 percent. For $\alpha = 1/3$, the estimated shear wave velocities (and therefore the elastic moduli) are always slightly underestimated.

In summary, although the values of α and the distance between receivers affect the results, the errors are relatively small as long as the distance between receivers is of the order of one wavelength or larger and the value of α is between 1/3 and 1. Perhaps the most significant observation is that, in spite of the various approximations, the final results are remarkably consistent.

TABLE 1 COMPUTED VALUES OF SHEAR WAVE VELOCITIES

No. of Frequencies	Δf (Hz)	v_s (ft/sec) of Pavement	Base	Subgrade
64	224	1,508	950	640
128	112	1,509	970	614
256	56	1,509	967	621
512	28	1,509	967	622
Actual value		1,513	948	633

TABLE 2 RESULTS OF INVERSION

α	v_s (ft/sec) of Pavement	Base	Subgrade
1/3	1,385	893	650
1/2	1,444	934	642
1	1,509	967	621
Actual value	1,513	948	633

TABLE 3 RESULTS FOR RECEIVERS SPACED AT $d/\lambda = 1$

α	v_s (ft/sec) of Pavement	Base	Subgrade
1/3	1,351	900	627
1/2	1,432	983	622
1	1,427	1,080	614
Actual value	1,513	948	633

TABLE 4 RESULTS FOR RECEIVERS SPACED AT $d/\lambda = 2$

α	v_s (ft/sec) of Pavement	Base	Subgrade
1/3	1,384	891	634
1/2	1,460	995	628
1	1,514	986	627
Actual value	1,513	948	633

CONCLUSIONS

Interpretation of the results of SASW testing is conducted at present by assuming that only plane Rayleigh waves are generated by the impact. A procedure that accounts for all other types of waves has been presented herein. The conditions under which the assumption that essentially only plane Rayleigh waves are measured during SASW testing is valid were studied. It was found that the distance between receivers relative to the wavelength has a great influence on the results. For a typical SASW setup in which the distance from the source to the first receiver is kept the same as the distance between the two receivers (Figure 1), waves with wavelengths larger than one-half the distance between receivers carry a substantial amount of body wave energy. It is recommended that field data be filtered so that the value of d/λ (distance between receivers over wavelength) is kept greater than 2. A value of 1 could be used if more data were required in the low-frequency range.

A simple procedure for backcalculating properties has also been presented to demonstrate the usefulness of the testing procedure.

REFERENCES

1. R. Jones. A Vibration Method for Measuring the Thickness of Concrete Road Slabs In Situ. *Magazine of Concrete Research,* Vol. 7, No. 20, July 1955.
2. R. Jones. In-Situ Measurement of the Dynamic Properties of Soil by Vibration Methods. *Geotechnique,* Vol. 8, No. 1, March 1958.
3. R. Jones. Surface Wave Technique for Measuring the Elastic Properties and Thickness of Roads: Theoretical Development. *British Journal of Applied Physics,* Vol. 13, 1962.
4. W. Heukelom and C. R. Foster. Dynamic Testing of Pavements. *Journal of the Soil Mechanics and Foundations Division,* ASCE, Vol. 86, No. SM1, Part 1, Feb. 1960.
5. Z. B. Fry. *Development and Evaluation of Soil Bearing Capacity, Foundations of Structures.* Technical Report 3-362, Report 1. U.S. Army Engineer Waterways Experiment Station, Vicksburg, Miss., 1963.
6. R. F. Ballard, Jr. *Determination of Soil Shear Moduli at Depth by In-Situ Vibratory Techniques.* Miscellaneous Paper 4-858. U.S. Army Engineer Waterways Experiment Station, Vicksburg, Miss., Nov. 1964.
7. J. S. Heisey, K. H. Stokoe II, and A. H. Meyer. Moduli of Pavement Systems from Spectral Analysis of Surface Waves. In *Transportation Research Record 852,* TRB, National Research Council, Washington, D.C., 1982, pp. 22-31.

8. S. Nazarian, K. H. Stokoe II, and W. R. Hudson, Use of Spectral Analysis of Surface Waves for Determination of Moduli and Thicknesses of Pavement Systems. In *Transportation Research Record 930,* TRB, National Research Council, Washington, D.C., 1983, pp. 38-46.
9. K. H. Stokoe II and S. Nazarian. Effectiveness of Ground Improvement from Spectral Analysis of Surface Waves. *Proc., Eighth European Conference on Soil Mechanics and Foundation Engineering,* Helsinki, Finland, May 1983.
10. S. Nazarian. *In Situ Determination of Elastic Moduli of Soil Deposits and Pavement Systems by Spectral-Analysis-of-Surface-Waves Method.* Ph.D. dissertation. University of Texas at Austin, Dec. 1984.
11. W. T. Thomson. Transmission of Elastic Waves Through a Stratified Soil Medium. *Journal of Applied Physics,* Vol. 21, Feb. 1950.
12. N. A. Haskell. The Dispersion of Surface Waves on Multilayered Media. *Bulletin of the Seismological Society of America,* Vol. 43, No. 1, Feb. 1953.
13. E. Kausel and J. M. Roesset. Stiffness Matrices for Layered Soils. *Bulletin of the Seismological Society of America,* Vol. 71, No. 6, Dec. 1981.
14. G. Gazetas. *Dynamic Stiffness Functions of Strip and Rectangular Footings on Layered Soil.* S.M. thesis. Massachusetts Institute of Technology, Cambridge, 1975.
15. R. J. Apsel. *Dynamic Green's Functions for Layered Media and Applications to Boundary Value Problems.* Ph.D. dissertation. University of California at San Diego, 1979.
16. G. Waas. *Linear Two Dimensional Analysis of Soil Dynamics Problems on Semi-Infinite Layered Media.* Ph.D. dissertation. University of California, Berkeley, 1972.
17. E. Kausel. *Forced Vibrations of Circular Foundations on Layered Media.* Research Report R74-11. Department of Civil Engineering, Massachusetts Institute of Technology, Cambridge, 1974.
18. E. Kausel. *An Explicit Solution for the Green Functions for Dynamic Loads in Layered Media.* Research Report R81-13. Massachusetts Institute of Technology, Cambridge, 1981.
19. K. Y. Shao. *Dynamic Interpretation of Dynaflect, Falling Weight Deflectometer and Spectral Analysis of Surface Waves Tests on Pavement Systems.* Research Report 437-1. Center for Transportation Research, Bureau of Engineering Research, The University of Texas at Austin, 1986.
20. S. W. Hull and E. Kausel. Dynamic Loads in Layered Half-Space. *Proc., 5th Engineering Mechanics Division Specialty Conference,* ASCE, Laramie, Wyo., 1984.

Publication of this paper sponsored by Committee on Flexible Pavement Design.

Nondestructively Delineating Changes in Modulus Profiles of Secondary Roads

SOHEIL NAZARIAN, KENNETH H. STOKOE II, AND ROBERT C. BRIGGS

To load-zone roads properly, mechanisms involved in the deterioration of pavements must be understood and monitored. The state of practice in nondestructively evaluating pavement systems is limited to determining changes in modulus profiles. For secondary roads, deflection basin methods [such as falling-weight deflectometer (FWD) and Dynaflect] are most effective in determining moduli of subgrades and are not as sensitive to moduli of the surface and base layers. On the other hand, the Spectral-Analysis-of-Surface-Waves (SASW) method is quite sensitive to moduli in the upper layers. In addition, the SASW method has the advantage of allowing the pavement system to be divided into numerous layers, say 10 to 15 in the upper 3 ft, so that detailed profiles can be determined. With this resolution, it is possible to delineate changes in the modulus profile from one measurement to the next. To illustrate the use of the SASW method on secondary roads, two sites were tested to determine the possible reasons for one section rutting and the other not. The rutted section was found to have layers with lower moduli or in which moduli appeared to be decreasing and hence possibly causing deterioration of the section. Also, the softening effect of rain on these pavements was studied. Softening occurred mainly in the upper portion of the subgrade. The FWD device was also used to determine moduli of the two sections. Moduli from the FWD tests are substantially lower than those from the SASW tests in the base layers mainly because of nonlinear behavior created during FWD testing. However, moduli of the subgrades are quite similar because of the linear behavior of this material in both types of tests. Deflection basins based on moduli of SASW tests are also compared with the FWD deflection basins. If the nonlinear effects are considered, the deflection basins based on moduli evaluated by the SASW tests compare well with those measured by the FWD device.

The Spectral-Analysis-of-Surface-Waves (SASW) method was used at two sites on Farm-to-Market (FM) Road 2001 located near Buda, Texas. This method was first used in March 1986 to determine the variation of in situ Young's modulus with depth. The objective of testing was to determine the sensitivity of the SASW method to the degree of deterioration of the pavement; surface observations of one test site revealed no deterioration, and at the second test site some deterioration was manifested in surface rutting. The two sites are representative of several similar comparative tests performed on different road sections in central Texas.

A second series of SASW tests was performed at the two sites on FM-2001 in June 1986. The objective of these tests was to determine the effect of heavy rains, which had occurred during the week before the tests, on the moduli of the different pavement layers. The effect of the rains was evaluated by comparing moduli from the second series of tests with those determined from the tests in March. A series of falling-weight deflectometer (FWD) tests was also performed on this day for comparison purposes. After completion of data reduction, the two sites were cored to verify the reported layer thicknesses.

SASW tests are performed at low strain levels where pavement and soil layers behave linearly. An algorithm has been developed to model in an approximate manner the effect on the deflection basin of the nonlinear behavior in the different pavement layers. With this model, deflection basins based on the small-strain moduli determined by the SASW tests but approximately modified to account for nonlinear behavior were computed. These nonlinear deflection basins were then compared with deflections measured by the FWD device. The two basins compare well when nonlinear behavior is taken into account.

Results of this study are presented herein, along with brief background information on the SASW method and an explanation of the test procedures and data analyses. A detailed description of the testing technique and the theoretical background can be found elsewhere (*1-3*).

SPECTRAL-ANALYSIS-OF-SURFACE-WAVES TESTING

General Background

The SASW method is a type of seismic testing that was developed for determining shear wave velocity and elastic shear modulus profiles at soil sites and elastic Young's modulus profiles at pavement sites (*1-3*). The SASW method is a nondestructive method in which both the source and the receivers are located on the ground surface. The source is simply a transient vertical impact that generates a group of surface waves of various frequencies that the medium transmits. Two vertical receivers located on the surface monitor the propagation of surface wave energy. By analysis of the phase information of the cross power spectrum for each frequency determined between the two receivers, phase velocity, shear wave velocity, and elastic moduli are determined.

S. Nazarian, Center for Transportation Research, and K. H. Stokoe II, Civil Engineering Department, University of Texas at Austin, Austin, Tex. 78712. R. C. Briggs, Pavement Management Section, Texas Department of Highways and Public Transportation, Dewitt C. Greer State Highway Building, Austin, Tex. 78701.

The key points in SASW testing are generation and measurement of surface waves (Rayleigh waves). Rayleigh wave velocity (V_R) is constant in a homogeneous half-space and independent of frequency. Each frequency (f) has a corresponding wavelength (L_R) according to

$$V_R = f \times L_R \tag{1}$$

Rayleigh wave and shear wave velocities are related by Poisson's ratio. In an isotropic elastic half-space, the ratio of Rayleigh wave to shear wave velocity increases as Poisson's ratio increases. The change in this ratio is small, and it can be assumed that the ratio is approximately equal to 0.90 without introducing an error large than 5 percent.

If the stiffness of a site varies with depth, the velocity of the Rayleigh wave (R-wave) will vary with frequency. The variation of R-wave velocity with frequency (wavelength) is called dispersion, and a plot of surface wave velocity versus wavelength is called a dispersion curve. The dispersion curve is developed from phase information of the cross power spectrum. This information provides the relative phase between two signals (two-channel recorder) at each frequency in the range of frequencies excited in the SASW test. For a travel time equal to one period of the wave, the phase difference is 360 degrees. Thus, for each frequency, the travel time between receivers can be calculated by

$$t(f) = \phi(f)/(360 \times f) \tag{2}$$

where

f = frequency,
$t(f)$ = travel time for a given frequency, and
$\phi(f)$ = phase difference in degrees for a given frequency.

The distance between the receivers (X) is a known parameter. Therefore, R-wave velocity at a given frequency [$V_R(f)$] is simply calculated by

$$V_R(f) = X/t(f) \tag{3}$$

and the corresponding wavelength of the R-wave is equal to

$$L_R(f) = V_R(f)/f \tag{4}$$

By repeating the procedure outlined by Equations 2-4 for every frequency, the R-wave velocity corresponding to each wavelength is evaluated and the dispersion curve is determined.

Rayleigh wave velocities determined by this method are not actual velocities of the layer but are apparent R-wave velocities (known as phase velocities). Existence of a layer with high or low velocity at the surface of the medium affects measurement of the velocities of the underlying layers. Therefore, a method for evaluation of shear wave velocities from phase velocities (apparent surface wave velocity) is necessary in SASW testing.

Inversion of the dispersion curve, or (in short) inversion, is the procedure of determining the shear wave velocity profile from the dispersion curve. Inversion consists of determination of the depth of each layer and the actual shear wave velocity of each layer from the apparent R-wave velocity versus wavelength information.

The inversion process used herein is based on a modified version of Thomson's (*4*) and Haskell's (*5*) matrix solution for elastic surface waves in a layered solid medium. To simplify the process of inversion, some assumptions were made: (*a*) the layers are horizontal, (*b*) the velocity of each layer is constant, and (*c*) the layers are homogeneous and linearly elastic. Assumptions *a* and *b* are quite reasonable for most pavement systems within the top 3 to 5 ft where the vast majority of SASW data is collected. Also, Assumption *b* (constant velocity within a layer) does not limit the variability in the complete modulus profile because numerous layers (5 to 10) can be used to represent the final profile. Assumption *c* is also quite realistic for the small-strain seismic waves used in these tests. Nonlinear behavior in the pavement system can then be accounted for by combining field (linear) and laboratory (nonlinear) testing as discussed in the section on nonlinear moduli.

The inversion process is an iterative one in which a shear wave velocity profile is assumed and a theoretical dispersion curve is constructed. The experimental and theoretical dispersion curves are compared and necessary changes are made in the assumed shear wave velocity profile until the two curves (experimental and theoretical dispersion curves) match within a reasonable tolerance. Detailed discussions of the inversion process are given elsewhere (*2, 3, 6*).

When the shear wave velocities have been determined, the following formulas are used to calculate shear and Young's moduli:

$$G = \rho \times V_s^2 \tag{5}$$

$$E = 2G(1 + \nu) \tag{6}$$

where

G = shear modulus,
E = Young's modulus,
ρ = mass density, and
ν = Poisson's ratio.

Field Procedure

The general configuration of the source, receivers, and recording equipment is shown in Figure 1*a*. Accelerometers were used as receivers for close receiver spacings (4 ft and less), and geophones with a natural frequency of 4.5 Hz were used as receivers for greater spacings. This was done to optimize recording of the wave passage; that is, accelerometers give more output over a wide frequency range at closer receiver spacings where high frequencies are present and geophones give more output at larger receiver spacings where low frequencies are excited.

The common receivers midpoint (CRMP) geometry (*1*) was used for testing. With this geometry the two receivers were moved away from an imaginary centerline midway between the receivers at an equal pace, and the source was

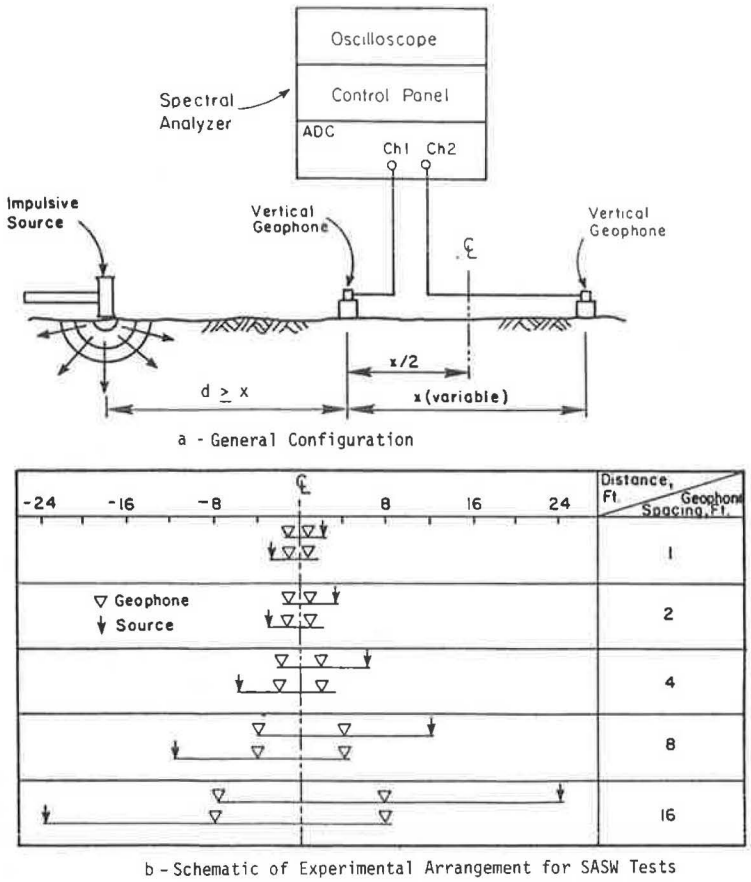

FIGURE 1 Field procedure used in SASW testing.

moved so that the distance between the source and the near receiver was equal to or greater than the distance between the two receivers. In addition, the location of the source was reversed for each receiver spacing so that forward and reverse profiles were run. This testing sequence is shown in Figure 1*b*. Distances between receivers of 0.5, 1, 2, 4, and 8 ft were used at each site.

Different sources were used. For close receiver spacings, a 4-oz hammer was used. For greater distances, sledgehammers were employed.

The recording device was a Hewlett-Packard 3562A Fourier spectral analyzer. A Fourier analyzer is a digital oscilloscope that by means of a microprocessor attached to it has the ability to perform directly in either the time or frequency domain. Fourier analysis is a power tool in decomposition of complicated waveforms, and testing could not be performed without such an analysis.

It should be emphasized that the field operation can be fully automated. Two different avenues are currently being pursued to automate field testing. The first consists of installing a powerful minicomputer and data-acquistion system in a van to control the impact system and recording and manipulating the receivers' output. The second is to modify an FWD system for this purpose. Both methods will reduce testing time to a few minutes per site.

EVALUATION OF NONLINEAR MODULI

There are two basic approaches used today to evaluate moduli of pavement systems in the field. The first approach is to employ high-intensity loads in an attempt to evaluate the nonlinear behavior of the pavement. Elastic theory is then used to backcalculate the modulus profile. The advantage of this approach is that an equivalent nonlinear modulus of the pavement may be determined. However, if these moduli are used to determine the stresses and strains in the pavement system, substantial errors may occur because the modulus profile is approximated with only three or four equivalent moduli and, hence, may only be appropriate for calculating surface displacements under loads similar to those used to evaluate the equivalent moduli. The FWD is a good example of this testing approach.

The second approach is to determine elastic moduli in situ and to perform laboratory tests on representative samples to define the decrease of modulus with increasing strain (and to some extent with the change in stress state). Then, by incorporating these two (laboratory and field) results, the actual nonlinear behavior of the pavement system can be determined for any load level. More than 30 years of research in earthquake engineering have shown that the second approach is quite realistic. The SASW testing method falls into this second category of testing.

As an example, a model used to describe the relationship between the modulus and strain for geotechnical materials is shown in Figure 2. The model is based on numerous resonant column tests on granular and cohesive soil samples (*7*). The model is quite representative of the behavior of subgrades, granular bases, and subbases. It can be seen that the effects of

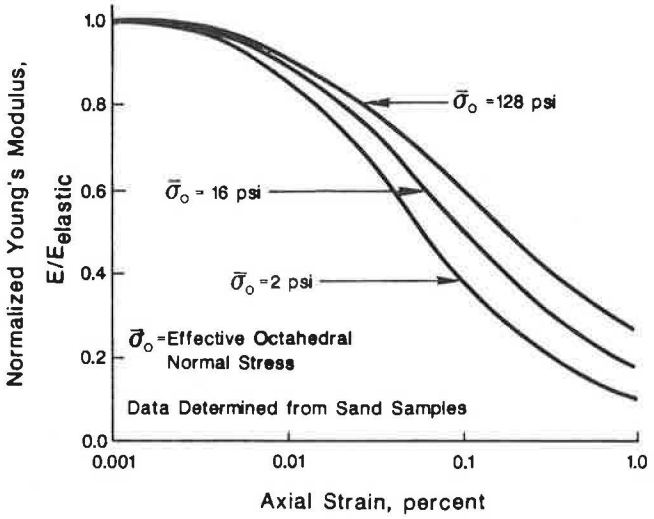

FIGURE 2 Nonlinear model used for determining equivalent linear moduli of geotechnical materials.

both normal strain and normal stress on moduli are considered in the model. Several important points can be deduced from Figure 2. First, as the octahedral normal stress increases in a layer, the material become stiffer (at a constant strain). Second, there is a threshold strain level below which the soil behaves elastically. This threshold level is slightly above 0.001 percent. Third, an increase in strain above the threshold level results in a reduction in the value of the modulus of the material and, hence, nonlinear behavior.

One important conclusion that can be drawn from the material behavior illustrated in Figure 2 is that results from the SASW and FWD tests should be quite similar if FWD tests are performed at low levels of load that only create small strains in all parts of the pavement system and if both testing techniques are analyzed correctly.

DESCRIPTION OF SITES

Two sites were tested in March 1986. The two sites were located 0.8 mi apart. Site 1 was at Milepost 2 on FM-2001 in the outer wheelpath of the westbound lane. Site 2 was about 0.8 mi to the west of the first site. The SASW test was carried out in the outer wheelpath of the eastbound lane at Site 2.

Visually, the pavement at Site 1 was in excellent condition, and no cracking or depression could be located. At Site 2 cracks were visible, and the pavement was depressed and rutted. The depth of rutting at this site was approximately 1 in.

Material profiles of the two sites were reported to be the same (on the basis of construction drawings). At each site, the first inch of material consisted of an asphalt-treated surface course. About 10 in. of granular base underlay the surface course. The base was, in turn, underlain by a clayey subgrade.

Coring the two sites (in February 1987) revealed the following profiles: At Site 1, the asphalt layer was 1.25 in. thick. The base consisted of two sublayers. The upper sublayer of the base, with a thickness of 6 to 7 in., consisted of good granular base materials. However, the lower sublayer of the base, 3 to 4 in. thick, had a very high clay content. The clay in this base layer was yellowish and appeared to have been placed with the granular base. The subgrade, which can be categorized as Houston black clay, was encountered at approximately 11 in. below the surface. The asphalt layer at Site 2 was approximately 1.5 in. thick. The base consisted of three distinct sublayers. The first sublayer was 2.5 in. thick and consisted of good base material similar to the material found in the upper sublayer of the base at Site 1. The second sublayer, which extended to a depth of 8 in. from the surface, was not as competent as the first sublayer and contained some clay. The third sublayer of the base was about 3 in. thick and consisted of a base material with a high content of yellowish clay. The Houston black clay subgrade was encountered at a depth of 11 in. below the surface.

MODULUS PROFILES FROM SASW TESTS

Before-Rain Tests

Dispersion curves from SASW testing at Sites 1 and 2 are shown in Figure 3. Typical spectral analysis functions measured at these sites for one receiver spacing are shown in Figure 4. The quality of the data collected in the field was quite good (as judged by the writers based on much previous experience).

Shear wave velocity profiles determined from inversion of the dispersion curves are given in Column 4 of Tables 1 and 2 for Sites 1 and 2, respectively. Seven layers with a total thickness of about 23 in. over an eighth layer (a half-space) were used in the inversion process at each site (Figure 5*a*). The thicknesses of the layers ranged from 1 in. near the surface to 12 in. in the upper portion of the subgrade. The number of layers was limited to eight because the intent was to use an elastic layered program (LAYER8 program) to obtain the theoretical deflections from the SASW modulus profiles. Program LAYER8 can only analyze a layered system with no more than eight layers.

As a first approximation in the inversion process, layer thicknesses reported in the construction records were used. The assumed layering subsequently changed during the final

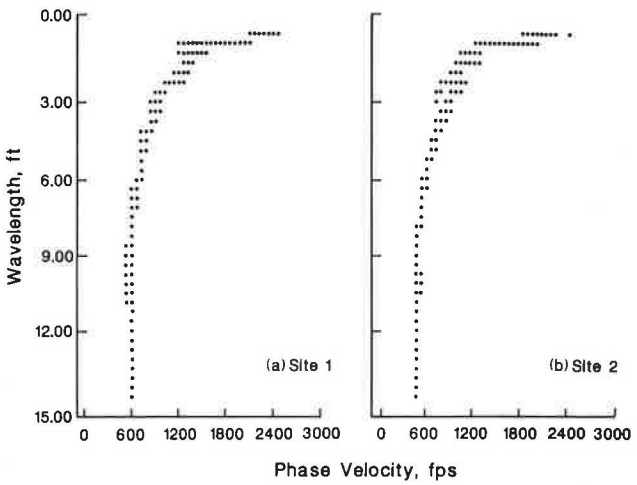

FIGURE 3 Dispersion curves obtained from SASW tests before rain.

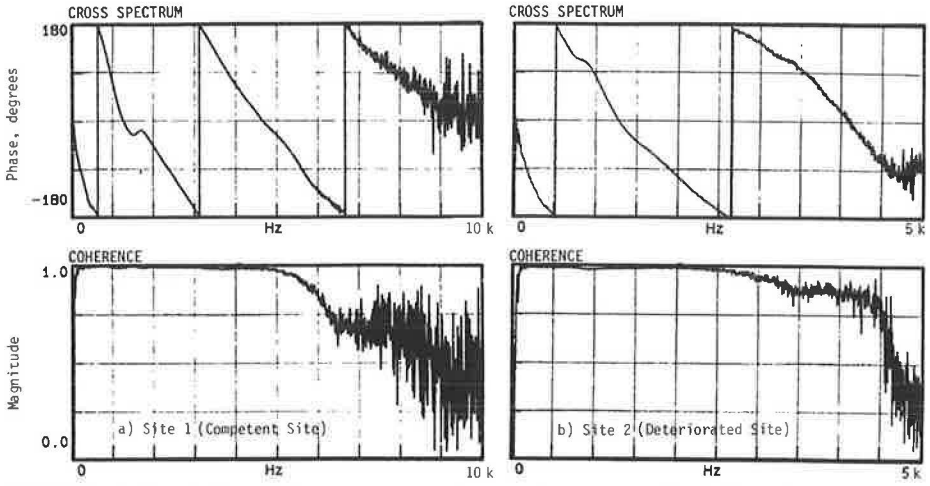

FIGURE 4 Spectral analysis measurements from surface wave testing before rain.

TABLE 1 VARIATION OF SHEAR WAVE VELOCITY AND YOUNG'S MODULUS WITH DEPTH FROM SASW TESTS AT SITE 1 (competent pavement)

Layer Number	Layer Thickness in.	Layer Depth[1] in.	Before Rain		After Rain	
			Shear Wave Velocity fps	Young's Modulus[2] ksi	Shear Wave Velocity fps	Young's Modulus[2] ksi
(1)	(2)	(3)	(4)	(5)	(6)	(7)
1	0.96	0.48	3063	592.0	3036	592.0
2	1.20	1.56	3007	570.6	3007	570.6
3	2.40	3.36	1470	136.4	1470	136.4
4	2.40	5.76	1465	135.4	1465	135.4
5	2.04	7.98	946	56.5	946	56.5
6	2.04	10.02	744	34.9	744	34.9
7	12.00	17.04	586	21.6	527	19.1
8	H-S[3]	---	608	23.4	547	20.6

[1] Depth to the midheight of the layer

[2] Based on an assumed total unit weight of 110 pcf for all materials

[3] Denotes Half-Space

TABLE 2 VARIATION OF SHEAR WAVE VELOCITY AND YOUNG'S MODULUS WITH DEPTH FROM SASW TESTS AT SITE 2 (deteriorated pavement)

Layer Number	Layer Thickness in.	Layer Depth[1] in.	Before Rain		After Rain	
			Shear Wave Velocity fps	Young's Modulus[2] ksi	Shear Wave Velocity fps	Young's Modulus[2] ksi
(1)	(2)	(3)	(4)	(5)	(6)	(7)
1	0.96	0.48	2968	555.9	2968	555.9
2	1.20	1.56	2577	419.0	2577	419.0
3	1.20	2.76	1144	82.6	1144	82.6
4	2.40	4.56	1114	78.3	1114	78.3
5	2.40	6.96	1064	71.5	1064	71.5
6	3.00	9.66	698	30.7	663	27.7
7	12.00	17.16	540	18.4	462	14.6
8	H-S[3]	---	563	20.4	496	16.9

[1] Depth to the midheight of the layer

[2] Based on an assumed total unit weight of 110 pcf for all materials

[3] Denotes Half-Space

inversion process as discussed later. In the inversion process, values of Poisson's ratio of 0.33, 0.33, and 0.45 were assumed for the asphaltic cement (AC), base, and subgrade, respectively. Misestimation of Poisson's ratio has a minimal effect on the shear wave velocities obtained by the inversion process (*2*).

On the basis of the shear wave velocity profiles given in Tables 1 and 2, Young's moduli at different depths were calculated using Equations 5 and 6. The resulting Young's modulus profiles are shown in Figures 5*c* and 5*e* and given in Tables 1 and 2 for Sites 1 and 2, respectively. To calculate Young's moduli, a total unit weight of 110 pcf was assumed for all layers. Because the objective of this paper is to determine the percentage difference in moduli of the different layers, misassumption of the total unit weight does not affect the generality of the discussion presented in the next section.

Analysis of Before-Rain Tests

The thicknesses of the different layers at Sites 1 and 2 estimated from the modulus profiles compare only generally with the layering based on the construction plans. Therefore it was decided to core the sites to determine the actual pavement profiles. For both sites, the total thicknesses of the base and wearing course agree well with the construction plans (11 in.). However, the differences in the materials used in the base were evident from coring. The layering found from

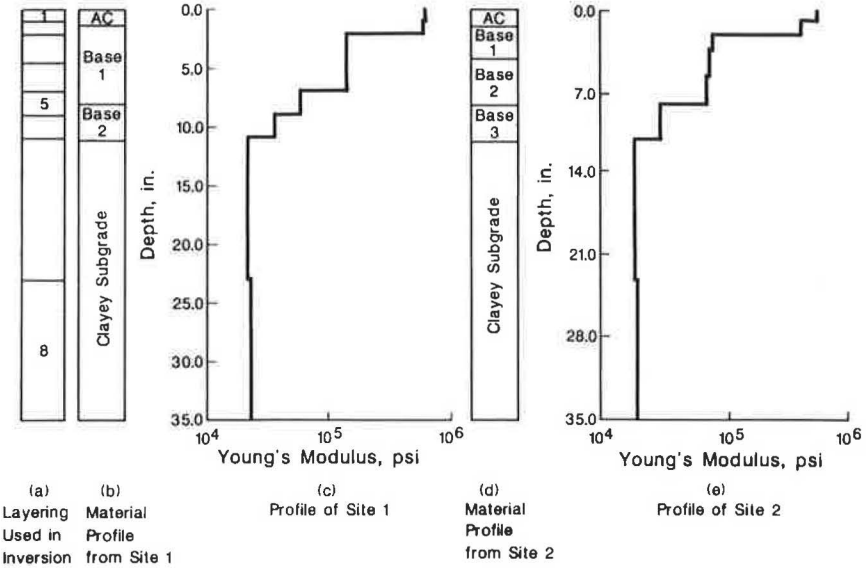

FIGURE 5 Composite profiles of the two sites for before-rain conditions.

coring supports the variation in the base moduli obtained from the SASW tests. The bottom of the base material exhibits a stiffness that is closer to the stiffness of the subgrade. This is probably because the bottom sublayer of the base has a high clay content. Also, the modulus of the top sublayer of the base is close to that of the surface layer. This may be due to a combination of reasons. First, additional compactive effort was applied to the base, especially the upper portion, when the asphaltic surface was placed. Second, because the top two layers at each site were each assumed to be about 1 in. thick in the inversion process, the stiffness of the lower of these two layers is an average of the asphalt and base moduli because the thickness of the asphalt layer was actually more than 1 in. but less than 2 in.

Because the SASW method is sensitive to deterioration of pavement, a brief discussion of the differences and similarities of the two dispersion curves is in order. The dispersion curves from Sites 1 and 2 are compared in Figure 6 on expanded scales. In Figure 6*a*, the two dispersion curves are compared over a range in wavelengths from 0 to 3 ft. It can be seen that the two curves follow each other quite well in the ranges of wavelengths less than 0.5 to 2.5 ft. However, in the range of wavelengths of 0.5 to 2.5 ft, the dispersion curve from Site 2 indicates phase velocities on the order of 10 to 25 percent less than those of Site 1. A very approximate rule of thumb [The following discussion is presented for a better understanding of the role of dispersion curves and is not meant to imply that it can be used as a replacement for the inversion process.] suggests that the effective depth of sampling is equal to one-third (*8*) to one-half (*9*) of the wavelength and that shear wave velocity is equal to 110 percent of phase velocity. If this rule is applied, it can be concluded that the shear wave velocity of the base material of the first site (competent pavement) is approximately 10 to 25 percent higher than that of the second site (deteriorated pavement). A 25 percent difference in shear wave velocities corresponds to a difference in moduli of about 56 percent.

In Figure 6*b* the dispersion curves in the range of wavelengths of 3 to 10 ft are shown. It can be seen that the two curves are quite similar with a difference of about 10 percent. In other words, on the basis of the rule of thumb, the subgrade of Site 1 has a shear wave velocity that is approximately 10 percent higher than the velocity of Site 2. The two curves show the same trend and velocities below wavelengths of 10 ft and, therefore, are not included.

The shear wave velocity profiles of the two sites (after the true inversion process, not rule of thumb) are compared in Table 3. The material profile from coring is included in Figure 5. It can be seen that the shear wave velocity of the asphalt layer is approximately equal for both sites. Parts of the base material (the first inch) show nearly the same stiffness as the AC layer, particularly at Site 1. Below the upper stiff portion of the base, the shear wave velocity of the base material at Site 1 is about 30 percent greater than that at Site 2. The bottom 2 in. of the base materials at both sites exhibit stiffnesses closer to those of the subgrades than the bases. The shear wave velocities of the subgrades are nearly the same, differing only by about 8 percent. A significant point is that the layering in the base materials observed from coring is well reflected in these profiles.

Young's moduli obtained from the two sites are compared in Figure 7 and Table 3. Based on Equations 5 and 6, the differences in the values of Young's moduli from the two sites should be the square of the differences in the shear wave velocities. Therefore the base materials are about 70 percent stiffer at Site 1 than at Site 2, and the subgrade is about 15 percent stiffer at Site 1 than at Site 2. One possible reason for the deterioration of the pavement at Site 2 is the softer base materials.

After-Rain Tests

Dispersion curves from SASW testing at Sites 1 and 2 in June are shown in Figure 8. The quality of the data collected in the field was again good.

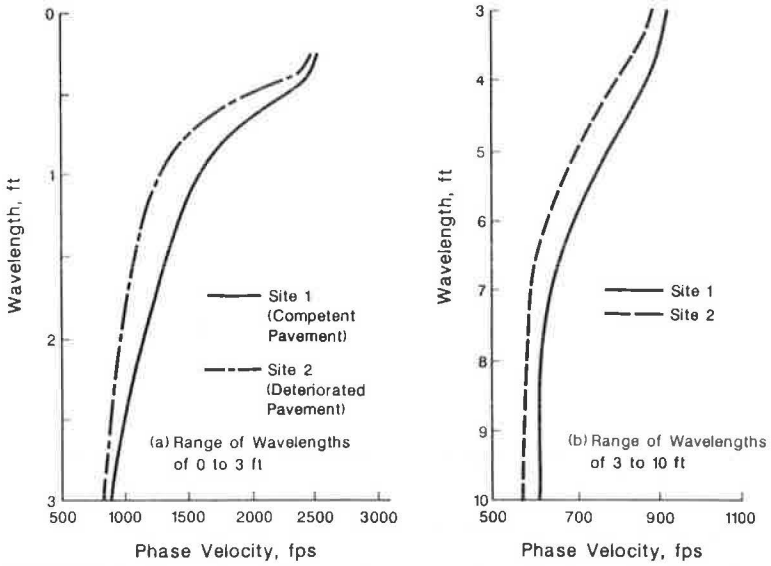

FIGURE 6 Comparison of dispersion curves from Sites 1 and 2 before rain.

TABLE 3 COMPARISON OF SHEAR WAVE VELOCITIES AND YOUNG'S MODULI DETERMINED BY SASW TESTS AT SITES 1 AND 2 BEFORE RAIN

Layer No.	Depth in.	Shear Wave Velocity fps		Velocity Difference percent	Young's Modulus ksi		Modulus Difference percent
		SITE 1	SITE 2	(3-4)/4	SITE 1	SITE 2	(6-7)/7
(1)	(2)	(3)	(4)	(5)	(6)	(7)	(8)
1	0.5	3063	2968	3.2	592.0	555.9	6.5
2	1.6	3007	2577	16.7	570.6	419.0	36.2
3	3.4	1470	1144	28.5	136.4	82.6	65.1
4	5.8	1465	1114	31.5	135.4	78.3	72.9
5	8.0	946	1064	-11.1	56.5	71.5	-21.0
6	10.0	744	698	6.6	34.9	30.7	13.7
7	17.0	586	540	8.5	21.6	18.4	17.4
8	H-S	608	563	8.0	23.4	20.4	17.0

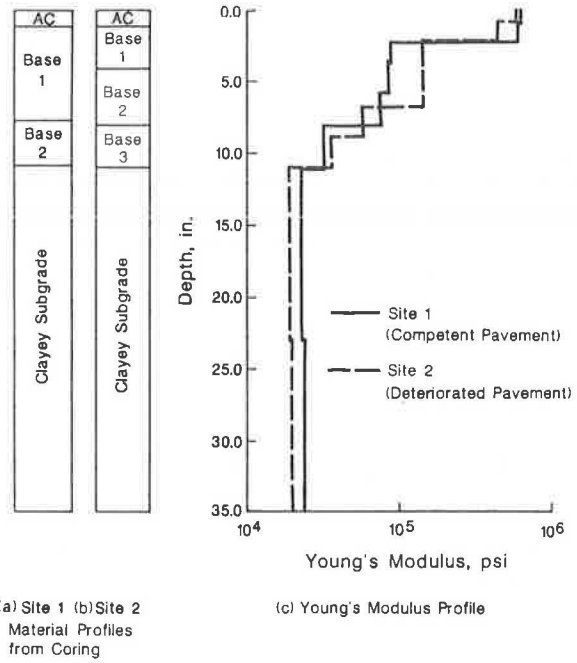

FIGURE 7 Comparison of Young's modulus profiles from Sites 1 and 2 before rain.

Shear wave velocity profiles determined from inversion of the dispersion curves are given in Column 6 of Tables 1 and 2 for Sites 1 and 2, respectively. As was done in the first series of tests, the same eight layers were used in the inversion process at each site to evaluate the stiffness in the top 35 in. of the pavements. It should be noted that, as the starting point in the inversion process, shear wave velocity profiles obtained from the first series of tests at these sites (March) were used.

Based on the shear wave velocity profiles, Young's moduli at different depths were calculated using Equations 5 and 6. The resulting Young's modulus profiles are shown in Figure 9 and given in Tables 1 and 2 for Sites 1 and 2, respectively.

Comparison of Moduli for Before- and After-Rain Conditions

Moduli obtained from the first series of tests when the pavement was not subjected to heavy rain and moduli from the second series, which was performed immediately after a week of heavy rain, are compared. Dispersion curves obtained from before- and after-rain tests are compared in Figure 10 for Sites 1 and 2. At both sites, the upper parts of the dispersion curves (say to a wavelength of 3 ft) are almost identical. This is an indication of similarity between the shear wave velocities of the two tests (i.e., before- and after-rain tests) to a depth of approximately 1 to 1.5 ft. In other words, the stiffnesses of AC and base layers were not affected by the rainfall. Phase velocities from after-rain tests were about 10 percent smaller than those from before-rain tests for wavelengths greater than about 4 ft, which means that the rain softened the subgrade.

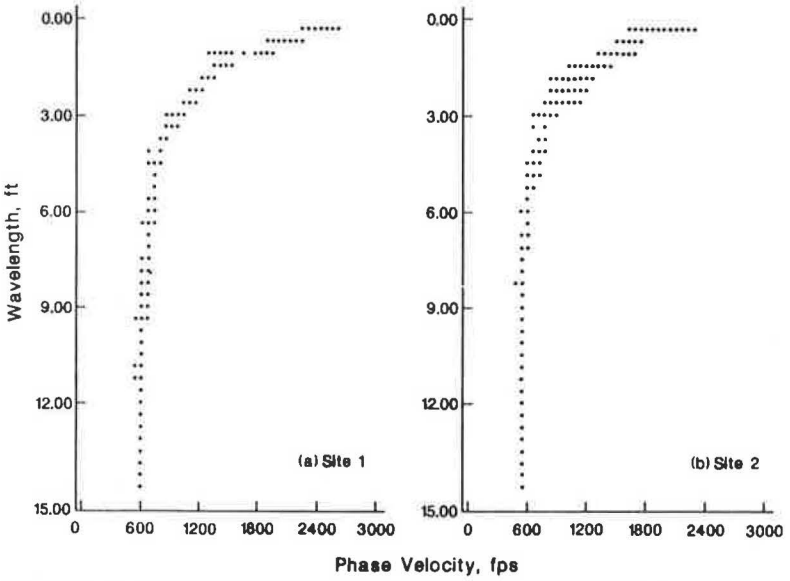

FIGURE 8 Dispersion curves obtained from SASW tests after rain.

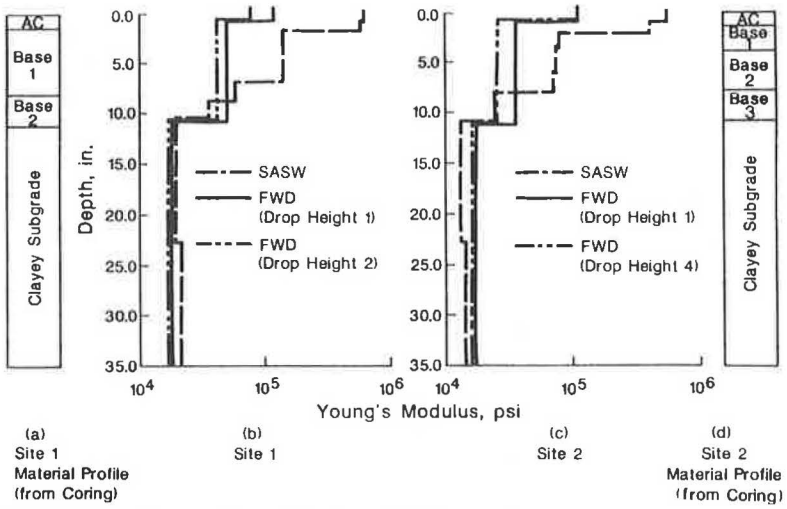

FIGURE 9 Composite profiles from SASW and FWD tests at the two sites after rain.

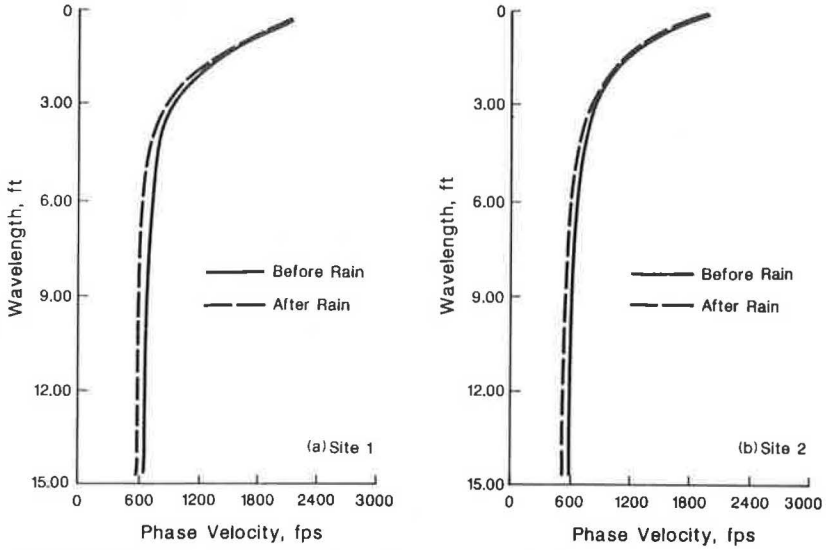

FIGURE 10 Comparison of dispersion curves obtained by SASW tests for before- and after-rain conditions.

Young's moduli from the two sets of tests performed at Sites 1 and 2 are compared in Figure 11. The moduli of the first six layers of Site 1 and the first five layers of Site 2 are the same for both series of tests. However, moduli of the last two layers of Site 1 are approximately 20 percent softer. Moduli of the the last three layers of Site 2 are as much as 30 percent softer.

Comparison of Moduli from SASW and FWD Tests

Unfortunately, FWD tests were not carried out during the first series of tests in March 1986. Therefore only FWD results for Sites 1 and 2 can be compared for the after-rain series. Measured deflection basins are given in Table 4 for nominal drop loads of 5 and 15 kips. The FWD sensors were spaced 1 ft apart. For both loads, the measured basins are quite sensitive to the overall differences between the pavement sites; that is, the deflections at Site 2 are larger than those at Site 1. However, at both sites, deflections measured at the farther sensors (5 and 6) are nearly the same, which indicates that subgrade moduli at the two sites are quite similar; the subgrade modulus at Site 2 is slightly smaller than that at Site 1. This is the same relationship that was found by the SASW tests.

Modulus profiles of the two sites backcalculated by basin fitting are given in Tables 5 and 6 for Sites 1 and 2, respectively. These modulus profiles appear to indicate that the cause of pavement deterioration at Site 2 (in comparison with Site 1) is the softness of the base layer, which represents the primary difference between the sites. Modulus profiles from the SASW tests for both the before- and after-rain conditions show the same trend.

Moduli determined from nominal loads of 5 and 15 kips are compared in Tables 5 and 6 for both sites. Moduli of base materials obtained from the smaller load are larger than those from the larger load at both sites. This is due to nonlinear behavior of the base material at the higher load as discussed subsequently.

Moduli obtained by the SASW and FWD tests are compared in Figure 9 and Table 5 for Sites 1 and 2, respectively. Subgrade moduli compare well in both cases. However, moduli of the base and AC layers are much higher from the SASW tests. This difference in base moduli is due mainly to nonlinear behavior caused by the high load levels in the FWD tests. It is difficult to comment on the difference in moduli of the AC layer, primarily because of the insensitivity of the FWD method to thin surface layers.

As a further comparison of moduli from FWD and SASW tests, moduli determined from the SASW tests were input to program LAYER8, a modified version of the NLAYER program (*10*), to determine a theoretical deflection basin for each site. These theoretical basins are denoted as SASW (L) and are compared with the measured ones [denoted as FWD (M)] in Table 4. Predicted deflections at the last three sensors compare well with the measured ones. The deflections of the first three sensors are smaller for the theoretical basins [SASW (L)] determined from moduli measured by the SASW method. The reason for the favorable comparisons between the deflections of Sensors 4-6 is most probably that these sensors monitor essentially linear behavior.

To investigate in an approximate fashion the effect of nonlinearity on the moduli of different layers, program LAYER8 (*10*) was modified to perform an equivalent linear analysis. In an equivalent linear analysis, a modulus at a known strain level is assumed. The strain is calculated on the basis of the assumed modulus and compared with the assumed strain. If the two strains are within an acceptable tolerance (say 10 percent), the assumed modulus is selected as the so-called "nonlinear" modulus or "equivalent linear" modulus. Otherwise a new modulus based on the average of the calculated and the assumed strains is assumed, and the process is repeated until the strains converge.

The model used to describe the relationship between the modulus and strain is shown in Figure 2. The model is quite suitable for subgrade and granular base materials. This model was assigned to all layers in the pavement systems (including the asphalt layer). Because nonlinearity occurs

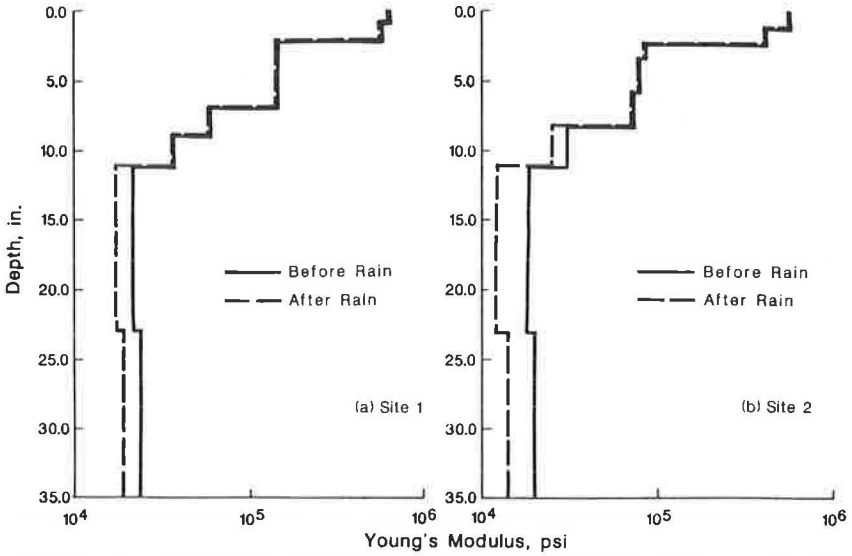

FIGURE 11 Comparison of moduli obtained by SASW tests at the two sites for before- and after-rain conditions.

TABLE 4 COMPARISON OF MEASURED AND THEORETICAL DEFLECTION BASINS FROM FWD AND SASW TESTS

Nominal Load, lb	Site	Deflection Basin Source	Deflections, mils Sensor Number 1	2	3	4	5	6	Mean Square Error, Percent
5000	1	FWD (M)*	13.3	6.4	3.2	1.9	1.5	1.1	---
		FWD (B)*	13.1	5.7	3.1	2.0	1.5	1.1	2.1
		SASW (L)**	8.0	4.7	2.8	1.8	1.3	1.0	8.3
		SASW (NL)**	11.8	6.0	3.3	1.8	1.3	1.0	2.4
	2	FWD (M)	16.2	7.9	3.4	2.1	1.5	1.2	---
		FWD (B)	16.2	6.1	3.2	2.0	1.5	1.2	4.0
		SASW (L)	11.0	6.1	3.5	2.2	1.6	1.2	6.6
		SASW (NL)	17.9	8.1	4.2	2.2	1.6	1.2	4.3
15000	1	FWD (M)	48.4	25.4	12.3	7.1	4.9	3.7	---
		FWD (B)	48.2	19.0	10.0	6.5	4.7	3.7	5.5
		SASW (L)	25.4	10.9	8.9	5.7	4.1	3.2	13.9
		SASW (NL)	50.8	23.4	11.2	6.8	4.7	3.2	3.2
	2	FWD (M)	63.1	34.2	13.1	6.6	4.9	4.0	---
		FWD (B)	63.5	21.1	10.6	6.9	5.0	4.0	7.2
		SASW (L)	35.1	19.5	11.8	7.0	5.1	3.8	10.5
		SASW (NL)	86.0	33.0	14.7	8.4	5.8	3.8	8.5

*M = Measured, B = Deflections from the fitted basin
**L = Linear, NL = Equivalent linear

TABLE 5 COMPARISON OF MODULI OBTAINED BY SASW AND FWD TESTS AT SITE 1

Layer	Layer Thickness, in.	Young's Modulus, ksi SASW	FWD 5 kips	FWD 15 kips	Difference, percent 5 kips (3)-(4)/(3)	Difference, percent 15 kips (3)-(5)/(3)
(1)	(2)	(3)	(4)	(5)	(6)	(7)
AC	1	592	115	75	80.6	87.3
Base	1.2	571			91.2	93.0
	2.4	136			63.2	70.6
	2.4	135			63.0	70.4
			50	40		
	2.0	56.5			16.0	29.2
	2.0	34.9			-30.2	-14.6
Subgrade	12	19.1			5.8	8.4
			18	17.5		
	∞	20.6			12.6	15.0

TABLE 6 COMPARISON OF MODULI OBTAINED BY SASW AND FWD TESTS AT SITE 2

Layer	Layer Thickness, in.	Young's Modulus, ksi SASW	FWD 5 kips	FWD 15 kips	Difference, percent 5 kips (3)-(4)/(3)	Difference, percent 15 kips (3)-(5)/(3)
(1)	(2)	(3)	(4)	(5)	(6)	(7)
AC	1	556	110	110	80.2	80.2
Base	1.2	419			91.6	94.0
	1.2	82.6			57.6	69.7
	2.4	78.3			55.3	68.1
			35.0	25.0		
	2.4	71.5			51.0	65.0
	3	27.7			-26.4	-9.8
Subgrade	12	14.6			17.8	13.0
			17.2	16.5		
	∞	16.9			-1.8	2.4

mainly in the base and subgrade layers, use of this approximation should not result in significant error.

To determine the nonlinear deflection basin, the modulus profile determined from the SASW tests was used as initial input to modified LAYER8. In addition, the profile at each site was divided into eight layers, as shown in Figure 5*a*, with the eighth layer extending to infinity. The algorithm was then used to calculate the equivalent linear modulus at the middle of each layer at radial intervals of 3 in., starting at the centerline of the loaded area and proceeding to a distance at which the initial and equivalent linear moduli were identical (i.e., the moduli were in the linear range, which occurred at distances of from 30 to 50 in. for these tests). It should be mentioned that, because radial variation in moduli cannot be accounted for in LAYER8, some approximation had to be introduced in the calculation of strains and stresses. This approximation was as follows: After the nonlinear modulus profile at each radial distance from the source was obtained, the original version of program LAYER8 (i.e., the linear elastic version) was used to calculate surface deflections. This was done by assigning the equivalent linear modulus profile obtained from the previous calculations at the sensor location of interest and then calculating the surface deflection at that sensor. Therefore, to obtain the deflection basin at each site, program LAYER8 was used six different times (for six sensors) with six different modulus profiles. [The effect of this approximation is under study with a finite-element analysis. However, any adverse effect of this approximation should be most important to deflections at the second and third sensors.]

Deflections obtained as described previously are included in Table 4 as the nonlinear SASW results [denoted as SASW

(NL)]. Deflections based on small-strain (linear) SASW moduli [denoted as SASW (L)] and the FWD basin-fitting procedure [denoted as FWD (B)] are also included in Table 4. It can be seen that the nonlinear SASW deflection basins follow the measured ones favorably, except for the nominal load of 15 kips at the deteriorated site where the deflection of the first sensor is overestimated by about 30 percent.

The percentage differences between the three sets of theoretical deflections [FWD (B), SASW (L), and SASW (NL)] and the measured FWD deflections at each site for the two nominal loads (5 and 15 kips) are shown in Figure 12. The average mean square error of each theoretical basin relative to the measured deflection basin is included in Table 4. The average mean square errors from the basin fitting of the FWD data and nonlinear SASW modulus profiles are quite close, indicating that (at least statistically) both basins (i.e., from basin fitting and from equivalent linear modulus profiles) are almost equally representative of the measured deflection basins. This favorable comparison is a good indication of the accuracy of the moduli obtained by the SASW method, with an added advantage that the nonlinear performance of the pavement system for any given load can be easily estimated. As an example, the ratios of equivalent linear moduli (for a nominal load of 5 kips) to elastic moduli at Site 1 (both obtained from SASW tests) are shown in Figure 13. Variation in the ratios with radial distance from the load for five points within the pavement system are shown. As can be seen in Figure 13, the asphalt layer and the deepest subgrade point do not exhibit much nonlinear behavior (assuming the asphalt layer has the relative change in modulus with strain shown in Figure 2). Also, it can be seen that, from the center of the loaded area out to normalized radial distances of about 1.5, the base material close to the base-subgrade interface is critical because it exhibits the highest amount of nonlinearity. From that point on, the subgrade exhibits a larger amount of nonlinearity. At normalized radial distances of 5 or more, all layers exhibit linear behavior.

SUMMARY AND CONCLUSIONS

One problem facing the engineer is evaluating the integrity of existing pavements. When secondary roads are load zoned, the mechanisms that cause failure of the pavement should be well understood in terms of delineation of possible zones of weakness or seasonal change. It is demonstrated that the SASW method can be used to evaluate effectively possible causes of deterioration in pavement sections. The SASW method is a powerful tool because of the numerous layers that can be used to create fine, detailed resolution in the modulus profile.

In network-level studies, the dispersion curves obtained from SASW tests can be used effectively to determine the approximate location of weak zones. However, the testing technique should be automated to achieve this goal. At the project level, modulus profiles of the pavement system from SASW testing can be determined in detail. At this time, a typical SASW test takes about 30 min to perform in the field and about 2 hr to reduce in the office. Both aspects of field testing and in-house data reduction are being automated to reduce the testing time and data reduction to several minutes for future network-level studies.

To illustrate the use of the SASW method on secondary roads, two sites were tested to evaluate the accuracy of layering determined from the modulus profiles, determine possible reasons for rutting at one of the sites, and evaluate any changes in the modulus profiles resulting from heavy rains. The following results were found.

1. Layering estimated from the modulus profiles at both sites differed somewhat from layers shown on the construction plans. Coring of the sites after completion of the SASW tests substantiated that the layering estimated from the SASW tests was more representative of the actual material profiles than were the construction plans.

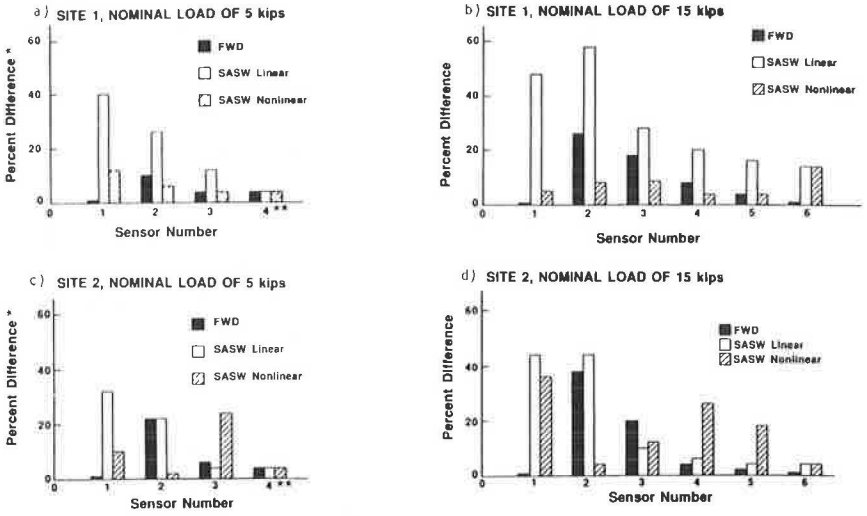

* Corresponds to the absolute value of: (measured FWD deflection minus deflection predicted from modulus profile) divided by deflection predicted from modulus profile
**Sensors 5 and 6 are not shown because in all cases differences were less than the accuracy of sensors (5/± .1 mil)

FIGURE 12 Comparison of deflection basins measured by FWD tests and those backcalculated from modulus profiles estimated from SASW and FWD tests.

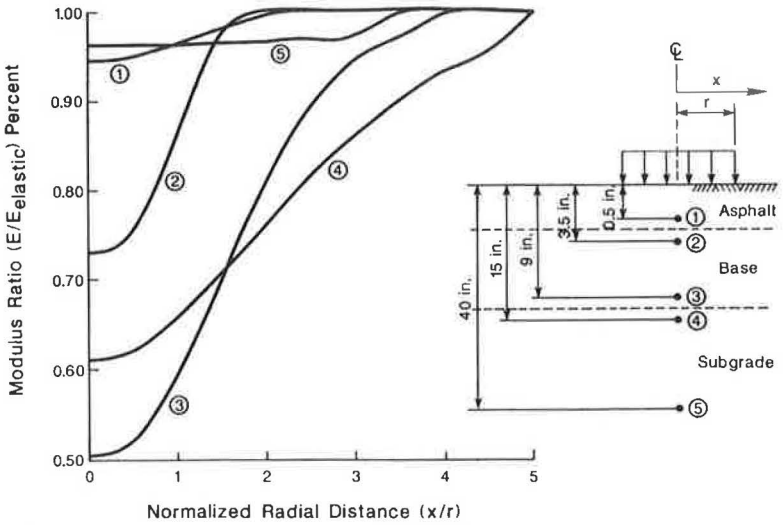

FIGURE 13 Distribution of reduction of modulus with depth and radial distance at Site 1 for FWD testing with a nominal load of 5 kips.

2. The reason for rutting at one of the two sites appears to be the base layer, which was about 70 percent softer at the rutted site, although a 15 percent softer subgrade at the rutted site may also have contributed to the surface rutting.
3. The effect of heavy rain at the two sites was primarily a softening of the subgrade. This softening turned out to be slightly more severe at the deteriorated site.

In addition to the SASW tests, FWD tests were performed at the two sites after the heavy rains for comparison purposes. These tests showed the following results:

1. Modulus profiles determined from the FWD and SASW tests indicate that both test methods show the relative softness of the base material at the rutted site.
2. Moduli determined from the FWD and SASW tests differed significantly for the base layer primarily because of the different strain levels associated with the two testing methods. Moduli of the base layer from the FWD tests were significantly lower, with moduli decreasing with increasing load levels as expected for nonlinear behavior.
3. Calculated deflections based on the SASW modulus profiles compare well with deflections measured by the FWD tests for the last three sensors. At the first three sensor locations, measured deflections are significantly greater than those predicted with the (linear) SASW modulus profiles. If nonlinear effects are taken into account, equivalent linear moduli from the SASW tests produce deflection basins that statistically follow the measured FWD deflection basins as well as those of the fitted FWD basin.

ACKNOWLEDGMENT

This work was supported by the Texas State Department of Highways and Public Transportation.

REFERENCES

1. S. Nazarian, K. H. Stokoe II, and W. R. Hudson. Use of Spectral-Analysis-of-Surface-Waves Method for Determination of Moduli and Thicknesses of Pavement Systems. In *Transportation Research Record 930,* TRB, National Research Council, Washington, D.C., 1983, pp. 38-45.
2. S. Nazarian. *In Situ Determination of Elastic Moduli of Soil Deposits and Pavement Systems by Spectral-Analysis-of-Surface-Waves Method.* Ph.D. dissertation. The University of Texas at Austin, 1984, 453 pp.
3. S. Nazarian and K. H. Stokoe II. Use of Surface Waves in Pavement Evaluation. In *Transportation Research Record 1070,* TRB, National Research Council, Washington, D.C., 1986, pp. 132-144.
4. W. T. Thomson. Transmission of Elastic Waves Through a Stratified Solid Medium. *Journal of Applied Physics,* Vol. 21, 1950, pp. 89-93.
5. N. A. Haskell. The Dispersion of Surface Waves on Multilayered Media. *Bulletin of Seismological Society of America,* Vol. 43, No. 1, 1953, pp. 17-34.
6. S. Nazarian and K. H. Stokoe II. Nondestructive Testing of Pavements Using Surface Waves. In *Transportation Research Record 993,* TRB, National Research Council, Washington, D.C., 1984, pp. 67-79.
7. S. H. Ni. *Evaluation of Dynamic Soil Properties Under Three-Dimensional States of Stress Using Resonant Column Equipment.* Ph.D. dissertation. The University of Texas at Austin, 1987.
8. H. S. Heisey, K. H. Stokoe II, W. R. Hudson, and A. H. Meyer. *Determination of In Situ Shear Wave Velocities from Spectral Analysis of Surface Waves.* Research Report 256-2. Center for Transportation Research, The University of Texas at Austin, 1982.
9. R. F. Ballard, Jr. *Determination of Soil Shear Moduli at Depth by In-Situ Vibratory Techniques.* Miscellaneous Paper 4-691. U.S. Army Engineer Waterways Experiment Station, Vicksburg, Miss., 1964.
10. J. Michelow. *Analysis of Stress and Displacements in an N-Layered Elastic System Under a Load Uniformly Distributed on a Circular Area.* California Research Corporation.

Publication of this paper sponsored by Committee on Flexible Pavement Design.

Combined Effect of Traffic Loads and Thermal Gradients on Concrete Pavement Design

VICTOR FARAGGI, CARLOS JOFRÉ, AND CARLOS KRAEMER

The purpose of this work is to study the behavior of concrete pavements under the simultaneous action of traffic and thermal gradients in concrete slabs. A new procedure for the structural design of concrete pavements in Spain is presented. A fatigue equation, taken from an adjustment of Tepfer's fatigue law and based on data on the behavior of several concrete pavements in Spain, is proposed. Analyses of loading stresses, thermal warping stresses, and simultaneous action stresses in slabs resting on a stratified semi-infinite solid were performed using a finite-element computer program. Empirical and theoretical equations for predicting the different values of thermal gradients and the frequency of their occurence were established; these equations are based on Fourier's law and data obtained from observations in Spain. A computer program was developed to obtain new equivalence factors based on the results of the calculations. New conversion formulas for axle loads, corresponding to the fatigue damage criterion adopted, were also developed. This simplified and more realistic design procedure was used to check some of the structural sections included in the Spanish Catalogue of Rigid Pavements. Finally, a new catalog, which takes into consideration the influence of the geometric characteristics of slabs (thickness and length) and the presence of thermal gradients, was proposed. Thermal gradients were estimated using a climatic regionalization of Spain.

It is usual, in structural calculations, to consider two types of stresses: those produced by applied loads (either permanent or variable) and those produced by thermal effects. Normally, these types of stress are computed separately and the results are subsequently added. This procedure is correct for buildings, the support conditions of which are the same for both types of stress. In concrete pavements, however, this is not true because, as is well known, slabs warp as a consequence of thermal gradients, and a part of each one temporarily detaches from the underlying layer. When slabs are warped, deformations produced by traffic loads can reestablish at least partial contact with the lower layer. From a mathematical point of view, the boundary conditions of the problem of calculating stresses and strains in a particular slab with a traffic load and a thermal gradient applied simultaneously are not the same as those that prevail when the two are considered separately. In some cases, it has been proved by measurements on existing pavements that the values of stresses calculated by adding individually obtained values are too low.

This problem is of special significance in Spain where climatic variations are very important in many regions and where, in addition, maximum legal single-axle loads are among the highest in the world (*1*).

Consequently, research was undertaken to calculate the combined effects of traffic loads and thermal gradients on concrete pavements.

This work was divided into two parts. In the first, theoretical phase, the following topics were studied:

- Establishment of a method of determining the frequency and range of thermal gradients in pavement slabs from climatic parameters such as temperature variations and insolation (*2*).
- Calculation of the maximum stresses produced in a pavement by the simultaneous application of traffic loads and thermal gradients. Because this problem is far from being solved in an analytical way, a computer program (RISC) (*3*) based on the finite-element method was employed to calculate these stresses in a series of cases. Then, several correlations were set up between the stresses calculated and the different parameters concerned (e.g., thermal gradients, length and thickness of slab).
- Selection of a fatigue law in line with the observed behavior of some Spanish concrete pavements.

There was also a practical part, based on the results obtained in the theoretical one, in which some problems were tackled, taking into account the particular climatic characteristics and load distributions of Spanish roads:

- Definition of a climatic division of Spain, taking into consideration the thermal gradients that occur.
- Definition of an average load and hourly distribution based on measurements taken by portable dynamic scales.
- Establishment of equivalence ratios among different axle loads, which takes into account such factors as climate and slab lengths.
- Establishment of equivalence ratios between an average Spanish truck and a standard axle load of 130 kN (29,225 lb) (maximum single-axle load legally permitted in Spain), also taking into account the previously mentioned factors.
- Revision of the current Spanish Catalogue of Structural Section for Rigid Pavements and proposals for a new one.

V. Faraggi, Department of Civil Engineering, University of Chile, Santiago, Chile. C. Jofré, Instituto Eduardo Torroja, Madrid, Spain. C. Kraemer, Universidad Politécnica de Madrid, Madrid, Spain.

THEORETICAL PHASE

Method of Calculating Thermal Gradients

Assuming that the quantity of heat absorbed by a body is equal to that released by it, this heat transmission is regulated by Fourier's law:

$$dT/dt = \lambda/c\rho\,[(\delta^2T/\delta x^2) + (\delta^2T/\delta y^2) + (\delta^2T/\delta z^2)] \quad (1)$$

where

T = body temperature (°C),
t = time (hr),
c = specific heat of the body (J/kg°K),
ρ = mass density (kg/cm^3),
λ = thermal conductivity of the body (W/m°K),
x, y = coordinates in the horizontal plane (m), and
z = coordinate perpendicular to the plane (x, y) (m).

If thermal flow inside a horizontal plane is insignificant, Equation 1 can be formulated as

$$dT/dt = a\,d^2T/d_z^2 \quad (2)$$

If a sinusoidal temperature variation over a period of time is assumed, the solution of Equation 2 can be written as

$$T_{zt} = t_M + t_o \exp(-z\sqrt{\text{II}/aT})\sin(2\text{II}t/T - z\sqrt{\text{II}/aT}) \quad (3)$$

where

T_{zt} = temperature at depth z at instant t;
t_M = average temperature of bottom or surface, or both, over an interval of 24 hr (°C);
t_o = range of temperature variation in the pavement surface during the 24-hr interval (°C);
T = period of cyclic variation (86,400-sec daily cycle) in temperature; and
a = diffusivity coefficient (m^2/sec).

As shown in Figure 1, the intensity of solar radiation from a cloudless sky increases continuously from sunrise to zenith and then decreases, also at a constant rate, until sundown. The fall in temperature does not end at sundown because thermal energy stored in the pavement is released through its surface throughout the night. Consequently, temperature variations of the pavement surface over a 24-hr period cannot be represented by a single sinusoidal function.

The interval during which temperature increases more or less corresponds to one-half of the sunlight period; the decreasing cycle also includes the night hours. Thus an evident dissymmetry appears in the development of the surface temperatures of the pavement throughout the day and when it is to be described in an analytical way, two expressions must be used, one of them applying to the interval from sunrise to zenith and the other from zenith to the following sunrise.

Consequently, during the interval between sunrise ($t = 0$) and zenith ($t = S_h$) and in accordance with Equation 3, the following expression can be used to calculate the surface temperature of the pavement:

$$T_{ot} = t_M + t_o \sin[\text{II}(2t - S_h)/2\,S_h] \quad (4)$$

where

T_{ot} = temperature of the surface of the pavement at instant t,
t_M = average temperature of the surface over a 24-hr period, and
t_o = range of temperature variation in the pavement surface over a 24-hr period (°C).

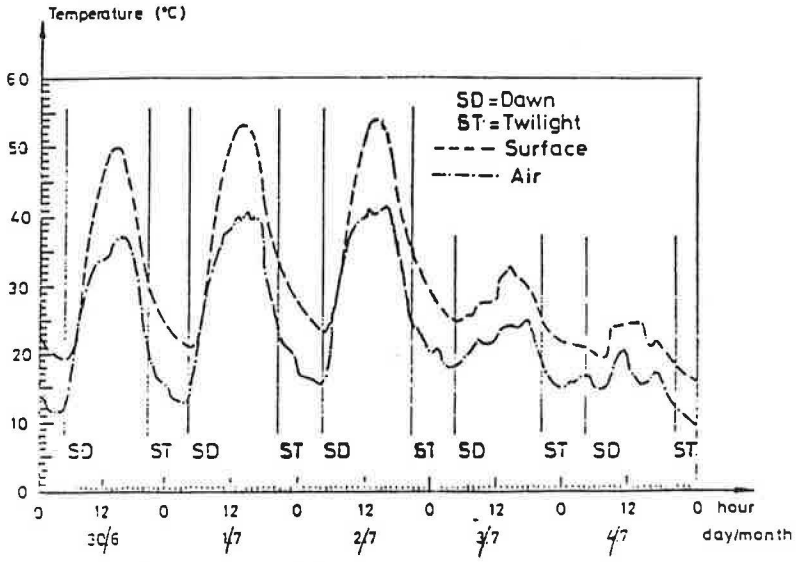

FIGURE 1 Development of air and pavement surface temperature on five consecutive days in summer.

During the time between one zenith and the following sunrise (T-S_h = 24 hr), the surface temperature can be computed by the following formula:

$$T_{ot} = t_M + t_o \sin(\{\Pi[4(t + S_n) - S_a]\}/2 S_a) \quad (5)$$

where S_n is interval between sundown and sunrise, in hours, and $S_a = 2[S_h + S_n]$.

For these parameters, the following values have been used:

- Summer period: $S_h = 10$ hr, $S_n = 7$ hr, $S_a = 34$ hr
- Winter period: $S_h = 8$ hr, $S_n = 10$ hr, $S_a = 36$ hr

At a certain depth (z), extreme values of temperature occur later than they do on the surface. For calculating the temperature variation at depth z, the following expressions, similar to Equations 4 and 5, can be used. A damping factor, representing the thermal inertia of the pavement material, has been introduced.

$$T_{zt} = t_M + t_o \exp(-z\sqrt{\Pi/a}\, S_{zh}) \sin\{[\Pi(2t - S_h)/2 S_n] - [z\sqrt{\Pi/a}\, S_{zh}]\} \quad (6)$$

and

$$T_{zt} = t_M + t_o \exp(-z\sqrt{\Pi/a}\, S_{za}) \sin(\{\Pi[4(t + S_n) - S_a]/2 S_a\} - z\sqrt{\Pi/a}\, S_{za}) \quad (7)$$

where

$$S_{zh} = z^2 S_h^2/a\pi u_z^2 \quad (8)$$

$$S_{za} = z^2 S_a^2/a\pi u_z^2 \quad (9)$$

and

$$u_z = (z/2)\sqrt{T/a\pi}$$

It has been assumed that $a = 0.31 \times 10^{-8}$ m^2/sec.

Also, in Expressions 7 and 8,

$t_M = t_A + t_I$,
t_A = air temperature (°C),
t_I = temperature increase due to insolation (°C),
$t_o = \Delta t_o + t_I$,
Δt_o = variation of air temperature, and

$$t_I = (0.6\,\alpha\, I_o/h) - 3.9. \quad (10)$$

In Formula 10,

α = normal absorptivity, assumed to be equal to 0.65 for heat transfer;
h = pellicular transfer coefficient, assumed to be equal to 20 W/°Km^2 for concrete; and
I_o = solar constant, equal to 1300 W/m^2.

In Figure 2 the intervals in which Expressions 4, 5, 6, and 7, respectively, apply are represented in a schematic manner.

To make the calculations in connection with these formulas, a computer program (TEMP 1) was developed. To harmonize the results of this program with those of some measurements taken in the field, three coefficients (α, β, and γ) were introduced. α is an adjustment coefficient, β a corrective wind coefficient, and γ a corrective rain coefficient.

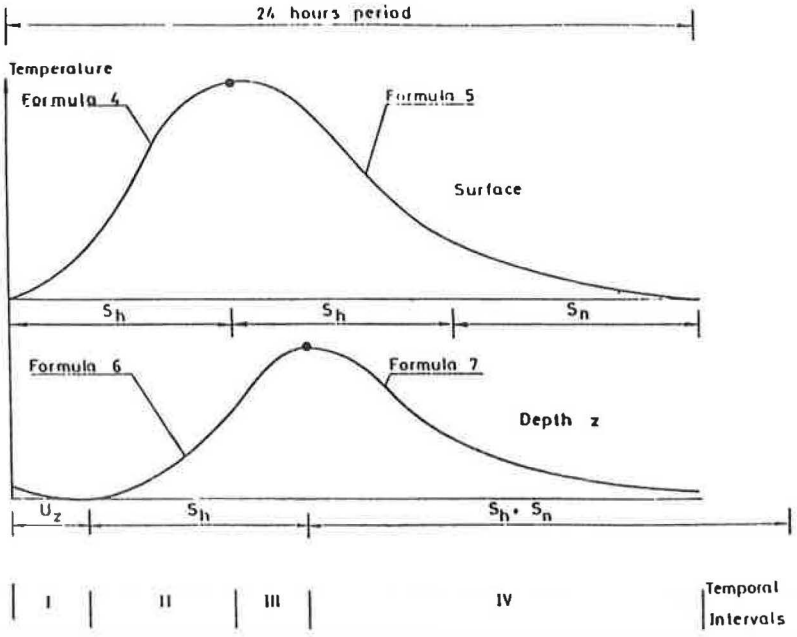

FIGURE 2 Domains of validity of Expressions 4-7.

The coefficient β is defined by the expression

$$\beta = \sqrt{(H + C)^2 + C^2} \quad (11)$$

where

H = α_k/λ (m^{-1}),
C = $\sqrt{\beta/at}$ (m^{-1}),
α_k = $7.38 + 4.91 \times W^{0.75}$ ($W/m^2\,°K$), and
W = wind speed (m/sec).

The γ coefficient represents the complement of rainy days per thousand.

These coefficients are introduced in calculating t_M and t_o as follows:

$$t_M = (t_A + t_J)\beta\gamma$$
$$t_o = (\Delta t_o + t_J)\beta\gamma(1 - \alpha) \quad (12)$$

Computation of Stresses Caused by the Combined Effect of Traffic Loads and Thermal Gradients

To compute the effect of simultaneously applying traffic loads and thermal gradients, several values of some relevant parameters were combined. These values are given in Table 1.

As can be seen in Figure 3, central load position (C) represents a single-wheel, single-axle load placed between two transverse joints. The wheel separation is 182.9 cm between centers, and the distance between the longitudinal joint and the outer wheel center is 45.7 cm. J represents the same load placed tangentially to a transverse joint.

If these load cases are compared with the classic ones studied by Westergaard (*4*), Case C can be assimilated to a combination of a central load and an edge load and Case J to a combination of an edge load and a corner one.

Of the various cases included in Table 1, those combining traffic loads with zero gradients were used to compare the results provided by the finite-element method with those obtained through other procedures [e.g., the Pickett and Ray influence charts (*5*)]. Both solutions adapted well.

Moreover, combinations of thermal gradients and zero traffic loads were employed to compare their results with those obtained by means of the Westergaard-Bradbury-Kelley theory. It was found that the solutions supplied by the classic theory are usually underestimates.

TABLE 1 VALUES OF DESIGN PARAMETERS CONSIDERED IN THE STUDY

Slab Length (cm)	Slab Thickness (cm)	Axle Load (kN)	Load Position	Thermal Gradient (°C/cm)
350	23	0	C	0
450	25	80	J	0.3
550	28	130		0.6
		160		0.8
				-0.4

It must be pointed out that, through these particular combinations (traffic load with zero gradient and thermal gradient with zero traffic load), it was possible to make a comparison between the stresses resulting from the addition of these values obtained separately for the two cases (as is assumed in some design procedures) and those calculated by considering the simultaneous presence of the same traffic load and the same thermal gradient.

In all cases the concrete slabs were assumed to be resting on a stratified elastic solid composed of the following layers:

- A cement-treated base 15 cm thick,
- A soil-cement subbase also 15 cm thick, and
- A subgrade with an infinite thickness and a California bearing ratio of 5.

Table 2 gives the maximum values of stresses obtained for the various combinations studied. It must be emphasized that, in order to be on the safe side, a single slab was considered in all cases (i.e., no load transfer through transverse joints was taken into account).

Because the program used requires a considerable amount of computer time, a regression analysis was performed on the results of the different combinations studied. The purpose was to obtain formulas that would give the maximum values of stresses (all expressed in the same way) as a function of the following parameters:

- Axle load (P) in tons,
- Thermal gradient (θ) in °C/cm, and
- Thickness (h) and length (L) of the slabs in cm.

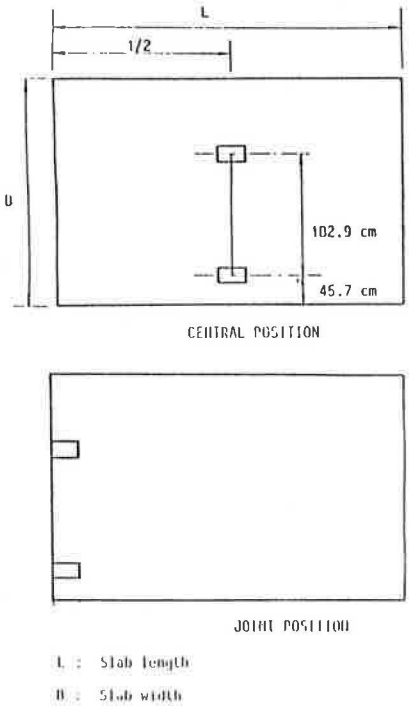

FIGURE 3 Different load positions considered in the study.

TABLE 2 MAXIMUM VALUES OF STRESS (MPa) IN CONCRETE SLABS SUBJECTED TO TRAFFIC LOADS OR THERMAL GRADIENTS, OR BOTH

Slab			Thermal Gradient																	
			0°C/cm at Axle Load (tons)			-0.4°C/cm at Axle Load (tons)				+0.3°C/cm at Axle Load (tons)				+0.6°C/cm at Axle Load (tons)				+0.8°C/cm at Axle Load (tons)			
Length (cm)	Thickness (cm)	Load Position	8	13	16	0	8	13	16	0	8	13	16	0	8	13	16	0	8	13	16
350	23	C	0.59	0.91	1.18	0.44	1.94	2.33	2.29	1.30	2.29	2.49	2.67	1.30	3.08	3.76	4.35			4.39	
		J	1.17	1.68	1.81			2.51				3.00				4.81		1.20	3.69	4.39	4.77
	25	C	0.56	0.85	1.06	0.77	1.74	2.07	2.11	1.20	2..00	2.68	2.94	1.20	3.03	3.59	3.97	1.20	4.39	5.17	5.76
		J	1.01	1.57	1.72	0.77	2.03	2.64	2.66		2.62	2.93			3.29	4.56	5.02			4.33	
	28	C	0.49	0.80	1.03	0.70	1.70	1.91	2.05	1.10	1.96	2.48	2.89	1.30	3.00	3.46	3.78			4.33	
		J	0.88	1.37	1.65			2.53				2.83				3.61				4.92	
450	23	C	0.59	1.06	1.33	1.55	1.96	2.49	2.52	1.28	2.43	2.74	3.04	1.89	3.38	4.10	4.67			5.29	
		J	1.13	1.68	2.04			2.49				2.95				4.81		1.70	4.41	4.90	5.28
	25	C	0.52	0.83	1.16	1.73	2.06	2.42	2.46	1.37	2.18	2.79	3.03	1.70	3.44	3.94	4.37	1.70	4.38	4.49	5.93
		J	1.00	1.57	1.97		2.46	2.57	2.70	1.37	2.51	2.75	3.37	1.70	3.17	4.41	5.01			4.95	
	28	C	0.47	0.76	0.94	1.73	2.06	2.34	2.53	1.45	2.28	2.70	3.06	1.54	3.38	3.90	4.23			4.86	
		J	0.85	1.40	1.51			2.74				1.98				3.73				5.00	
550	23	C	0.65	1.05	1.34	2.10	2.40	2.62	2.46	1.31	2.38	2.76	2.47	2.48	3.56	4.30	4.87			5.05	
		J	1.18	1.68	2.05			2.51				2.90				4.64			4.57	5.06	5.46
	25	C	0.56	0.92	1.16	2.20	2.20	2.29	2.46	1.42	2.39	2.99	2.68	2.35	3.48	4.09	4.52	2.35	4.48	5.16	5.74
		J	0.99	1.57	1.97		2.60	2.77	2.63	1.42	2.63	2.83	3.73	2.35	2.65	4.41	5.05			5.24	
	28	C	0.50	0.82	1.03	2.03	2.10	2.16	2.40	1.52	2.27	2.77	3.19	2.13	3.60	4.03	4.36			4.87	
		J	0.89	1.37	1.63			2.60				1.97				3.86					

NOTE: C = central load position and J = joint load position.

Stresses calculated by these formulas are expressed in MPa. Several types of correlations were studied both for the central load position and for the joint one. Exponential formulas provided the best results, and they are included hereafter, as are the correlation coefficients (Rs) obtained in each case.

1. Traffic loads without gradients:
Central load position

$$\sigma_c = e^{0.356}(P^{1.046}L^{0.128}/h^{1.219}) \quad (13)$$
$(R = 0.985)$

Joint load position

$$\sigma_j = e^{2.042}(P^{0.802}L^{0.0403}/h^{1.215}) \quad (14)$$
$(R = 0.890)$

2. Traffic loads and thermal gradients:
Central load position

$$\sigma_c = e^{-0.193}(P^{0.36}L^{0.25}\theta^{0.589}/h^{0.18}) \quad (15)$$
$(R = 0.956)$

Joint load position

$$\sigma_j = e^{3.503}(P^{0.357}L^{-0.079}\theta^{0.507}/h^{0.701}) \quad (16)$$
$(R = 0.886)$

3. Thermal gradients without traffic loads:
Central load position

$$\sigma_c = e^{-6.113}(L^{1.125}\theta^{0.319}/h^{0.028}) \quad (17)$$
$(R = 0.886)$

In this last case, the formula deduced for the joint load position does not have a correlation coefficient similar to the previous ones, and for this reason it has not been included.

As can be seen, the proposed formulas provide very good correlations for the central load position. As far as the joint position is concerned, the accuracy of the adjustment is also most striking but less satisfactory.

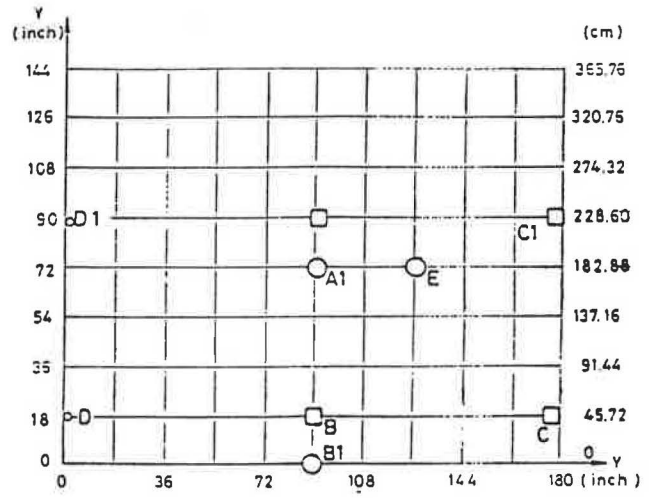

FIGURE 4 Finite-element mesh and critical points for the load positions considered.

As was to be expected, the slab points at which the maximum stresses occur vary with the case in question. These points are shown in Figure 4 which also shows the finite-element mesh employed in the computer program.

Tables 3-5 give the values of stresses σ_x and σ_y (parallel to the edges) at these particular points and also the maximum stress. Usually, this is parallel to one edge or joint, or very close to it.

Table 6 gives a comparison between the stresses obtained considering the simultaneous effect of a traffic load and a thermal gradient and the values that result from adding the stresses obtained when each factor is considered separately. In the authors' opinion, the results in this table are one of the most interesting findings of the present work.

As can be seen, in virtually all the cases considered in Table 6 the stresses obtained for a traffic load and a thermal gradient applied at the same time are clearly greater than the sum of the stresses calculated separately. As a consequence, the results obtained by the latter procedure, and employed in some design procedures, are unsafe.

Table 7 gives the percentage of rates between the stresses computed by these two procedures. As can be seen, these rates are very high in most cases and have a great effect on design calculations.

An analysis of the stresses shows that, for an axle load equal to 130 kN, maximum values are obtained when this load is placed near a transverse joint, which is in keeping with Westergaard's theory (*4*).

However, differences between the stresses resulting from central and joint positions of the axle load (a very important factor when there are no gradients) decrease when the gradients increase. Even for gradients of about +0.3°C/cm, stresses caused by axle loads on the so-called central position are slightly higher than those caused by the same load placed near a transverse joint.

Adjustment of a Fatigue Law

Because the only damage factor considered in the present work was pavement fatigue, an essential step was to adapt a fatigue law suitable for the concrete. As is well known, this problem can be regarded as still unsolved (*6*). A great many researchers have dealt with fatigue phenomena of concrete under bending, and they have proposed different laws that give inconsistent results when compared. After different possibilities were analyzed, the following fatigue law, which takes into account the ratio between the maximum and the minimum applied stresses, was proposed:

$$\log_{10}NF = 11\,[1 - (\sigma_{max}/MR)]/(1 - R) \quad (18)$$

where

NF = number of loading cycles producing failure;
σ_{max} = maximum applied stress;
MR = modulus of rupture of the concrete at 28 days (third-point loading method) increased by 10 percent to consider strength gain with age;

TABLE 3 MAXIMUM VALUES OF STRESSES (MPa) AT CRITICAL POINTS (central load position)

Point (coordinates x, y)	θ = 0°C/cm P = 13 t			θ = -0.4°C/cm P = 13 t			θ = +0.3°C/cm P = 13 t			θ = +0.6°C/cm P = 13 T		
	σ_x	σ_y	σ_{max}	σ_x	σ_y	σ_{max}	σ_x	σ_y	σ_{max}	σ_x	σ_y	σ_{max}
A[a] (L/2, 3H/8)	-0.76	0.07	-0.76	1.01	2.41	2.41	-1.36	-2.05	-2.05	-2.97	-1.67	-2.98
B (L/2, H/8)	-0.83	-0.10	-0.83	0.10	0.76	0.82	-1.74	-2.77	-2.77	-3.95	-1.92	-3.95

NOTE: Negative values correspond to tension in bottom fibers.
[a]L = slab length (4.57 m); H = slab width (3.66 m).

TABLE 4 MAXIMUM VALUES OF STRESSES (MPa) AT CRITICAL POINTS (joint load position)

Point (coordinates x, y)	θ = 0°C/cm P = 13 t			θ = -0.4°C/cm P = 13 t			θ = +0.3°C/cm P = 13 t			θ = +0.6°C/cm P = 13 T		
	σ_x	σ_y	σ_{max}	σ_x	σ_y	σ_{max}	σ_x	σ_y	σ_{max}	σ_x	σ_y	σ_{max}
C[a] (L, H/8)	-0.13	-1.56	-1.57	0.05	-0.95	-1.04	-2.28	-2.35	-2.35	-0.43	-3.43	-3.52
C1 (L, 5H/8)	-0.12	-1.48	-1.52	-0.12	-0.96	-1.02	-2.23	-2.76	-2.76	-0.39	-4.39	-4.39
E (0.7L, H/2)	0.52	0.09	0.52	2.61	2.20	2.61	-0.75	-1.03	-1.03	-1.13	-1.30	-1.35

NOTE: Negative values correspond to tension in bottom fibers.
[a]L = slab length (4.57 m); H = slab width (3.66 m).

TABLE 5 MAXIMUM VALUES OF STRESSES (MPa) AT CRITICAL POINTS IN SLAB SUBJECTED ONLY TO THERMAL GRADIENTS

Point (coordinates x, y)	θ = -0.4°C/cm P = 0 t			θ = +0.3°C/cm P = 0 t			θ = +0.6°C/cm P = 0 t		
	σ_x	σ_y	σ_{max}	σ_x	σ_y	σ_{max}	σ_x	σ_y	σ_{max}
A[a] (L/2, 3H/8)	1.33	0.80	1.33	-1.13	-0.71	-1.13	-1.40	-0.53	-1.40
B (L/2, H/8)	0.84	0.03	0.84	-1.26	-0.26	-1.26	-1.59	-0.25	-1.59
C (L, H/8)	0.02	0.12	0.12	-0.11	-0.67	-0.78	-0.13	-0.75	-0.91
C1 (L, 5H/8)	0.005	0.2	0.2	-0.07	-1.16	-1.16	-0.08	-1.26	-1.27
E (0.7 L, H/2)	0.65	0.87	0.88	-0.94	-0.85	-0.94	-1.17	-0.85	-1.18
A1 (L/2, H/2)	1.72	1.37	1.72	-1.11	-0.78	-1.11	-1.38	-0.76	-1.38
B1 (L/2, 0)	0.75	-0.002	0.75	-1.37	-0.62	-1.37	-1.70	-0.06	-1.70

NOTE: Negative values correspond to tension in bottom fibers.
[a]L = slab length (4.57 m); H = slab width (3.66 m).

$R = \sigma_{min}/\sigma_{max}$,
σ_{min} = minimum stress; and
σ_{max} = maximum stress.

For instance, when the pavement is subjected to a certain thermal gradient, σ_{min} is the stress due to this gradient and σ_{max} the stress caused by the combined effect of this gradient and a traffic load.

The numerical coefficient 11 included in Expression 19 differs slightly from those proposed by other researchers

TABLE 6 COMPARISON OF STRESSES OBTAINED IN DIFFERENT CASES.

Point (coordinates x, y)	θ = -0.4°C/cm, P = 130 kN			θ = -0.4°C/cm, P = 130 kN			θ = +0.6°C/cm, P = 130 kN			θ = +0.6°C/cm, P = 130 kN		
	σ_x	σ_y	σ_{max}	σ_x	σ_y	σ_{max}	σ_x	σ_y	σ_{max}	σ_x	σ_y	σ_{max}
Central Load Position												
				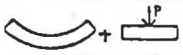						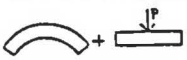		
A[a] (L/2, 3H/8)	1.04	2.41	2.42	0.57	0.87	0.87	-2.97	-1.67	-2.98	-2.17	0.46	-2.17
B (L/2, H/8)	0.102	0.76	0.82	0.01	-0.07	-0.07	-3.95	-1.92	-3.95	-2.39	-0.35	-2.39
Joint Load Position												
				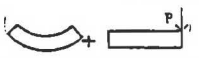								
C (L, H/8)	0.05	-0.95	-1.04	-0.11	-1.44	-1.44	-0.43	-3.43	-3.52	-0.26	-2.31	-2.31
C1 L, 5H/8)	-0.12	-0.96	-1.02	-0.012	-1.20	-1.20	-0.39	-4.39	-4.41	-0.20	-2.78	-2.78
E (0.7L, H/2)	2.61	2.14	2.61	1.17	0.97	1.17	-1.13	-1.30	-1.35	-0.66	-0.76	-0.76

NOTE: Negative values correspond to tension in bottom fibers.

[a]L = slab length (4.57 m); H = slab width (3.66 m).

TABLE 7 INCREASES IN THE STRESSES OBTAINED BY SIMULTANEOUS ACTION OF TRAFFIC LOADS AND THERMAL GRADIENTS COMPARED WITH THOSE OBTAINED SEPARATELY

Load (kN)	Load Position	Thermal Gradient (°C/cm)	Stress Increase	
			Absolute (MPa)	Percentage
130	C	-0.4	1.55	278
130	C	+0.6	0.81	137
130	J	-0.4	1.44	224
130	J	+0.6	1.62	158

NOTE:: C = central load position; J = joint load position.

[e.g., Domenichini and Marchiona (*6*)]. It was obtained by adjustment in order to match the fatigue law to the field behavior of several Spanish concrete pavements:

- Some stretches of the Mediterranean Motorway are situated in a region with a mild, maritime climate. The concrete pavements are composed of slabs that are 25 cm thick and variable in length. They are subjected to average daily traffic (ADT) of about 10,000 vehicles, and the proportion of heavy vehicles amounts to 20 percent. The largest slabs, 500 cm long, began to crack 6 years after they were opened to traffic,
- The Villalobas Bypass on National Highway 301 is situated in a continental climatic zone and subjected to an ADT of 16,000 vehicles, with 25 percent heavy vehicles. The concrete pavement is 23 cm thick with transverse joints placed at varying intervals. Cracking in the largest slabs, 600 cm long, was observed as early as only 6 months and 1 year after they were opened to traffic.

PRACTICAL WORK

As an application of the theoretical results obtained in the first part of this work, some of the subjects included in the current Spanish standard (6-2-IC) for the design of rigid pavements were evaluated. In consideration of the different climatic zones in Spain and the composition of the traffic, the following items were analyzed:

- The equivalence factors between axle loads: the current Spanish standard assumed the fourth-power law established from the results of the AASHO test;
- The damaging factor of an average Spanish truck, expressed in terms of standard axles of 130 kN: the current Spanish standard recommends an equivalence of 0.5 standard axle per average commercial vehicle; and
- The structural sections proposed in this standard.

To perform these practical applications, two prior analyses had to be carried out:

- A climatic division of Spain on the basis of the occurrence of thermal gradients and
- An evaluation of the "aggressiveness" of the average Spanish traffic on the national network, taking into account the axle load range, which was obtained with the help of portable dynamic scales.

Climatic Division of Spain Based on the Occurrence of Thermal Gradients

To establish climatic divisions, data collected by the National Meteorological Service were analyzed, using July and

December data as representative of the average for winter and summer periods, respectively. The following parameters were considered:

- Average air temperature (t_A) and its daily variation about the mean (Δt_A);
- Average number of rainy days taken into account in the γ coefficient of the formulas; and
- Wind speed, which influences the β coefficient.

On the basis of the analysis of these data, Spain was divided into three climatic zones called maritime, standard continental, and extreme continental, respectively. They are characterized by the parameters given in Table 8.

By introducing these values into Expressions 4-7 and grouping them together, the percentages for the occurrence of gradients are obtained for the different climatic zones (Table 9). It must be pointed out, however, that the values given in this table can only be considered a first approach. More accurate calculations would require field measurements and correlation of the results with temperature variations, pluviometry, wind regime, cloudiness, and so forth.

Traffic Load Distribution

To calculate the effect of traffic, the results of a measuring campaign with dynamic scales carried out on several Spanish roads were used. The following traffic load distributions were obtained:

1. The results of traffic distribution by axle load are given in Table 10. It was assumed that this distribution was constant throughout the day.
2. Hourly distribution of traffic.

The results that represent the mean hourly distribution, expressed in terms of ADT percentage, are given in Table 11. The results presented are the average of those for six roads located in the main network.

Combined Distribution of Traffic Load and Thermal Gradients

The combined distribution of the thermal gradients that occur throughout the year in the different climatic zones and the hourly distribution of traffic are given in Table 12.

TABLE 8 CHARACTERISTIC PARAMETERS

Climate	Parameter				
	t_A	Δt_A	α	β	γ
Marine					
Summer	26°C	±6°C	0.4	0.736	1.0
Winter	12°C	±5°C	0.6	0.845	0.3
Standard continental					
Summer	28°C	±8°C	0.35	0.736	1.0
Winter	6°C	±4°C	1.0	0.845	0.2
Extreme continental					
Summer	28°C	±8°C	0.1	0.850	1.0
Winter	3°C	±6°C	-2.0	0.845	0.2

Equivalence Factors Between Different Axle Loads Taking into Consideration Climate and Slab Lengths

As was seen previously, the damaging effect of axle loads depends on whether or not they are combined with thermal gradients. In the absence of gradients, the correlations deduced show an acceptable linearity between the applied loads and the resultant stresses: The exponent of load P in Expressions 13 and 14 is close to 1. However, when a thermal gradient occurs, this linearity disappears; the exponent of load P takes on values of about 0.36 in Expressions 15 and 16. Consequently it is impossible to establish a single equivalence factor between two different axle loads, as adopted in a simplified way in Spanish standard 6-2-IC. Even the slight corrections in these equivalence factors introduced by the AASHO Interim Guide for the Design of Pavements that only takes into account slab thickness can give incorrect results.

If a relationship in the shape of a power law is adopted

$$N_i \times P_i^{\gamma} = N_j \times P_j^{\gamma}$$

TABLE 9 PERCENTAGES OF OCCURRENCE OF THERMAL GRADIENTS

Interval of Thermal Gradient (°C/cm)	Climate		
	Maritime	Standard Continental	Extreme Continental
-0.2 to +0.2	56.93	56.21	37.50
+0.2 to +0.4	16.66	15.97	16.66
+0.4 to +0.5	2.08	3.13	5.02
+0.5 to +0.6	2.08	3.13	5.02
+0.6 to +0.8	0.25	0.375	0.50
-0.2 to -0.4	22.00	21.185	34.94
Total	100.00	100.00	100.00

TABLE 10 TRAFFIC DISTRIBUTION BY AXLE LOADS

Axle Load Interval (kN)	Percentage
0-20	51.910
20-40	8.510
40-60	15.780
60-80	10.470
80-100	4.970
100-120	4.090
120-140	3.090
140-160	1.050
160-180	0.102
180-200	0.089
Total	100.000

TABLE 11 AVERAGE HOURLY DISTRIBUTION OF COMMERCIAL TRAFFIC

Hour	ADT Percentage
9-10	6.69
10-11	6.78
11-12	6.88
12-13	5.23
13-14	5.92
14-15	5.43
15-16	4.63
16-17	5.98
17-18	6.11
18-19	6.90
19-20	6.55
20-21	4.99
21-22	4.64
22-23	3.00
23-24	1.80
0-1	1.37
1-2	0.87
2-3	0.64
3-4	0.74
4-5	0.85
5-6	1.37
6-7	2.13
7-8	4.70
8-9	5.79
Total	100.00

TABLE 12 COMBINED DISTRIBUTION OF TRAFFIC AND THERMAL GRADIENTS

Gradient Interval (°C/cm)	Gradient Adopted in Calculations (°C/cm)	ADT (%) Maritime Climate	Standard Continental Climate	Extreme Continental Climate
-0.2 to 0.2	0.0	60.65	57.05	46.11
0.2 to 0.4	0.2	17.75	16.21	20.49
0.4 to 0.5	0.4	2.22	3.18	6.17
0.5 to 0.6	0.5	2.22	3.18	6.17
0.6 to 0.8	0.6	0.27	0.38	0.61
-0.2 to -0.4	-0.4	16.89	20.00	20.45
Total		100.00	100.00	100.00

exponent γ can present quite marked differences depending not only on the thickness of the slab but also on its length in the particular climatic zone where the pavement is situated and even on the bending strength of the concrete.

Table 13 gives the values of exponent γ, taking as reference a standard axle of 130 kN and taking into account the previously mentioned parameters. These values range from 5.7 to 12.6; therefore, it takes considerably higher values than the value of 4 usually admitted.

The figures in Table 13 constitute another proof of the great influence of overloading on pavement behavior. The longer the slabs, the more pronounced is its influence.

TABLE 13 EQUIVALENCE FACTORS: VALUES OF γ EXPONENT IN THE EQUATION $(P/130)^{\gamma}$
(P = Azle Load and Standard Axle Load = 130 kN)

L (cm)	H (cm)	Climate: Maritime MR1	Maritime MR2	Standard Continental MR1	Standard Continental MR2	Extreme Continental MR1	Extreme Continental MR2
350	21	5.5	7.0	6.3	7.2	5.9	6.9
	23	5.7	6.5	5.9	6.8	5.7	6.7
	25	5.4	6.2	5.7	6.5	5.6	6.6
	28	5.4	6.1	5.6	7.2	5.7	6.6
400	21	5.6	7.4	6.6	7.6	6.4	7.6
	23	6.1	7.0	6.3	7.3	6.2	7.4
	25	5.9	6.8	6.2	7.3	6.6	7.3
	28	6.0	6.9	6.3	7.2	6.6	7.6
450	21	5.7	7.8	7.0	8.2	6.9	8.3
	23	6.4	7.5	6.7	7.9	6.9	8.3
	25	6.4	7.5	6.8	7.9	7.1	8.4
	28	7.0	8.0	7.3	8.3	7.7	8.8
500	21	5.8	8.4	7.5	9.0	7.7	9.4
	23	6.9	8.3	7.4	8.8	7.7	9.4
	25	7.1	8.4	7.6	9.0	8.1	9.6
	28	8.3	9.5	8.6	9.9	9.1	10.5
550	21	5.9	9.4	8.2	10.1	8.6	10.8
	23	7.6	9.3	8.2	10.0	8.8	10.8
	25	8.0	9.7	8.6	10.4	9.3	11.2
	28	10.2	11.7	10.5	12.0	11.0	12.6

Note: L = slab length, H = slab thickness, MR1, MR2 = modulus of rupture of the concrete, equal to 5.0 MPa and 4.5 MPa, respectively

CONCLUSIONS

1. The effects of the simultaneous action of traffic loads and thermal gradients do not correspond to the sum of traffic stresses and thermal stresses. When a pavement slab is curled downward the stresses due to traffic loads are greater than the sum of the thermal stresses and traffic stresses calculated separately. If the slab is curled upward, the stresses produced by the simultaneous action of thermal gradient and traffic loads are similar to or greater than the sum of the stresses calculated separately. Consequently, current design procedure is inadequate.

2. The length of slabs is an important parameter that must be considered in the design of pavements. The greatest fatigue damage occurs during the simultaneous action of traffic loads and thermal gradient when the latter value equals or exceeds 0.6 °C/cm. Consequently, the equivalence factors between axle loads are functions of the thickness and length of the slabs and depend on the frequency and value of the thermal gradients.

3. The equivalence between axle loads can be expressed by a relation like the AASHO equation, in which the exponent γ ranges between 5.5 and 12.6. γ depends on the geometric characteristics of the slabs, the climatic conditions of the environment, and the modulus of rupture of concrete.

REFERENCES

1. R. Crespo del Río. El espectro del tráfico pesado en España. *Revista Carreteras del MOPU,* March 1986.
2. E. S. Barber. Calculation of Maximum Pavement Temperature from Weather Reports. *Bulletin 168,* HRB, National Research Council, Washington, D.C., 1957, pp. 1-8.
3. K. Majidzadeh, G. J. Ilves, and H. Skyluth. *Mechanistic Design of Rigid Pavements,* Vols. I and II; *Design and Implementation Manual.* Final Report. FHWA, U.S. Department of Transportation, 1983.
4. H. M. Westergaard. Analytical Tools for Judging Results of Structural Tests of Concrete Pavements. *Public Roads,* Vol. 14, No. 11, Dec. 1933.
5. G. Pickett and G. K. Ray. Influence Charts for Concrete Pavements. *Proc.*, ASCE, Vol. 116, 1951.
6. L. Domenichini and A. Marchiona. Influence of Stress Range on Plain Concrete Pavement Fatigue Design. *Proc., 2nd International Conference on Concrete Pavement Design,* Purdue University, West Lafayette, Ind., 1981.

Publication of this paper sponsored by Committee on Rigid Pavement Design.

Effect of Concrete Overlay Debonding on Pavement Performance

THOMAS VAN DAM, ELEANOR BLACKMON, AND M. Y. SHAHIN

The objectives of this paper were to determine the effect of bond loss on response and performance of bonded concrete overlays and to examine present bonding techniques and bond loss detection methodologies. A finite-element model called ILLI-SLAB was used to evaluate pavement response to load, and Westergaard-Bradbury equations were used to determine curling stresses. It was found that loss of bond adversely affects maximum pavement tensile stress (thus fatigue life) and maximum pavement deflections. It is also believed that curling stresses may cause unbonded thin overlays to separate from the underlying slab, causing extremely high stress in the overlay if a load is applied. The only way bond can be obtained is to follow good construction techniques. A summary of these techniques is presented in the paper. On the basis of the deflection analysis it was concluded that it may be possible to detect bond loss using nondestructive testing of corner deflections.

The objective of this study, sponsored by the Federal Aviation Administration, was to determine the effect of bond loss on the structural behavior and future performance of a pavement. Recommended bonding methodologies and techniques for detection of delamination in bonded concrete overlays were also addressed.

In the last 25 years, the gross weights of aircraft have increased significantly, leading to increased stress in many pavements. Many airports have experienced significant changes from light to heavy aircraft or increases in traffic volume, or both. Fully bonded portland cement concrete (PCC) overlays are often used to increase an existing pavement's load-carrying capacity. A fully bonded overlay adds directly to the pavement's load-carrying capacity by creating a monolithic pavement structure.

This study addressed the effect of commercial aircraft loading on sections with bonded PCC overlays, a type of section that may occur at airports that have experienced growth. To this end a relatively thin (for airports) 8-in. slab was assumed with bonded overlays of 3, 6, or 9 in. Unbonded overlays with the same thicknesses were also examined to model the effect of debonding. A Boeing 727 was used for the loading analysis because it usually provides the most critical commercial aircraft loading.

Bonded overlays have been used on many projects (*1-4*) with varied results. When failure occurred, it was usually attributed to loss of bond at the pavement-overlay interface. Studies have shown (*4, 5*) that loss of bond is common to some degree in almost all bonded concrete overlays; but when a substantial loss of bond occurs, the slab no longer acts as a monolithic structure, thus reducing the structural capacity of the pavement.

U.S. Army Construction Engineering Research Laboratory, P.O. Box 4005, Champaign, Ill. 61820-1305.

APPROACH

To determine the effect bond loss has on the structural behavior of overlaid concrete pavements, stresses due to loading and temperature curling were examined. This study used two different slab sizes: a 12.5- × 15.0-ft slab and a 20.0- × 20.0-ft slab. The load was applied by a Boeing 727 aircraft with a gross weight of 170,000 lb, tire pressure of 168 psi, and a tire imprint area assumed to be 12 × 20 in. It was assumed that the original pavement had a thickness of 8 in., and the PCC overlay thickness was 3, 6, or 9 in. Two different subgrade modulus of reaction values (*K*-values of 200 and 500 pci) were used and the slabs were modeled with a load transfer efficiency (LTE) of 25 percent (stress unloaded side/stress loaded side = 0.25). The procedure was repeated for the unbonded case. The load was applied at two different locations on the slab to produce maximum tensile stress and deflection. Maximum tensile stress in the concrete slab was obtained through an edge loading condition at the center of the longitudinal joint. Maximum pavement deflection occurred when the load was applied at the corner of the slab.

To determine stresses due to loading, the pavement section was analyzed using a finite-element model called ILLI-SLAB. Developed at the University of Illinois in 1977, ILLI-SLAB uses the classical theory of a medium-thick plate on a Winkler foundation (*6*). This model can analyze one- or two-layer concrete pavements with joints or cracks, and it allows for different load transfer values. The model can also analyze a bonded or unbonded condition at the layer interface.

Concrete slabs are also subjected to stresses due to the temperature gradients through the slabs. These stresses, known as curling stresses, can be high enough to cause failure (*7-9*). During the day, positive temperature gradients (surface is hotter than the bottom) that form across the slab may be as great as 3°F/in. At night, when the bottom of the slab is warmer than the surface, a gradient of -1.5°F/in. can be obtained (*7, 8*). Westergaard (*10*) derived a set of equations for estimating the magnitude of the curling stresses at the interior and edge of a slab. Bradbury (*11*) developed coefficients to easily solve the Westergaard equations. The

Westergaard-Bradbury method for analyzing curling stresses was used in this study. Curling-stress equations have also been developed by Darter (*8*). Both equations were developed for monolithic sections and are probably not valid when examining sections with unbonded overlays that act independently from the underlying slab. For this reason, the more basic equation (Westergaard-Bradbury) was used for this attempt to model the curling stresses in overlays.

The most critical stresses developed through curling are due to the positive temperature gradient that occurs when the temperature of the top of the pavement is higher than that of the bottom. This positive temperature gradient produces tensile stresses in the bottom of the slab. Stresses due to an applied load will add to the curling stresses, producing a much more critical stress level. This phenomenon has been investigated by a number of researchers (*8-10*). In this study, the edge-curling stress was predicted for each slab by the Westergaard-Bradbury equation, and the curling stress was directly added to the load-induced maximum tensile stress to estimate the total maximum tensile stress for the slab.

This approach can only be applied for bonded concrete overlays, because when bond has been lost, the overlay and existing slab act independently. Two different approaches were used to analyze the unbonded case. The first approach was to treat the unbonded overlay as if it were a lone slab sitting on an extremely stiff subgrade and to use the Westergaard-Bradbury equation to determine the edge-curling stress in the overlay. This curling stress was then added to the stress due to loading in order to determine the total maximum tensile stress in the overlay.

The second approach assumed that the overlay had curled up off the underlying slab. When such separation of the overlay and the underlying slab occurs, the overlay will experience no support. Thus an applied load will create extremely high stresses in the overlay. The ILLI-SLAB finite-element model was used to examine two cases in which part of an overlay experienced no support. The two cases simulated areas of nonsupport at corner and interior positions (Figure 1). The aircraft load was placed over the area of nonsupport and the resulting stresses were determined.

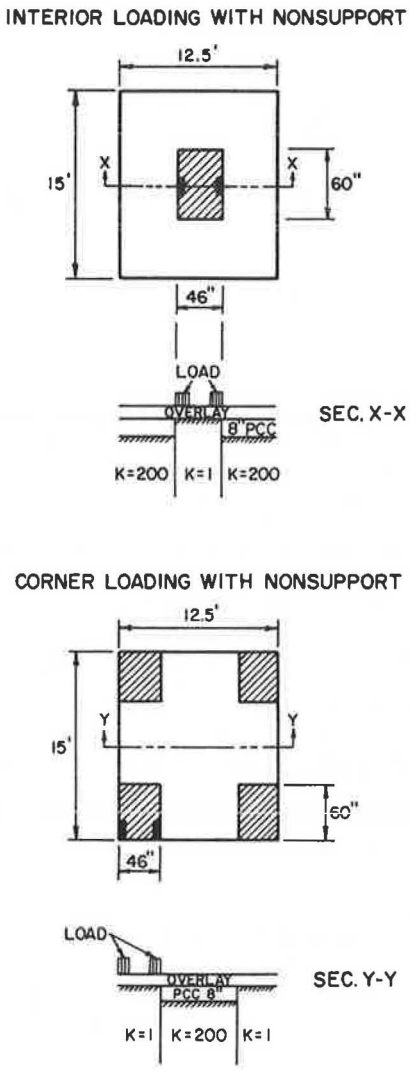

FIGURE 1 Boeing 727 interior and corner loading over areas of nonsupport.

ANALYSIS

The comprehensive analysis was performed assuming a Boeing 727 load. The maximum tensile stress and the maximum deflection induced by the applied load were determined using ILLI-SLAB. Curling stresses were determined using the Westergaard-Bradbury equations and ILLI-SLAB. The results of slab behavior due to load and temperature gradients are presented in the following subsections.

Loading Stresses

The maximum tensile stress occurs in the composite slab when it is subjected to edge loading along its longitudinal joint. A summary of stresses caused by a Boeing 727 loading is given in Table 1. The results are presented graphically in Figures 2-4. Figure 2 shows the maximum tensile stresses generated in the 12.5- × 15.0-ft slab for three overlay thicknesses and two different moduli of subgrade reaction. Figure 3 shows the same results for the 20.0- × 20.0-ft slab, and Figure 4 shows a comparison of the two slab sizes for modulus of subgrade reaction K = 200 pci.

From Figures 2 and 3, it can be observed that the maximum tensile stress in the slab is reduced by one-half when the overlay thickness is increased from 3 to 9 in. It is also evident that a stiffer subbase-subgrade leads to slightly lower maximum tensile stresses. As seen in Figure 4, when stresses in the 12.5- × 15.0-ft slab are compared with those in the 20.0- × 20.0-ft slab, little difference is noted. Thus slab size, at least within the range of the two slabs studied, has little influence on the resulting maximum tensile stresses caused by load.

Of primary interest is that loss of bond leads to a large increase in the maximum tensile stress in the slabs. It should be noted that the maximum tensile stress always occurs in the underlying slab except when the overlay is unbonded. When a bonded condition exists, the neutral axis is at the center of the

TABLE 1 MAXIMUM TENSILE STRESSES AND PAVEMENT LIFE FOR EDGE-LOADING CONDITION

Slab Size (ft)	Overlay Thickness (in.)	K (pci)	Overlay Bond	Stress (psi)	Pavement Life Coverages
12.5 × 15.0	3	200	Bonded	787	106
12.5 × 15.0	6	200	Bonded	547	777
12.5 × 15.0	9	200	Bonded	401	8,363
12.5 × 15.0	3	200	Unbonded	1,142	26
12.5 × 15.0	6	200	Unbonded	890	63
12.5 × 15.0	9	200	Unbonded	652[a]	272
12.5 × 15.0	3	500	Bonded	641	298
12.5 × 15.0	6	500	Bonded	466	2,416
12.5 × 15.0	9	500	Bonded	350	30,602
12.5 × 15.0	3	500	Unbonded	900	60
12.5 × 15.0	6	500	Unbonded	717	165
12.5 × 15.0	9	500	Unbonded	536[a]	888
20.0 × 20.0	3	200	Bonded	788	106
20.0 × 20.0	6	200	Bonded	588	493
20.0 × 20.0	9	200	Bonded	416	6,067
20.0 × 20.0	3	200	Unbonded	1,136	26
20.0 × 20.0	6	200	Unbonded	887	64
20.0 × 20.0	9	200	Unbonded	654[a]	867
20.0 × 20.0	3	500	Bonded	638	306
20.0 × 20.0	6	500	Bonded	465	2,456
20.0 × 20.0	9	500	Bonded	357	25,054
20.0 × 20.0	3	500	Unbonded	899	60
20.0 × 20.0	6	500	Unbonded	715	168
20.0 × 20.0	9	500	Unbonded	538[a]	867

[a]Maximum tensile stress in overlay.

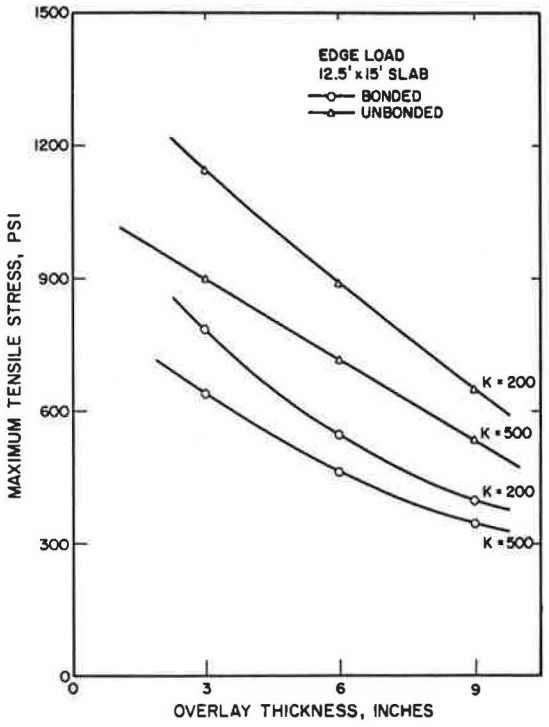

FIGURE 2 Effect of bonded and unbonded overlay thickness on tensile stress in 12.5- × 15.0-ft slab.

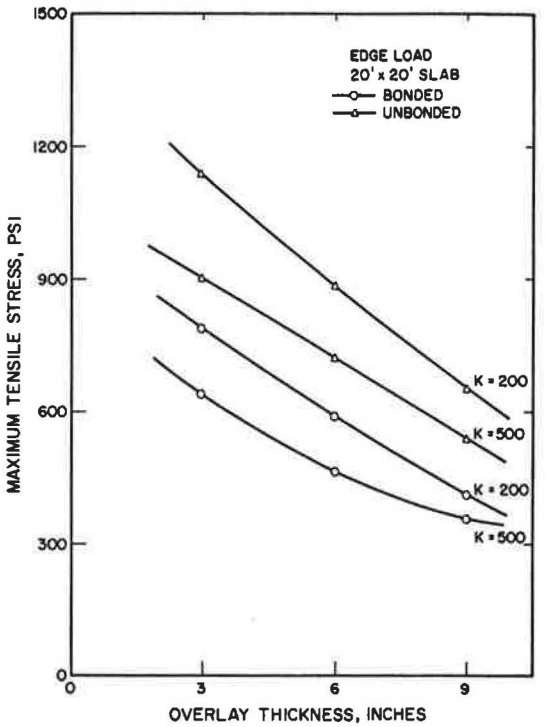

FIGURE 3 Effect of bonded and unbonded overlay thickness on tensile stress in 20.0- × 20.0-ft slab.

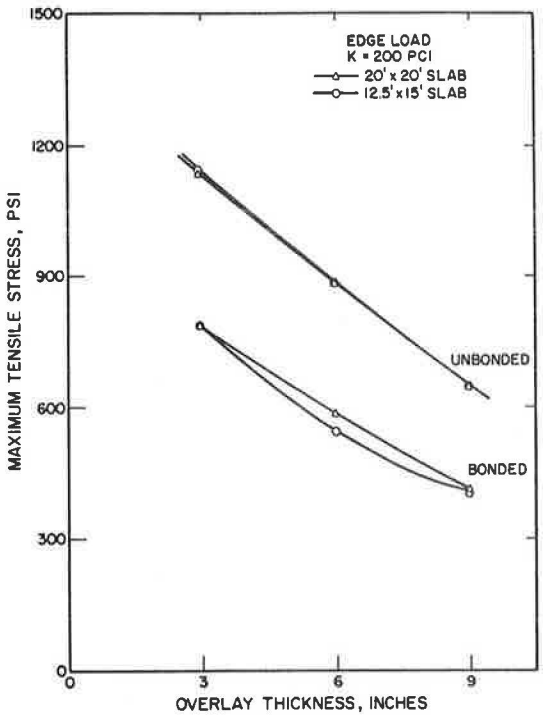

FIGURE 4 Effect of bonded and unbonded overlay thickness on slabs with subgrade K = 200 pci; stress for unbonded slabs is identical for both slab sizes.

composite slab; thus the stress at the top will have the same magnitude as that at the bottom, opposite only in direction (i.e., compression at top and tension at bottom, Figures 5 and 6). When fully bonded, the overlay will never experience tensile forces unless it is thicker than the underlying slab, and even then the tensile stresses will be quite small in comparison with the tensile forces generated in the bottom of the existing slab. For the unbonded case, each layer has a neutral axis placed at its center (Figures 5 and 6). The only time that more tensile stress could build up in the overlay than in the existing slab is when the overlay has a thicker section than the existing pavement. Table 2 gives the maximum tensile stresses that occur in the overlay for both the bonded and the unbonded condition.

The effect of these tensile stresses on pavement life was also analyzed. The modulus of rupture of the concrete was estimated using the following relationship developed by ERES Consultants (*12*):

$$MR = 209(E)^{0.736} \quad (1)$$

where E is the modulus of the concrete in millions of pounds per square inch.

For an E-value of 5 million psi, the MR was calculated to be 683 psi. When the modulus of rupture had been determined, a second equation, also developed by ERES Consultants (*12*), was used to estimate the number of applied stress repetitions (coverages) required to cause 50 percent cracking of the slabs. The Federal Aviation Administration defines one coverage as occurring when "each point in the pavement within the limits of the traffic lane has experienced a maximum stress, assuming the stress is equal under the full tire print" (*13*). A Boeing 727 has a pass (departure) to coverage ratio of 3.48. The ERES equation is as follows:

$$\text{Log (coverages)} = 2.27(MR/STRESS) + 0.056 \quad (2)$$

where

Log (coverages) = the number of coverages to 50 percent slab cracking,
MR = the third-point modulus of rupture calculated from the dynamic modulus of elasticity, and
$STRESS$ = the critical stress in the slab resulting from ILLI-SLAB.

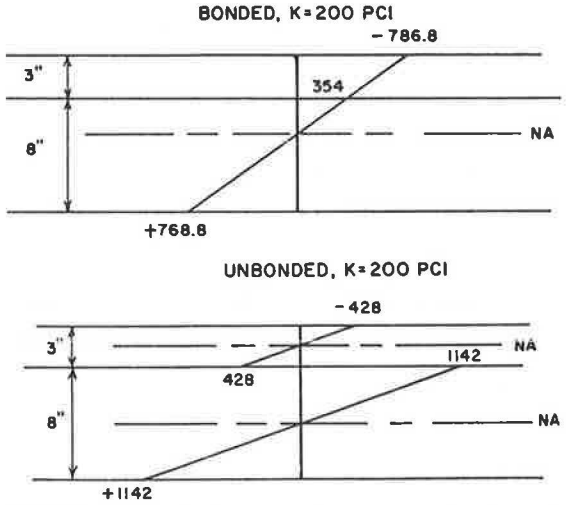

FIGURE 5 Neutral axes and maximum tensile and compressive stresses for bonded and unbonded 3-in. overlays.

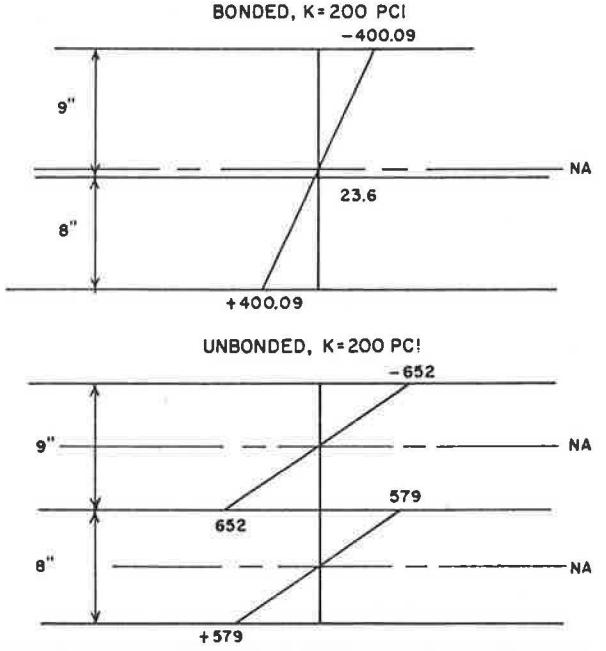

FIGURE 6 Neutral axes and maximum tensile and compressive stresses for bonded and unbonded 9-in. overlays.

TABLE 2 MAXIMUM TENSILE STRESSES CALCULATED IN THE OVERLAY FOR EDGE-LOADING CONDITION

Slab Size (ft.)	Overlay Thickness (in.)	K (pci)	Overlay Bond	Tensile Stress in Overlay (psi)
12.5 × 15.0	3	200	Bonded	-
12.5 × 15.0	6	200	Bonded	-
12.5 × 15.0	9	200	Bonded	23.6
12.5 × 15.0	3	200	Unbonded	428
12.5 × 15.0	6	200	Unbonded	668
12.5 × 15.0	9	200	Unbonded	652
12.5 × 15.0	3	500	Bonded	-
12.5 × 15.0	6	500	Bonded	-
12.5 × 15.0	9	500	Bonded	20.6
12.5 × 15.0	3	500	Unbonded	338
12.5 × 15.0	6	500	Unbonded	538
12.5 × 15.0	9	500	Unbonded	536
20.0 × 20.0	3	200	Bonded	-
20.0 × 20.0	6	200	Bonded	-
20.0 × 20.0	9	200	Bonded	24.5
20.0 × 20.0	3	200	Unbonded	426
20.0 × 20.0	6	200	Unbonded	665
20.0 × 20.0	9	200	Unbonded	654
20.0 × 20.0	3	500	Bonded	-
20.0 × 20.0	6	500	Bonded	-
20.0 × 20.0	9	500	Bonded	21.0
20.0 × 20.0	3	500	Unbonded	337
20.0 × 20.0	6	500	Unbonded	536
20.0 × 20.0	9	500	Unbonded	538

NOTE: Dashes indicate never in tension.

The resulting relationship between stress and coverages is shown in Figure 7. As can be seen, even relatively small increases in critical pavement tensile stress can lead to quite large decreases in pavement life. Using this relationship, the predicted pavement life for each slab condition was calculated (Table 1).

The following observations can be made:

1. Slab size, within the range of the two slab sizes studied, will not significantly alter predicted pavement life. A 9-in.-thick overlay bonded to a 20.0- × 20.0-ft. slab that rests on a subgrade with K = 500 pci is predicted to withstand 25,054 coverages whereas a similar bonded overlay on a 12.5- × 15.0-ft slab will withstand 30,602 coverages. As the overlays become thinner, the difference in the two predicted pavement lives becomes quite small.

2. Increasing the modulus of subgrade reaction will increase the number of coverages. For a 9-in. bonded overlay on a 20.0- × 20.0-ft slab and a subgrade K = 500 pci, a total of more than 25,000 coverages can be expected. If the subgrade stiffness is decreased to 200 pci, only 6,067 coverages are predicted for the same bonded overlay. In every instance, identical slabs will undergo less load-related tensile stress when supported by a stiffer subgrade.

3. Loss of bond will lead to a significant decrease in pavement life. A 9-in. bonded overlay on the 20.0- × 20.0-ft slab with a modulus of subgrade reaction K = 200 pci will provide for more than 6,000 coverages. Without the bond, the number of allowable coverages drops to 267. The substantial loss in pavement life caused by the absence of bond between the overlay and the existing slab emphasizes how critical bond is to pavement performance.

Failure of almost all pavement sections will occur at the bottom of the existing slab where the tensile stresses are greatest. The exceptions are the slabs that have a 9-in. debonded overlay; in that case the overlay will have higher tensile stress than the thinner underlying slab. It is evident from this examination that one of the most important parameters in determining the life of pavement and overlay is the quality of the bond.

The effect of debonding on deflection was also investigated. Maximum pavement deflection occurs when the load is applied to the corner of the slab. A summary of the maximum deflection results of the ILLI-SLAB model is given in Table 3. Figures 8-10 show the deflection data in graphic form. Stiffer subgrades will reduce deflection by a substantial amount—as much as 49 percent. Figure 8 shows the resulting deflections

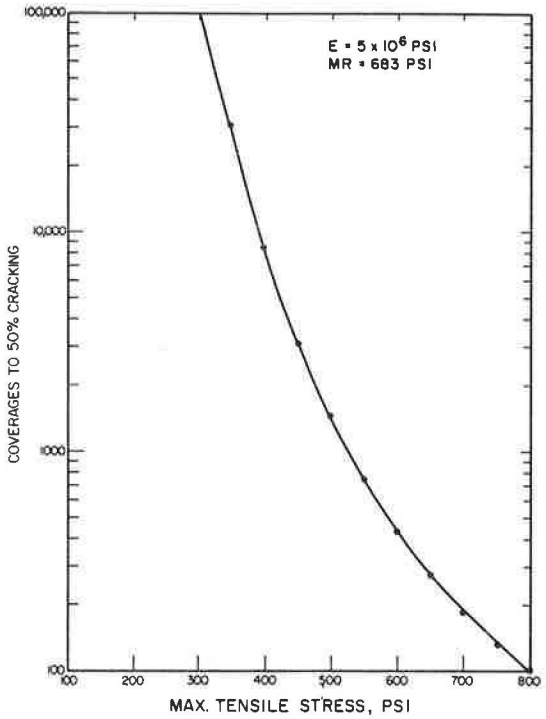

FIGURE 7 Effect of slab stresses on pavement life (coverages to 50 percent cracking).

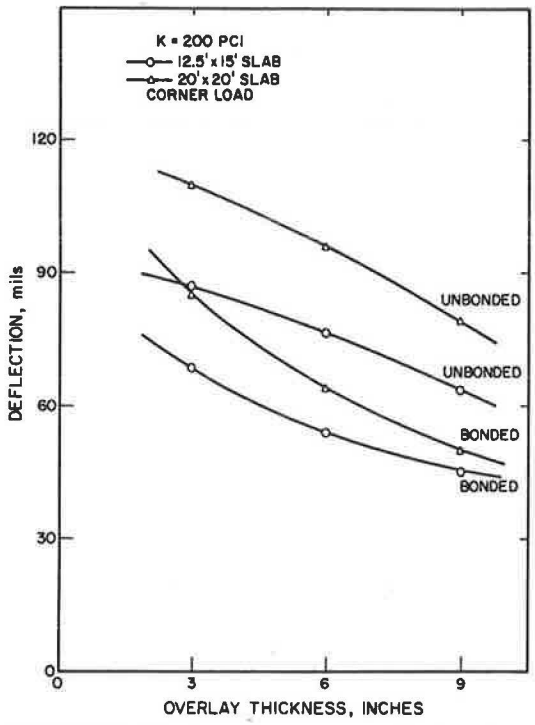

FIGURE 8 Maximum pavement deflection for varying overlay thicknesses in bonded and unbonded slabs with subgrade K = 200 pci.

TABLE 3 MAXIMUM CORNER DEFLECTIONS CALCULATED FOR CORNER LOADING

Slab Size (ft)	Overlay Thickness (in.)	K (pci)	Overlay Bond	Deflection (mils)
12.5 × 15.0	3	200	Bonded	68.8
12.5 × 15.0	6	200	Bonded	54.2
12.5 × 15.0	9	200	Bonded	45.5
12.5 × 15.0	3	500	Bonded	35.7
12.5 × 15.0	6	500	Bonded	28.8
12.5 × 15.0	9	500	Bonded	23.8
12.5 × 15.0	3	200	Unbonded	86.8
12.5 × 15.0	6	200	Unbonded	76.3
12.5 × 15.0	9	200	Unbonded	63.6
12.5 × 15.0	3	500	Unbonded	44.3
12.5 × 15.0	6	500	Unbonded	40.4
12.5 × 15.0	9	500	Unbonded	34.0
20.0 × 20.0	3	200	Bonded	85.9
20.0 × 20.0	6	200	Bonded	63.8
20.0 × 20.0	9	200	Bonded	50.4
20.0 × 20.0	3	500	Bonded	45.6
20.0 × 20.0	6	500	Bonded	36.0
20.0 × 20.0	9	500	Bonded	28.7
20.0 × 20.0	3	200	Unbonded	110.6
20.0 × 20.0	6	200	Unbonded	96.3
20.0 × 20.0	9	200	Unbonded	78.6
20.0 × 20.0	3	500	Unbonded	57.7
20.0 × 20.0	6	500	Unbonded	52.2
20.0 × 20.0	9	500	Unbonded	43.4

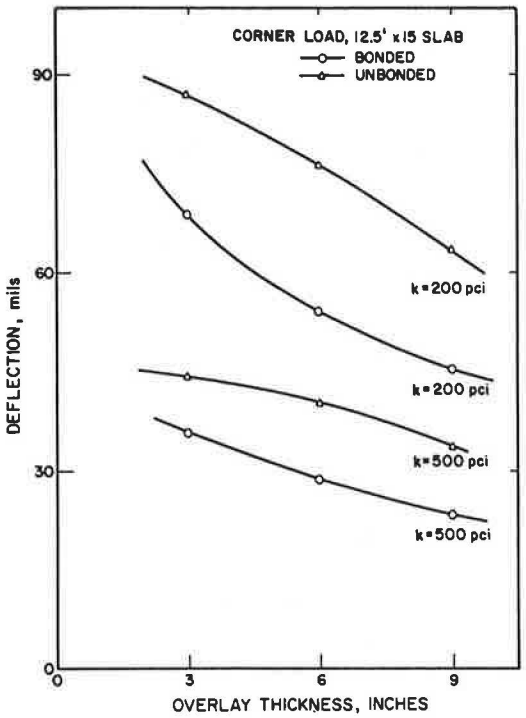

FIGURE 9 Maximum pavement deflection for varying overlay thicknesses in bonded and unbonded 12.5- × 15.0-ft slabs.

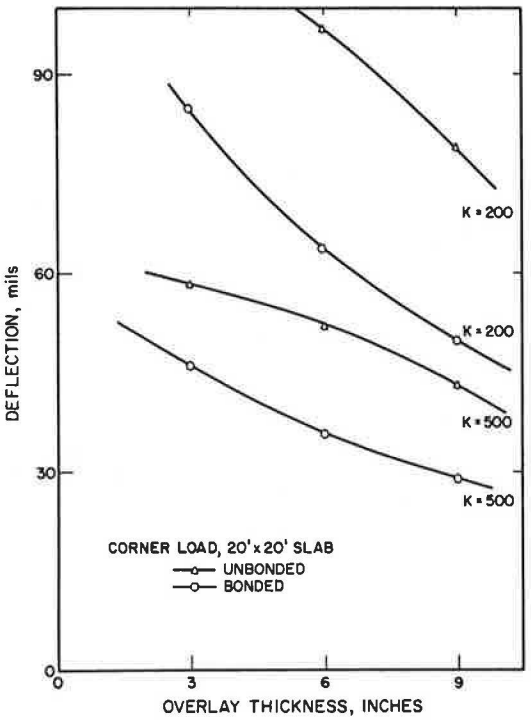

FIGURE 10 Maximum pavement deflection for varying overlay thicknesses in bonded and unbonded 20.0- × 20.0-ft slabs.

for two slab sizes. A larger slab is subjected to higher deflections if all other factors are held constant.

More important to this study is how maximum pavement deflection is influenced by the bond between the overlay and the existing slab. As can be seen in Figures 9 and 10, when all other factors are held constant, there is a large difference in corner deflections between the bonded and unbonded sections. Table 4 gives the percentage difference in deflection between bonded and unbonded sections. These differences vary from 19.4 to 35.9 percent with larger differences associated with thicker overlays. This finding is of great significance to the detection of debonding, as will be discussed later.

Curling Stresses

Temperature differentials that occur in the slab produce other stresses in the pavement. Depending on the climatic conditions, these stresses, known as curling stresses, can be extremely high. The Westergaard-Bradbury equations were used to predict the magnitude of the stresses, which developed at the interior and edge of a slab, caused by the slab's resistance to curling. In the analysis, a temperature gradient of 3°F/in. was used and values were calculated for 12.5- × 15.0-ft and 20.0- × 20.0-ft slabs 11, 14, and 17 in. thick. These thicknesses correspond to 3-, 6-, and 9-in. fully bonded overlays on an 8-in. slab. Two modulus of subgrade reaction values were examined, 200 and 500 pci. The results of this analysis are given in Table 5.

The effects of the combined load- and temperature-induced stresses on pavement design and performance were not the primary objective of this study, but this condition is extremely important in the evaluation of the effect of bond loss on the performance of bonded overlays. When the stress due to load is added to the edge-curling stress, extremely high stress levels are obtained. Table 6 gives the total tensile stress found when the stresses due to edge loading and temperature curling are added. The bonded condition is easily evaluated because it can be treated as a monolithic slab and all of the tensile stresses occur in the bottom of the slab. The Westergaard-Bradbury equations for layered systems are applicable to the bonded condition. However, the equations are not directly applicable to the unbonded condition because it consists of two separate layers.

The temperature gradient across the slab is not linear; it undergoes the greatest change in the top 4 in. of the pavement surface (Figure 11) (*14*). Therefore the highest temperature gradient will be located in the overlay, not in the underlying slab. It is believed that this condition can lead to the separation of the overlay from the original pavement when the temperature gradient is high and bond is absent. If a positive temperature gradient exists in the slab (the pavement surface is hotter than the bottom) and the overlay separates from the underlying slab, the weight of the overlay is supported by its corners and edges. If an interior load is then applied, large tensile stresses occur in the bottom of the overlay near the corners. If the temperature gradient is negative (i.e., warmer on the bottom than the top), the corners have a tendency to curl up off the underlying support. A corner load applied to the nonsupported area causes extremely high stresses in the top of the overlay.

TABLE 4 DEFLECTION DIFFERENCE BETWEEN SLABS WITH BONDED AND UNBONDED OVERLAYS

Slab Size (ft)	Overlay Thickness (in.)	K (pci)	Deflection (mils)		Percentage Difference
			Bonded	Unbonded	
12.5 × 15.0	3	200	68.8	86.8	20.7
12.5 × 15.0	6	200	54.2	76.3	29.0
12.5 × 15.0	9	200	45.5	63.6	28.5
12.5 × 15.0	3	500	35.7	44.3	19.4
12.5 × 15.0	6	500	28.8	40.4	28.7
12.5 × 15.0	9	500	23.8	34.0	30.0
20.0 × 20.0	3	200	84.9	110.6	23.2
20.0 × 20.0	6	200	63.8	96.3	33.8
20.0 × 20.0	9	200	50.4	78.6	35.9
20.0 × 20.0	3	500	45.6	57.7	21.0
20.0 × 20.0	6	500	36.0	52.2	31.0
20.0 × 20.0	9	500	28.7	43.4	33.9

TABLE 5 COMPARISON OF EDGE AND INTERIOR STRESSES FOR BONDED SLABS

Slab Size (ft)	Total Slab Thickness (in.)	K (pci)	Edge Stress (psi)	Interior Stress (psi)
12.5 × 15.0	11	200	247.5	276.6
12.5 × 15.0	14	200	220.5	236.8
12.5 × 15.0	17	200	108.4	189.1
12.5 × 15.0	11	500	342.4	392.0
12.5 × 15.0	14	500	351.8	396.1
12.5 × 15.0	17	500	331.5	362.6
20.0 × 20.0	11	200	305.2	461.0
20.0 × 20.0	14	200	372.8	494.1
20.0 × 20.0	17	200	357.0	502.5
20.0 × 20.0	11	500	412.5	485.3
20.0 × 20.0	14	500	472.5	555.9
20.0 × 20.0	17	500	497.2	585.0

TABLE 6 TOTAL TENSILE STRESS FROM LOAD AND TEMPERATURE IN SLABS WITH BONDED OVERLAYS

Slab Size (ft)	Total Slab Thickness (in.)	Subgrade K (pci)	Tensile Stress (psi)		
			ILLI-SLAB	Westergaard Curling	Total
12.5 × 15.0	11	200	787	248	1,035
12.5 × 15.0	14	200	547	220	767
12.5 × 15.0	17	200	401	108	509
12.5 × 15.0	11	500	641	342	983
12.5 × 15.0	14	500	466	352	818
12.5 × 15.0	17	500	350	332	682
20.0 × 20.0	11	200	788	305	1,093
20.0 × 20.0	14	200	588	373	961
20.0 × 20.0	17	200	416	357	773
20.0 × 20.0	11	500	638	412	1,050
20.0 × 20.0	14	500	465	472	937
20.0 × 20.0	17	500	357	497	854

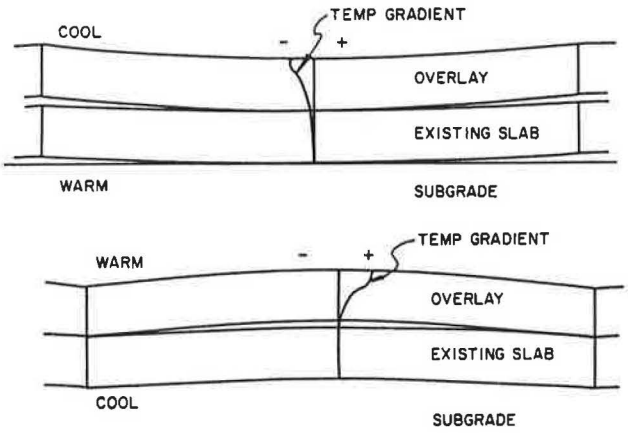

FIGURE 11 Slab separation caused by differential curling of unbonded slabs.

The phenomenon of differential slab curling in unbonded overlays was investigated by Lall and Lees (*15*). It was found that, when the corners of the overlay curl up off the underlying layer, the load-stress relation indicates that the slab undergoes three distinct phases as the incremental load is applied: (a) free bending, (b) support of the overlay by the underlying layer increasing from zero to full, and (c) full support of the overlay. Under these conditions, the critical stress will always occur in the overlay, not in the underlying slab.

The first attempt to determine the total tensile stresses that occur in debonded overlays used the calculated ILLI-SLAB stresses and the Westergaard-Bradbury equation for slabs 3, 6, and 9 in. thick on a very stiff subgrade (K = 10,000 pci). The results of the Westergaard-Bradbury analysis are given in Table 7. Because the Westergaard-Bradbury equations can only be used for one-layer systems, the use of a very stiff subgrade was an attempt at modeling the existing slab. For this analysis to be valid, the slabs would have to remain completely in contact with the underlying slab so that full support could be maintained. As mentioned, the overlay and existing slab may curl differentially as shown in Figure 11. Also, it is unlikely that the Westergaard-Bradbury equations were ever intended for use with such a high subgrade stiffness, which casts doubt on the validity of the results. The curling stress for each overlay was added to the load-induced tensile stress in each overlay calculated using ILLI-SLAB. Table 7 gives the total maximum tensile stress in the overlay found using this method. It is noted that these total maximum tensile stresses increase as the overlay becomes thicker. Because of the assumption that constant support is maintained and the limitations of the Westergaard-Bradbury equations, it is thought that this approach does not accurately represent actual pavement response.

A second approach was used in an effort to determine the total maximum tensile stress that occurs in an unbonded overlay that curls off the underlying slab. ILLI-SLAB was used to model two 12.5- × 15.0-ft overlaid slabs that contained areas of nonsupport (Figure 1). The wheel loads were placed over the nonsupported areas, and the resulting stresses are given in Table 8. These stresses are due only to the applied load. ILLI-SLAB considers the self-weight of the slab to be equal to zero, thus producing no stress in the slab due to its own weight. ILLI-SLAB does, however, incorporate the increased load-related stress levels produced when the overlay is not supported by the underlying slab.

It is admitted that the stresses that appear in Table 8 are unrealistically high because of the inability of the present ILLI-SLAB model to add support when the curled overlay comes into contact with the underlying slab. It is noted that any separation between the two slabs would be quite small, and they would readily come into contact if load were applied. Thus the high calculated stresses are not a true representation of field response.

There is, nevertheless, value in the data. The first point to be made is that the magnitude of the stress is many times greater for the thinner overlays than for the thicker overlays. The 3-in. overlay for the corner loading condition had 10 times the stress of that found for the 9-in. overlay. It must be realized that the 3-in. overlay will also have a greater

TABLE 7 TOTAL TENSILE STRESS IN UNBONDED OVERLAYS FROM LOAD AND TEMPERATURE

Slab Size (ft)	Overlay Thickness (in.)	Subgrade K (pci)	Tensile Stress (psi)		
			ILLI-SLAB	Westergaard Curling[a]	Total
12.5 × 15.0	3	200	428	116	544
12.5 × 15.0	6	200	668	232	900
12.5 × 15.0	9	200	652	348	1,000
12.5 × 15.0	3	500	338	116	454
12.5 × 15.0	6	500	538	232	770
12.5 × 15.0	9	500	536	348	884
20.0 × 20.0	3	200	426	116	542
20.0 × 20.0	6	200	665	232	897
20.0 × 20.0	9	200	654	348	1,002
20.0 × 20.0	3	500	337	116	453
20.0 × 20.0	6	500	536	232	768
20.0 × 20.0	9	500	538	348	886

[a]Westergaard calculations for unbonded overlays made using K = 10,000 psi (assumed stiffness of underlying slab).

TABLE 8 MAXIMUM TENSILE STRESS IN NONSUPPORTED UNBONDED OVERLAYS

Overlay Thickness (in.)	Load Position	Maximum Overlay Stress (psi)	Slab Deflection (in.)
3	Corner	16,278	2.50
6	Corner	3,292	0.82
9	Corner	1,628	0.48
3	Interior	2,332	0.14
6	Interior	1,271	0.08
9	Interior	802	0.05

tendency to curl off its support because (a) its average temperature gradient will be higher than that of the thicker overlays because the largest change in temperature occurs in the top 4 in. of the pavement surface and (b) it has less self-weight to prevent it from curling than do the thicker overlays. Thus a thinner overlay is much more likely to curl off its support than is a thicker overlay, and when loaded the thinner nonsupported overlay will experience greater stress than a thicker nonsupported overlay.

A second point to be made is that the stresses determined for the interior condition were much less than those found for the corner condition. These two findings agree with data obtained from field surveys in which debonding of bonded overlays results in characteristic corner and edge cracking of the overlay. This problem is far more prevalent in thin bonded overlays, possibly because the overlay has curled up off the underlying surface. Maximum tensile stress always occurs at the bottom of the underlying slab for thin overlays if the two layers remain in contact. Only when the two layers separate because of curling will the maximum tensile stress occur in the overlay. This evidence suggests that it is critical that a strong bond be established at all parts of the slab, particularly at the edges and corners.

ACHIEVING BOND

Obtaining a good bond between the overlay and the existing pavement section is crucial to the successful performance of the overlay. Much has been written about proper construction techniques for bonded concrete overlays. The following is a brief summary of some important aspects of achieving a good bond.

The most important factor in obtaining a successful bond is preparation of the existing surface before placement of the overlay. According to Bergren (*4*), "The most critical factor that affects bond . . . is that the surface must be extremely clean and dry prior to the placement of the grout and subsequent placement of the concrete resurfacing." Common surface-cleaning techniques use high-pressure water, sandblasting, or metal shot to remove surface contaminants. When the unsound concrete and surface contaminants have been removed from the existing pavement (and it has been allowed to dry if water cleaning was used), a bonding medium must be applied. Bonding media such as sand-cement grouts, neat cements, or commercially available epoxies and latex cements have been used successfully. It is important that the bonding agent not be allowed to dry before placement of the resurfacing material, otherwise a good bond cannot be obtained.

Research has shown that when bond has been established it will remain. Gillette (*1*) stated that "wherever loss of bond occurs, it probably developed soon after construction; little or no growth in the loss of bond area occurs over a period of time and under traffic." Thus when bond loss occurs it is due to conditions present during or shortly after construction. The primary cause of bond loss is to be found in the preparation of the existing pavement surface. Inadequate removal of unsound concrete or tire rubber, paint strips, and oil could prevent the bond from developing. A wet pavement surface, a thick layer of grout, or thin and watery grout could also contribute to bond loss. When bond is lost, characteristic distress occurs in the resurfacing, such as edge and corner breaks caused when the delaminated areas are subjected to load. Starting as hairline cracks, the distress eventually spalls and ravels and may result in displacement of the broken overlay.

DETECTING DEBONDING

Present practices rely on "sounding" of the pavement surface or coring to determine if debonding has occurred. Sounding of the pavement can be done manually by dropping a steel rod onto the surface or striking it with a hammer. A delaminated overlay will resound with a thud, and a bonded pavement will ring. There is also automated equipment that is based on this principle. Cores from an overlaid section can be visually and physically examined to determine if debonding has occurred. Both of these procedures are time consuming and expensive and are not normally done during routine pavement evaluation.

The results of the ILLI-SLAB analysis indicate that debonded sections have significantly higher corner deflections under load than do bonded sections, even without differential curling. Therefore it is theoretically possible to find debonding between the overlay and the existing slab by comparing the corner deflections produced through nondestructive testing (NDT) with those calculated using a finite-element model. Significantly higher NDT corner deflections would indicate that a problem in the pavement structure may exist and that one of the possible causes could be loss of bond between the

layers. Further examination of the distressed locations, possibly a limited coring program, could then be used to positively identify the causes of the higher deflection.

There are some problems that may possibly be encountered with this proposed procedure. The first can be attributed to NDT itself. Great variation in deflections can occur because of changes in weather or seasonal changes. The NDT program must be well planned, and such factors must be taken into account when deflections are calculated. Second, it would probably be common for slabs to contain both bonded and debonded areas. At the present time, ILLI-SLAB cannot model this condition; thus how partial bonding influences corner deflection is not known. Further investigation and field verification are necessary to prove the proposed method.

CONCLUSION

This study has shown that portland cement concrete slabs composed of an existing slab and a bonded overlay respond to load and curling forces differently than does an existing slab with an unbonded overlay. The absence of bond destroys the monolithic structure of the pavement section, detrimentally affecting the maximum pavement tensile stress and deflection due to load. Curling stresses are a major factor in the total maximum tensile stress in the pavement section, but they are not easily determined for the unbonded condition. The following conclusions are drawn from this study:

1. Maximum pavement tensile stress and deflection due to load decrease as subgrade becomes stiffer for both the bonded and the debonded overlay condition.
2. For the two slab sizes studied, maximum tensile stress due to load is relatively unaffected by slab size whereas maximum deflection increases as slab size increases.
3. The existence of a good bond between the overlay and the existing slab greatly reduces maximum tensile stress and corner deflections due to load.
4. An unbonded overlay may separate from the underlying slab because of a high temperature gradient across the overlay, the relatively low self-weight of the overlay, and the extremely stiff supporting layer.
5. Thinner unbonded overlays are more likely to separate from the underlying slab and will suffer higher maximum tensile stresses due to load than do thicker overlays.
6. Good construction practices must be used to guarantee that a good bond forms between the overlay and the existing pavement.
7. It may be possible to use NDT corner deflections to determine if debonding of the overlay has occurred.

REFERENCES

1. R. W. Gillette. A 10-Year Report on Performance of Bonded Concrete Resurfacings. In *Highway Research Record 94*, HRB, National Research Council, Washington, D.C., 1965, pp. 61-76.
2. M. I. Darter and E. J. Barenberg. *Bonded Concrete Overlays: Construction and Performance.* Paper GL-80-11. U.S. Army Engineer Waterways Experiment Station, Vicksburg, Miss., Sept. 1980.
3. E. J. Felt. Resurfacing and Patching Concrete Pavements with Bonded Concrete. *HRB Proc.*, Vol. 35, 1956, pp. 444-469.
4. J. V. Bergren. Bonded Portland Cement Concrete Resurfacing. In *Transportation Research Record 814*, TRB, National Research Council, Washington, D.C., 1981, pp. 66-70.
5. *Resurfacing with Portland Cement Concrete.* NCHRP Project 99. TRB, National Research Council, Washington, D.C., Dec. 1982.
6. M. R. Thompson, E. J. Barenberg, A. M. Ioannides, and J. A. Fischer. *Development of a Stress-Dependent Finite Element Slab Model.* Department of Civil Engineering, University of Illinois, Urbana, 1983.
7. L. W. Teller and E. C. Sutherland. The Structural Design of Concrete Pavements, Part 2: Observed Effects of Variations in Temperature and Moisture on the Size, Shape, and Stress Resistance of Concrete Pavement Slabs. *Public Roads*, Vol. 16, No. 9, 1935.
8. M. I. Darter. *Design of Zero-Maintenance Plain Jointed Concrete Pavement*, Vol. I: *Development of Design Procedure.* FHWA Report FHWA-RD-77-111. FHWA, U.S. Department of Transportation, June 1977.
9. E. J. Yoder and M. W. Witczak. *Principles of Pavement Design*, 2d ed. Wiley-Interscience, New York, 1975.
10. H. M. Westergaard. Analysis of Stresses in Concrete Pavements Due to Variations in Temperature. *HRB Proc.*, Vol. 6, 1926, pp. 201-217.
11. R. D. Bradbury. *Reinforced Concrete Pavements.* Wire Reinforcement Institute, Washington, D.C., 1938.
12. ERES Consultants. *Non-Destructive Structural Evaluation of Airfield Pavements.* U.S. Army Engineer Waterways Experiment Station, Vicksburg, Miss., Dec. 1982.
13. *Airport Pavement Design and Evaluation.* Advisory Circular 150/5320-6C. FAA, U.S. Department of Transportation, Dec. 7, 1978.
14. B. J. Dempsey. *A Heat-Transfer Model for Evaluating Frost Action and Temperature Related Effects in Multilayered Pavement Systems.* Ph.D. dissertation. University of Illinois, Urbana, 1969.
15. B. Lall and G. Lees. Analysis of Stresses in Unbonded Concrete Overlay. In *Transportation Research Record 930*, TRB, National Research Council, Washington, D.C., 1983, pp. 25-31.

The views of the authors do not purport to reflect the position of the Department of the Army or the Department of Defense.

DISCUSSION

GEORGE T. KOROVESIS AND ANASTASIOS M. IOANNIDES
University of Illinois, Urbana, Ill. 61801.

The authors have undoubtedly presented a valuable piece of work—an attempt to determine the effect of debonding of concrete overlays on pavement response. As they point out, when it comes to the calculation of curling stresses in a slab resting on a dense liquid (Winkler) subgrade, the only analytical model available is that proposed by Westergaard. He suggested that "stresses due to variations of temperature

are to be combined with the stresses due to the loads" and that "this combination, in most cases, is a simple matter of addition" (*1*). Since the 1920s superposition has been the conventional way of investigating this combined effect [see, for example, Bradbury (*2*)], although as early as 50 years ago Teller and Sutherland (*3*) provided experimental data indicating the shortcomings of this approach. The authors have also used it to obtain the total stress, by summing the stress due to the load alone plus the stress due to the temperature differential alone.

The validity of the superposition approach depends on whether the following two basic conditions are met in the calculation of both of the individual stress components:

- Small deformations and
- Same boundary conditions.

Even if it is accepted that the deformations are indeed small in the two cases, it cannot usually be accepted that the boundary conditions are the same. If a flat slab is loaded, practically all points on its bottom surface are in contact with the subgrade (except, perhaps, for a few points far away from the load). However, under curling conditions, a large portion of the slab may lose contact with the subgrade, depending on the temperature differential and the radius of relative stiffness. If load is then placed on an unsupported area, superposition will not apply.

Results from ILLI-SLAB given in Table 9 illustrate this assertion. They were obtained using a new subroutine recently implemented in ILLI-SLAB to calculate stresses due to curling and external loads, combined or individually, and account for the presence of gaps underneath the slab and for loss of support. The finite-element model employed is the one proposed by Huang and Wang (*4*) and Chou (*5*). Through an iterative procedure, this formulation also accommodates the regaining of subgrade support.

The limited amount of data given in Table 9 indicates that edge loading generally remains critical with respect to stresses, especially under a positive (daytime) temperature differential. Under a high negative (nighttime) gradient, a slab resting on a stiff subgrade may develop a higher combined stress under corner loading. The total stress computed by superposition underestimates the corresponding one from ILLI-SLAB in the cases of interior and edge loading when the slab is under a positive gradient, particularly when the temperature differential is large and the subgrade is stiff. On the other hand, superposition will lead to a conservative estimate of the combined stress during nighttime conditions, as well as under corner loading during the day especially for soft subgrades and a large positive differential. It is therefore observed that superposition and ILLI-SLAB agree only when the two previously mentioned conditions are satisfied (i.e., when a low gradient is applied on a slab resting on a soft subgrade).

Note that, in practice, the wisdom of relying on curling stresses to relieve part of the stress induced by external loads is debatable. Fortunately, given that for interior and edge loading this will occur only under nighttime conditions, the decision to allow for such stress relief is largely inconsequential as far as the fatigue life of the pavement is concerned.

Westergaard's theory (*1*), in the form of the Bradbury (*2*) coefficient (C), has been used by the authors to obtain curling stresses. This theory is also based on certain assumptions and should not be used indiscriminately. The two basic assumptions are

- Infinite and weightless slab and
- Full contact between slab and subgrade.

Other pertinent assumptions may be found elsewhere (*6*).

The data in Table 10 indicate that, for relatively large slabs resting on a soft subgrade and under a small temperature differential, there is good agreement between ILLI-SLAB results and Westergaard theory. When the basic assumptions are not fulfilled, a finite-element program like ILLI-SLAB, which can take into account the self-weight of the slab and the loss of subgrade support, should be used instead of the Westergaard theory. ILLI-SLAB results in Table 10 indicate that the case of a negative temperature differential is not merely a mirror image of the corresponding positive gradient condition, as suggested by Westergaard and Bradbury. Under a positive gradient a short slab resting on a stiff

TABLE 9 COMPARISON OF SUPERPOSITION AND ILLI-SLAB RESULTS

K (psi)	ΔT (°F)	Interior Load				Stress Under Edge Load (psi)				Corner Load			
		L	C	TS	TI	L	C	TS	TI	L	C	TS	TI
200	-21	384	-64	320	293	658	-26	632	579	-482	-54	-536	-413
200	-42	384	-83	301	241	658	-32	626	511	-482	-62	-544	-418
200	+21	384	70	454	484	658	40	698	753	-482	72	-410	-378
200	+42	384	89	473	585	658	55	713	839	-482	97	-385	-332
500	-21	329	-84	245	212	579	-33	546	456	-415	-69	-484	-435
500	-42	329	-101	228	163	579	-36	543	387	-415	-77	-492	-449
500	+21	329	88	417	509	579	59	638	744	-415	92	-323	-330
500	+42	329	105	434	661	579	72	651	880	-415	113	-302	-268

NOTE: Slab is 12.5 × 15.0 ft; E = 5 million psi, μ = 0.15, h = 14 in.; ε_t = 5×10^{-6} in./in./°F; load = B-727 (two loads 12 × 20 in. at 268 psi); L = stress due to external load; C = curling stress due to temperature differential; TS = total stress (superposition); TI = total stress (ILLI-SLAB). All stresses are tensile and are positive when at the bottom of the slab and negative when at the top. For each loading condition, all stresses act at the same location.

TABLE 10 COMPARISON OF BRADBURY AND ILLI-SLAB CURLING STRESSES

				Stress at Interior (psi)					
				δT = +1.5°F/in.			δT = -3.0°F/in.		
K (pci)	h (in.)	Lx/l	Ly/l	IS	B	Percentage	IS	B	Percentage
50	8	4.16	3.33	64	61	105	-103	-121	85
50	8	5.55	3.33	107	106	101	-183	-212	86
50	10	3.52	2.82	50	48	104	-80	-99	81
50	10	4.70	2.82	100	98	102	-160	-194	82
50	10	5.87	2.82	138	138	100	-239	-277	86
50	10	7.05	2.82	159	161	99	-297	-323	92
50	14	2.74	2.19	30	28	107	-51	-60	85
50	14	3.65	2.19	75	71	106	-115	-133	86
500	8	7.40	5.92	119[a]	145	82	-187	-291	64
500	8	9.87	5.92	146	148	99	-262	-295	89
500	10	6.26	5.01	113[a]	162	70	-155	-325	48
500	10	8.35	5.01	159[a]	182	87	-254	-365	70
500	10	10.44	5.01	176	179	98	-320	-358	89
500	10	12.53	5.01	177	176	101	-339	-352	96
500	14	4.87	3.89	91[a]	159	57	-110	-317	35
500	14	6.49	3.89	165[a]	221	75	-197	-442	45

NOTE: Slab length = 15 to 30 ft; slab width = 12 ft; E = 4 million psi; μ = 0.15; $\varepsilon_t = 5 \times 10^{-6}$ in./in./°F; IS = ILLI-SLAB; B = Bradbury (interior); Percentage = (IS/B) × 100%. All stresses are tensile and positive when at the botton of the slab and negative when at the top.
[a]A higher stress occurs at the edge.

subgrade may experience a maximum curling stress at its edge rather than at the interior.

The theoretical curling stress will underestimate ILLI-SLAB's prediction when a short slab is under a positive temperature differential and the subgrade is soft. The reverse is true when a short slab rests on a stiff subgrade or is under a negative gradient. Slab length is thus a more important parameter when the temperature differential is considered than it is under an external load alone. The slab size ratio (L/l), of the slab length to the radius of relative stiffness, required for the development of the infinite-slab bending stress under an external load, was found to be only about 5.0 (*7*). A value closer to 10.0 is indicated by the curves in Figure 12 [i.e., slab size remains influential even with much larger slabs (*2*)]. Longer slabs under the same temperature differential are subject to more bending action because a greater part of the slab loses contact with the subgrade.

Note that a stiffer subgrade does not always mean lower stresses in the slab or a longer life expectancy for the pavement when combined stresses are considered. Examples of this are given in Tables 9 and 10, in which curling stresses are higher for stiffer subgrades, as both ILLI-SLAB and the Westergaard-Bradbury theory indicate. This effect becomes more pronounced for shorter slabs under lower gradients.

It should be pointed out that there is appreciable difference between the curve for the coefficient C given by Bradbury (*2*, Figure 2) and that given by Yoder and Witczak (*8*, Figure 3.4). The original by Bradbury, which also agrees with Westergaard's data (*1*), is probably a better choice and was used in deriving the results in Table 10. Both curves are reproduced in Figure 12.

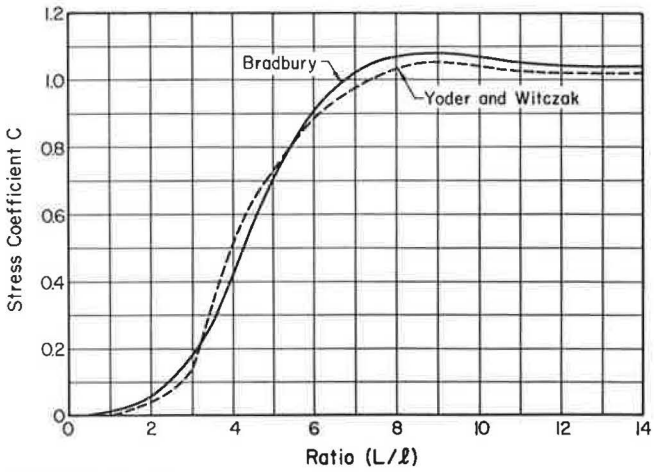

FIGURE 12 Chart for curling stress coefficient (C).

REFERENCES

1. H. M. Westergaard. Analysis of Stresses in Concrete Pavements Due to Variations of Temperature. *HRB Proc.*, Vol. 6, 1926, pp. 201-217.
2. R. D. Bradbury. *Reinforced Concrete Pavements.* Wire Reinforcement Institute, Washington, D.C., 1938.
3. L. W. Teller and E. C. Sutherland. The Structural Design of Concrete Pavements, Part 2: Observed Effects of Variations in Temperature and Moisture on the Size, Shape, and Stress Resistance of Concrete Pavement Slabs. *Public Roads*, Vol. 16, No. 9, 1935.
4. Y. H. Huang and S. T. Wang. Finite-Element Analysis of Rigid Pavements with Partial Subgrade Contact. In *Transportation Research Record 485*, TRB, National Research Council, Washington, D.C., 1974, pp. 39-54.

5. Y. T. Chou. *Structural Analysis Computer Programs for Rigid Multicomponent Pavement Structures with Discontinuities—WESLIQID and WESLAYER*. Reports 1-3, Technical Report GL-81-6. U.S. Army Engineer Waterways Experiment Station, Vicksburg, Miss., May 1981.
6. H. M. Westergaard. Stresses in Concrete Pavements Computed by Theoretical Analysis. *Public Roads*, Vol. 7, No. 2, April 1926. (Also in *HRB Proc.*, Vol. 5, Part I, 1926, pp. 90-112 as Computation of Stresses in Concrete Roads.)
7. A. M. Ioannides, M. R. Thompson, and E. J. Barenberg. Westergaard Solutions Reconsidered. In *Transportation Research Record 1043*, TRB, National Research Council, Washington, D.C., 1985, pp. 13-23.
8. E. J. Yoder and M. W. Witczak. *Principles of Pavement Design*, 2d ed. Wiley-Interscience, New York, 1975.

AUTHORS' CLOSURE

The authors appreciate the additional insights into debonded concrete overlay temperature- and load-induced stresses presented by Korovesis and Ioannides.

Publication of this paper sponsored by Committee on Pavement Rehabilitation.